Title
A 2D-local linear stability analysis of asymptotically-expanded jet-in-crossflows

Author
Ren, Da Wei David

Publication Date
2023

Peer reviewed|Thesis/dissertation

UNIVERSITY OF CALIFORNIA

Los Angeles

A 2D-local linear stability analysis of asymptotically-expanded jet-in-crossflows

A dissertation submitted in partial satisfaction

of the requirements for the degree

Doctor of Philosophy in Mechanical Engineering

by

Da Wei David Ren

2023

ABSTRACT OF THE DISSERTATION

A 2D-local linear stability analysis of asymptotically-expanded jet-in-crossflows

by

Da Wei David Ren
Doctor of Philosophy in Mechanical Engineering
University of California, Los Angeles, 2023
Professor Ann R. Karagozian, Co-Chair
Professor Leonardo Alves, Co-Chair

The jet-in-crossflow is a critical flowfield for a range of aerospace propulsion systems, both airbreathing and rocket engines. A jet-in-crossflow or transverse jet is typically composed of a jet issuing from a circular outlet perpendicularly to a uniform air crossflow. Previous experiments deploying hot-wire anememetry or laser-based optical diagnostics such as planar laser-induced fluorescence (PLIF) or particle image velocimetry (PIV) have found that there is a transition in the jet's upstream shear layer from convective to absolute instability as the jet-to-crossflow velocity ratio R or momentum flux ratio J decreases. Typically, convectively unstable jets-in-crossflow are correlated with more asymmetric cross-sections while more symmetric jet cross-sections are typically associated with absolutely unstable transverse jets at lower R values, usually below 3 (Gevorkyan *et al.*, 2016). Besnard *et al.* (2022) demonstrated that even low-amplitude asymmetric acoustic excitation affected the symmetry of a convectively unstable jet-in-crossflow. Such a finding suggests that there may be a linear origin to symmetry-breaking in the face of a theoretically symmetric flow field.

This dissertation describes a numerical investigation of the spatial linear stability char-

acteristics of a jet-in-crossflow for the axisymmetric and helical azimuthal modes using a 2D-local viscous linear stability analysis. This study uses the viscous hyperbolic-tangent (tanh) and uniformly valid asymptotic solution (UVAS) base flows developed by Alves *et al.* (2008) and Alves & Kelly (2008) as viscous extensions of the cylindrical vortex sheet solution of Coelho & Hunt (1989), who performed asymptotic expansion-based linear stability analyses of the same base flows. This present work may be considered a 'fully-coupled' extension of their work because we presently account for all base flow-eigenfunction azimuthal coupling.

The eigenspectra from the present fully-coupled linear stability analysis indicate that the axisymmetric mode spatially stabilises as R decreases - in contradiction with experimental measurements (Megerian *et al.*, 2007; Davitian *et al.*, 2010; Shoji *et al.*, 2020*a*), direct numerical simulation results (Iyer & Mahesh, 2016), and with the prior asymptotic expansion-based linear stability analysis of Alves *et al.* (2008); Alves & Kelly (2008). The wavenumber and preferred Strouhal number trends, however, are in qualitative agreement with experimental measurements. The first, second, and third helical modes all stabilise as R decreases, with the axisymmetric mode being more unstable than the helical modes. All helical modes exhibit degeneracy-breaking, as was found from multiple mode analysis of an inviscid base flow by Alves *et al.* (2007); these modes are symmetric or anti-symmetric with respect to the plane of symmetry found in the jet-in-crossflow base flows.

A novel upwind-based treatment of the linearised convective term is developed to explore features of the eigenfunctions while eliminating non-physical oscillations in the high Reynolds number regime. This consists of a hybrid central-upwind finite difference discretisation scheme suitable for convection-dominated flows that allows for surgical suppression of non-physical numerical oscillations while still yielding similar eigenvalues to purely central difference schemes. Given that only the near-wake region needed this winding, the overall scheme consists of a 4^{th}-order central finite difference for all non-convective terms, a hybrid 2^{nd}-1^{st}-order scheme for the near-wake region and a hybrid 4^{th}-3^{rd}-order scheme elsewhere.

A linear activation function is used to smooth the transition from one regime to another. This approach was effective in both Cartesian and polar coordinates.

Given that the primary difference between the present fully-coupled and prior asymptotic expansion-based linear stability analyses lies in the number of supported base flow-eigenfunction azimuthal couplings, a weakly-coupled discrete Fourier-transformed linear stability analysis is developed to allow an exploration of the effect of base flow-eigenfunction azimuthal couplings on the eigenvalues. This weakly-coupled approach can highlight the essential velocity eigenfunctions or azimuthal interactions that affect the eigenvalues the most and may be considered as a sort of reduced-order model. By reproducing the base flow-eigenfunction couplings as closely as possible without repeating the same approach, the weakly-coupled linear stability analysis yields quantitatively similar axisymmetric eigenvalues as Alves & Kelly (2008). That is to say, the UVAS base flow spatial destabilises as R decreases. As the number of Fourier modes N_f increases, and therefore the number of base flow-eigenfunction couplings supported, the axisymmetric mode appears to become more similar to the fully-coupled results, with stabilisation as R decreases. Hence, a mechanism is proposed wherein an inadequately-expanded asymptotic base flow leads to incomplete base flow-eigenfunction couplings that deleteriously affect the eigenvalues. Without those couplings, the surviving terms may contribute to eigenvalue stabilisation.

To explore this hypothesis further, a spatial kinetic energy budget analysis is developed, showing the contribution of various physical mechanisms ('Advection', 'Production', and 'Pressure-velocity') to the spatial growth of the kinetic energy. The 'Pressure-velocity' correlation term is unique to the spatial formulation. Typically, for example, for a one-dimensional parallel Blasius boundary layer, the 'Pressure-velocity' term suppresses the energy when the disturbance is destabilising and supplies the energy when the disturbance is stabilising, per Hama *et al.* (1980). This implies that the 'Pressure-velocity' term becomes an increasing percentage of the total energy budget as the flow destabilises. Indeed, in the present analysis for the jet-in-crossflow, the axisymmetric mode from the fully-coupled

analysis exhibits a decreasing contribution from the 'Pressure-velocity' term, consistent with our observed stabilisation when R is decreased. In contrast, the spatial kinetic energy budget for the weakly-coupled analysis found that the 'Pressure-velocity' contribution increases substantially for low R, suggesting destabilisation. All mode coupling terms are negative contributions to the energy budget - supporting the proposed mechanism.

Based on the present studies, it is clear that future directions for research would include obtaining a more representative jet-in-crossflow base flow by extending the tanh or UVAS base flows to higher orders of $1/R$ or from using time-averaged experimental or numerical simulation data. Such a base flow could also be used to inform non-modal stability or resolvent analyses to better match impulsively or harmonically forced jets-in-crossflow. The wavemaker (in a 2D-local sense) could also be found, which may synergise with the passive tab disturbance of the jet-in-crossflow.

The dissertation of Da Wei David Ren is approved.

Jeffrey D. Eldredge

Robert T. M'Closkey

Kunihiko Taira

Leonardo Alves, Committee Co-Chair

Ann R. Karagozian, Committee Co-Chair

University of California, Los Angeles

2023

For Dawn Mao

and

For the memory of Eric Liu Wai Kong and Will Wai Hang Lee

TABLE OF CONTENTS

LIST OF FIGURES

LIST OF TABLES

NOMENCLATURE

(r, θ, z) Cylindrical coordinates

(x, y, z) Cartesian coordinates

$\Im()$ Imaginary component operator on the contents inside of the parentheses

$\Re()$ Real component operator on the contents inside of the parentheses

Acronyms and Initialisms

CVP Counter-rotating vortex pair

DNS Direct numerical simulation

LES Large Eddy Simulation

LSA Linear stability analysis

PIV Particle image velocimetry

PLIF Planar laser-induced fluorescence

USL Upstream shear layer

Greek symbols

ϵ Disturbance amplitude parameter for expansion

λ Crossflow-to-jet velocity ratio U_∞/U_j

μ Dynamic viscosity

ν Kinematic viscosity

ω Complex angular temporal frequency

ρ Fluid density

θ_0/R_0 Momentum thickness normalised by the jet or nozzle or pipe radius

θ_∞ Momentum thickness of the crossflow

θ_i Momentum thickness of the inner jet of a coaxial jet

θ_j Momentum thickness of the jet

θ_o Momentum thickness of the flow from the annular portion of a coaxial jet

Roman symbols

$\bar{u}$ Base flow velocity component (time-invariant)

$\hat{u}$ Linearised velocity component after normal Fourier mode decomposition

DR Diameter ratio for a coaxial jet base flow DR $\coloneqq D_0/D_i$

VR Velocity ratio for a coaxial jet base flow VR $\coloneqq u_{z,o}/u_{z,i}$

Re Reynolds number

St_D Strouhal number fD/U_j

C Concentration of fluid

D Jet exit diameter

f_0 Natural frequency

f_f Forcing frequency

J Jet-to-crossflow momentum flux ratio $\rho_j U_j^2/\rho_\infty U_\infty^2$

k Complex wavenumber. Also known as the axial Fourier wavenumber

m	Azimuthal mode number. Also known as the azimuthal Fourier wavenumber
p	Pressure
R	Jet-to-crossflow velocity ratio U_j/U_∞
R_0	Jet or nozzle or pipe exit radius
S	Jet-to-crossflow density ratio ρ_j/ρ_∞
s	Upstream shear layer trajectory parameterised coordinate
s_c	Jet centreline trajectory parameterised coordinate
t	Time
u	Velocity component
u'	Nonlinear disturbance velocity component
U_∞	Velocity of the crossflow
U_j	Velocity of the jet

ACKNOWLEDGMENTS

I would not be here with the support, encouragement, and kindness of many people. Firstly, I would like to thank my advisors, Professor Ann Karagozian and Professor Leo Alves, for guiding me, for cultivating my research ability, and for sharing their vast experience in the field with me. Professor Karagozian offered me a once-in-a-lifetime opportunity to realise my dream of doing advanced research, supported a dramatic pivot from experimental to numerical research, and mentored me to become a more well-rounded person. For that and more, I am infinitely grateful. Her deep insight in the jet-in-crossflow, fluid mechanics, and the sciences was always impressive. I was relieved when Professor Alves agreed to come on board as a co-chair, especially given that so much of this research is built on his prior work. His deep expertise about that as well as computational science helped to shape accelerate my transition to numerical research. For that, I am also infinitely grateful.

I am also thankful to the members of my committee, Professors Sam Taira, Robert M'Closkey, and Jeff Eldredge for offering feedback that has improved this work. The transition from experimental to numerical research has been a lengthy and full of unexpected obstacles, but I am glad for the wisdom from my committee members to help smooth out a bumpy ride.

Thank you to Professor Larry Li who took a chance on me all those years ago. His enthusiasm and talent for teaching showed me the wonders of fluid mechanics; I would have been doing something quite different without him. He introduced me to opportunities in the research world too, and mentored me for many years in professional and personal matters. I can confidently say that I will forever owe a debt of gratitude to him.

A special thanks is reserved for Dawn Mao, who is definitely real - she just goes to a different school in Canada. Your tireless support and companionship have helped me grow throughout the years. The stress of undergoing a PhD was more bearable with you. I know that this path on which we walk has not been the easiest, but I am glad to walking with

you.

It takes a village. Thank you to the 'villagers' in no particular order: Andres Vargas, Elijah Harris, Andrea Besnard, Daniel Ahn, Stephen Schein, Yui-Jui Chang, Rene Arevalo, Nadia Alvarez, Jean Marques, Peter Wright, Richard Abrantes, Shao-Ching Huang, Vedasri Godswarthi, Arin Haypeytian, Mathias Ross, Ryder Liu, Mathieu le Provost, Simon He, Anand Varma, Anthony Mannion, and Yuanhang Zhu.

I gratefully acknowledge that this research was supported by the National Science Foundation under grants CBET-1437014, and CBET-1933310, and by the Air Force Office of Scientific Research (AFOSR) under grants FA9550-15-1-0261, and FA9550-19-1-0191.

VITA

2014–2018	B.S. (Physics), Hong Kong University of Science and Technology, Hong Kong
2014–2018	HKSAR Government Scholarship
2015	Paul Ching Wu Chu Scholarship
2017	Mr. Armin and Mrs. Lillian Kitchell Undergraduate Research Award
2018	APS Undergraduate Research Award
2018–2020, 2022–2023	Fellowship, UCLA Mechanical and Aerospace Department
2018–present	Graduate Student Researcher and Graduate Teaching Assistant, Mechanical and Aerospace Department, University of California, Los Angeles

PUBLICATIONS AND PRESENTATIONS

E. W. Harris, S. G. Schein, D. D.W. Ren, and A. R. Karagozian. Synchronization and dynamics of the axisymmetrically excited jet in crossflow. *Physical Review Fluids*, 8, 033902 (2023)

R. J.E. Abrantes, Y.-W. Mao, and D. D.W. Ren. Rate coefficient function estimation using Gaussian process regression. *Journal of Quantitative Spectroscopy and Radiative Transfer*, 283, 108134 (2022)

D. D.W Ren, L. S.d.B. Alves, and A. R. Karagozian. Linear stability of a jet-in-crossflow, presented at the SoCal Fluids Symposium XV, Los Angeles, CA, April 2022.

D. D.W Ren, A. R. Karagozian, D. B. Souza, R. Freitas, and L. S.d.B. Alves. Adjoint-based analysis of jet-in-crossflow linear stability, presented at the 74th APS/DFD Meeting, Phoenix, AZ, November 2021.

D. D.W Ren, L. S.d.B. Alves, and A. R. Karagozian. Towards adjoint- accelerated base flow optimisation of a jet-in-crossflow, presented at the SoCal Fluids Symposium XIV virtually April 2021.

A. Besnard, E.W. Harris, S. Schein, A. Dembry, D. D.W Ren, A.R. Karagozian and L. S.d.B. Alves. Asymmetric Excitation of Convectively Unstable Jets in Crossflow, presented at the 72nd APS/DFD Meeting, Seattle, WA, November 2019.

D. D.W Ren, L. K.B. Li. Global Helical Modes in Low-Density Jets: Spatiotemporal intermittency, presented at the 71st APS/DFD Meeting, Atlanta, GA, November 2018.

D. D.W Ren, L. K.B. Li. Global Helical Modes in Low-Density Jets, presented at the APS March Meeting, Los Angeles, CA, March 2018.

D. D.W Ren, Y. Zhu, and L. K.B. Li.“A Self-Excited Jet, presented at the APS/DFD Meeting, Denver, CO, November 2017.

D. D.W Ren, S. Tripathi, and L. K.B. Li. Low-Cost Multispectral Imaging for Remote Sensing of Lettuce Health. *Journal of Applied Remote Sensing*, 2017. DOI:10.1117/1.JRS .11.016006

CHAPTER 1

Introduction

1.1 Applications of a Jet-in-Crossflow

A major design challenge for the next generation of gas turbines is the reduction of greenhouse gas emissions while increasing fuel efficiency. The latter is generally achieved by increasing inlet pressures and temperatures at the expense of the former (Karagozian, 2010). In addition, higher temperatures engender considerable material fatigue, thereby risking catastrophic failure. A jet-in-crossflow can be used for primary fuel/oxidiser injection or for dilution injection (Keffer & Baines, 1963). The former can control the reactant mixture ratio and thus control NOx emissions independently of CO emissions (Bowman, 1992). The latter can control the temperature pattern factor within the combustion chamber to prolong turbomachinery lifetimes. Additionally, these jets-in-crossflow can be issued over individual turbine blades for thermal insulation (Bons *et al.*, 2001), for thrust-vector control in missiles, and for scramjet engine fuel injection (Curran, 2001). As this involves a high-speed crossflow, ramjet/scramjet engine design has motivated study of the supersonic (Wang *et al.*, 1995), and even the reacting jet-in-crossflow (Nair *et al.*, 2019). Essential to all technological applications of the jet-in-crossflow is control over the jet penetration, jet spread, and mixing. These parameters can be different depending on the application. Dilution injection, for instance, requires a high degree of jet penetration in order to effectively mix hotter reactants with a cooler diluent prior to the encounter with turbine blades. On the other hand, film cooling of individual turbine blades requires a minimal jet penetration to allow the jet to adhere to the blade surface with minimal molecular mixing.

1.2 Archetypal Jet-in-Crossflow Features & Dynamics

1.2.1 Essential Parameterisations

A wealth of complex vortex structures arises from the interplay of the jet with the crossflow, some of which are described in Figure 1.1. Principally, these are: the counter-rotating vortex pair (CVP), the upstream shear layer (USL) vortices, the horseshoe vortices, and the upright wake vortices (Mahesh, 2013). The orientation of the inertial reference frame bases x, y, and z, jet upstream shear layer (USL) trajectory (parameterised by 's'), and the jet centreline trajectory (parameterised by 's_c') are also identified in Figure 1.1. These represent the default orientation throughout this document unless stated otherwise.

As jet-in-crossflow dynamics are fundamentally dependent on the flow conditions, it becomes necessary to define quantities to characterise the flow. Common dimensionless parameters are: the jet-to-crossflow density ratio $S \coloneqq \rho_j/\rho_\infty$, the jet-to-crossflow velocity ratio $R \coloneqq U_j/U_\infty$, the jet-to-crossflow momentum flux ratio $J \coloneqq \rho_j U_j^2/\rho_\infty U_\infty^2 = SR^2$, and the jet Reynolds number based on the jet diameter D $\mathrm{Re}_j \coloneqq U_j D/\nu_j$. The upstream shear layer of the jet naturally oscillates at a frequency f_0, which is nondimensionalised as the Strouhal number $\mathrm{St}_0 \coloneqq f_0 U_j/D$. For external forcing at frequency f_f, there is the corresponding forcing Strouhal number $\mathrm{St}_f \coloneqq f_f U_j/D$. The momentum thickness θ_j of the windward (upstream or leading-edge) portion of the jet, the momentum thickness of the crossflow θ_∞, and the crossflow Reynolds number $\mathrm{Re}_\infty \coloneqq U_\infty D/\nu_\infty$ are also used to characterise the flowfield. Note that momentum thicknesses derived from the leeward (downstream or trailing-edge) and windward portions of the jet are dissimilar in general (Megerian *et al.*, 2007).

Physical scaling arguments from Margason (1968) have led to a fairly robust centreline velocity trajectory for incompressible jets-in-crossflow:

$$\frac{z}{RD} = A\left(\frac{x}{RD}\right)^m \tag{1.1}$$

where A and m are empirical fitting coefficients. x and z are the downstream and transverse coordinates, respectively, as defined in Figure 1.1. For a jet issued from a straight pipe with crossflow velocity ratios $5 \leq R \leq 35$, the parameters are: $A \approx 2.0$ and $m \approx 0.28$ (Pratte & Baines, 1967). By contrast, jets issued from convergent nozzles with crossflow velocity ratios $5 \leq R \leq 25$ should use $A \approx 1.5$ and $m \approx 0.27$ for a more accurate fit according to Smith & Mungal (1998).

The scaling described by Equation (1.1) relies on the velocity ratio R adequately capturing the flow physics. Improved scalings, then, could be obtained by incorporating (i) the crossflow boundary layer thickness, (ii) the jet momentum thickness, and (iii) the velocity profile more explicitly. Experimental (New *et al.*, 2006) and numerical (Muppidi & Mahesh, 2005) investigations led to the following improved velocity trajectory scaling:

$$\frac{z}{RD} = A_1 \left(\frac{x}{RD} \right)^{m_1} \left(\frac{h}{RD} \right)^{m_2} \tag{1.2}$$

with 'h' parameterising the height above which the jet will no longer be vertical, determined by trajectories of jets-in-crossflow a small distance downstream of the jet exit when the jet commences to bend. Muppidi & Mahesh (2005) opted for h as the vertical y-coordinate where $x/D = 0.05$. The deflection occurs possibly due to pressure gradient imposed by the crossflow overcoming the vertical inertia of the jet. Further discussions regarding how jet-in-crossflow velocity trajectories are characterised can be found in Karagozian (2010). The centreline trajectory can be obtained in two ways. The primary method is based on experimentally-obtained centreplane scalar concentration data in a modified method inspired by Smith & Mungal (1998) as described fully in Gevorkyan *et al.* (2016). Given the mean centreplane scalar concentration field, a least-squares power-law fit is used for the maximum jet fluid concentration loci using Equation (1.1) (Margason, 1968). The converged result yields the jet centreline concentration trajectory 's_c' shown in Figure 1.1. Details on this method can be found in Gevorkyan *et al.* (2016). An alternative method, described in Megerian *et al.* (2007); Davitian *et al.* (2010), involves sweeping a hot-wire streamwise along

the centreline of jet-in-crossflow at various z/D heights. The inflection point is considered as the shear layer position, and therefore the upstream shear layer trajectory 's' is determined.

1.2.2 Vortical Features

The jet-in-crossflow remains enigmatic for its complex and nonlinear vortical features such as the counter-rotating vortex pair (CVP), the upstream shear layer (USL) vortices, the horseshoe vortices that wrap around the jet potential core, and the upright wake vortices (Smith & Mungal, 1998). It is thought that the CVP leads to improved molecular mixing as compared to free jets (Kelso *et al.*, 1996); experimentally, the potential core terminates closer to the jet exit plane as the crossflow velocity increases (i.e., R decreases) (Megerian *et al.*, 2007). The most prominent feature in the far-field is the counter-rotating vortex pair (CVP) (Cortelezzi & Karagozian, 2001). The CVP possibly arises from the injection of impulse from the jet into the crossflow (Broadwell & Breidenthal, 1984) that results in the roll-up of the upstream shear layer induced by the Kelvin-Helmholtz instability mechanism (Kelso *et al.*, 1996) in the nearfield. This explanation can justify CVP formation even in a steady jet-in-crossflow (Broadwell & Breidenthal, 1984). A general framework is found through the vortex dynamics. The vortex sheet is rolled-up in the nearfield of the jet exit just as in free jets. Then, it experiences shearing by the crossflow and a pressure difference between the windward and leeward portions of the jet that redirect the shear layer vorticity. Experiments indicate that this leads to tilting and folding of the vortex ring that eventually produce the counter-rotating vortex pair (CVP) farther downstream. This has been diagrammatically represented in Figure 1.2. The evolution, growth, and downstream breakdown of this CVP enhances the entrainment of ambient fluid into the jet, thereby enhancing mixing when compared to the free jet injected into quiescent surroundings (Cortelezzi & Karagozian, 2001; Kelso *et al.*, 1996; Karagozian, 2010). Note that the existence of the CVP does not contribute to mixing significantly (Smith & Mungal, 1998). The nearfield dependence of the farfield-dominating CVP is perhaps best demonstrated by (Peterson & Plesniak, 2004). Even

minor vortical disturbances in the upstream jet flow can enhance or hinder CVP formation.

There are horseshoe vortices that wrap around the jet due to the localised counter-current shear between crossflow and the upstream portion of the jet and due to the wall boundary layer separation (Fric & Roshko, 1994; Smith & Mungal, 1998). These vortices can have stationary, coalescing, and even oscillating modes (Kelso & Smits, 1995). Within certain R and Re regimes, the horseshoe vortex may oscillate with the same Strouhal number $\mathrm{St}_\infty = fD/U_\infty$ as the upright wake vortices downstream (Kelso & Smits, 1995). In addition, the horseshoe vortex is nonlinearly coupled with the upstream shear layer vortices as the horseshoe vortex affects the nearfield velocity profile (Andreopoulos, 1985).

Downstream, smoke-visualisation experiments demonstrate that there tornado-like upright vortices that entrain boundary layer fluid into the jet wake. These wake vortices are formed by the separation of the boundary layer downstream of the jet (Fric & Roshko, 1994).

The upstream shear layer vortices dominate the jet near-field dynamics (Megerian *et al.*, 2007), and are thought to significantly affect CVP evolution (Kelso & Smits, 1995; Cortelezzi & Karagozian, 2001; Muppidi & Mahesh, 2005). Issuing from the jet exit, the vortex sheet appears to oscillate until it 'rolls-up' at a natural frequency St_0 much in the same manner as in a free jet. Indeed, a similar type of Kelvin-Helmholtz instability (Thomson, 1871; Von Helmholtz, 1868) as seen in free jets can be partially attributed to generating these upstream shear layer oscillations (Kelso *et al.*, 1996; Fric & Roshko, 1994). However, crossflow introduces complications, and so the upstream shear layers behave more richly than a purely Kelvin-Helmholtz mechanism would allow (Megerian *et al.*, 2007; Davitian *et al.*, 2010; Getsinger *et al.*, 2012, 2014).

1.2.3 Jet-in-Crossflow Structural Evolution

To characterise how vortex structures of the jet-in-crossflow evolve spatially, numerous investigators have employed numerical simulations, experimental high-speed smoke visualisation,

and experimental laser-based optical diagnostic methods (Fric & Roshko, 1994; Smith & Mungal, 1998; Muppidi & Mahesh, 2005; Cortelezzi & Karagozian, 2001; M'Closkey *et al.*, 2002; Davitian *et al.*, 2010; Shapiro *et al.*, 2006; Getsinger *et al.*, 2012). Laser-based optical diagnostic methods, such as planar laser-induced fluorescence (PLIF), can image an isolated two-dimensional slice of the flowfield in a non-invasive manner.

A prototypical set of acetone PLIF snapshots of a $\mathrm{Re}_j = 1900$ jet-in-crossflow produced from a flush nozzle, demonstrating instantaneous centreplane and mean cross-sectional images at $x/D = 2.5,\ 5.5,\ 10.5$ is presented in Figure 1.3. The rows, from top to bottom, correspond to momentum flux ratios $J = 61, 30, 18, 12, 3$, obtained by varying crossflow velocity only. The leftmost column corresponds to instantaneous centreplane PLIF snapshots, whereas the remaining rows correspond to ensemble-averaged cross-sectional PLIF snapshots at $x/D = 2.5,\ 5.5,\ 10.5$ from left to right. The centreplane view refers to a x-z orientation of the laser sheet that bisects the jet exit, whereas the cross-sectional view refers to a x-y orientation of the laser sheet at a given x/D location downstream.

Focusing on the centreplane PLIF snapshots, (Figures 1.3(a, e, i, m, q)), the stronger crossflow (decreasing J) bends the jet more dramatically downstream, causes shear layer vortices to roll-up nearer to the source of the jet, and reduces the spacing between concomitant vortices (indicating an increased oscillation frequency). As the initial collection of vortex rings advects downstream, their spacing abruptly increases and henceforth the size of the vortices increase. This is an indication of vortex pairing and merger. Below a critical parameter $J_{\mathrm{crit}} \approx 8$, vortex spacing remained approximately constant along the upstream shear layer until turbulent breakdown, indicating an absence of vortex pairing/merger and an insensitivity to disturbances. As will be discussed further in Sections 1.3 and 1.5, observations made from laser diagnostic methods corroborate findings from hot-wire anemometry very well (Getsinger *et al.*, 2012, 2014).

In a noiseless environment, the jet-in-crossflow should be symmetric about the centreplane x-z axis given an axisymmetric jet velocity profile, a uniform crossflow, and smooth

boundaries. Repeated experimental and numerical studies, however, have revealed an asymmetric time-averaged jet cross-section downstream (Kuzo, 1995; Muldoon & Acharya, 2010; Kamotani & Greber, 1972; Smith & Mungal, 1998; Gutmark *et al.*, 2011; Getsinger *et al.*, 2014; Gevorkyan *et al.*, 2016; Besnard *et al.*, 2022). Examples of this asymmetry are displayed in Figure 1.3 for a $Re_j = 1900$ jet-in-crossflow issued from a flush nozzle. Many more asymmetries are possible, some of which are documented in Besnard (2019).

As the crossflow velocity increases (decreasing J), the jet cross-section typically becomes increasingly symmetric. When $J \lesssim 12$, the cross-section remains symmetric. Additionally, increasing the jet Reynolds number Re_j while maintaining a constant momentum flux ratio J also improves cross-sectional symmetry (Getsinger *et al.*, 2014; Shan & Dimotakis, 2006). Note that jets-in-crossflow issued from flush pipes display similar trends (Narayanan *et al.*, 2003; Muldoon & Acharya, 2010; Getsinger *et al.*, 2014; Gevorkyan *et al.*, 2016, 2018).

One potential explanation of this breakdown of symmetry comes from linear stability analysis of the jet-in-crossflow (see Section 1.4) (Alves *et al.*, 2007, 2008; Iyer & Mahesh, 2016). Given that Alves *et al.* (2007) showed that an inviscid high-R jet-in-crossflow could have non-degenerate helical modes, it is possible that one helical preferentially grows downstream, inducing a slight rotation. Linear stability analysis (LSA) will described in Sections 1.3 and 1.4.

1.2.4 Mixing of a Jet-in-Crossflow

Jets-in-crossflow can be used to enhance or reduce mixing in industrial applications, as discussed in Section 1.1 (Keffer & Baines, 1963; Bowman, 1992; Bons *et al.*, 2001). This evocative term 'mixing' encompasses a multitude of complex processes and is subsequently difficult to quantitatively characterise. Phenomenologically, mixing is the degradation of 'large' coherent fluid agglomerations to smaller length scales through numerous mechanisms. By enhancing the rate of diffusion-driven fluid transport through granulation, the local fluid concentration naturally becomes diluted (Danckwerts, 1952; Zwietering, 1959). As mixing

also relies flow entrainment and turbulent stirring/swirling/folding/stretching of flow structures, a comprehensive quantification of mixing requires measurement of multiple temporal and spatial scales (Mathew *et al.*, 2005; Danckwerts, 1952; Gubanov & Cortelezzi, 2010). Hence, numerous mixing metrics have been developed, such as the 'spatial probability distribution function' (Kollman, 1990), 'Spatial Mixing Deficiency' (Bockhorn *et al.*, 2010), 'Mix-Norm', 'Mix Variance' (Mathew *et al.*, 2003; Mathew *et al.*, 2005), and 'Unmixedness' (Dimotakis & Miller, 1990). As our study is conducted at relatively low Re, molecular diffusion dominates scalar concentration advection. Hence, concentration gradients are most significant for the physical process of mixing (Gevorkyan *et al.*, 2016).

The Unmixedness, defined in Equation (1.3), is the second moment of the scalar concentration field normalised by the variance of an unalloyed flowfield (Dimotakis & Miller, 1990).

$$U = \frac{1}{L_y L_z} \iint_{\Omega} \frac{(\frac{C}{C_0} - \frac{\bar{C}}{C_0})^2}{\frac{\bar{C}}{C_0}(1 - \frac{\bar{C}}{C_0})} \, \mathrm{d}y \, \mathrm{d}z \tag{1.3}$$

where $\frac{C}{C_0}$ is the local normalised jet concentration at location (y, z), Ω represents the domain of integration, and $\frac{\bar{C}}{C_0}$ represents the spatially-averaged concentration field. By convention, $\frac{C}{C_0} = 1$ indicates the presence of only jet fluid whereas $\frac{C}{C_0} = 0$ indicates the presence of only crossflow fluid. Hence, a homogeneously-mixed flowfield has $\frac{C}{C_0} = \frac{\bar{C}}{C_0}$ everywhere, where $\frac{\bar{C}}{C_0}$ is the spatially-averaged concentration field.

To enable comparison between centreplane and cross-sectional acetone planar laser-induced fluorescence (PLIF) imaging, between flow conditions, and across x/D locations, it is necessary to define a reference concentration. The convention of this group is to take the time-averaged concentration field $\frac{\bar{C}}{C_0}$ of a $S = 1,\ J = 3$ jet-in-crossflow issued from a flush-nozzle imaged at $x/D = 10.5$ as the standard against which any given instantaneous cross-sectional acetone-PLIF image must be recalibrated (Gevorkyan *et al.*, 2016). On the other hand, centreplane PLIF imaging takes the standard as the $S = 1,\ J = 7$ flush noz-

zle injected jet-in-crossflow at the jet centreline trajectory location $s_c/D = 15$ (Gevorkyan *et al.*, 2016). A seven-pixel wide vertical slice of the centreplane image is considered the area of interest whose concentration can be normalised with the cross-sectional image. The area, $L_y L_z$, of the upper and lower boundaries can be padded or trimmed with zero-valued pixels to match means such that $\frac{\bar{C}}{C_0}$ matches the aforementioned reference mean for all flow conditions. Cross-sectional images are mean-matched by padding or trimming the horizontal and vertical boundaries with zero-valued pixels.

As $U_\infty \to 0$, the flow approaches zero concentration variance and hence homogeneity. Note that the instantaneous Unmixedness values are averaged over all flowfield snapshots to provide statistically relevant results.

Unmixedness from both cross-sectional U_{yz} and centreplane $U_{c,xz}$ scalar concentration fields indicated enhanced mixing as the jet advected downstream, given that the J value was fixed (see Figures 1.4(a-b), respectively).

As can also be seen from Figure 1.4, a lower momentum flux ratio J generally corresponds to improved mixing at a fixed s_c/D station. This, as discussed in Section 1.2.3, corresponds to increasingly symmetric jet cross-sections downstream. Furthermore, as will be discussed further in Section 1.3, lower J-value jets-in-crossflow have stronger shear layer oscillations. The J-dependence remains valid for variable density jets-in-crossflow; jets-in-crossflow maintained at a high J exhibit enhanced mixing as the density ratio S is lowered. For $J \lesssim 7$, however, lowering the density ratio worsens mixing (Getsinger *et al.*, 2012; Gevorkyan *et al.*, 2016).

1.3 Hydrodynamic Instabilities of a Jet-in-Crossflow

Jet-in-crossflow dynamics appear to depend on upstream shear layer vortex behaviour (Getsinger *et al.*, 2014). This motivates a study of the 'stability' of the jet-in-crossflow. Reviews of linear stability analysis are given in Drazin & Reid (1981); Lin (1955); Chandrasekhar (1961);

Criminale *et al.* (2003).

Briggs (1964) and Bers (1973) further defined the notions of 'absolute' and 'convective' instability, which were imported to fluid mechanics by (Huerre & Monkewitz, 1990). These are illustrated by the response of a wavepacket in Figure 1.5. Note that these only consider the stability of the flow localised at a given station, not the flow overall. If a localised, impulsive, and infinitesimal disturbance grows spatially but slower than the rate at which it is advected downstream, the flow is considered to be 'locally convectively unstable' (CU) and is called an amplifier (see Figure 1.5(a)). If the disturbance grows spatially quicker than it is convected away downstream, the disturbance can return to its source or even further upstream. The flow, then, is 'locally absolutely unstable' (AU) and is called self-excited or a dynamical oscillator (see Figure 1.5(b)) (Huerre & Monkewitz, 1990, 1985; Chomaz *et al.*, 1988; Chomaz, 2005). Absolute instability implies that any initial linear perturbation triggers sustained oscillations even if the perturbation is removed. This all assumes there is an uninterrupted energy transfer from the base flow continuously (Li, 2011). The critical bifurcation point is when the disturbance grows in-place and further downstream but advection prevents the disturbance from travelling upstream (see Figure 1.5(c)). In other words, when the disturbance wave has zero group velocity (Huerre & Monkewitz, 1990).

The axisymmetric free jet is considered to be the basis of a jet-in-crossflow (Besnard, 2019) and is an open shear flow that exhibits convective and absolute instability. This flowfield is numerically predicted to become convectively unstable above a critical Reynolds number Re_c (Mollendorf & Gebhart, 1973; Lessen & Singh, 1973; Morris, 1976; Kambe, 1969). By reducing the density ratio $S = \rho_j/\rho_\infty$ below a critical value S_c (Monkewitz & Sohn, 1988; Monkewitz *et al.*, 1990) and/or with sufficient external flow (Jendoubi & Strykowski, 1994), linear stability analyses suggest that the free jet can transition to absolute instability.

These linear stability analyses predictions can be validated by obtaining the following experimental results. Convective instability (i) is sensitive to even weak external disturbances such as background noise or deliberate excitation (Gutmark & Ho, 1983) and (ii) amplifies a

broad range of disturbances whose growth rates are frequency-dependent and thus produces a broadband frequency spectrum. The transition to absolute instability involves (i) distinct change of the frequency spectrum to exhibit strong, pure-tone spectra with higher harmonics, (ii) significant change of the dominant natural Strouhal number, (iii) insensitivity to external perturbations, and (iv) reduction of energy transfer from the fundamental to the subharmonic frequency (Megerian *et al.*, 2007; Davitian *et al.*, 2010; Getsinger *et al.*, 2012).

For an equidensity ($S = 1.00$) jet-in-crossflow with $\mathrm{Re}_j = 2000$ or 3000 jets issuing from flush and elevated nozzles, Megerian *et al.* (2007) used hot-wire anemometry to measure the frequency spectra of the unforced upstream shear layer for various velocity ratios $1.15 \leq R \leq \infty$. Note that, unlike Gevorkyan *et al.* (2016), the nearfield jet-in-crossflow trajectories were obtained purely from hot-wire anemometry. Megerian *et al.* (2007) traversed the hot-wire streamwise across the centreline of the jet outlet at vertical locations from $z/D = 0.1$ up to $z/D = 5.0$, where $D = 3.81$ mm is the inner jet diameter. The upstream shear layer location was determined as the local inflection point of the vertical velocity fluctuation at each z/D location. Details can be found in Megerian *et al.* (2007).

Higher velocity ratios R have trajectories that more closely resemble the near-vertical course of the free jet. As $R \to 1.15$, the upstream shear layer trajectory increasingly curves leeward and reduces jet penetration as the crossflow velocity rises. The hot-wire was traversed along this upstream shear layer trajectory. At regular intervals $0.1 \leq s/D \leq 4.0$, samples of the local velocity time series were taken and converted to frequency space via the power spectral density (Megerian *et al.*, 2007). The result for three dynamically distinct R values can be represented in a spectral contour plot as shown in Figure 1.6 with samples of their corresponding power spectral density in Figure 1.6 at various s/D values. The colours of the spectral contour plots of Figures 1.6(a-c) represent the magnitude of the instability at a given Strouhal number. This Strouhal number $\mathrm{St} = f_0 U_j / D$ uses the natural frequency f_0 given as the first dominant frequency to become unstable away from the jet exit plane. This is in contrast to the downstream 'preferred mode' (Petersen & Samet, 1988; Hussain &

Zaman, 1981; Garnaud *et al.*, 2013). The free jet and the weak crossflow (high velocity ratio R) jet-in-crossflow exhibit a strong subharmonic ($f_0/2$ or St/2) that grows to dominate the downstream (high s/D) spectra, as seen in Figures 1.6(a,b,d,e). This is typically attributed to the nonlinear vortex pairing and merger phenomenon that has been seen in free jets and axisymmetric vortex sheet (Becker & Massaro, 1968; Crow & Champagne, 1971). We also observe tonal interference between the hot-wire and the jet exit plane (Megerian *et al.*, 2007; Davitian *et al.*, 2010; Getsinger *et al.*, 2012) that has been documented in free jet studies (Hussain & Zaman, 1978).

As we decrease the velocity ratio from $R \to \infty$ to $R \approx 3.1$ by increasing the crossflow velocity but maintaining the jet outlet velocity, we observe the following *gradual* changes: (i) the initiation of shear layer oscillations lowers towards the jet exit plane, (ii) the oscillation strength increases, (iii) the fundamental frequency f_0 changes, (iv) the tonal interference weakens, and (v) the subharmonic frequency weakens (Megerian *et al.*, 2007; Davitian *et al.*, 2010; Getsinger *et al.*, 2012). Note that the jet flow rate was kept constant while only the crossflow velocity was varied. This kept the jet nearfield frequency dynamics constant and therefore only the effect of crossflow is considered. Throughout this gradual transition, the jet-in-crossflow remains sensitive to external disturbances and exhibits broadband frequency spectra. This indicates that equidensity $R > 3.1$ jets-in-crossflow are typically convectively unstable.

Experimentally, the sensitivity to disturbances can be studied with small-amplitude forcing of the base flow at a range of frequencies (Megerian *et al.*, 2007). Megerian *et al.* (2007) applied single-frequency sinusoidal axisymmetric excitation upstream of the jet exit to a jet-in-crossflow at 1% of the mean jet velocity $\bar{U_j}$. Application of this weak forcing to a jet without crossflow ($R \to \infty$) led to strong shear layer oscillations at the forcing frequency f_f with a greatly weakened natural shear-layer f_0. This is characteristic behaviour of convective instability (Huerre & Monkewitz, 1990; Crow & Champagne, 1971; Becker & Massaro, 1968). For weak crossflows $6.4 < R < \infty$, this spectral sensitivity to external forcing remained simi-

lar to that of the free jet (Megerian *et al.*, 2007). Corresponding frequency spectra featured a stronger subharmonic and harmonics of f_f, indicating that weak forcing has induced vortex pairing and merger (Megerian *et al.*, 2007). This behaviour has been seen in excited free jets and shear layers (Li, 2011; Ho & Huerre, 1984). Lowering R by increasing the crossflow velocity led to a weakened effect of external forcing; the spectral peak of the natural frequency f_0 was less diminished and the forcing frequency f_f was less prominent. For $R < 3.5$, external forcing had very little effect on the upstream shear layer spectra compared to the unforced case (Megerian *et al.*, 2007). This indicates that the jet-in-crossflow exhibits self-sustained oscillations consistent with absolute instability.

In addition, decreasing R solely through an increase of crossflow velocity, we observe dramatic and fundamental changes in the frequency spectra. We observe (i) puretone frequency spectra with clear higher harmonics and no tonal interference, (ii) initiation of shear layer oscillations very close to the jet outlet, (iii) a dramatic change of the dominant frequency, (iv) insensitivity to external perturbations, and (v) reduction of subharmonic spectral peak strength (Megerian *et al.*, 2007; Davitian *et al.*, 2010). This strongly indicates there was a transition from convective to absolute instability at $R_{crit} \approx 3.1$ for a flush, equidensity jet-in-crossflow (Davitian *et al.*, 2010). Note that R_{crit} for an elevated jet is lower due to a stabilising region of coflow near the leading-edge of the nozzle (Megerian *et al.*, 2007). A more detailed quantification of the critical velocity ratio that follows the method described for counter-current mixing layers by Strykowski & Niccum (1991) but applied to the unforced jet-in-crossflow is detailed in Davitian *et al.* (2010).

To obtain a more 'global' view of this transition from convective to absolute instability, Getsinger *et al.* (2014) used laser diagnostic methods such as planar laser-induced fluorescence (PLIF) and particle image velocimetry (PIV) to image the entire flowfield both cross-sectionally and along the flow centerline. Principally, Getsinger *et al.* (2014) correlate local shear layer stability with global vortex roll-up. Firstly, the downstream s/D locations where oscillations commence in the spectral contour plots of Figure 1.6(a-c) match with

the onset of vortex roll-up as seen from centerline PIV imaging. The growing subharmonic mode downstream for convectively unstable jets-in-crossflow correspond to vortex pairing and merger, as seen with PIV images. Decreasing the velocity ratio R or momentum flux ratio J by increasing the crossflow velocity brought the onset of vortex roll-up closer to the jet exit, reduced the spacing between concomitant vortices (indicating an increased oscillation frequency), and bent the vortex trajectory leeward. Below a critical parameter $J_{\text{crit}} \approx 8$, vortex spacing remained approximately constant along the upstream shear layer until turbulent breakdown, indicating an absence of vortex pairing/merger and an insensitivity to disturbances. Additionally, vortex roll-up initiated very close to the jet exit and vortex spacing decreased - corresponding well to hot-wire measurements.

The significance of the jet momentum thickness is indicated by comparing the critical velocity/momentum flux ratios of a flush nozzle (thin momentum thickness) and a flush pipe (thick momentum thickness) at $Re = 1900$ (Getsinger *et al.*, 2014). Using hot-wire anemometry along the upstream shear layer, they observed that $J \leq 12$ jets-in-crossflow produced by a flush pipe led to weaker shear layer oscillations and an absence of tonal interference compared to a flush nozzle. In other words, a thick initial shear layer is not conducive to quicker and closer onset of shear layer oscillations for convectively unstable jets-in-crossflow; the injection of a thin shear layer from a flush nozzle into a crossflow causes a rapid jump in momentum thickness that strengthens shear layer instability (Getsinger *et al.*, 2014). These observations aligned with previous experimental (Megerian *et al.*, 2007) and numerical (Alves *et al.*, 2008) results. Decreasing $J < 10$ led to an abrupt transition to strong oscillations close to the jet exit with clear harmonics, just as for a flush nozzle. A potential physical explanation is that a transition to absolute instability requires a crossflow of sufficiently high velocity to enter the jet orifice (Getsinger *et al.*, 2014; Iyer & Mahesh, 2016). This is an indication of how a counter-current shear model of the windward portion of the jet-in-crossflow could lead to improved predictions of transition to absolute instability. Centreplane acetone planar laser-induced fluorescence (PLIF) imaging, demonstrated to correspond well with the

trends indicated by hot-wire anemometry, reveal that flush pipe jets-in-crossflow generally have smaller and weaker vortical structures than flush nozzle jets-in-crossflow (Getsinger *et al.*, 2014). Additionally, weak oscillations without a coherent frequency at higher J values generally lead to asymmetric jet structures, while strong and coherent oscillations at lower J values generally lead to symmetric jet structures downstream. The jet structure asymmetry is likely due to minor upstream crossflow boundary layer asymmetries close to the wind tunnel floor (Getsinger *et al.*, 2014; Besnard, 2019). This is partly evidenced by the asymmetry parity reversal upon the construction of a new wind tunnel with a reversed crossflow boundary layer asymmetry (Besnard, 2019).

Getsinger *et al.* (2014) also considered ensemble-averaged cross-sectional (yz) PIV and acetone PLIF imaging at the downstream wake region of $x/D = 2.5,\ 5.5,\ 10.5$. The convectively unstable jet-in-crossflow, being sensitive to external disturbances, appears to generally yield asymmetric, rotated, or otherwise distorted counter-rotating vortex pairs (CVP) downstream for the flush pipe, flush nozzle, and elevated nozzle. The flush nozzle even produced a tertiary streamwise vortex (Getsinger *et al.*, 2014). Reduction of J or R by solely increasing the crossflow velocity generally led to more symmetric CVP structures irrespective of the means of jet issuance. Absolutely unstable jets-in-crossflow appears to have very symmetric downstream cross-sections, in particular (Getsinger *et al.*, 2014).

Direct numerical simulations (DNS) also confirm these instability dynamics for jets-in-crossflow. Iyer & Mahesh (2016) match the Reynolds number $\mathrm{Re}_j = 2000$ and nozzle geometry of Megerian *et al.* (2007) with $R = 2,\ 4$ in their DNS study. By sampling the vertical velocity at various s/D locations to qualitatively mimic the method of Megerian *et al.* (2007), Iyer & Mahesh (2016) obtain very good correspondence to the experimental data of Megerian *et al.* (2007). That is to say, at $R = 4$, the spectra are broadband and exhibit a subharmonic peak growing downstream. $R = 2$, however, exhibits higher amplitude pure-tone oscillations with a clear harmonic without a subharmonic. Note that peak Strouhal numbers do not match, but that is expected because the base flows are not identical. They observe that

the flow within the nozzle oscillates at the dominant shear layer instability frequency (Iyer & Mahesh, 2016), indicating the source of the oscillation frequency is predetermined by jet flow conditions, or that this frequency information is transferred by the horseshoe vortices or crossflow in-flow (Kelso *et al.*, 1996). Following this, they developed a counter-current shear layer model localised to a small recirculation zone at the windward portion of the jet exit, inspired by the counter-current mixing layer studies of Strykowski & Niccum (1991). They speculate that sufficient local counterflow ratio could trigger absolute instability. Shoji *et al.* (2020*a*) and de Souza *et al.* (2021) explore this concept further in detailed experiments and in linear stability theory, respectively.

An additional means for a jet-in-crossflow transition to absolute instability is by lowering the density ratio $S < S_{\text{crit}}$. This scenario is experimentally studied by (Getsinger *et al.*, 2012) by varying the $N_2 - He$ mixture composition of the jet between $0.14 \leq S \leq 1.00$ with $\text{Re}_j = 1800$ and $5 \leq J < \infty$. They determined that transition to absolute instability occurs when $S \leq S_{\text{crit}} \approx 0.45$ regardless of momentum flux ratio J. This means they measured upstream shear layer spectra exhibiting strong, puretone oscillations with unambiguous higher harmonics without tonal interference (Getsinger *et al.*, 2012). Additionally, when $J \leq J_{\text{crit}} \approx 10$, absolute instability can occur regardless of density ratio S. In summary, the small-valued corner of the S-J space is the domain of absolute instability.

Generalising the detection of convective and absolute instability beyond the upstream shear layer, Davitian *et al.* (2010) used hot-wire anemometry to measure the frequency spectra at seven radial-azimuthal locations at various s/D stations downstream for $R = 1.15,\ 3.0,\ 3.3$, $\text{Re} = 2000$ jet-in-crossflow. The convectively unstable flow at $R = 3.3$ exhibited a broadband frequency spectrum at the upstream shear layer, as discussed above. The downstream shear layer exhibited spectra with higher amplitudes at lower frequencies that decayed as frequency increased. This is a typical indication of wake behaviour. Notably, the spectra just outside of the jet diameter at the port ($y > 0$) and starboard ($y < 0$) portions of the jet exhibited strong, narrow-peak oscillations. Measurements just inside the

jet diameter, however, yielded a broadband spectrum for $y > 0$ but a puretone spectrum for $y < 0$. This is possibly an indication of the inherent symmetry-breaking preference for spatial helical growth rates (Alves *et al.*, 2008), or possibly due to symmetry-breaking experimental procedure (Davitian *et al.*, 2010). As R decreased by solely increasing the crossflow velocity, the instabilities behaved symmetrically. That is, oscillations were puretone and qualitatively similar regardless of azimuthal location. $R = 1.15$ flow was even insensitive to blockage of the jet outflow by the hot-wire itself.

To summarise, decreasing R for convectively unstable jets-in-crossflow experimentally leads to:

- The initiation of upstream shear layer oscillations closer to the jet exit
- Increasing upstream shear layer oscillation strength
- A shift of the fundamental frequency f_0 while maintaining a broadband frequency spectrum
- The weakening of tonal interference due to the physical obstruction created by the hot-wire
- The reduction of energy transfer from the fundamental to the subharmonic and therefore a reduction of subharmonic mode strength
- Increasingly symmetric downstream CVP structures
- Decreasing sensitivity to external perturbations

Below a critical parameter such as the velocity ratio $R_{crit} \approx 3.1$ (Davitian *et al.*, 2010), the density ratio $S_{crit} \approx 0.4$, or the momentum flux ratio $J_{crit} \approx 10$ (Getsinger *et al.*, 2012), the jet-in-crossflow transition to absolute instability, which manifests as global instability experimentally. Global instability leads to:

- Narrow, pure-tone frequency spectra with higher harmonics
- The absence of tonal interference due to the hot-wire
- The initiation of shear layer oscillations very close to the jet exit
- A weak subharmonic mode
- Highly symmetric CVP structures
- Symmetric nearfield frequency spectra around the periphery of the jet
- Insensitivity to even moderate amplitude external disturbances

1.4 Linear Stability Analysis

Numerical stability analyses were also performed to understand the convective to absolute instability behaviour of the jet-in-crossflow. The qualitative behaviours of various types of instability were described in Section 1.3. Mathematically, we consider the generally nonlinear, time-dependent incompressible flow governing equations compactly represented by:

$$\mathcal{L}\vec{q} = 0 \tag{1.4}$$

where $\mathcal{L}$ is a continuous operator and $\mathbf{q}$ represents our hydrodynamic variables of velocity $\mathbf{v}$ and pressure p. Typically, the governing equations are non-dimensionalised with characteristic length- and time-scales of the flow. The governing equations given in Equation (1.4) have a steady-state solution for velocity $\bar{q}$ and pressure $\bar{p}$, also known as the base flow, fixed-point, or point attractor (Li, 2011). This base flow can be found analytically for a small range of flows, numerically by simulating the flow for sufficient duration or experimentally by taking an ensemble time-averaged velocity field. If any infinitesimally small perturbation of this fixed point causes the flow to permanently deviate from the fixed point, then the flow is 'unstable'. Otherwise, it is 'stable'.

Determining the stability of the nonlinear set of partial differential equations represented by Equation (1.4) is generally intractable. Therefore, linear stability analysis typically requires linearisation of the system about the base flow. That is, we expand each variable about a small disturbance from the base flow by ϵ in a Taylor series as:

$$\mathbf{q} = \bar{\mathbf{q}} + \epsilon \mathbf{q'} \tag{1.5}$$

where $\bar{\mathbf{q}}$ represents the steady-state solution and $\mathbf{q'}$ represents the disturbance variable. For linearity, we neglect all resultant quadratic or higher-order terms (Drazin & Reid, 1981). The $\mathcal{O}(1)$ terms are assumed to be automatically satisfied given the base flow, so we only consider the $\mathcal{O}(\epsilon)$ set of disturbance governing equations denoted as:

$$\mathcal{L}'\mathbf{q'} = 0 \tag{1.6}$$

where $\mathcal{L}'$ represents the $\mathcal{O}(\epsilon)$ terms of governing equations discretised about a given base flow. Note that time variable is only expressed as first derivative, and so we expect $\exp(i\omega t)$ to be a solution. $\omega \in \mathbb{C}$ contains the frequency and/or the temporal growth rate. The disturbance variable $\mathbf{q'}$ is then expanded into normal Fourier modes:

$$\mathbf{q'} = \hat{\mathbf{q}}(\mathbf{x}_i)\ \exp(i(\Phi \coloneqq \mathbf{k} \cdot \mathbf{x}_h - \omega t)) + \text{c.c.} \tag{1.7}$$

where $\hat{\mathbf{q}}(\mathbf{x}_i)$ is the mode amplitude that varies only along the set of inhomogeneous disturbance direction $\mathbf{x}_i$, $\mathbf{x}_h$ is the set of homogeneous disturbance directions, and $\mathbf{k} \in \mathbb{C}^3$ is the vector of wavenumbers and/or spatial growth rates. The wavenumber and the temporal frequency are connected via $\omega = kc$, where c is the phase speed of the wave. 'c.c.' denotes the complex conjugate. Inserting the Fourier mode decomposition of Equation (1.7) yields the new set of coupled governing equations represented by a matrix operation:

$$\hat{\mathcal{L}}(\omega, \mathbf{k}, \mathbf{x}, t, \bar{\mathbf{v}}, \bar{p})\hat{\mathbf{q}} = 0 \tag{1.8}$$

with associated boundaries conditions:

$$\mathbf{f}(\mathbf{x}) \; on \; \partial\Omega \tag{1.9}$$

where $\partial\Omega$ represents the boundary of the domain of interest.

Given that typical disturbance boundary conditions are homogeneous, this becomes a characteristic value problem or an *eigenvalue* problem (Drazin & Reid, 1981; Lin, 1955). Equation (1.8) is also known as a dispersion relation or a characteristic equation. Temporal stability analyses prescribe $\mathbf{k} \in \mathbb{R}^n$ to solve for the complex ω eigenvalues, where $0 \leq n \in \mathbb{Z} \leq 2$ is the number of homogeneous directions. Temporal instability occurs when $\Im(\omega) > 0$ at the wavenumber k. Symmetrically, spatial stability analysis prescribe constant, monochromatic temporal frequency $\omega \in \mathbb{R}$ to solve for the complex $\mathbf{k}$ eigenvalues. Spatial instability occurs when $\Im(k) < 0$ at the corresponding frequency ω. Spatial instability analysis generally yields more straightforward comparison with experiments despite being considered a nonlinear approach. Typically, temporal stability analysis is used to obtain classical marginal stability criteria while spatial stability analysis is used to identify the convective to absolute instability condition. Note that it is not possible to convert from a temporal to a spatial stability analysis (or vice versa) via the phase speed $\omega = kc$ or the group velocity (Gaster, 1962).

Table 1.1: Types of classical linear stability analyses. Modified from Juniper *et al.* (2014)

Type	**Base flow form**	**Eigenfunction Amplitude**	**Eigenfunction Phase Φ**
Local 1D	$\bar{q}(x_1)$	$\hat{q}(x_1)$	$k_2x_2 + k_3x_3 - \omega t$
BiGlobal	$\bar{q}(x_1, x_2)$	$\hat{q}(x_1, x_2)$	$k_3x_3 - \omega t$
2D Local	$\bar{q}(x_2, x_3)$	$\hat{q}(x_2, x_3)$	$k_1x_3 - \omega t$
TriGlobal	$\bar{q}(x_1, x_2, x_3)$	$\hat{q}(x_1, x_2, x_3)$	$-\omega t$

There are a few main varieties of linear stability theory as illustrated by Table 1.1. Descending the table involves imposing fewer restrictions on the flow dynamics at the cost of increasing complexity. The most restrictive requires the parallel flow assumption, whereby we assume that the flow that only the bulk flow direction (x_1 here known as the inhomogeneous direction x_i) has non-negligible derivatives. The remaining derivatives are negligible, corresponding to the homogeneous directions x_h. This leads to 'local 1D' analysis via Equations (1.6) and (1.7). Supposing that we can only neglect one homogeneous direction, we can have linear 'BiGlobal' stability analysis or 2D local stability analysis via Equations (1.6) and (1.7). The former corresponds to when the base flow is defined along the inhomogeneous direction whereas the former corresponds to when the base flow is taken as a 'slice' of the flowfield at a particular station in the inhomogeneous direction. Therefore, 2D local linear stability analysis may be considered as extending the spirit of the 1D parallel flow assumption. Finally, the most general scenario is where we assume disturbances are significant in all direction. This leads to linear 'TriGlobal' stability analyis, the most computationally expensive of all, (Juniper *et al.*, 2014). All are generalised, n-D eigenvalue problems.

Huerre & Monkewitz (1990) introduced the notions of convective and absolute instability to fluid mechanics. As previously discussed in Section 1.3, convective instability requires the wavepacket to be convected downstream more rapidly than it can grow upstream. Equivalently, this requires a positive group velocity. By contrast, absolute instability is defined as wavepacket growing upstream faster than it can convected downstream. The critical transition point, then, from convective to absolute instability requires a zero group velocity. Equation (1.10) mathematically describes the sufficient condition for absolute temporal instability for a given wavenumber $\mathbf{k}_{\text{crit}}$ *and* a classically unstable mode (Barletta & Alves, 2014). This condition of zero group velocity is equivalent to the location of a saddle point in the complex k-space of the dispersion relation. To obviate a discussion of uniqueness, the most physically relevant saddle point has the largest growth rate.

$$v_g \coloneqq \frac{\partial \omega}{\partial \mathbf{k}}\Big|_{\mathbf{k}=\mathbf{k}_{\text{crit}}} = 0, \qquad s.t. \Im(\omega(\mathbf{k}_{\text{crit}})) < 0 \tag{1.10}$$

The absolute growth rate, $\Im(\omega(\mathbf{k}_{\text{crit}})) > 0$ if the instability is absolutely unstable and $\Im(\omega(\mathbf{k}_{\text{crit}})) < 0$ is convectively unstable (Coenen *et al.*, 2008). An additional constraint for saddle point physicality is the Briggs-Bers criterion (Briggs, 1964; Bers, 1973; Huerre & Monkewitz, 1990). This states that the saddle point must be composed of one branch that originates from solely the $\Im(k) > 0$ half-plane and another branch from only the $\Im(k) < 0$ half-plane. The $\Im(k) > 0$ branch represents upstream exponential spatial growth ($x < 0$) while the $\Im(k) < 0$ branch represents downstream exponential spatial growth ($x < 0$). Note that convective instability is also observed if either branch intersects with the $\Im(k) = 0$ axis (Barletta & Alves, 2014).

Alves *et al.* (2007) perform an asymptotically-expanded inviscid linear stability analysis using an inviscid model of an asymptotically high-R ($R \gtrsim 3.5$)jet-in-crossflow developed by Coelho & Hunt (1989). This base flow is an analytical model where asymptotic perturbation theory was applied to distort a cylindrical vortex sheet with an asymptotically weak crossflow. Hence, this inviscid base flow becomes less representative of reality as R decreases from the free jet limit. This base flow yielded trajectories and vortical structures that corresponded well to experimental observations Coelho & Hunt (1989) in the high-R regime, and so offered an opportunity to avoid prohibitively expensive DNS and subsequent TriGlobal stability analysis. Given that the base flow was expanded in terms of $\lambda = 1/R$, Alves *et al.* (2007) expanded the linear stability analysis also in terms of λ, the inverse velocity ratio. That is to say, given that λ is very small and the base flow is of the form $\bar{q} \coloneqq \bar{q}_0 + \lambda^1 \bar{q}_1 + \lambda^2 \bar{q}_2$, then the frequency, eigenvalue, and eigenfunctions can also asymptotically expanded in terms of λ. After substituting in these expanded variables into the linearised governing equations, it is possible to separate the governing equations into three distinct sets of governing equations at $\mathcal{O}(\lambda^0), \mathcal{O}(\lambda^1), \mathcal{O}(\lambda^2)$. These equations are solved sequentially to higher orders of λ. This was done partially for computational parsimony reasons, because direct numerical

simulations (Alves, 2006) indicated that the base flow followed the azimuthal dependencies elucidated by Coelho & Hunt (1989), and it allowed the investigation of each azimuthal mode m separately. Therefore it was reasonably expected that the linear disturbances should also exhibit the same dependencies at various orders of λ. The additional expansion of the eigenvalues and eigenfunctions in terms of λ does further constrain the range of validity to high values of R (low values of λ). Henceforth, an approach that involves expanding the linear stability analysis in terms of λ, i.e., decomposing the stability problem to distinct governing equations at different orders of $\mathcal{O}(\lambda)$, will be termed 'asymptotic-expansion based linear stability analysis'.

Alves *et al.* (2007) obtain the spatial growth rates of the axisymmetric $m = 0$ and first two helical $m = \pm 1, \pm 2$ modes using the aforementioned asymptotic expansion-based linear stability analysis. This perturbation expansion (PE) analysis prevented any interaction between azimuthal modes and they found that there was the positive and negative helical modes yielded the same equations i.e., they were degenerate. By convention, positive (negative) corresponds to clockwise (counter-clockwise) direction. This PE linear stability analysis found that the axisymmetric mode eigenspectrum was identical to that of the free jet (Batchelor & Gill, 1962), the first helical mode becomes more unstable as R decreases for intermediate Strouhal numbers and for further downstream stations, and the second helical mode can also become more unstable as R decreases but less so than the first helical mode. The first (second) helical mode is more unstable than the axisymmetric mode when $St > 0.6$ ($St > 1.44$) (Alves *et al.*, 2007).

By contrast, Alves *et al.* (2007) developed a multiple Fourier mode expansion approach (MMA) to linear stability analysis. The frequency, eigenvalues, and eigenfunctions are not expanded in terms of λ in the MMA analysis. Rather, the governing equations and eigenfunctions undergo a discrete Fourier transform. This MMA approach therefore azimuthally couples the jet disturbances with the crossflow and also permits the helical modes to be theoretically non-degenerate when symmetry is not explicitly imposed.

When symmetry is explicitly imposed, Alves *et al.* (2007) find that the axisymmetric and first helical mode become more spatially unstable as R decreases to $R = 5$. When symmetry is not explicitly imposed, the linearised stability equations depended on the sign of the azimuthal mode, and so degeneracy-breaking helical eigenvalues were possible. Indeed, most strikingly, the $m = +1$ helical mode was slightly more spatially unstable than the $m = -1$ for $R = 5$ despite using a symmetric base flow (Alves *et al.*, 2007). The same degeneracy-breaking was observed for the second helical mode too (Alves, 2006). Therefore, the MMA analysis found that there may be a slight but intrinsic asymmetry to the inviscid linear stability of an inviscid jet-in-crossflow. This intrinsic symmetric-breaking as well as the dominance of the higher helical modes at higher R for certain frequency ranges further downstream may potentially explains why convectively unstable (high R) jets-in-crossflow exhibit asymmetric downstream cross-sections (Alves *et al.*, 2007).

The vortex sheet solution of Coelho & Hunt (1989) is meant to represent an inviscid jet-in-crossflow, but experimental jets-in-crossflow typically have non-zero momentum thicknesses (Megerian *et al.*, 2007), meaning that a viscous base flow is needed. Two different viscous extensions of the Coelho & Hunt (1989) solution were presented by Alves *et al.* (2008) and Alves & Kelly (2008). This approach avoids the use of costly direct numerical simulations.

Alves *et al.* (2008) develop an ad-hoc viscous jet-in-crossflow in a manner inspired by viscous linear stability analyses of axisymmetric free jet (Michalke, 1971; Morris, 1976). Keeping the functional form and azimuthal dependencies of the expanded base flow of Coelho & Hunt (1989) the same, a hyperbolic-tangent (tanh) function was deployed as a suitable smoothing function for the stitching of inboard and outboard inviscid velocity profiles. Henceforth, this base flow shall be referred to as the 'tanh' base flow. This tanh base flow was designed to satisfy conservation of mass, but conservation of momentum was not guaranteed. More details can be found in Section 4.4.1 and Alves (2006).

Alves *et al.* (2008) again leverage the fact that the base flow is expanded in terms of λ to also expand the frequency, eigenvalue, and eigenfunctions to create an asymptotic

expansion-based linear stability analysis. As a result, the helical modes are degenerate. Linearised governing equations were solved at each order of λ, as mentioned previously. This analysis found that, as R decreased, the axisymmetric mode became more spatially unstable, the preferred Strouhal number increased, and the range of unstable frequencies widened (particularly when $R \lesssim 10$). By contrast, the first and second helical modes became more spatially stable as R decreased. These trends of Alves *et al.* (2008) were generally consistent for various momentum thicknesses. At $R \approx 10$, the axisymmetric mode is of comparable growth rate to the first helical mode. Above this, the helical mode becomes dominant. This again suggests that the helical instability is perhaps associated with the CVP symmetry breaking at high R (Alves *et al.*, 2008). Comparisons with experimental spatial growth rates and Strouhal numbers of of the axisymmetric mode of the tanh jet-in-crossflow mode for various R values, as can be seen in Figures 1.7 and 1.8 respectively, demonstrate excellent correspondence.

In order to address the fact that the tanh base flow did not generally satisfy momentum conservation, Alves & Kelly (2008) developed the uniformly valid asymptotic solution (UVAS) base flow. This involves solving the incompressible Navier-Stokes equations asymptotically expanded in terms of λ and a solution was sought with the same azimuthal dependencies as the solution of Coelho & Hunt (1989). Note that the UVAS solution fundamentally assumes that the viscous shear layer is small to enable a similarity solution to be found. The method of matched asymptotic expansions (Van Dyke, 1964) was used to incorporate the farfield solution of Coelho & Hunt (1989). More details can be found in Section 4.4.2 and Alves (2006).

Again, Alves & Kelly (2008) use an asymptotic expansion-based linear stability analysis approach for the UVAS base flow. As a result, the helical modes are degenerate. Due to the fact that the UVAS base flow was only expanded up to $\mathcal{O}(\lambda^1)$, it was not possible to obtain the eigenspectra for the first helical mode, but second helical mode data are available. As R decreased, the axisymmetric mode become more spatially unstable and the preferred

Strouhal number increased, but less dramatically than for the tanh base flow. In fact, the UVAS eigenspectra changed very little until $R < 10$. They found that by removing the $\mathcal{O}(\lambda^1)$ axial velocity component of the base flow U_1, the corresponding axisymmetric mode monotonically stabilised as R decreased. This component U_1 provided a small amount of localised counterflow near the upstream shear layer and therefore is essential to axisymmetric mode destabilisation. By contrast, the second helical mode stabilised as R decreased.

In summary, 2D-local linear stability analyses of base flow that model the jet-in-crossflow predict the existence of an inviscid axisymmetric instability mode. The axisymmetric mode is expected to increasingly destabilise as R decreases or at least stay as unstable as the axisymmetric free jet for the inviscid base flow scenario (Alves *et al.*, 2007, 2008; Alves & Kelly, 2008).

A DNS and TriGlobal stability analysis of a low $R = 3$ jet-in-crossflow with a near-parabolic jet velocity profile from Bagheri *et al.* (2009) reinforces the suggestion of global instability on a theoretical foundation. Using the jet velocity profile as an inhomogeneous boundary condition, they obtain a time-averaged base flow with a highly symmetric CVP, horseshoe vortex, and ring-like shear layer vortices. Qualitatively, the flow appears to exhibit self-sustained oscillations. Their most unstable global mode resembles a wavepacket travelling coaxially with the bent CVP (Bagheri *et al.*, 2009). They also identify a low-frequency region close to the wall as shedding shear layer vortices that is spatially separated from the global modes downstream. This is an indication of a wavemaker (Chomaz, 2005; Giannetti & Luchini, 2007). In one sense, this indicates that a pocket of absolute instability is triggering self-sustained oscillations. However, their approach is limited in that (i) their near-parabolic velocity profile is not generally associated with low velocity ratio jets-in-crossflow (Megerian *et al.*, 2007; Davitian *et al.*, 2010) and (ii) their simulation does not incorporate the jet nozzle/pipe geometry, thereby excluding the potential effect of crossflow penetrating the jet at low R.

Recognising the significance of the jet nozzle geometry, Regan & Mahesh (2017) conduct

a DNS and TriGlobal stability analysis of a $R = 2$ and $R = 4$ jet-in-crossflow issuing from a $D = 3.81$ mm fifth-order polynomial flush nozzle to match the experimental conditions of Megerian *et al.* (2007). For both of these velocity ratios, global stability analysis has obtained global eigenvalues very close to the experimentally-measured oscillation frequencies, although those eigenvalues do not always have the highest growth rates. The convectively unstable $R = 4$ jet-in-crossflow interestingly appears to have global modes concentrated in the downstream shear layer oscillating at various frequencies dominating the flow. By contrast, the absolutely unstable $R = 2$ jet-in-crossflow has a dominant global mode consisting of high-frequency oscillations originating in the upstream shear layer. This mode decays rapidly around the end of the potential core, however. Instead, the large-scale, low-frequency wake global modes dominate the spectral energy.

Linear stability theory will be applied to the jet-in-crossflow in this document. Details will be expounded upon in Section 4.

1.5 Experimentally disturbed jets-in-crossflow

1.5.1 Axisymmetric forcing

As indicated by linear stability analyses in Section 1.4, the jet-in-crossflow is most unstable to the axisymmetric mode across a large range of velocity ratios R (Alves *et al.*, 2007, 2008). Therefore, introducing axisymmetric disturbances of various frequencies is a natural strategy to control the jet-in-crossflow, alter mixing characteristics, and investigate the absolute/convective nature of the linear instability.

1.5.1.1 Square-wave forcing

A square wave generated by modulating the jet inflow e.g., via a solenoidal valve or a piston represents an injection of inertia that can expedite vortex roll-up, increase jet penetration

length, and affect jet/crossflow fluid mixing (Johari *et al.*, 1999; Gharib *et al.*, 1998). Johari *et al.* (1999) defined the stroke ratio to be:

$$\frac{L}{D} \coloneqq \frac{1}{A\ D} \int_0^\tau \int_A u_{j,\max}\ \mathrm{d}A\ \mathrm{d}t \approx \frac{\bar{U}_j \tau}{D} \tag{1.11}$$

where A is the area of the jet outlet, D is the jet diameter, $u_{j,\max}$ is the jet centerline velocity, τ is the duration of a single square wave's 'on'-phase, and $\bar{U}_j$ is the mean jet velocity.

Gharib *et al.* (1998) find the universal critical L/D value for a vortex ring with maximum circulation to be $3.6 \leq L/D \leq 4.5$, which seem to be associated with maximum fluid carrying/entrainment volume. Indeed, the direct numerical simulations (DNS) of Sau & Mahesh (2007) found that the optimal L/D ratio for passive scalar mixing of a vortex ring formed in the absence of crossflow is 3.6.

One limitation of fully-modulated jet flow is the significant alteration of the base flow, which requires substantial energy. For this reason, Shapiro *et al.* (2006) use less disruptive and less energy-demanding acoustic axisymmetric excitation for $R = 2.6, 4.0$ jets-in-crossflow at various L/D ratios and forcing frequencies f_f. The square-wave forcing matches $u'_{j,\mathrm{rms}} = \sqrt{\frac{1}{T}\int_{t_0}^{t_0+T}(u_j - \bar{U}_j)^2 \mathrm{d}t}$ to keep the injected impulse constant although L/D was varied. Results indicate that forcing where $f_f \ll f_0$ yields the greatest jet penetration, even if the forcing frequency was not a subharmonic of the natural frequency, agreeing with Johari *et al.* (1999). However, the most deeply penetrating jet structures does not always lead to the best mixing due to bifurcation of the jet (Shapiro *et al.*, 2006). They also reveal two critical L/D ranges for optimal jet penetration and mixing irrespective of f_f: $1.7 \leq L/D \leq 2.0$ and $3.2 \leq L/D \leq 4.2$. The latter somewhat corresponds to the universal $3.6 \leq L/D \leq 4.5$ range for vortex rings from Gharib *et al.* (1998). However, the former L/D range appears to be a new characteristic scale arising from the effect of crossflow for the jet-in-crossflow (Shapiro *et al.*, 2006). A direct numerical simulation by Sau & Mahesh (2010) consider the forced jet-in-crossflow under similar flow conditions as that of Shapiro *et al.* (2006), and yielded

similar results to experiments.

Shoji *et al.* (2019) considers the effect of compensated square-wave excitation on equidensity $5 \leq J \leq 41$ jet-in-crossflow mixing and structure. As found previously by M'Closkey *et al.* (2002) and Shapiro *et al.* (2006), there is a range of stroke ratios L/D for each J that produces deeply-penetrating vortices, but these flows are not always the most mixed. Instead, improved mixing appears to be strongly correlated with more symmetric jet cross-sections for convectively unstable jets-in-crossflow (Shoji *et al.*, 2019) and that square-wave forcing can make the cross-section more symmetric.

1.5.1.2 Sinusoidal forcing

Low-amplitude sinusoidal forcing can be used to probe the linear stability characteristics of the jet-in-crossflow upstream shear layer (Megerian *et al.*, 2007). Sinusoidal forcing of a high R-value jet-in-crossflow is extremely effective; hot-wire measurements along the shear layer indicate the natural frequency f_0 is significantly weaker while the forcing frequency f_f and its (sub)harmonics dominate the spectrum even with relatively low-amplitude forcing (Megerian *et al.*, 2007). This is evidence for convective instability in the high-R regime. By contrast, weak sinusoidal forcing of a low R-value jet-in-crossflow led to little change in the shear layer frequency spectrum (Megerian *et al.*, 2007). This is possibly because the acoustic forcing was inadequate to disrupt the self-excitation of the natural frequency f_0 and is therefore evidence for absolute instability in the low-R regime. It is possible that the primary instability lies in the upstream shear layer due to the $R = 4$ jet-in-crossflow having a wavemaker along the upstream shear layer while the $R = 2$ jet-in-crossflow having a wavemaker in a narrow region around the upstream portion of the jet (Regan & Mahesh, 2019*b*,*a*). A wavemaker is the most upstream region of absolute instability (Chomaz, 2005; Li, 2011), the region most sensitive to localised forcing (Giannetti & Luchini, 2007), and is responsible for dictating global mode frequency (Chomaz, 2005).

1.5.2 Lock-in

Acoustic excitation of bluff-body wakes (Provansal *et al.*, 1987), free jets (Sreenivasan *et al.*, 1989), and flames (Li & Juniper, 2013) that naturally oscillate at frequency f_0 can be forced to oscillate at the forcing frequency $f_f \neq f_0$. This process is termed 'lock-in'. As expected, the amplitude required to 'lock-in' the wake to the natural frequency is zero. Deviation from the natural frequency $|f_f - f_0| > 0$ requires increasingly higher forcing amplitudes for lock-in - generally in a linear manner. The result is a V-shaped lock-in diagram otherwise known as a Arnold tongue in dynamical systems (Godrèche & Manneville, 1998).

Davitian *et al.* (2010) demonstrate that sufficiently strong axisymmetric sinusoidal excitation well upstream of the jet exit plane can induce lock-in. For a particular forcing frequency, low-amplitude forcing leads to minor changes in the frequency spectra except for the appearance of a small peak at f_f. Higher amplitude forcing yields quasiperiodicity (Sreenivasan *et al.*, 1989; Broze & Hussain, 1994), where the frequency spectrum features linear combinations of the natural and forcing frequencies and that both f_f and f_0 signals remain. Only when the forcing amplitude is sufficiently high is the natural frequency completely suppressed, leaving the forcing frequency and its harmonics dominant in the spectrum (i.e., lock-in). Davitian *et al.* (2010) produce lock-in diagrams for the $1.15 \leq R \leq 6.4$ jet-in-crossflow.

Davitian *et al.* (2010) find that, as R increases, it becomes easier to lock-in the upstream shear layer oscillations across a wider range of forcing frequencies. By contrast, Megerian *et al.* (2007) find that low-amplitude sinusoidal forcing has very little impact on the spectrum if the velocity ratio is $R \leq 3.5$. This is a key piece of evidence indicating a transition from convective to absolute instability that occurs around $R \approx 3.5$. Interestingly, they find an asymmetric lock-in response; the amplitude required to induce lock-in is larger when $f_f/f_0 < 1$ compared to when $f_f/f_0 > 1$.

Shoji *et al.* (2020*b*) also explores the lock-in and quasiperiodicity dynamics of an equidensity $7 \leq J \leq \infty$ jet-in-crossflow with sinusoidal, axisymmetric acoustic excitation. The lock-in diagram is shown in Figure 1.9. Shoji *et al.* (2020*b*) find that the convectively unstable jet-in-crossflow upstream shear layer with $J = 18$ and 61 is not always locked-in to axisymmetric sinusoidal forcing when $f_f > f_0$. Linear stability analyses of jets-in-crossflow (Alves *et al.*, 2008; Alves & Kelly, 2008) indicate that the axisymmetric mode is stable for low frequencies. This correlates with the higher forcing amplitude required to lock-in the flow for $f_f < f_0$. However, the axisymmetric mode destabilises as temporal frequency is increased up to a finite extent. This frequency ceiling decreases as J or R decreases (Alves *et al.*, 2008; Alves & Kelly, 2008). This also correlates well with the ease of lock-in when $f_f > f_0$. Hence, the foundations of lock-in potentially lie in linear stability analysis.

1.5.3 Asymmetric Forcing of a Jet-in-Crossflow

Besnard *et al.* (2022) acoustically force a convectively unstable $\mathrm{Re}_j = 1900$, $J = 61$ jet-in-crossflow in an asymmetric manner. Using PLIF, PIV, and hot-wire anemometry, the effects of various types of asymmetric forcing on the structure and mixing, and symmetry of a jet-in-crossflow are quantified. The acoustic forcing setup consists of a tetrad of speakers arranged azimuthally equidistantly from a $D = 4.04$ mm flush nozzle to impose a helical-like wave travelling in a clockwise (CW) or counter-clockwise (CCW) manner. For the $\mathrm{Re}_j = 1900$, $J = 61$ jet-in-crossflow under consideration, the natural frequency f_0 is broadband: $1600 \lesssim f_0 \lesssim 1900$. The jet-in-crossflow is forced with numerous forcing strategies at frequencies f_f range from 875 to 3500 Hz (Besnard *et al.*, 2022). The general trends are: (i) even low amplitude forcing of any form can change the downstream CVP/jet structure, (ii) almost any type of forcing improved jet-to-crossflow fluid mixing, but especially so further downstream, (iii) a locked-in jet-in-crossflow is more homogeneously mixed than a quasiperiodic jet-in-crossflow, which in turn is usually better mixed than the unforced jet-in-crossflow, ceteris paribus, and (iv) lock-in generally led to more symmetric CVPs.

Clockwise (CW) and counter-clockwise (CCW) four-speaker forcing for $875 \leq f_f \leq 3500$ Hz are considered. The effect of forcing on the upstream shear layer frequency spectra is illustrated in Figure 1.10. A hot-wire, at $s/D = 2.0$, is used to produce frequency spectra under four-speaker asymmetric excitation both clockwise and counter-clockwise at forcing frequency $f_f = 1000, 1600, 1900, 2600$ Hz when the natural frequency $1600 \leq f_0 \leq 1900$ Hz. The forcing amplitude (measured by the disturbance pressure in Pascals) required to lock-in the upstream shear layer increases as $|f_f - f_0|$ increases. It is significantly more difficult to achieve lock-in when $f_f > f_0$, which perhaps explains why mixing improvements are greater for $f_f < f_0$. Notably, CW forcing leads to more symmetric CVPs while CCW forcing yields more amorphous blob structures in PLIF downstream (see Figure 1.11).

To obtain the most pertinent flow features, one could employ the Proper Orthogonal Decomposition (POD). POD was applied to hydrodynamics by Lumley (1967) (see Berkooz *et al.*, 1993). The method of snapshots (snapshot POD) by Sirovich (1987) can convert non-time-correlated instantaneous snapshots of a flowfield to POD bases ordered by fluctuation 'energy' levels. The term 'energy' is used because velocity information from PIV is typically used for POD. Scalar data such as the concentration fields from PLIF can also be used for snapshot POD, but the concept of 'energy' is generalised (Gurka *et al.*, 2006). Gevorkyan *et al.* (2018) were able to obtain the dominant POD mode from PLIF from simultaneous PLIF and PIV snapshots for the unforced jet-in-crossflow.

Besnard *et al.* (2022) performs snapshot POD analysis for 500 non-time-correlated snapshots of acetone-PLIF-based concentration fields of a jet-in-crossflow subjected to asymmetric forcing. This leads to the reconstruction of the original flowfield from a collection of mutually orthonormal POD bases ordered in descending 'energy'.

Figure 1.12(a) depicts the most energetic (i.e., dominant) two POD modes for the unforced $J = 61$ jet-in-crossflow with acetone PLIF snapshots taken along the centreplane. Clearly, the predominant structure of the unforced jet-in-crossflow corresponds to the coherent vortices of the upstream shear layer. Modes 1 and 2 cumulatively represent only 7% of

the total scalar energy (SE) of the unforced flowfield. With four-speaker forcing of the same $J = 61$ flowfield, the dominant modes (seen in Figures 1.12(b) and (c)) have accumulated far more energy (47% and 60%, respectively), indicating forcing that improved the repeatability and coherence of the shear layer vortex train. The upstream shear layer structures also initiate much closer to the jet exit and modes 1 and 2 appear to be paired. This appears to correspond to the POD modes of absolutely unstable jets-in-crossflow exhibiting vortex coherent vortex roll-up.

There are differences between the POD modes of clockwise and counter-clockwise forcing strategies, seen in Figures 1.12(b) and (c), respectively. Clockwise forcing appears to produce shear layers superposed by a sinusoid spatially while the structural and energy differences between modes 1 and 2 suggest they are not paired. Counter-clockwise forcing, however, have similar mode shapes and energies, indicating mode pairing. The counter-clockwise forced POD modes also appear to exhibit stronger wake-like structures (Besnard *et al.*, 2022).

To demonstrate the time-variation of the flowfield, POD mode coefficients can be plotted over time. As the dominant structures are expected to be periodic, the coefficients of the POD modes can be plotted against each other as an analogous version of a phase portrait. Simple periodic oscillations of paired modes are represented as a circle in the POD 'phase portrait', as seen for absolutely unstable jets-in-crossflow of Gevorkyan *et al.* (2018). Convectively unstable flows, recalling from Sections 1.3 and 1.4, are sensitive to external disturbances and have more broadband oscillation frequencies. Those oscillations, then, do not maintain a fixed puretone frequency. Hence, the POD 'phase portrait' is much noisier. Note that two POD modes whose coefficients' phase portraits yield a closed loop oscillate at a related frequency: $1/2f, f, 2f, \ldots$ (Vernet *et al.*, 2009; Bidan *et al.*, 2012).

The POD mode coefficient phase portraits are presented in Figure 1.13. Figure 1.13(a) corresponds to PLIF POD mode coefficients for the unforced, convectively unstable $J = 61$ jet-in-crossflow. Figures 1.13(b) and (c) correspond to the clockwise and counter-clockwise 4-speaker asymmetric forcing at $f_f = 1000$ Hz at a forcing amplitude of $P' = 0.65$ Pa,

respectively. The latter forcing conditions lead to 1 : 1 lock-in of the upstream shear layer, as measured by previous hot-wire spectral analyses.

As expected, the unforced and convectively unstable $J = 61$ jet-in-crossflow yielded amorphous 'blobs' in PLIF POD phase space as the oscillations were irregular and out of phase, as can be seen in Figure 1.13(a). The broadband natural frequency $1600 \lesssim f_0 \lesssim 1900$ Hz. By contrast, when $f_f = 1000$ Hz $< f_0$ and when the upstream shear layer was locked-in at a forcing amplitude of $P' = 0.65$ Pa, the phase portraits appear to show a pointed triadic structure, particularly in the 3-coefficient phase portraits. This suggests a coupling of three modes simultaneously. The pattern when the third and fourth mode coefficients' phase portraits suggests there is a secondary oscillation in the flow (Besnard, 2019).

To understand if inherently asymmetrical helical instability growth rates are involved in this symmetry-breaking, the jet-in-crossflow is forced with two- and one-speaker forcing. Perhaps as expected, four-speaker leads to better mixing than either two- or one-speaker forcing. Additionally, all cross-sections are more symmetric having undergone even two- or one-speaker forcing without the forcing amplitude to reach lock-in. Curiously, this scheme has reveals that the jet-in-crossflow responds negligibly to forcing of the left upstream speaker, as evidenced by significant similarity to the unforced spectra and PLIF cross-sections.

As indicated by the global stability analysis of Regan & Mahesh (2017), the jet-in-crossflow depends on the downstream shear layer as well as its upstream counterpart. This can be seen experimentally with two- or one-speaker forcing along the downstream portion of the jet. Here, downstream left forcing appears to be the most effective. Note that is unclear if this forcing setup is forcing primarily the downstream shear layer or the wake structures directly. Nevertheless, the jet is not significantly sensitive to downstream forcing.

A convectively unstable $J = 24$ and an absolutely unstable $J = 6$ jet-in-crossflow are also briefly considered by Besnard (2019); Besnard *et al.* (2022). These flows already have fairly symmetric cross-sections downstream, particularly at $x/D = 10.5$. Any type of forcing yields symmetric, unambiguous CVP lobes for the $J = 24$ jet, with the single right upstream

speaker forcing producing the most symmetric cross-section. Mixing along the centerline increases significantly with forcing, but the cross-sectional mixing increases only somewhat. This suggests that external forcing symmetrises the CVP, meaning that the laser sheet from which mixing statistics were quantified captures the gap between CVP lobes. In other words, forcing marginally increases the symmetry and structure, thereby marginally improving mixing. Forcing of the absolutely unstable $J = 6$ jet-in-crossflow does not change the structure, and thereby the mixing behaviour exhibited no change.

1.5.4 Tabbed jet-in-crossflow

Harris *et al.* (2021) place a small triangular tab blocking no more than 4% of the jet exit area immediately downstream of the jet exit. The nozzle structure was moved upstream slightly to accommodate the tab insert while ensuring crossflow encountered a flush tab insert. This small tab could be considered as a passive base flow modification or a zero-frequency disturbance that may affect the upstream shear layer instability, jet evolution, as well as mixing characteristics for a range of momentum flux ratios for an equidensity jet-in-crossflow.

Considering that the jet-in-crossflow transitions from convective to absolute instability at $J_{\text{crit}} \approx 8$ Shoji *et al.* (2020*a*), an absolutely unstable $J = 7$ and a convectively unstable $J = 61$ jet-in-crossflow were considered.

For the absolutely unstable $J = 7$ jet-in-crossflow, placing the tab on the upstream part of the jet exit dramatically weakened the upstream shear layer instability to resemble the characteristics of a convective instability and created a new oscillation frequency in the spectrum. Placement in the downstream portion also made the upstream shear layer behave in a convectively unstable manner. Correspondingly, placement in the downstream portion worsened the mixing capability and contributed to a more asymmetric CVP - typical for a convectively unstable flow (Gevorkyan *et al.*, 2016). However, placement in the upstream portion yielded the best mixing despite substantial weakening of the upstream shear layer

instability.

For the convectively unstable $J = 61$ jet-in-crossflow, placing the tab upstream was very impactful; the instability greatly weakened. However, placing the tab downstream or at other azimuthal locations had little impact on the instability. Interestingly, placing the tab at any azimuthal orientation led to improved mixing over the tabless insert - with placing the tab upstream leading to the greatest mixing.

Harris *et al.* (2021) commented that the tab study generally yielded results that aligned the wavemaker predictions of Regan & Mahesh (2019*a*) and speculated that the small tab created a locally thicker shear layer and this is generally associated with a weaker instability. Broadly speaking, the DNS of Morse & Mahesh (2023) has found similar phenomena for $R = 2, 4$ equidensity jets-in-crossflow.

1.6 Goals of the present research

The theme of the present work is to complement prior and ongoing experimental investigations of the incompressible jet-in-crossflow (Gevorkyan *et al.*, 2016, 2018; Shoji *et al.*, 2020*a*,*b*; Harris *et al.*, 2021, 2023). From such experiments, there is a general need to (i) better understand the convective-to-absolute instability transition, (ii) predict/explain the natural unforced upstream shear layer instability behaviour, (iii) explain the response to variable-amplitude acoustic excitation, especially asymmetrically applied excitation, (iv) develop physics-informed control strategies that leverage linear mechanisms, and (v) investigate the origins of the asymmetric evolution of the jet-in-crossflow in the face of a theoretically symmetric flow field (particularly in the high R regime).

Therefore, the goal of the present work is firstly to develop a 2D-local fully-coupled linear stability analysis framework with the viscous tanh and UVAS base flow models that represent the jet-in-crossflow developed by Alves *et al.* (2008) and Alves & Kelly (2008). This framework allows the incorporation of viscous instability mechanisms, the calculation of ar-

bitrarily high helical modes, and the representative of all possible base flow-eigenfunction azimuthal couplings (viz., a fully-coupled approach). This fully-coupled viscous linear stability analysis may be considered an extension of the asymptotic expansion-based linear stability analysis of Alves & Kelly (2008), which neglected certain base flow-eigenfunction couplings for computational simplicity and with approximations based on physical reasoning.

Inviscid or high-Reynolds number linear stability analyses of these convection-dominated base flows may yield non-physical oscillations. Therefore, a new upwind-based discretisation of the linearised convection term will be developed to ensure that the eigenfunctions are smooth.

Another goal is to explore the effect of the base flow-eigenfunction azimuthal couplings on the eigenvalues by developing a weakly-coupled discrete Fourier linear stability analysis approach. This weakly-coupled formulation can also highlight the essential velocity eigenfunction terms or base flow-eigenfunction coupling terms that affect the eigenvalues the most. Hence, this approach offers physical interpretations for designing control strategies or for explaining experimental jet-in-crossflow behaviour.

Another goal is to develop a spatial kinetic energy budget analysis approach to compliment the linear stability analyses by providing additional interpretability. Typically, a perturbation sensitivity analysis of the numerical and physical hyperparameters contributes some insight to the underlying physics. However, this approach enables the quantification of the contribution of various physical mechanisms to an eigenvalue a posteriori.

The remainder of this document is arranged as follows: Chapter 2 outlines the governing equations and numerical approaches employed for the linear stability analysis of 1D base flows for verification purposes while Chapter 3 presents the linear stability analysis results of 1D base flows for validation purposes. Chapter 4 describes the governing equations, base flows, and numerical approaches employed for the 2D-local linear stability analysis applied to the jet-in-crossflow. Therein lies verification against other 2D base flows to establish trust in the framework, a description of the models that the jet-in-crossflow velocity field, and a

spatial kinetic energy budget analysis to interpret the resultant linear stability results. An elaboration of the asymptotic expansion-based linear stability analysis approach of Alves & Kelly (2008) is also contained in Chapter 4. Chapter 5 details the results of the 2D-local linear stability analysis of the jet-in-crossflow with subsequent discussion and interpretation. Finally, Chapter 6 contains overall conclusions and recommendations for future research directions.

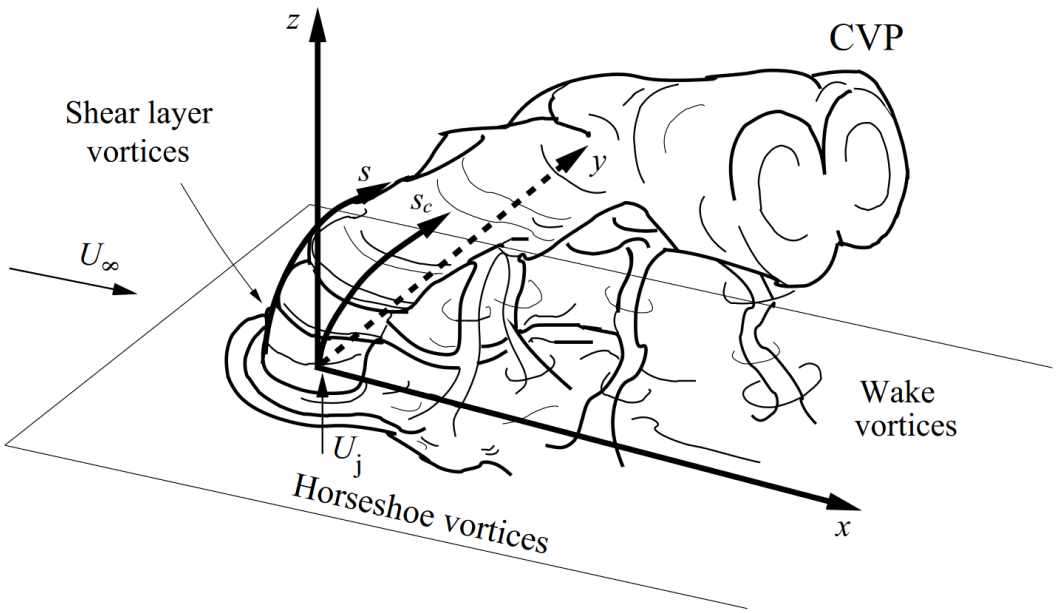

Figure 1.1: Diagram of a flush-injected circular jet perpendicularly into a uniform crossflow with key vortical features highlighted. Inertial reference frame bases x, y, z, the jet upstream shear layer trajectory parameter 's' and the centreline jet trajectory parameter 's_c' are depicted. Image adapted from Fric & Roshko (1994)

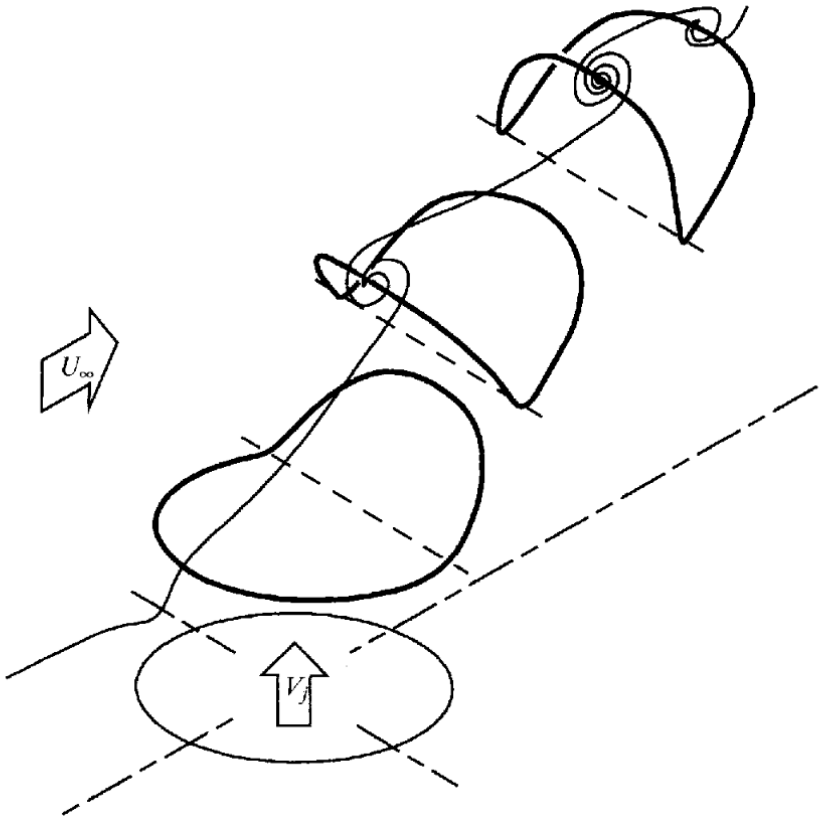

Figure 1.2: Diagram of a jet-in-crossflow nearfield vortex rings tilting and folding as they evolve downstream into a counter-rotating vortex pair. Image adapted from Kelso *et al.* (1996)

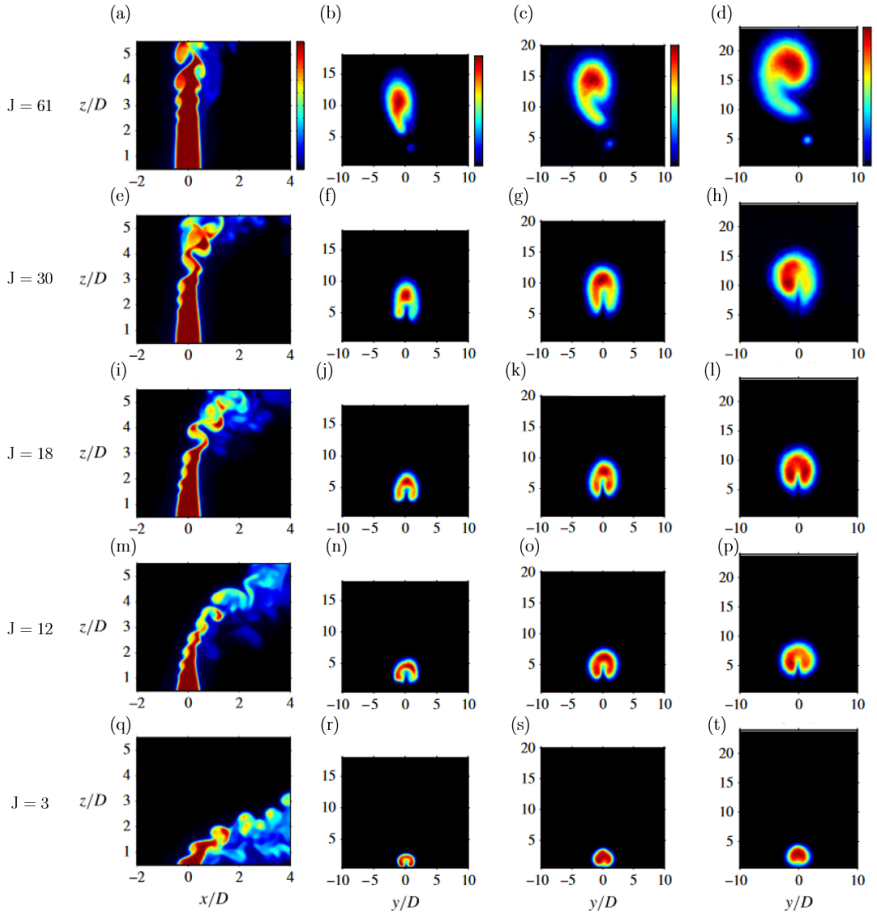

Figure 1.3: Representative acetone PLIF images for a flush nozzle injected equidensity $S = 1$ jet-in-crossflow at $\mathrm{Re}_j = 1900$ for various momentum flux ratios J. (a) displays instantaneous centreplane PLIF snapshots. (b), (c), and (d) displays the ensembled-averaged cross-sectional PLIF snapshots imaged at $x/D = 2.5,\ 5.5,\ 10.5$, respectively. Row 1, 2, 3, 4, 5 correspond to $J = 61, 30, 18, 12, 3$, respectively. Images were averaged over 300 snapshots. Images from Getsinger *et al.* (2014)

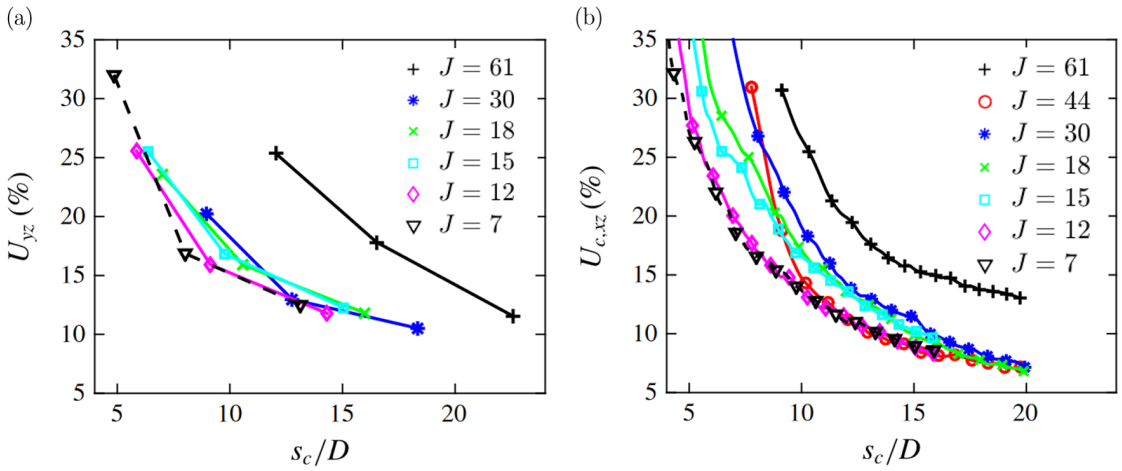

Figure 1.4: Unmixedness from (a) cross-sectional U_{yz} and (b) centreplane $U_{c,xz}$ acetone planar laser-induced fluorescence (PLIF) plotted against jet centreline trajectory parameter s_c/D for various momentum flux ratios J. Note that the thin slice to enable concentration matching is aligned along x-z. Figure from Gevorkyan *et al.* (2016)

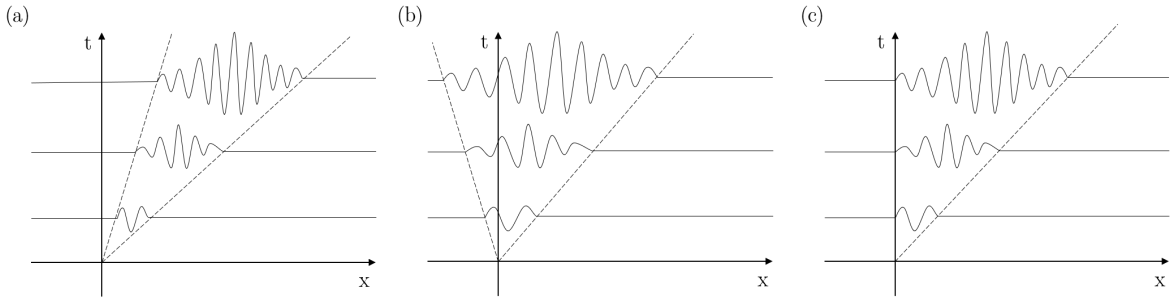

Figure 1.5: Illustrations of (a) a convectively unstable system's response to a disturbance, (b) an absolutely unstable system's response to a disturbance, and (c) a marginally absolutely unstable system's response to a disturbance. Adapted from Huerre & Monkewitz (1990).

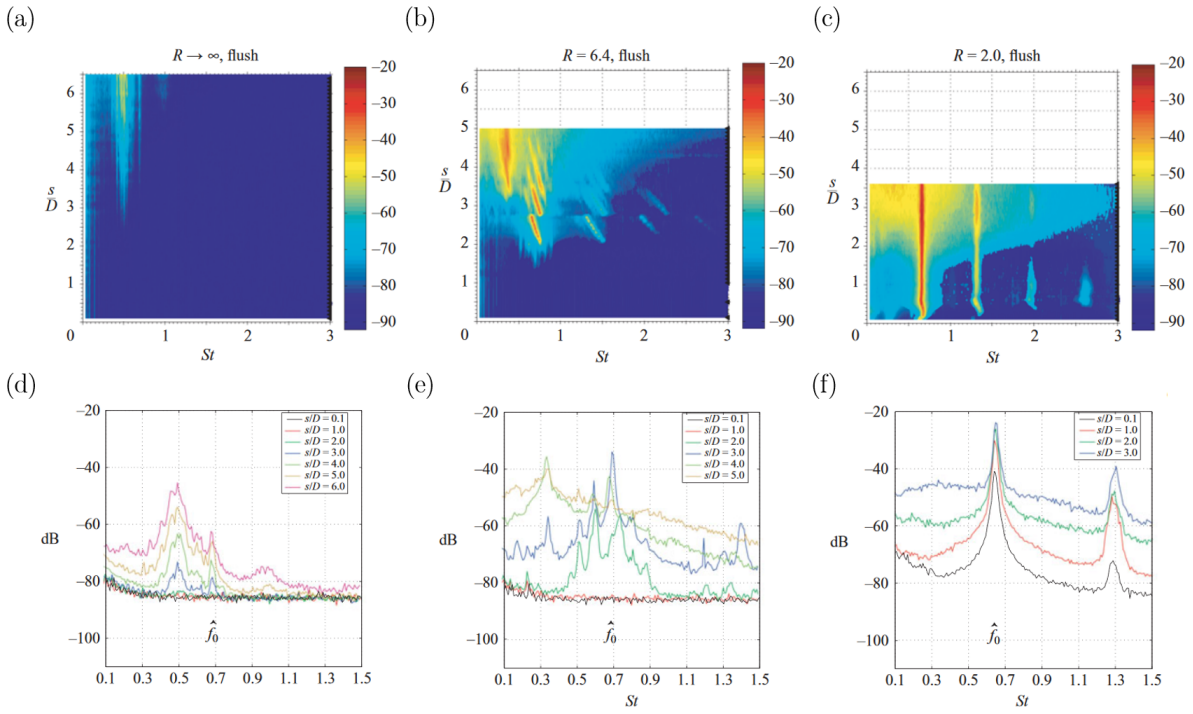

Figure 1.6: Above: Experimental $\mathrm{Re}_j = 2000$, flush nozzle jet-in-crossflow spectral contours for velocity ratios (a) $R \to \infty$, (b) $R = 6.4$, and (c) $R = 2.0$. Below: Corresponding experimental power spectral densities for velocity ratios (d) $R \to \infty$, (e) $R = 6.4$, and (f) $R = 2.0$. Figure from Megerian *et al.* (2007)

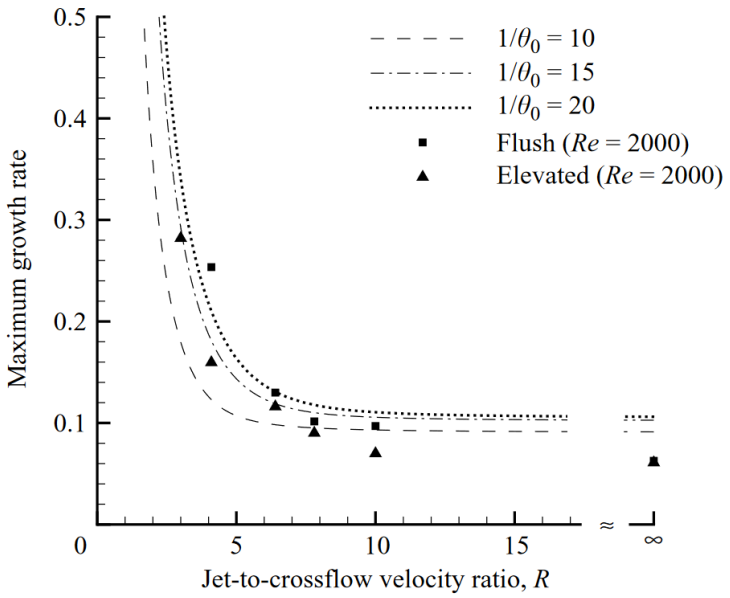

Figure 1.7: Comparison of spatial growth rates $-\Im[\alpha]\theta_0$ across velocity ratios R at Re $=$ 2000, 3000 between the linear stability analysis of Alves *et al.* (2008) and the experiments of Megerian *et al.* (2007). Figure from Alves *et al.* (2008)

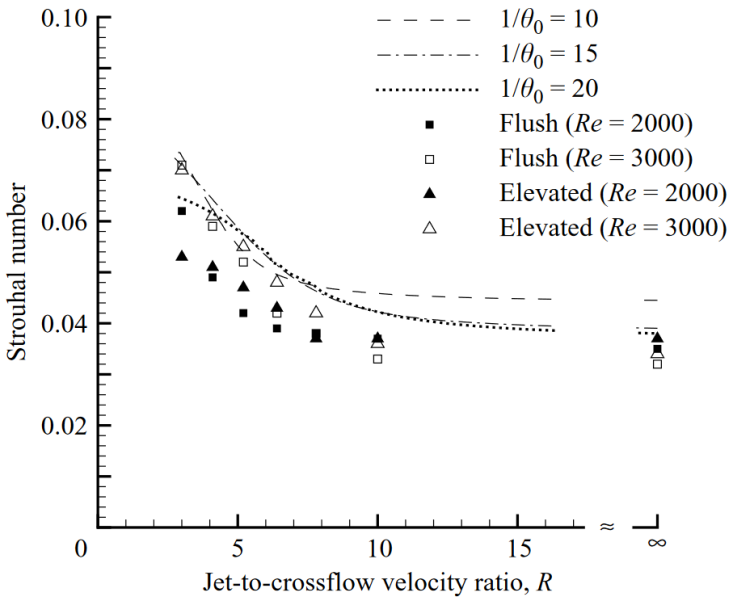

Figure 1.8: Comparison of dominant Strouhal number of the axisymmetric mode across velocity ratios R at Re = 2000, 3000 between the linear stability analysis of Alves *et al.* (2008) and the experiments of Megerian *et al.* (2007). Figure from Alves *et al.* (2008)

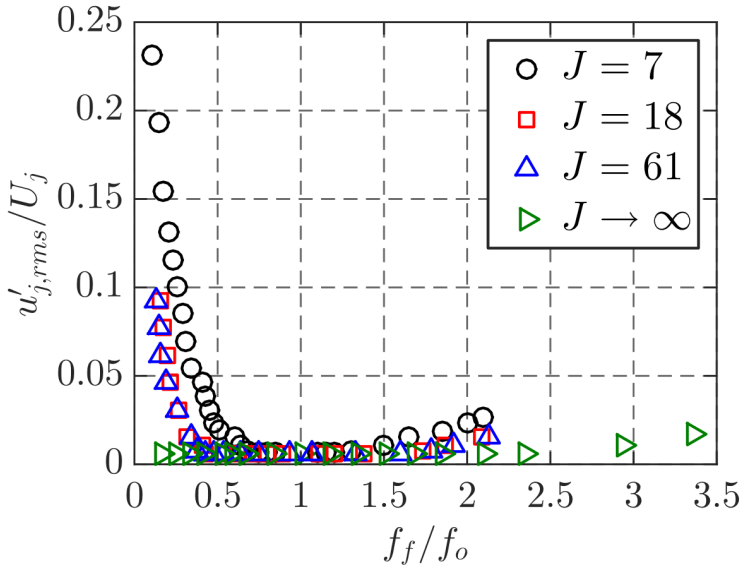

Figure 1.9: Lock-in diagram for the equidensity jet-in-crossflow at $J = 7, 18, 61, \infty$ subject to acoustic axisymmetric sinusoidal forcing at various forcing frequencies f_f and forcing amplitudes required for lock-in $u'_{j,\mathrm{rms}}/U_j$, measured at the shear layer locations $s/D = 2.0$ for the transverse jets and $s/D = 4.0$ for the free jet. Figure from Shoji *et al.* (2020*b*)

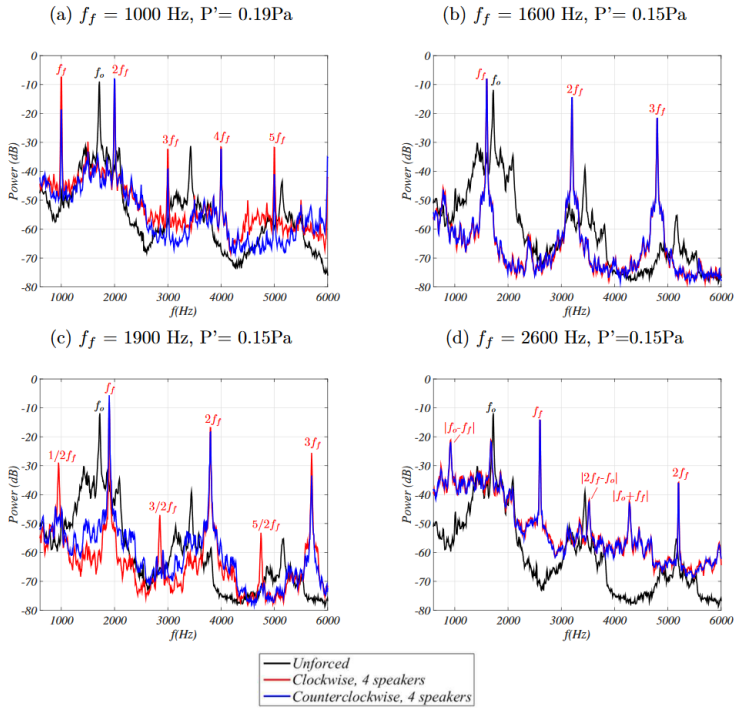

Figure 1.10: Frequency spectra of vertical velocity perturbations measured by hot-wire anemometry at $s/D = 2.0$ for the J= 61 jet-in-crossflow. The black lines correspond to the unforced frequency spectra whereas the red (blue) lines correspond to clockwise (counter-clockwise) excitation from four speakers. The natural frequency of the upstream shear layer was broadband: $1600 \leq f_0 \leq 1900$. Figure from Besnard *et al.* (2022).

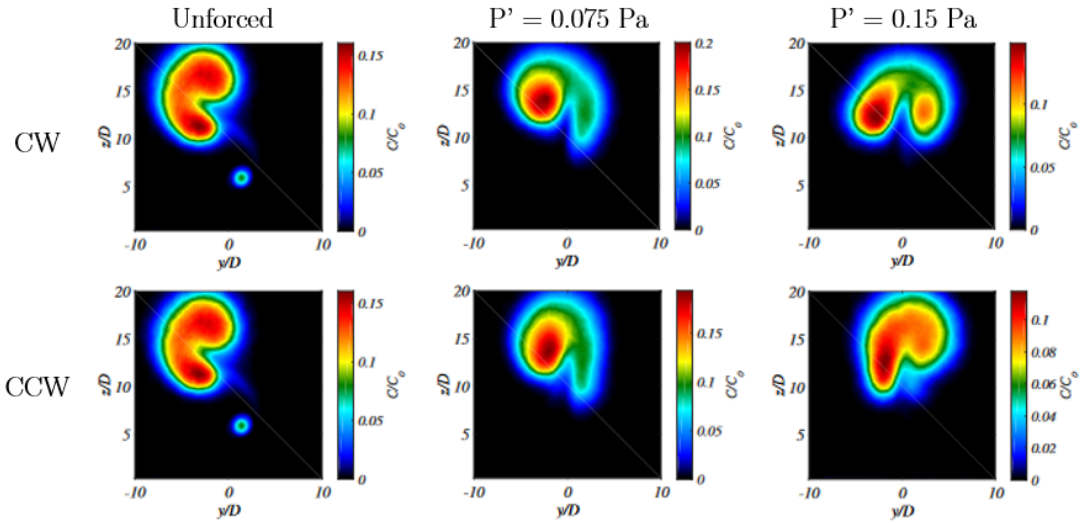

Figure 1.11: Averaged cross-sectional y-z acetone PLIF images for the $J = 61$ jet-in-crossflow with a natural frequency $1600 \leq f_0 \leq 1900$. Forcing frequency $f_f = 1600$ Hz. Top (bottom) row corresponds to clockwise (counter-clockwise) four-speaker forcing. Forcing amplitude as indicated. Figure from Besnard *et al.* (2022).

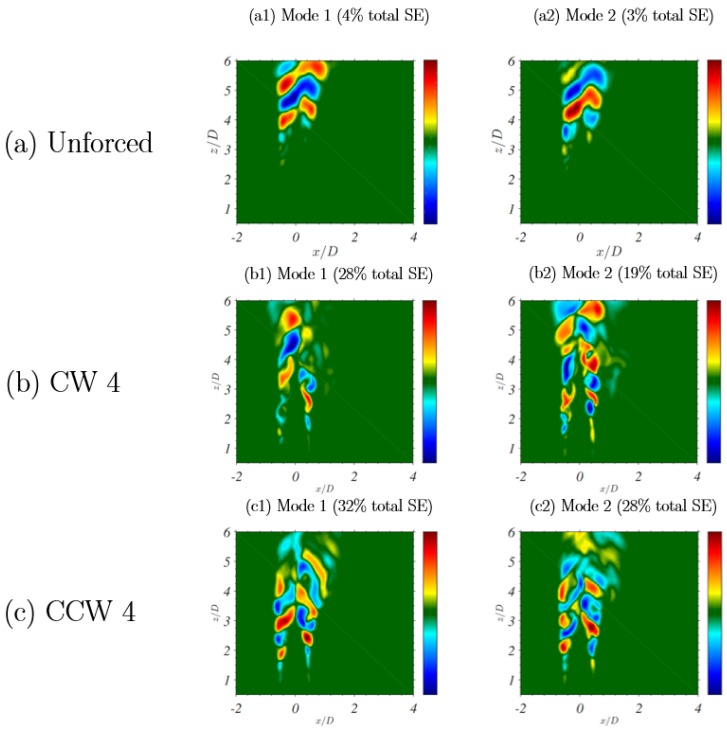

Figure 1.12: The first two POD modes from instantaneous centreplane PLIF snapshots of a $J = 61$ jet-in-crossflow under (a) no forcing, (b) clockwise 4-speaker forcing at $f_f = 1000$ Hz at an amplitude of $P' = 0.65$ Pa, and (c) the same forcing as (b) but in a counter-clockwise manner. The proportion of total scalar fluctuation energy of each mode is denoted in the brackets. Figure rearranged from Besnard *et al.* (2022).

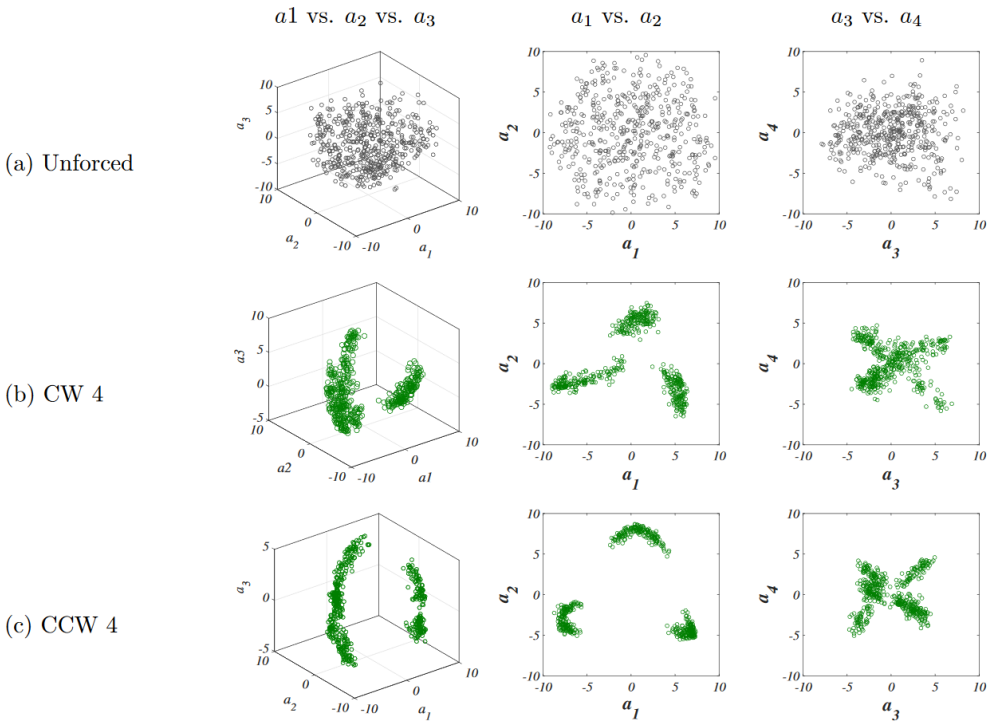

Figure 1.13: Phase portraits of POD coefficients for the first 4 instantaneous centerplane PLIF POD modes of a $J = 61$ jet-in-crossflow. (a) unforced jet-in-crossflow, (b) clockwise 4-speaker forcing at $f_f = 1000$ Hz, and (c) counter-clockwise 4-speaker forcing at $f_f = 1000$ Hz at $P' = 0.65$ Pa. Black symbols represent the unforced condition while green symbols represent 1:1 lock-in of the upstream shear layer. Figure from Besnard *et al.* (2022).

CHAPTER 2

Governing equations and numerical methods for stability analysis for 1D base flows

To enable the development of a 2D stability analysis framework, it is necessary to firstly consider a 1D paradigm. A code for 1D spatial modal linear stability analysis in a matrix-forming approach, described in Section 2.1, was obtained from Rômulo Bessi Freitas and Professor Leonardo Alves (Freitas, 2019). This chapter will describe linear modal/non-modal stability analyses of axisymmetric pipes and free jets which have been performed to date; they are designed to prepare for future application to the jet-in-crossflow.

Round pipe flow, famously documented by Reynolds (1883), can experimentally transition to turbulence given a sufficiently high Reynolds number (Reynolds, 1883), and/or sufficiently rough pipe walls (Cotrell *et al.*, 2008), or if the pipe boundary conditions are non-axisymmetric (Han *et al.*, 2000). Turbulence can also be induced with small, but finite-amplitude disturbances (Davey & Nguyen, 1971; Itoh, 1977*a*,*b*), in axisymmetry-breaking elliptical pipes (Kerswell & Davey, 1996), and rotating pipes (Wang & Rusak, 1996; Zaturska & Banks, 1995). But, numerous temporal and spatial linear stability analyses find that fully-developed, stationary, round pipe flow is linearly stable to all infinitesimal disturbances (Gill, 1965; Davey & Drazin, 1969; Garg & Rouleau, 1972). This apparent contradiction between experimental observations and numerical findings has produced a wealth of pipe instability data suitable for numerical validation. Non-modal stability analyses of pipe Poiseuille flow have found that algebraic (non-exponential) growth resulting from the nonmodal nature of the linear stability operator contributes to the transition to turbulence observed in experi-

ments (Schmid & Henningson, 2001; Criminale *et al.*, 2003; Trefethen & Embree, 2005).

2.1 Modal stability analysis

Section 1.4 discussed the general framework of modal linear stability analysis, illustrated in Eqs. (1.4) - (1.8). The families of linear stability analyses are described in Table 1.1. For validation, we analysed the stability of the round (i.e., axisymmetric) shear flows of pipes and free (non-coflowing or non-transverse) jets. For simplicity, we elected to consider a one-dimensional parallel axisymmetric base flow whereby the axial and azimuthal directions were considered to be homogeneous directions, in contrast to the approaches of Huang & Chen (1974); Zikanov (1996) and Martin & Meiburg (1991); Plaschko (1979); Cohen & Wygnanski (1987); Kiwata *et al.* (2011) for the pipe and jet, respectively. Therefore, by Table 1.1, we conducted a local 1D linear stability analysis.

2.1.1 Dimensional nonlinear governing equations

For these instability analyses of pipe and jet flows, cylindrical coordinates (z, r, θ) aligned along the pipe/jet axis were the most natural. The flow was assumed to be viscous, Newtonian, and incompressible. Hence, the following dimensional Navier-Stokes governing equations were obtained:

$$\tilde{\nabla} \cdot \tilde{\mathbf{u}} = 0 \tag{2.1a}$$

$$\frac{\partial \tilde{\mathbf{u}}}{\partial \tilde{t}} + (\tilde{\mathbf{u}} \cdot \tilde{\nabla})\tilde{\mathbf{u}} + \frac{1}{\rho}\tilde{\nabla}\tilde{p} - \nu\tilde{\nabla}^2\tilde{\mathbf{u}} = 0 \tag{2.1b}$$

where $\tilde{\mathbf{u}} = (\tilde{u}_r, \tilde{u}_\theta, \tilde{u}_z)^T$ is the dimensional velocity vector-function and $\tilde{p}$ is the dimensional pressure field. ρ is the constant density and ν corresponds to the constant dynamic viscosity of the fluid. Eq. (2.1) was written to correspond with Eq. (1.4).

Explicitly, the dimensional Navier-Stokes equations in Eq. (2.1) were rearranged and

expanded in cylindrical coordinates as:

$$\frac{\partial \tilde{u}_r}{\partial \tilde{r}} + \frac{\tilde{u}_r}{\tilde{r}} + \frac{1}{\tilde{r}}\frac{\partial \tilde{u}_\theta}{\partial \theta} + \frac{\partial \tilde{u}_z}{\partial \tilde{z}} = 0 \tag{2.2a}$$

$$\begin{aligned}\frac{\partial \tilde{u}_r}{\partial \tilde{t}} + \tilde{u}_r\frac{\partial \tilde{u}_r}{\partial \tilde{r}} + \frac{\tilde{u}_\theta}{\tilde{r}}\frac{\partial \tilde{u}_r}{\partial \theta} - \frac{\tilde{u}_\theta^2}{\tilde{r}} + \tilde{u}_z\frac{\partial \tilde{u}_r}{\partial \tilde{z}} &= -\frac{1}{\rho}\frac{\partial \tilde{p}}{\partial \tilde{r}} \\ &+ \nu\left(\frac{\partial^2 \tilde{u}_r}{\partial \tilde{r}^2} + \frac{1}{\tilde{r}}\frac{\partial \tilde{u}_r}{\partial \tilde{r}} - \frac{\tilde{u}_r}{\tilde{r}^2} + \frac{1}{\tilde{r}^2}\frac{\partial^2 \tilde{u}_r}{\partial \theta^2} - \frac{2}{\tilde{r}^2}\frac{\partial \tilde{u}_\theta}{\partial \theta} + \frac{\partial^2 \tilde{u}_r}{\partial \tilde{z}^2}\right)\end{aligned} \tag{2.2b}$$

$$\begin{aligned}\frac{\partial \tilde{u}_\theta}{\partial \tilde{t}} + \tilde{u}_r\frac{\partial \tilde{u}_\theta}{\partial \tilde{r}} + \frac{\tilde{u}_\theta}{\tilde{r}}\frac{\partial \tilde{u}_\theta}{\partial \theta} + \frac{\tilde{u}_r\,\tilde{u}_\theta}{\tilde{r}} + \tilde{u}_z\frac{\partial \tilde{u}_\theta}{\partial \tilde{z}} &= -\frac{1}{\rho}\frac{1}{\tilde{r}}\frac{\partial \tilde{p}}{\partial \theta} \\ &+ \nu\left(\frac{\partial^2 \tilde{u}_\theta}{\partial \tilde{r}^2} + \frac{1}{\tilde{r}}\frac{\partial \tilde{u}_\theta}{\partial \tilde{r}} - \frac{\tilde{u}_\theta}{\tilde{r}^2} + \frac{1}{\tilde{r}^2}\frac{\partial^2 \tilde{u}_\theta}{\partial \theta^2} + \frac{2}{\tilde{r}^2}\frac{\partial \tilde{u}_r}{\partial \theta} + \frac{\partial^2 \tilde{u}_\theta}{\partial \tilde{z}^2}\right)\end{aligned} \tag{2.2c}$$

$$\begin{aligned}\frac{\partial \tilde{u}_z}{\partial \tilde{t}} + \tilde{u}_r\frac{\partial \tilde{u}_z}{\partial \tilde{r}} + \frac{\tilde{u}_\theta}{\tilde{r}}\frac{\partial \tilde{u}_z}{\partial \theta} + \tilde{u}_z\frac{\partial \tilde{u}_z}{\partial \tilde{z}} &= -\frac{1}{\rho}\frac{\partial \tilde{p}}{\partial \tilde{z}} \\ &+ \nu\left(\frac{\partial^2 \tilde{u}_z}{\partial \tilde{r}^2} + \frac{1}{\tilde{r}}\frac{\partial \tilde{u}_z}{\partial \tilde{r}} + \frac{1}{\tilde{r}^2}\frac{\partial^2 \tilde{u}_z}{\partial \theta^2} + \frac{\partial^2 \tilde{u}_z}{\partial \tilde{z}^2}\right)\end{aligned} \tag{2.2d}$$

2.1.2 Non-dimensional nonlinear governing equations

This cylindrical coordinate system was non-dimensionalised to become (z, r, θ) with the dynamical variables of interest being $\mathbf{u} = (u_r, u_\theta, u_z)^T$ and p. The characteristic length scale was taken to be the pipe or initial jet radius R_0 and the velocity scale was taken to be the maximum velocity $u_{\max}$ (defined to be the value along the centreline for the axisymmetric pipe and free jet) to non-dimensionalise the governing equations. For the jet-in-crossflow base flow models considered in Sections 4 and 5, $u_{\max}$ is defined as the maximum velocity of the free jet limit of the jet-in-crossflow base flow (typically the value at $r = 0$). However, it is worth noting that direct comparison between the numerical and experimental jet-in-crossflow base flows for a particular axial station was enabled by obtaining the $u_{\max}$ value from the experimental jet-in-crossflow velocity field. This value was typically located in the downstream portion of the potential core.

$u = \tilde{u}/u_{\max}$, $r = \tilde{r}/R_0$, and $t = \tilde{t}/(R_0/u_{\max})$ represent the non-dimensionalised ve-

locity components, radial coordinate, and time, respectively. $\nabla = R_0\tilde{\nabla}, p = \tilde{p}/(\rho u_{\max}^2)$ are the dimensionless gradient operator and the pressure, respectively. The resultant non-dimensionalised and nonlinear governing equations in cylindrical coordinates are:

$$\frac{\partial u_r}{\partial r} + \frac{u_r}{r} + \frac{1}{r}\frac{\partial u_\theta}{\partial \theta} + \frac{\partial u_z}{\partial z} = 0 \tag{2.3a}$$

$$\begin{aligned}\frac{\partial u_r}{\partial t} + u_r\frac{\partial u_r}{\partial r} + \frac{u_\theta}{r}\frac{\partial u_r}{\partial \theta} - \frac{u_\theta^2}{r} + u_z\frac{\partial u_r}{\partial z} &= -\frac{\partial p}{\partial r} \\ &+ \frac{1}{\mathrm{Re}}\left(\frac{\partial^2 u_r}{\partial r^2} + \frac{1}{r}\frac{\partial u_r}{\partial r} - \frac{u_r}{r^2} + \frac{1}{r^2}\frac{\partial^2 u_r}{\partial \theta^2} - \frac{2}{r^2}\frac{\partial u_\theta}{\partial \theta} + \frac{\partial^2 u_r}{\partial z^2}\right)\end{aligned} \tag{2.3b}$$

$$\begin{aligned}\frac{\partial u_\theta}{\partial t} + u_r\frac{\partial u_\theta}{\partial r} + \frac{u_\theta}{r}\frac{\partial u_\theta}{\partial \theta} + \frac{u_r\ u_\theta}{r} + u_z\frac{\partial u_\theta}{\partial z} &= -\frac{1}{r}\frac{\partial p}{\partial \theta} \\ &+ \frac{1}{\mathrm{Re}}\left(\frac{\partial^2 u_\theta}{\partial r^2} + \frac{1}{r}\frac{\partial u_\theta}{\partial r} - \frac{u_\theta}{r^2} + \frac{1}{r^2}\frac{\partial^2 u_\theta}{\partial \theta^2} + \frac{2}{r^2}\frac{\partial u_r}{\partial \theta} + \frac{\partial^2 u_\theta}{\partial z^2}\right)\end{aligned} \tag{2.3c}$$

$$\begin{aligned}\frac{\partial u_z}{\partial t} + u_r\frac{\partial u_z}{\partial r} + \frac{u_\theta}{r}\frac{\partial u_z}{\partial \theta} + u_z\frac{\partial u_z}{\partial z} &= -\frac{\partial p}{\partial z} \\ &+ \frac{1}{\mathrm{Re}}\left(\frac{\partial^2 u_z}{\partial r^2} + \frac{1}{r}\frac{\partial u_z}{\partial r} + \frac{1}{r^2}\frac{\partial^2 u_z}{\partial \theta^2} + \frac{\partial^2 u_z}{\partial z^2}\right)\end{aligned} \tag{2.3d}$$

Note that the Reynolds number is $\mathrm{Re} \coloneqq u_{\max}R_0/\nu$ for both the pipe and jet.

2.1.3 Base flows

Base flows (also known as steady-state solutions, fixed-point solutions, and point attractors (Li, 2011)), are necessary to linearise the governing the equations, as mentioned in Section 1.4. These base flows can be analytical solutions of the Navier-Stokes equations or can be time-averaged measurements from numerical simulations or experiments. Note that it is sometimes necessary or desirable to employ selective frequency damping (SFD) methods to obtain a viable numerical base flow of a globally unstable flow field (Åkervik *et al.*, 2006; Casacuberta *et al.*, 2018).

2.1.3.1 Axisymmetric pipe base flow

Laminar fully-developed axisymmetric pipe flow is a rare example of an exact solution of the nonlinear partial differential Navier-Stokes equations. The solution was almost simultaneously obtained by Hagen (Hagen, 1839) and Poiseuille (Poiseuille, 1840) independently. The flow is assumed to be: (i) steady for time-invariance, (ii) fully-developed for a parallel flow, (iii) axisymmetric to eliminate azimuthal dependence, (iv) obeying viscous no-slip boundary conditions applied to the pipe walls, and (v) pressure-driven along the pipe z direction.

These assumptions allowed the non-dimensional Navier-Stokes equations of Eqs. (2.3) to be simplified to become:

$$\frac{\partial p}{\partial z} = \frac{1}{\mathrm{Re}}\left(\frac{\partial^2 u_z}{\partial r^2} + \frac{1}{r}\frac{\partial u_z}{\partial r}\right) \tag{2.4}$$

Reminiscent of separable solutions of partial differential equations which yield ordinary differential equations of the Sturm-Liouville type, non-trivial solutions of Eq. (2.4) require that the pressure gradient is non-zero and constant. This is also because a fully-developed axisymmetric velocity profile $u_z = u_z(r)$ must be independent of z. Note the velocity must be finite at the centreline ($r = 0$) and there is a no-slip condition on the pipe wall ($r = R_0$). Hence, the dimensionless Hagen-Poiseuille velocity profile is:

$$\vec{\bar{u}}_b = \bar{u}_z(r)\hat{\mathbf{e}}_z = u_{\max}(1 - r^2)\hat{\mathbf{e}}_z \tag{2.5}$$

where R_0 is the constant, fixed pipe radius and $u_{\max} = -\frac{\mathrm{Re}}{4}\frac{\partial p}{\partial z}R_0^2$ is the maximum velocity (which is along the pipe centreline). $\hat{\mathbf{e}}_z$ is the unit vector along the pipe z direction. By convention, the centreline velocity $u_{\max} \coloneqq 1$ and the pipe radius $R_0 \coloneqq 1$ to provide a convenient dimensionless reference point. Therefore, the velocity profile for Hagen-Poiseuille pipe flow used in this document is:

$$\bar{u}_z(r) = (1 - r^2) \tag{2.6}$$

This convention led to the following pressure base flow p along z:

$$\bar{p}(r) = p_0 - \frac{4}{\mathrm{Re}} z \tag{2.7}$$

where p_0 is the static pressure at $z = 0$ that drives the flow through the pipe and the Reynolds number is $\mathrm{Re} \coloneqq u_{\max} R_0 / \nu$. Note that the base flow here was considered to be fully-developed along the pipe axis z coordinate. Hence, the base flow was invariant along z, unlike in parabolised stability theory. As the fully-developed pipe flow is a bounded shear flow, the most unstable modal instability is expected to be the form of Tollmein-Schlichting waves (Gipon, 2018). Note the boundary conditions of axisymmetric pipe flow is found in Section 2.1.5.1. The overbar notation is used to denote a base flow.

2.1.3.2 Axisymmetric jet base flow

Unlike the fully-developed axisymmetric pipe flow, the axisymmetric free jet does not have a general analytical solution, partially because the jet velocity profile evolves spatially as the momentum and mass flux of the jet mixes with that of the ambient fluid. Considering the limiting case of a point-momentum flux source to represent the extreme far-field of a round jet, a steady self-similar solution exists (Schlichting, 1933; Batchelor & Gill, 1962; Schlichting, 1968; Landau & Lifshitz, 1987):

$$\bar{u}_z(r) = \frac{1}{(1 + r^2)^2} \tag{2.8}$$

Note that the resulting velocity profile is non-dimensionalised by the maximum velocity along the centreline and the jet radius (Schlichting, 1933). This far-field or self-similar velocity profile is valid regardless of the velocity profile at the jet exit. Additionally, the

velocity profile in Eq. (2.8) is valid if the jet is laminar or turbulent (Schlichting, 1968).

The nearfield velocity profile of a free jet largely depends on the geometry of the jet issuer. For example, the velocity profile immediately downstream of a jet issued from a long pipe is that of fully-developed Hagen-Poiseuille flow (Kambe, 1969). That is,

$$\bar{u}_z(r) = (1 - r^2) \tag{2.9}$$

which has been non-dimensionalised by the centreline velocity and the jet radius as in Eq. (2.6). By contrast, a jet issuing from a convergent nozzle can be idealised with a 'top-hat' velocity profile. Note that this has also been called an inviscid cylindrical vortex sheet by Batchelor & Gill (1962) and Coelho & Hunt (1989):

$$\bar{u}_z(r) = \begin{cases} 1 & \text{if } 0 \leq r \leq 1 \\ 0 & \text{otherwise} \end{cases} \tag{2.10}$$

Intermediate velocity profiles between the fully boundary layer flow of Eq. (2.9) and the boundary layer-free flow of Eq. (2.10) clearly depend on the momentum thickness θ that arises from the jet exit geometry. As analytical solutions of a generalised velocity profile have not yet been found, the following empirically-robust velocity profiles have been historically employed in modal stability analyses of jets:

$$\bar{u}_z(r) = \frac{1}{2}\left\{1 + \tanh\left[\frac{R_0}{4\theta}\left(\frac{1}{r} - r\right)\right]\right\} \tag{2.11}$$

This is a popular member of the Michalke family of jet velocity profiles (Michalke, 1984) that were obtained from fitting experimental data of Freymuth (1966) and Michalke (1971). Spatial linear stability analyses by Michalke (1984) and Morris (1976) yield results that compare favourably with the experimentally-measured velocities obtained by Crow & Champagne (1971) around two diameters downstream of the jet exit. Crighton & Gaster (1976)

suggest that the hyperbolic-tangent profile should be valid for modelling axisymmetric free jets up to six diameters downstream, beyond which the fully-developed jet velocity profile is more appropriate.

To represent a broadening velocity profile at arbitrary locations downstream, it is possible to use the following velocity profile:

$$\bar{u}_z(r) = \begin{cases} 1 & \text{if } 0 \leq r \leq 1 \\ \exp\left(-(r-1)^2/\delta^2\right) & \text{if } r > 1 \end{cases} \tag{2.12}$$

where δ is an tuning parameter that affects the broadness of the velocity profile. This profile is used by Boronin *et al.* (2013), which was used to validate the temporal non-modal stability code.

There are numerous other velocity profiles that are generally derived from empirical modelling of experimental measurements such as those of Mattingly & Chang (1974); Morris (1976); Gareev *et al.* (2022), but they will not be discussed here.

2.1.4 Linearised governing equations

To linearise the governing equations, we firstly expanded each variable about a small disturbance from the base flow by ϵ in a Taylor series as follows:

$$q \coloneqq \bar{q} + \epsilon q' \tag{2.13}$$

where q represents any scalar dynamical variable such as pressure or a velocity component, $\bar{q}$ represents its base flow, and q' represents the disturbance variable. After substituting Eq. (2.13) into the governing equations, all terms of order $\bar{q} \sim \mathcal{O}(1)$ are classified as base flow terms whereas all terms of order $\epsilon q' \sim \mathcal{O}(\epsilon)$ are referred to as the disturbance variables. Higher order terms of ϵ were neglected in this Taylor series expansion. ϵ was considered as the amplitude-scale of the linear, infinitesimal, scalar disturbance. For clarity, as the

disturbance amplitude diminishes $\epsilon \to 0$, the original base flow is recovered. If $\epsilon \gg 0$, then the disturbance is considered to have such a large amplitude that the nonlinear phenomena are non-negligible, and thus the stability analysis would no longer be considered a linear. This implies that the results of linear stability analyses are not strictly applicable to predicting or understanding nonlinear flow behaviour, but linear disturbances can be the origin of nonlinear behaviour (Mattingly & Chang, 1974; Crow & Champagne, 1971).

The expansion of Eq. (2.13) and the base flow of Eqs. (2.6)-(2.7) were substituted into the non-dimensional and nonlinear governing equations of Eqs. (2.3). There were three resultant collections of equations: those without a multiplicative ϵ term, those with a multiplicative ϵ term, and those with a multiplicative ϵ^2 term. They are called the $\mathcal{O}(1)$, $\mathcal{O}(\epsilon)$, and $\mathcal{O}(\epsilon^2)$ equations, respectively. The $\mathcal{O}(1)$ equations are assumed to be automatically satisfied by the base flow and so will not be displayed here. The second-order $\mathcal{O}(\epsilon^2)$ terms were considered to be too small in amplitude when $\epsilon \ll 1$ and hence negligible for linear stability analysis. The linear disturbance $\mathcal{O}(\epsilon)$ equations are, however, of great interest and are displayed below:

$$\frac{\partial u_r'}{\partial r} + \frac{u_r'}{r} + \frac{1}{r}\frac{\partial u_\theta'}{\partial \theta} + \frac{\partial u_z'}{\partial z} = 0 \tag{2.14a}$$

$$\begin{aligned}\frac{\partial u_r'}{\partial t} + \bar{u}_z\frac{\partial u_r'}{\partial z} &= -\frac{\partial p'}{\partial r} \\ &+ \frac{1}{\mathrm{Re}}\left(\frac{\partial^2 u_r'}{\partial r^2} + \frac{1}{r}\frac{\partial u_r'}{\partial r} - \frac{u_r'}{r^2} + \frac{1}{r^2}\frac{\partial^2 u_r'}{\partial \theta^2} - \frac{2}{r^2}\frac{\partial u_\theta'}{\partial \theta} + \frac{\partial^2 u_r'}{\partial z^2}\right)\end{aligned} \tag{2.14b}$$

$$\begin{aligned}\frac{\partial u_\theta'}{\partial t} + \bar{u}_z\frac{\partial u_\theta'}{\partial z} &= -\frac{1}{r}\frac{\partial p'}{\partial \theta} \\ &+ \frac{1}{\mathrm{Re}}\left(\frac{\partial^2 u_\theta'}{\partial r^2} + \frac{1}{r}\frac{\partial u_\theta'}{\partial r} - \frac{u_\theta'}{r^2} + \frac{1}{r^2}\frac{\partial^2 u_\theta'}{\partial \theta^2} + \frac{2}{r^2}\frac{\partial u_r'}{\partial \theta} + \frac{\partial^2 u_\theta'}{\partial z^2}\right)\end{aligned} \tag{2.14c}$$

$$\begin{aligned}\frac{\partial u_z'}{\partial t} + u_r'\frac{\partial \bar{u}_z}{\partial r} + \bar{u}_z\frac{\partial u_z'}{\partial z} &= -\frac{\partial p'}{\partial z} \\ &+ \frac{1}{\mathrm{Re}}\left(\frac{\partial^2 u_z'}{\partial r^2} + \frac{1}{r}\frac{\partial u_z'}{\partial r} + \frac{1}{r^2}\frac{\partial^2 u_z'}{\partial \theta^2} + \frac{\partial^2 u_z'}{\partial z^2}\right)\end{aligned} \tag{2.14d}$$

Eqs. (2.14) can be easily rearranged to fit the form of Eq. (1.6). This is a local-1D

analysis because we employ a 1D quasi-parallel base flow approximation where the base flow is approximated to not evolve in the streamwise direction. The resultant normal Fourier modes decomposition (also termed an ansatz) used here is:

$$u_r' \coloneqq \hat{u}_r(r)\ \exp(i(kz + m\theta - \omega t)) \tag{2.15a}$$

$$u_\theta' \coloneqq \hat{u}_\theta(r)\ \exp(i(kz + m\theta - \omega t)) \tag{2.15b}$$

$$u_z' \coloneqq \hat{u}_z(r)\ \exp(i(kz + m\theta - \omega t)) \tag{2.15c}$$

$$p' \coloneqq \hat{p}(r)\ \exp(i(kz + m\theta - \omega t)) \tag{2.15d}$$

where m is considered to the azimuthal mode number to reflect the origin of this analysis from the Fourier transform. Substitution of the Fourier modes of Eqs. (2.15) into the linearised $\mathcal{O}(\epsilon)$ disturbance governing equations (Eqs. (2.14)) yielded the following dispersion relation:

$$\frac{\mathrm{d}\hat{u}_r}{\mathrm{d}r} + \frac{\hat{u}_r}{r} + \frac{im}{r}\hat{u}_\theta + ik\hat{u}_z = 0 \tag{2.16a}$$

$$i(k\bar{u}_z - \omega)\hat{u}_r + \frac{\mathrm{d}\hat{p}}{\mathrm{d}r} = \frac{1}{\mathrm{Re}}\left[\frac{\mathrm{d}^2\hat{u}_r}{\mathrm{d}r^2} + \frac{1}{r}\frac{\mathrm{d}\hat{u}_r}{\mathrm{d}r} - \left(k^2 + \frac{m^2+1}{r^2}\right)\hat{u}_r - i\frac{2m}{r^2}\hat{u}_\theta\right] \tag{2.16b}$$

$$i(k\bar{u}_z - \omega)\hat{u}_\theta + i\frac{m}{r}\hat{p} = \frac{1}{\mathrm{Re}}\left[\frac{\mathrm{d}^2\hat{u}_\theta}{\mathrm{d}r^2} + \frac{1}{r}\frac{\mathrm{d}\hat{u}_\theta}{\mathrm{d}r} - \left(k^2 + \frac{m^2+1}{r^2}\right)\hat{u}_\theta + i\frac{2m}{r^2}\hat{u}_r\right] \tag{2.16c}$$

$$i(k\bar{u}_z - \omega)\hat{u}_z + \hat{u}_r\frac{\mathrm{d}\bar{u}_z}{\mathrm{d}r} + ik\hat{p} = \frac{1}{\mathrm{Re}}\left[\frac{\mathrm{d}^2\hat{u}_z}{\mathrm{d}r^2} + \frac{1}{r}\frac{\mathrm{d}\hat{u}_z}{\mathrm{d}r} - \left(k^2 + \frac{m^2}{r^2}\right)\hat{u}_z\right] \tag{2.16d}$$

Note that Eq. (2.16) can be easily rearranged to conform to Eq. 1.8. Solving this dispersion relation or eigenvalue problem for the unknown ω (k) eigenvalue is the basis of temporal (spatial) modal stability analysis. Therefore, $\hat{u}_r$, $\hat{u}_\theta$, $\hat{u}_z$, and $\hat{p}$ of Eq. (2.15) may be interpreted as unknown eigenfunctions that must also be solved for.

Within this framework, the disturbance eigenfunctions may be interpreted as temporally and spatially travelling oscillatory waves of an ostensibly steady-state (equilibrium) base flow solution. These waves may grow, decay, or maintain amplitude in time or space.

Note that the highly restrictive assumption of 1D quasi-parallel flow allows the disturbance equations (Eqs. (2.14)) to be simplified to Orr-Sommerfeld or Rayleigh form. This former has condensed four equations into a single fourth-order differential equation in terms of the velocity, vorticity, or streamfunction. The Rayleigh form consists of a single second-order differential equation in terms of vorticity, streamfunction, or pressure by taking the inviscid limit. (Drazin & Reid, 1981; Criminale *et al.*, 2003).

Strictly speaking, the normal mode expansion of Eq. (2.15) belies a Fourier transform and the requirement of separability (Criminale *et al.*, 2003). To illustrate this, firstly, the disturbance terms q' undergo a Fourier transform as follows:

$$\mathring{q}(k;r;m;t) = \iint_{\Omega} q'(r,\theta,z,t) e^{i(kz+m\theta)} \, \mathrm{d}\theta \, \mathrm{d}z \tag{2.17}$$

where the domain of integration Ω is the entire domain considered for the stability problem. For this current study, this domain is typically from $-\infty$ to $+\infty$ or from 0 to ∞.

Next, a separable solution in time is sought (or imposed) with:

$$\mathring{q}(k;r;m;t) = \sum_{n=0}^{\infty} \hat{q}_n(k;r;m) \, \mathrm{e}^{-i\omega_n t} \tag{2.18}$$

where ω_n is a complex frequency in general. Implicitly, these equations are linear and consequently there can be no interactions between distinct Fourier modes. That is to say, a mode cannot contribute to the evolution of amplitude or phase of another mode or itself.

Within a stability context, only the most unstable eigenvalues are sought. Therefore, one may consider Eqs. (2.16) as the result of a Fourier transform of Eqs. (2.14) for a particular value of k or ω. Note that the eigenvalue problem framework is similar to von Neumann stability analysis, which is typically used to determine the stability limits of a numerical scheme (LeVeque, 2007).

2.1.5 Boundary conditions

To solve an eigenvalue problem, it is necessary to impose boundary conditions. Owing to the geometry of the axisymmetric pipe/jet, there are boundary conditions on the centreline ($r = 0$) (called regularity at the origin) and on the pipe wall ($r = R_0 = 1$) or infinitely far away from the jet exit ($r \to \infty$) (called decay at infinity). The boundary conditions at the origin are necessary both to impose the correct physical behaviour but also to avoid any coordinate singularity at $r = 0$. Governing equations involving the radial coordinate generally have a $1/r^n$ term, where n can be $1, 2$. When the equations are evaluated at or near $r = 0$ using finite difference methods, for example, this term can appear to dominate the solution or introduce non-physical behaviour. However, this is considered a coordinate singularity because a change of coordinate system removes the apparent blow-up (Boyd, 2001). For one-dimensional problems, imposing regularity conditions at the pole can suffice to remove the coordinate singularity. These are typically referred to as 'boundary' conditions, but the pole $r = 0$ is not a boundary in the physical sense; rather it is a result of numerically discretising a set of one dimensional governing equations. The other limit of a numerical grid in r should be ∞ in an analytical analysis. However, computational constraints mean that the radial domain must be truncated to a finite extent. Given that the disturbance eigenfunctions are presumed to decay far from the jet exit, it is possible to conserve computational resources by truncating the domain in r to a sufficiently large value that the eigenvalues and eigenfunctions are invariant to the domain extent in this study.

The linearised disturbance Navier-Stokes equations (Eqs. (2.14)) in cylindrical coordinates can potentially yield a singularity at the centreline ($r = 0$). To obviate this singularity, to produce boundedness, and to maintain smoothness, the following non-trivial conditions apply to the centreline (Batchelor & Gill, 1962; Garg & Rouleau, 1972; Khorrami *et al.*, 1989):

$$\lim_{r\to 0} \frac{\partial \mathbf{u}'}{\partial \theta} = 0 \tag{2.19a}$$

$$\lim_{r\to 0} \frac{\partial p'}{\partial \theta} = 0 \tag{2.19b}$$

where $\mathbf{u}' = (u'_r, u'_\theta, u'_z)^T$ is the disturbance velocity vector. Expanding Eq. (2.19a), we have:

$$\lim_{r\to 0} \frac{\partial \mathbf{u}'}{\partial \theta} = \frac{\partial u'_r}{\partial \theta}\ \hat{\mathbf{e}}_r + u'_r \frac{\mathrm{d}\hat{\mathbf{e}}_r}{\mathrm{d}\theta} + \frac{\partial u'_\theta}{\partial \theta}\ \hat{\mathbf{e}}_\theta + u'_\theta \frac{\mathrm{d}\hat{\mathbf{e}}_\theta}{\mathrm{d}\theta} + \frac{\partial u'_z}{\partial \theta}\ \hat{\mathbf{e}}_z + u'_z \frac{\mathrm{d}\hat{\mathbf{e}}_z}{\mathrm{d}\theta} \tag{2.20}$$

where $\hat{\mathbf{e}}_r, \hat{\mathbf{e}}_\theta, \hat{\mathbf{e}}_z$ are the unit vectors in radial, azimuthal, and axial directions, respectively. The derivatives of the unit vectors are known as:

$$\frac{\mathrm{d}\hat{\mathbf{e}}_r}{\mathrm{d}\theta} = \hat{\mathbf{e}}_\theta; \quad \frac{\mathrm{d}\hat{\mathbf{e}}_\theta}{\mathrm{d}\theta} = -\hat{\mathbf{e}}_r; \quad \frac{\mathrm{d}\hat{\mathbf{e}}_z}{\mathrm{d}\theta} = 0 \tag{2.21}$$

Eq.(2.21) and the normal Fourier mode decomposition of Eqs. (2.15) are substituted into Eq. (2.20) to produce:

$$\lim_{r\to 0} \frac{\partial \mathbf{u}'}{\partial \theta} = (im\hat{u}_r - \hat{u}_\theta)\hat{\mathbf{e}}_r + (\hat{u}_r + im\hat{u}_\theta)\hat{\mathbf{e}}_\theta + (im\hat{u}_z)\hat{\mathbf{e}}_z = 0 \tag{2.22}$$

For the centreline condition of Eq.(2.19a) to hold, each component of Eq.(2.22) must be zero.

Similarly, the pressure centreline condition of Eq. (2.19b) yields:

$$\lim_{r\to 0} \frac{\partial p'}{\partial \theta} = im\hat{p} = 0 \tag{2.23}$$

The conditions of Eq. (2.22) and (2.23) are dependent on the azimuthal wavenumber m. The results are summarised in Eq. (2.24):

$$\begin{cases} \hat{u}_r(r=0) = \hat{u}_\theta(r=0) = 0, \quad \hat{u}_z(r=0) \text{ finite}, \ \hat{p}(r=0) \text{ finite}, & \text{if } m = 0. \\ \hat{u}_z(r=0) = \hat{p}(r=0) = \hat{u}_r(r=0) \pm i\hat{u}_\theta(r=0) = 0, & \text{if } m = \pm 1. \\ \hat{u}_r(r=0) = \hat{u}_\theta(r=0) = \hat{u}_z(r=0) = \hat{p}(r=0) = 0, & \text{if } |m| \geq 2. \end{cases} \tag{2.24}$$

The conditions derived in Eq.(2.24) apply to both the axisymmetric pipe and the axisymmetric jet.

2.1.5.1 Axisymmetric pipe

Following the above derivation leading to Eq. (2.24), round pipe boundary conditions along the centreline $r = 0$ (Garg & Rouleau, 1972) are as follows:

$$\begin{cases} \hat{u}_r = \hat{u}_\theta = 0, \quad \hat{u}_z \text{ finite}, \ \hat{p} \text{ finite}, & \text{if } m = 0. \\ \hat{u}_z = \hat{p} = \hat{u}_r \pm i\hat{u}_\theta = 0, & \text{if } m = \pm 1. \\ \hat{u}_r = \hat{u}_\theta = \hat{u}_z = \hat{p} = 0, & \text{if } |m| \geq 2. \end{cases} \tag{2.25}$$

The physical no-slip condition on the rigid impermeable pipe wall arising from viscosity leads to the following velocity boundary conditions for all azimuthal modes $m \in \mathbb{Z}$ (Garg & Rouleau, 1972):

$$\hat{u}_r(r = R_0) = \hat{u}_\theta(r = R_0) = \hat{u}_z(r = R_0) = 0 \tag{2.26}$$

The pressure boundary condition on the wall for all azimuthal modes m is conventionally set to be:

$$\frac{\mathrm{d}\hat{p}}{\mathrm{d}r} = \frac{1}{\mathrm{Re}} \frac{\mathrm{d}^2\hat{u}_r}{\mathrm{d}r^2} \tag{2.27}$$

where the physical interpretation is that the pressure gradient at the wall is exclusively balanced by the wall-normal viscous shear forces. Note that the viscous shear stress on the

wall is expected to be small. Replacing the right-hand side of Eq.(2.27) with a small, even zero, value has negligible impact on accuracy (Khorrami *et al.*, 1989).

2.1.5.2 Axisymmetric jet

Again, the jet boundary conditions along the centreline ($r = 0$) are the same as the pipe boundary conditions in Eq.(2.25), reproduced below (Batchelor & Gill, 1962; Morris, 1976).

$$\begin{cases} \hat{u}_r = \hat{u}_\theta = 0, \quad \hat{u}_z \text{ finite}, \ \hat{p} \text{ finite}, & \text{if } m = 0. \\ \hat{u}_z = \hat{p} = \hat{u}_r \pm i\hat{u}_\theta = 0, & \text{if } m = \pm 1. \\ \hat{u}_r = \hat{u}_\theta = \hat{u}_z = \hat{p} = 0, & \text{if } |m| \geq 2. \end{cases} \qquad \text{(2.25 revisited)}$$

Very far away from the jet exit, the disturbance velocity and pressure asymptotically tends to zero, leading to the velocity boundary condition for all azimuthal modes m (Batchelor & Gill, 1962; Morris, 1976):

$$\hat{u}_r(r \to \infty) = \hat{u}_\theta(r \to \infty) = \hat{u}_z(r \to \infty) \to 0 \tag{2.28}$$

The pressure boundary condition as $r \to \infty$ for all azimuthal modes m is defined to be (Batchelor & Gill, 1962; Morris, 1976):

$$\hat{p} \to 0 \tag{2.29}$$

Note that this particular choice of the farfield pressure boundary condition helps to resolve the indeterminacy of the pressure eigenfunction that results from the pressure appearing only as a gradient for incompressible flow analyses.

2.1.6 Temporal formulation

Determining the complex temporal frequency $\omega \in \mathbb{C}$ given a real spatial wavenumber $k \in \mathbb{R}$, Reynolds number $\mathrm{Re} = u_{\max} R_0/\nu$, and azimuthal wave number m from the dispersion relation of Eqs. (2.16) and the relevant boundary conditions above is known as a generalised eigenvalue problem. Within the hydrodynamic stability theory framework, it is known as a 1D temporal stability analysis, whereby the frequency ω is solved for as the eigenvalue. A flow with given wavenumber k is temporally unstable (stable) when $\Im(\omega) > 0$ ($\Im(\omega) < 0$) because a disturbance wave grows (decays) over time. To isolate the temporal behaviour, the spatial growth rate $\Im(k) \coloneqq 0$ to guarantee neither growth nor decay in space. Consequently, Eqs. (2.16) was formulated for the temporal stability analysis as a generalised eigenvalue problem as follows:

$$\begin{pmatrix} \mathcal{D}_t & i\frac{2m}{r}\frac{1}{\mathrm{Re}} & 0 & \frac{\mathrm{d}}{\mathrm{d}r} \\ -i\frac{2m}{r}\frac{1}{\mathrm{Re}} & \mathcal{D}_t & 0 & i\frac{m}{r} \\ \frac{\mathrm{d}\bar{u}_z}{\mathrm{d}r} & 0 & \mathcal{D}_t - \frac{1}{\mathrm{Re}}\frac{1}{r^2} & ik \\ \frac{1}{r} + \frac{\mathrm{d}}{\mathrm{d}r} & i\frac{m}{r} & ik & 0 \end{pmatrix} \vec{\hat{q}}_t = \omega \begin{pmatrix} i & 0 & 0 & 0 \\ 0 & i & 0 & 0 \\ 0 & 0 & i & 0 \\ 0 & 0 & 0 & 0 \end{pmatrix} \vec{\hat{q}}_t \tag{2.30}$$

where the operator $\mathcal{D}_t$ was defined as: $\mathcal{D}_t \coloneqq ik\bar{u}_z - \frac{1}{\mathrm{Re}}\left[\frac{\mathrm{d}^2}{\mathrm{d}r^2} + \frac{1}{r}\frac{\mathrm{d}}{\mathrm{d}r} - \left(k^2 + \frac{m^2+1}{r^2}\right)\right]$ and the eigenvector $\hat{\mathbf{q}}_t$ was defined as: $\hat{\mathbf{q}}_t \coloneqq \begin{pmatrix} \hat{u}_r(r) & \hat{u}_\theta(r) & \hat{u}_z(r) & \hat{p}(r) \end{pmatrix}^T$. Note that the relevant boundary conditions from Section 2.1.5 were applied to this temporal eigenvalue problem. Physically, this may be interpreted as spatially oscillatory disturbance waves that may grow or decay in time. Use of the term 'eigenvector' (meaning a vector composed of eigenfunctions) denotes a conceptual transition from analytical mathematics to computational physics here.

2.1.7 Spatial formulation

By contrast, the determination of the complex wavenumber $k \in \mathbb{C}$ given a real temporal frequency $\omega \in \mathbb{R}$, Reynolds number $\mathrm{Re} = u_{\max} R_0/\nu$, and azimuthal wave number m from the

dispersion relation of Eqs. (2.16) and the relevant boundary conditions above is a 1D spatial stability analysis. The wavenumber k is solved for as the eigenvalue, instead. Similar to the temporal scenario, the flow given a frequency ω is spatially unstable (stable) if $\Im(k) < 0$ ($\Im(k) > 0$) because a disturbance wave grows (decays) over space z. As there are quadratic k^2 terms in the dispersion relation due to viscous effects, Eqs. (2.16) were expanded with a companion matrix (Bridges & Morris, 1984) to produce an eigenvalue problem as follows:

$$\begin{pmatrix} \mathcal{D}_s & -\frac{\mathrm{d}\bar{u}_z}{\mathrm{d}r} & 0 & 0 & 0 & 0 & 0 \\ 0 & \mathcal{D}_s - \frac{1}{\mathrm{Re}}\frac{1}{r^2} & -i\frac{2m}{r^2}\frac{1}{Re} & -\frac{\mathrm{d}}{\mathrm{d}r} & 0 & 0 & 0 \\ 0 & i\frac{2m}{r^2}\frac{1}{\mathrm{Re}} & \mathcal{D}_s - \frac{1}{\mathrm{Re}}\frac{1}{r^2} & -i\frac{m}{r} & 0 & 0 & 0 \\ 0 & -\frac{1}{r} - \frac{\mathrm{d}}{\mathrm{d}r} & -i\frac{m}{r} & 0 & 0 & 0 & 0 \\ 0 & 0 & 0 & 0 & \mathbf{I} & 0 & 0 \\ 0 & 0 & 0 & 0 & 0 & \mathbf{I} & 0 \\ 0 & 0 & 0 & 0 & 0 & 0 & \mathbf{I} \end{pmatrix} \vec{\hat{q}}_s = k \begin{pmatrix} i\bar{u}_z & 0 & 0 & i & \frac{1}{\mathrm{Re}} & 0 & 0 \\ 0 & i\bar{u}_z & 0 & 0 & 0 & \frac{1}{\mathrm{Re}} & 0 \\ 0 & 0 & i\bar{u}_z & 0 & 0 & 0 & \frac{1}{\mathrm{Re}} \\ i & 0 & 0 & 0 & 0 & 0 & 0 \\ \mathbf{I} & 0 & 0 & 0 & 0 & 0 & 0 \\ 0 & \mathbf{I} & 0 & 0 & 0 & 0 & 0 \\ 0 & 0 & \mathbf{I} & 0 & 0 & 0 & 0 \end{pmatrix} \vec{\hat{q}}_s \tag{2.31}$$

where the operator $\mathcal{D}_s$ was defined as: $\mathcal{D}_s \coloneqq i\omega + \frac{1}{\mathrm{Re}}\left[\frac{\mathrm{d}^2}{\mathrm{d}r^2} + \frac{1}{r}\frac{\mathrm{d}}{\mathrm{d}r} - \frac{m^2}{r^2}\right]$ and the eigenvector $\vec{\hat{q}}_s$ was defined as: $\vec{\hat{q}}_s \coloneqq \begin{pmatrix} \hat{u}_r(r) & \hat{u}_\theta(r) & \hat{u}_z(r) & \hat{p}(r) & k\hat{u}_r(r) & k\hat{u}_\theta(r) & k\hat{u}_z(r) \end{pmatrix}^T$. Note that the relevant boundary conditions are applied to this spatial eigenvalue problem.

2.1.8 Numerical eigenvalue solvers

There are numerous methods to solve a generalised eigenvalue problem such as those of Eqs. (2.30) or (2.31). Spectral collocation techniques based on Chebyshev polynomials are commonly used for axisymmetric pipe analyses because of the natural mesh refinement near the boundaries, the simplification of boundary condition treatment, and exponential grid convergence (Schmid & Henningson, 2001; Khorrami *et al.*, 1989). As mentioned in the introduction of Section 2, the spatial modal stability problem is solved with a matrix-forming approach with finite-difference schemes `FORTRAN` code provided by Rômulo Bessi Freitas and

Professor Leonardo Alves (Freitas, 2019). A shooting method-based approach is possible for this 1D-local quasi-parallel stability analysis, but is not generally possible for the 2D-local stability analysis considered in Section 4. The temporal stability problem and subsequent spatial/temporal non-modal stability were extended from the spatial modal stability analysis code.

Central to the numerical solution of an eigenvalue problem is the spatial discretisation over a given domain. Second-, fourth-, and sixth-order centred finite difference first and second derivatives based on Taylor series expansions were used to discretise the domain. The mesh was generally non-uniform to refine regions of interest in the domain for numerical parsimony (Freitas, 2019).

2.1.8.1 Direct approach

After discretising the domain of Eqs. (2.30) or (2.31), the matrix forming approach permits any general computational eigenvalue solver package to obtain eigenvalues and eigenvectors. This quasi-parallel 1D-local stability analysis employed the `BLAS` and `LAPACK` libraries in `FORTRAN`, particularly the subroutine `ZGGEV` (Blackford *et al.*, 2002; Anderson *et al.*, 1999). `ZGGEV` was selected for its suitability for generalised eigenvalue problems with complex, non-symmetrical square matrices. This generalised eigenvalue problem is often symbolically depicted as $\mathbf{Ax} = \lambda\mathbf{Bx}$, where λ are the eigenvalues that satisfy the characteristic equation $\det(\mathbf{A} - \lambda\mathbf{B}) = 0$ and $\mathbf{x}$ is the eigenvector. `ZGGEV` enacts the QZ algorithm, a variant of the QR algorithm for the generalised eigenvalue problem by Moler & Stewart (1973). Note that the QR algorithm is not used because the matrix $\mathbf{B}$ is generally singular, and therefore cannot be inverted, so $\mathbf{B}^{-1}\mathbf{Ax} = \lambda\mathbf{x}$ cannot be obtained numerically. Both the QR and QZ algorithms are categorised as 'direct' methods because the entire computational eigenspectrum is obtained simultaneously.

The QZ algorithm of Moler & Stewart (1973) relies on the theorem that $\mathbf{Ax} = \lambda\mathbf{Bx}$ is unitarily equivalent to $\mathbf{QAZy} = \lambda\mathbf{QBZy}$. Consequently, the eigenvalues of the two problems

are identical and the eigenvectors are related as: $\mathbf{x} = \mathbf{Z}\mathbf{y}$. Hence, the QZ algorithm is suitable for singular $\mathbf{B}$ matrices and for infinite eigenvalues (Watkins, 2000). Firstly, $\mathbf{B}$ is reduced to upper triangular form by a series of Householder reflections $\mathbf{B} \leftarrow \mathbf{Q}_{N-1}\mathbf{Q}_{N-2}\dots\mathbf{Q}_1\mathbf{B}$ that are also pre-multiplied to $\mathbf{A} \leftarrow \mathbf{Q}\mathbf{A}$. The upper triangular form of B can be considered the $\mathbf{R}$ matrix from QR decomposition. The matrix $\mathbf{A}$ is converted to upper Hessenberg form with a similar set of Householder reflections. Denote the k^{th} step as $\mathbf{A} \leftarrow \mathbf{Q}_k\mathbf{A}$ and $\mathbf{B} \leftarrow \mathbf{Q}_k\mathbf{B}$. The matrix $\mathbf{Z}_k$ is found to preserve the upper triangular (Schur) form of $\mathbf{B}$ i.e., $\mathbf{B} \leftarrow \mathbf{B}\mathbf{Z}_k$ and $\mathbf{A} \leftarrow \mathbf{A}\mathbf{Z}_k$. Secondly, QZ steps are iteratively performed to convert $\mathbf{A}$ to a quasi-triangular form while preserving $\mathbf{B}$ as an upper triangular matrix. This is done by effectively conducting a QR step on $\mathbf{A}\mathbf{B}^{-1}$ but without forming the matrix explicitly to obviate any singularities in $\mathbf{B}$. The end result should be the unitary matrices $\mathbf{Q}$ and $\mathbf{Z}$ such that $\mathbf{Q}\mathbf{A}\mathbf{Z}$ and $\mathbf{Q}\mathbf{B}\mathbf{Z}$ are each upper triangular (generalised Schur forms). The diagonals a_{ii} and b_{ii} of the upper triangular matrices $\mathbf{A}$ and $\mathbf{B}$ are the eigenvalues $\lambda = a_{ii}/b_{ii}$. Eigenvectors y of $\mathbf{Q}\mathbf{A}\mathbf{Z}\mathbf{y} = \lambda\mathbf{Q}\mathbf{B}\mathbf{Z}\mathbf{y}$ can be transformed to eigenvectors $\mathbf{x}$ of $\mathbf{A}\mathbf{x} = \lambda\mathbf{B}\mathbf{x}$ with the relation $\mathbf{x} = \mathbf{Z}\mathbf{y}$.

2.1.8.2 Projection or iterative methods

The QZ algorithm has a cost of $\mathcal{O}(N^3)$ floating point operations per second (FLOPs), where N is the leading dimension size of the matrices $\mathbf{A}$ and $\mathbf{B}$ (Anderson *et al.*, 1999). For larger matrices, corresponding to more refined spatial meshes here, this cost may be prohibitively high. As the matrix $\mathbf{B}$ is singular in general, there may be non-physical or infinite eigenvalues. Iterative methods, then, can be numerically parsimonious by computing only a subset of $M \leq N$ eigenvalues/eigenvectors and can be specialised to eigenvalues around a coordinate of interest σ. In fact, direct methods are wholly inappropriate for solving 2D or 3D stability analyses formulated in a matrix-forming approach owing to the scaling of leading dimension sizes of such matrices as was discussed by Theofilis (2003). It is worth mentioning that it is possible to reduce the leading dimension sizes of spatial eigenvalues problem by avoiding the companion matrix method and instead employing the Jacobi-Davidson iterative method for

solving polynomial eigenvalue problems as was demonstrated by Heeg & Geurts (1997).

For a Hermitian (self-adjoint i.e., $\mathbf{A} = \mathbf{A}^{\dagger}$) matrix, the Lanczos algorithm can expediently produce a subset of $M \leq N$ extremal (maximal/minimal) eigenvalues and corresponding eigenvectors (Lanczos, 1950). This was originally formulated tridiagonalise Hermitian matrices. To solve the eigenvalue problem of $\mathbf{A}\mathbf{x} = \lambda\mathbf{x}$, where $\mathbf{A}$ is sized $N \times N$ and is Hermitian, the Krylov subspace is $\mathcal{K}_M(\mathbf{A}, \mathbf{v}_1)$ where $\mathbf{v}_1 \in \mathbb{C}_N$ is an arbitrary initial vector which unity Euclidean norm. The tridiagonal matrix of $\mathbf{T}_M$ is constructed iteratively to represent the matrix $\mathbf{A}$ in the Krylov subspace. Eigenvalues and eigenvectors of $\mathbf{T}_M$, a tridiagonal matrix, are parsimoniously obtained via the QR algorithm, for example (Lanczos, 1950; Anderson *et al.*, 1999).

The Arnoldi method (Arnoldi, 1951) is a generalised extension of the Lanczos approach to solving for eigenvalues and eigenvectors for even non-Hermitian matrices (Ericsson, 1986; Saad, 2011). Given an arbitrary initial vector $\mathbf{v}_1$ with a unity norm, the Krylov subspace $\mathcal{K}_M(\mathbf{A}, \mathbf{v})$ is again formed. The Krylov matrix is defined as: $\mathbf{K}_M = [\mathbf{v}_1, \mathbf{A}\mathbf{v}_1, \mathbf{A}^2\mathbf{v}_1, \ldots, \mathbf{A}^{M-1}\mathbf{v}_1]$. The goal of the Arnoldi algorithm is to project the original matrix $\mathbf{A}$ onto the Krylov subspace $\mathcal{K}_M(\mathbf{A}, \mathbf{v})$ in a Rayleigh-Ritz approximation of $\mathbf{A}$. $M \leq N$ vectors $\mathbf{v}_1, \mathbf{v}_2, \ldots \mathbf{v}_M$ span the Krylov subspace $\mathcal{K}_M(\mathbf{A}, \mathbf{v})$. Algorithm 1 describes a basic Arnoldi algorithm, one implementation of which was provided by Rômulo Bessi Freitas and Professor Leonardo Alves (Freitas, 2019).

Algorithm 1: Basic Arnoldi Algorithm

Input: $N \times N$ matrix $\mathbf{A}$

Output: $M \times M$ matrix $\mathbf{H}_M$

Initialisation: Arbitrary $N \times 1$ vector $\mathbf{v}_1$ with unity norm;

for $j = 1, 2, \ldots$ **do**

  /* Construct the Krylov matrix K_M */

  $\mathbf{w} = \mathbf{A}\mathbf{v}_i$;

  /* Gram-Schmidt Orthonormalisation */

  for $i = 1, \ldots, j$ **do**

    $h_{i,j} = \mathbf{v}_i^* \mathbf{w}$; // Form the Hessenberg matrix H_M

    $\mathbf{w} = \mathbf{w} - \mathbf{v}_i h_{i,j}$; // Orthogonalise v_i

  end

  $h_{j+1,j} = \|\mathbf{w}\|_2$; // Normalise the Hessenberg matrix H_M

  if $h_{j+1,j} = 0$ **then**

    return ;

  end

  $\mathbf{v}_{j+1} = \frac{\mathbf{w}}{h_{j+1,j}}$; // Normalise the vector v_i

end

The eigenvalues and eigenvectors of the $M \times M$ upper Hessenberg matrix $\mathbf{H}_M$ (also known as the Ritz matrix) can be computed by the QR algorithm, for example. Some of the resultant eigenvalues and eigenvectors, called the Ritz eigenvalues and Ritz vectors, respectively, approximate the eigenvalues and eigenvectors of $\mathbf{A}$. Typically, the Ritz eigenvalues converge to the largest eigenvalues of $\mathbf{A}$. The $N \times M$ matrix $\mathbf{V}_M$ is composed of the M Arnoldi vectors $\mathbf{v}_1, \ldots \mathbf{v}_M$ and $\mathbf{H}_M = \mathbf{V}_M^* \mathbf{A} \mathbf{V}_M$ (Arnoldi, 1951). This Arnoldi method is implemented for the modal (eigenvalue) stability problem in `FORTRAN` by Rômulo Bessi Freitas and Professor Leonardo Alves (Freitas, 2019). More details can be found there in Freitas (2019).

Ritz eigenvalues may not be the most relevant eigenvalues for stability analyses, however.

The shift-and-invert preconditioning technique allows the user to select a region around which Arnoldi will search for eigenvalues by leveraging the tendency for Arnoldi solvers to find the largest eigenvalues of $\mathbf{A}$. We can denote the generalised eigenvalue problems of stability analyses of Eqs. (2.30) and (2.31) as $\mathbf{Ax} = \lambda\mathbf{Bx}$ and the search coordinate as σ. Rearranging, an equivalent equation is:

$$\Big((\mathbf{A} - \sigma\mathbf{B})^{-1}\mathbf{B}\Big)\hat{\mathbf{q}} = \frac{1}{\lambda - \sigma}\hat{\mathbf{q}} \tag{2.32}$$

Supposing that the eigenvalue problem described in Eq. (2.32) is solved with Algorithm 1, the eigenvalues $\lambda_{Arnoldi}$ are related to the eigenvalues of $\mathbf{Ax} = \lambda\mathbf{Bx}$ by:

$$\lambda = \frac{1}{\lambda_{\text{Arnoldi}}} + \sigma \tag{2.33}$$

while the eigenvectors do not require transformation.

2.2 Non-modal stability analysis

To extend the modal stability analysis code, we considered non-modal temporal and spatial stability analysis. All linear spatial (Garg & Rouleau, 1972) and temporal (Lessen *et al.*, 1968; Salwen *et al.*, 1980; Patera & Orszag, 1982; Zikanov, 1996) modal stability analyses indicated that fully-developed axisymmetric pipe flow are asymptotically and exponentially stable at any Reynolds number $\mathrm{Re} \coloneqq u_{\max}R_0/\nu$. Small disturbances of any given frequency and wavenumber must, then, decay over both space and time. This numerical finding lies in stark contrast against the experimental observation of turbulence in pipe flows (Reynolds, 1883). The apparent paradox between predictions of linear stability and the experimental reality of a subcritical bifurcation to turbulence for pipe flows has inspired the search for 'bypass' mechanisms such as the 'lift-up' or 'shift-up' mechanisms for plane-parallel flows (Ellingsen & Palm, 1975; Landahl, 1980). These mechanisms were later found to be re-

sultant from *non-modal* growth potentially causing bifurcation to nonlinear or secondary instabilities.

Modal analyses consider the asymptotic ($t \to \infty$ or $z \to \infty$) behaviour of a flow because a small disturbance growing exponentially would eventually dominate the flow. For orthogonal (also known as normal) operators, modal analyses suffice. Some linear stability governing equations, the Rayleigh or Orr-Sommerfeld equations of shear flows included, can support *algebraic* growth because the associated operators are non-normal. This algebraic growth resulting from the non-orthogonality of eigenvectors (commonly associated with shear flows) has been known for some time (Garg & Rouleau, 1972; Gustavsson, 1989) but it was only relatively recently that linear stability operators of shear flows could produce significantly high 'transient' amplification (Trefethen *et al.*, 1993). This may address how fully-developed axisymmetric pipe flow, for instance, can subcritically transition to turbulence (Schmid & Henningson, 1994). Hence, *non*-modal stability analysis has been applied to parallel channel flow, planar Poiseuille, planar Couette flow, boundary layers, and round jets (Farrell, 1988; Reddy *et al.*, 1993; Reddy & Henningson, 1993; Andersson *et al.*, 1999; Luchini, 2000; Wang *et al.*, 2021; Ivanov *et al.*, 2023). For completeness, we extended the spatial modal stability code to temporal and spatial non-modal stability analysis.

A temporal non-modal stability analysis has been conducted on low velocity ratio ($R = 1.5,\ 1.6$) jets-in-crossflow that indicates a tremendous potential for non-modal growth on the order of $\mathcal{O}(10^{12})$. The corresponding symmetric optimal initial condition to induce maximal transient growth was shown to consist of near-horizontal vortices upstream of the jet exit near the upstream shear layer paired with an angled wave packet directed towards the CVP (Peplinski *et al.*, 2015).

Regan & Mahesh (2019*a*) performed a temporal non-modal stability analysis for a $R = 2$ (absolutely unstable) and a $R = 4$ (convectively unstable) jet-in-crossflow with a Reynolds number $\mathrm{Re}_D \coloneqq 2000$ to match the experimental conditions and geometry of Megerian *et al.* (2007). The base flows used in the analysis were obtained from 3D direct numerical sim-

ulations using the computational methodology described in Regan & Mahesh (2017). By determining the 'optimal' (or most dangerous or most amplified) initial condition that leads to the most growth over a prescribed time horizon, optimal control strategies may be found (Regan & Mahesh, 2019*a*). They found that the $R = 2$ and $R = 4$ jets-in-crossflow exhibit distinct short-term amplification characteristics: the $R = 2$ jet-in-crossflow responds most to symmetric-breaking perturbations while the $R = 4$ jet-in-crossflow responds most to symmetric perturbations in the downstream shear layer.

An experimental validation of spatial non-modal stability analyses of a high Reynolds number axisymmetric free jet has been performed by Ivanov *et al.* (2023) using the experimental configuration described by Zayko *et al.* (2018) and Gareev *et al.* (2022). Particle image velocimetry and hot-wire anemometry measurements indicate that the spatial initial disturbances evolve in a manner that qualitiatively aligns with numerical predictions from the optimal perturbation well. Their approach also identified a 'lift-up'-like mechanism for non-modal growth in free jets (Ivanov *et al.*, 2023).

2.2.1 Temporal formulation

We assumed that the temporal stability problem of Eqs. (2.30) has been solved for its eigenvalues $\omega \in \mathcal{C}$ and their corresponding eigenvectors $\hat{\mathbf{q}}_t = (\hat{u}_r, \hat{u}_\theta, \hat{u}_z, \hat{p})^T$. The shift-and-invert Arnoldi formulation, described in Section 2.1.8, produces eigenvalues in descending order of proximity to the coordinate $\sigma \in \mathbb{C}$.

Firstly, we considered a velocity disturbance function $\mathbf{q}(r) = (u_r(r), u_\theta(r), u_z(r))^T$ (the prime $'$ has been dropped here). The energy density-based inner product used for temporal non-modal stability analyses is the same as that of Schmid & Henningson (1994) for validation purposes:

$$(\mathbf{q}_1, \mathbf{q}_2)_2 = \pi \int_\Omega \mathbf{q}_1^\dagger \ \mathbf{q}_2 \ r \ \mathrm{d}r = \pi \int_\Omega (u_r^* u_r + u_\theta^* u_\theta + u_z^* u_z) \ r \ \mathrm{d}r \tag{2.34}$$

where $\mathbf{q}_1$ and $\mathbf{q}_2$ are any velocity disturbance vectors, Ω represents the spatial domain which extends from the centreline $r = 0$ to the pipe radius $r = R_0$ for the pipe base flow or from $r = 0$ to the end of the spatial domain for the jet base flow, which is $r \to \infty$ in principle. The † symbol represents the conjugate transpose viz., $\mathbf{q}^\dagger = (\mathbf{q}^*)^T$. The corresponding ℓ^2 norm, then, is:

$$\|\vec{q}\|_2 = (\mathbf{q}, \mathbf{q}) \tag{2.35}$$

where $\mathbf{q}$ represents any velocity disturbance vector.

Recall that solving the temporal stability problem of Eqs. (2.30) yields eigenvalues ω and eigenvectors $\hat{\mathbf{q}}_t$. Any velocity disturbance can be approximately decomposed as a sum of n eigenvectors $\hat{\mathbf{q}}_t$ as follows:

$$\mathbf{q} = e^{i(m\theta+kz)} \sum_{j=1}^{n} \kappa_j \hat{\mathbf{q}}_{t,j}(r) e^{-i\omega_j t} \tag{2.36}$$

where ω_j is the j^{th} eigenvalue, $\hat{\mathbf{q}}_{t,j}(r) = (\hat{u}_r, \hat{u}_\theta, \hat{u}_z)^T$ represents corresponding eigenvector, and $\kappa_j \in \mathbb{C}$ is a scalar coefficient that is to be modified to maximise the energy gain at a given time t defined in Eq. (2.37). $m \in \mathbb{Z}$ is the azimuthal mode number and $k \in \mathbb{R}$ is the spatial wavenumber. The non-modal optimal gain was defined to be:

$$G = G(m, k, \mathrm{Re}, t) \coloneqq \max_{(\kappa_1, \ldots \kappa_n)^T} \frac{\|\mathbf{q}(t)\|_2^2}{\|\mathbf{q}(0)\|_2^2} \tag{2.37}$$

where the gain was optimised over all free parameters $(\kappa_1, \ldots \kappa_n)^T$ for a given t and Re. $\mathbf{q}(0)$ is the energy at the initial time and is present at the denominator to normalise the initial gain to be unity. Hence, linear non-modal growth occurs if $G(t) > 1$. Note that the optimal initial disturbance that maximises the gain G at time t_1 is generally not identical to the optimal initial disturbance that maximises the gain at time $t_2 \neq t_1$. It is possible to optimise the gain with any optimisation routine or with the calculus of variations (Butler & Farrell,

1992), but this optimal gain problem can be reformulated as an ℓ^2-norm that can be solved with the singular value decomposition (SVD) (Schmid & Henningson, 1994) as follows:

$$G(m, k, \mathrm{Re}, t) = \|\mathbf{F}\mathbf{\Lambda}_t\mathbf{F}^{-1}\|_2^2 \tag{2.38}$$

where $\mathbf{\Lambda}_t \coloneqq \mathrm{diag}(e^{-i\omega_1 t}, e^{-i\omega_2 t}, \ldots, e^{-i\omega_n t})$ and $\mathbf{F}$ was from the Cholesky decomposition of the $n \times n$ correlational matrix $\mathbf{M} = \mathbf{F}^\dagger\mathbf{F}$. $M_{ij} \coloneqq (\hat{\mathbf{q}}_i, \hat{\mathbf{q}}_j)_2$ energy inner product of Eq. (2.34) is applied to the i^{th} and j^{th} eigenvector of Eq. (2.30).

Let the matrix $\mathbf{B} \coloneqq \mathbf{F}\mathbf{\Lambda}_t\mathbf{F}^{-1}$ be decomposed with the singular value decomposition as:

$$\mathbf{B}\mathbf{V}_B = \mathbf{U}_B\mathbf{\Sigma}_B \tag{2.39}$$

for the unitary matrices $\mathbf{V}_B, \mathbf{U}_B$ and $\mathbf{\Sigma}$ consists of the singular values of $\mathbf{B}$ such that $\mathbf{\Sigma} = \mathrm{diag}(\sigma_1, \ldots, \sigma_N)$ where $\forall 1 \leq i \leq n, \sigma_i \in \mathbb{R}^+$ and $\sigma_1 \geq \sigma_2 \geq \cdots \geq \sigma_n$. Hence, $\|\mathbf{B}\|_2 = \|\mathbf{F}\mathbf{\Lambda}_t\mathbf{F}^{-1}\|_2$ is the principal singular value σ_1. The column vectors of $\mathbf{V}_B$ ($\mathbf{U}_B$) are principal right (left) singular vectors. The leading terms resulting from the singular value decomposition can be written as:

$$\mathbf{B}\mathbf{v}_1 = \sigma_1\mathbf{u}_1 \tag{2.40}$$

This relation describes how an input $\mathbf{v}_1$ is amplified by a non-modal gain $\|\mathbf{B}\|_2 = \sigma_1$. To convert $\mathbf{v}_1$, the leading right singular vector, to the optimal initial disturbance coefficients $\boldsymbol{\kappa}$, the following mapping is applied:

$$\boldsymbol{\kappa} = \mathbf{F}^{-1}\mathbf{v}_1 \tag{2.41}$$

The transformation has projected $\mathbf{v}_1$ onto a space spanned by the n eigenvectors $\hat{q}_1, \ldots \hat{q}_n$. The optimal initial condition is constructed with Eq. (2.36). Note that the definition of the

energy inner product in Eq. (2.34) is not unique and should generally account for the physical energy components (Schmid & Henningson, 1994).

2.2.2 Spatial formulation

There is a highly analogous formulation for the spatial problem, first developed for the fully-developed axisymmetric pipe flow problem by Reshotko & Tumin (2001). Their approach has since been applied to annular Poiseuille-Couette flows, compressible boundary layers, and axisymmetric free jets (Daly, 2013; Tumin & Reshotko, 2001; Boronin *et al.*, 2013). Spatial non-modal stability analysis, as will be detailed shortly, is conducted very similarly to temporal non-modal stability analysis but belies profoundly different philosophies (Reshotko & Tumin, 2001). Unlike temporal non-modal stability analysis, a spatial non-modal stability analysis is generally considered an ill-posed problem owing the presence of spatially unstable eigenvalues (viz., $\Im(k) < 0$). According to the signalling problem (Ashpis & Reshotko, 1990; Tumin, 1996), which considers how a flowfield with a clear streamwise direction responds to a single-frequency sinusoidal disturbance activated at an initial time at a particular station, there exists upstream-propagating and downstream-propagating waves which may grow or decay spatially in their direction of propagation from a given source (Huerre & Monkewitz, 1985). A modal stability analysis permits both upstream- and downstream-propagating eigenmodes to exist due to the ambiguity of the disturbance source in this context. It is possible to interpret spatially unstable modes with $\Im(k) < 0$ as existing in the portion of the flowfield upstream of the disturbance generator (Gill, 1965; Reshotko & Tumin, 2001). Given that a spatial non-modal stability analysis considers eigenfunction interaction-driven algebraic growth over space caused by disturbances emanating from an arbitrary streamwise station for flows that are not absolutely unstable, we consider only the downstream-propagating waves and therefore neglect the spatially unstable eigenmodes. In this manner, spatial non-modal stability analysis may be considered as a type of initial value problem just as its temporal counterpart (Reshotko & Tumin, 2001; Schmid & Henningson, 2001;

Chomaz, 2005).

Following the temporal formulation framework, spatial non-modal stability analysis also begins when a velocity disturbance function vector $\mathbf{q}(r) = (u_r(r), u_\theta(r), u_z(r))^T$ (the prime $'$ notation has again been dropped here). The energy density-based inner product used for spatial non-modal stability analyses is kept to match that of Reshotko & Tumin (2001) for validation purposes:

$$(\mathbf{q}_1, \mathbf{q}_2)_2 = \int_\Omega \mathbf{q}_1^\dagger \ \mathbf{q}_2 \ r \ \mathrm{d}r = \int_\Omega (u_r^* u_r + u_\theta^* u_\theta + u_z^* u_z) \ r \ \mathrm{d}r \tag{2.42}$$

where $\mathbf{q}_1$ and $\mathbf{q}_2$ are any velocity disturbance vectors, Ω represents the spatial domain which extends from the centreline $r = 0$ to the pipe radius $r = R_0$ for the pipe base flow or to the end of the spatial domain for the jet base flow. The corresponding ℓ^2-norm is identical to that of Eq. (2.35), reproduced below.

$$\|\mathbf{q}\|_2 = (\mathbf{q}, \mathbf{q}) \tag{2.35 revisited}$$

Any velocity disturbance can be composed of a collection of n eigenvalues k and corresponding eigenvectors $\hat{\mathbf{q}}_s$ of Eqs. (2.31) as follows:

$$\mathbf{q} = e^{i(m\theta - \omega t)} \ \sum_{j=1}^{n} \kappa_j \hat{\mathbf{q}}_{s,j}(r) e^{ik_j z} \tag{2.43}$$

where k_j is the j^{th} eigenvalue, $\hat{\mathbf{q}}_{s,j}(r) = (\hat{u}_r, \hat{u}_\theta, \hat{u}_z)^T$ represents corresponding eigenvector, and $\kappa_j \in \mathbb{C}$ is a scalar coefficient that will be modified to maximum the energy gain at a given downstream location z defined in Eq. (2.44). $m \in \mathbb{Z}$ is the azimuthal mode number and $k \in \mathbb{R}$ is the spatial wavenumber. Note that all upstream-propagating eigenmodes are excluded from this spatial non-modal stability analysis. The non-modal optimal gain is defined to be:

$$G = G(m, \omega, \mathrm{Re}, t) \coloneqq \max_{\boldsymbol{\kappa}} \frac{\|\mathbf{q}(z)\|_2^2}{\|\mathbf{q}(0)\|_2^2} \tag{2.44}$$

where the gain was optimised over $\boldsymbol{\kappa} = (\kappa_1, \ldots, \kappa_n)^T$ for a given z and Re. This optimal gain can also be obtained by the singular value decomposition by firstly rearranging the problem as:

$$G(m, \omega, \mathrm{Re}, t) = \|\mathbf{F}\boldsymbol{\Lambda}_z\mathbf{F}^{-1}\|_2^2 \tag{2.45}$$

where $\boldsymbol{\Lambda}_z \coloneqq \mathrm{diag}(e^{ik_1 z}, e^{ik_2 z}, \ldots, e^{ik_n z})$ and $\mathbf{F}$ results from the Cholesky decomposition of the $n \times n$ correlational matrix $\mathbf{M} = \mathbf{F}^\dagger\mathbf{F}$. $M_{ij} \coloneqq (\hat{\mathbf{q}}_i, \hat{\mathbf{q}}_j)_2$ energy inner product of Eq. (2.42) is applied to the i^{th} and j^{th} eigenvector of Eq. (2.31). Note that the matrices $\mathbf{F}$ and $\mathbf{M}$ are not the same as for the temporal case, in general.

The principal singular value of $\mathbf{F}\boldsymbol{\Lambda}_z\mathbf{F}^{-1}$, denoted at σ_1, is equal to $\|\mathbf{F}\boldsymbol{\Lambda}_z\mathbf{F}^{-1}\|_2$. The principal right singular vector $\mathbf{v}_1$ can be transformed to the optimal initial disturbance coefficients as follows:

$$\boldsymbol{\kappa} = \mathbf{F}^{-1}\mathbf{v}_1 \tag{2.46}$$

where $\mathbf{F}$ is obtained from the spatial formulation.

CHAPTER 3

Results and discussion for 1D linear stability analysis

The governing equations, various 1D base flows base flows, and numerical solution procedure outlined in Section 2 have been used and their results are presented in the following. Specifically, all permutations of spatial and temporal as well as linear modal and non-modal stability analyses for one-dimensional axisymmetric pipe and free jet flows have been performed and described here. Base flows and boundary conditions can be found in Sections 2.1.3 and 2.1.5, respectively.

The purpose of this 1D linear stability analysis study is to verify that the numerical procedure developed and described in Section 2 can procedure linear stability results that have been previously reported in the literature. A verified and multi-faceted linear stability framework for 1D flows can be a foundation upon which to develop a numerical solver for 2D linear stability problems.

3.1 Axisymmetric pipe Poiseuille flow

Both modal and non-modal, as well as temporal and spatial linear stability analyses are performed for axisymmetric pipe Poiseuille flow owing to its historic nature as a canonical flow of interest and subsequent ubiquity of stability data (Reynolds, 1883).

To verify our temporal non-modal stability analysis, we refer to Schmid & Henningson (1994), while spatial non-modal stability analyses are compared against Reshotko & Tumin (2001). The dimensionless base flow is taken to be Eq. (2.6) and the boundary conditions

are given in Eqs. (2.25)-(2.27) for both analyses.

The temporal non-modal stability problem is described in Sec. 2.2.1 while the spatial non-modal stability problem is described in Sec. 2.2.2. The temporal modal stability problem is defined in Eq. (2.30) while the spatial modal stability problem is defined in Eq. (2.31).

3.1.1 Modal Stability Analysis

Modal stability analysis is conducted partially to verify the extensions to the code but also to obtain eigenvectors for non-modal stability analysis. Modal stability analysis principally yields eigenvalues that indicate how linear perturbations evolve after the short-time transient dynamics have abated. Temporal stability is indicated by the sign of the imaginary component of the eigenvalue: $\Im(\omega) > 0$ indicates temporal linear instability while $\Im(\omega) < 0$ indicates temporal linear stability. Spatial stability, similarly, is when $\Im(k) > 0$ while spatial instability occurs when $\Im(k) < 0$.

3.1.1.1 Temporal analysis

Schmid & Henningson (1994) employed a Chebyshev spectral approach to obtain the Y-shaped eigenvalue spectra for Hagen-Poiseuille pipe flow. For verification purposes, they tabulated the most unstable $31 - 33$ eigenvalues $\omega \in \mathbb{C}$ for $\mathrm{Re}_D = u_{\max} D/\nu = 3000$, wavenumber $k = 1$ flow for azimuthal mode numbers $m = 0,\ 1,\ 2,\ 3$. Spectral methods are generally used due to their exponential convergence rate upon refining the mesh, their computational parsimony, and their acceptable accuracy given 'coarse' meshes. Chebyshev mesh points, however, are generally inflexible as only the boundaries can be greatly refined. Some grid transformations can be applied to redistribute Chebyshev mesh points to other regions of interest (Boyd, 2001), but spectral methods remain unsuitable for complex geometries. Fortunately, the regions of greatest shear (and therefore the regions of greatest grid refinement) are expected to be near the mesh domains for pipe flow, and so Chebyshev

spectral approaches are well-suited to solve this physical problem.

We employed a uniform 1001 point mesh with sixth-order central finite-difference discretisation scheme of the flow domain from $r = -1$ to $r = 1$ rather than a Chebyshev spectral approach as future studies of the free jet and jet-in-crossflow may require a more flexible meshing strategy. As the shift-and-invert preconditioning step is applied to the Arnoldi algorithm (see Section 2.1.8.2), a focal point σ is necessary for the eigenvalue search. For this section describing temporal stability, $\sigma \coloneqq k + 0i$, where k is the wavenumber considered.

For verification of the modal part of the linear stability analysis code, eigenvalue spectra of $\mathrm{Re}_D = 3000,\ k = 1,\ m = 0,\ 1,\ 2,\ 3$ are obtained against the reference values of Schmid & Henningson (1994) (plotted in Figure 3.1). As can be seen from Figure 3.1, the eigenvalues of Schmid & Henningson (1994) compare favourably with our eigenvalues for all azimuthal modes $0 \leq m \leq 3$. The maximum ℓ^2 norm of the eigenvalue error, occurring furthest from the eigenvalue search focal point σ, is $\mathcal{O}(10^{-4})$, with the exception of a single anomalous point for $m = 0$ which appears to have a zero pressure eigenfunction.

We can see that we have obtained the classic 'Y'-shaped eigenvalue spectrum commonly associated with temporal pipe flow stability. By comparison to planar Poiseuille flow, eigenvalues can be categorised as wall modes (scaled phase speed $c = \omega/(k\mathrm{Re}) \to 0$ for $k\mathrm{Re} \gg 0$), centre modes ($c \approx \bar{U}_{pipe} = 1$ for $k\mathrm{Re} \gg 0$), and mean modes ($c = 2/3$ as $k\mathrm{Re} \to 0$) (Drazin & Reid, 1981; Schmid & Henningson, 1994).

3.1.1.2 Spatial analysis

It is also necessary to validate the code for the spatial stability analysis of an axisymmetric pipe.

Garg & Rouleau (1972) have conducted a spatial stability analysis based on a power series expansion of the governing equations solved by Runge-Kutta integration. Eigenvalues are solved with a contour-integral approach. They tabulate the most unstable eigenvalue for

$\mathrm{Re} = 10,000,\ \omega = 0.5$ pipe Poiseuille flow at $m = 0$ and $m = 1$. Those values as well as the result from our solver (using a 1001 point uniform mesh with $\sigma = \omega + 0i$) are presented for comparison in Table 3.1.

Table 3.1: Most unstable spatial eigenvalues k of pipe Poiseuille flow at $\mathrm{Re} = 10,000,\ \omega = 0.5$ for $m = 0$ and $m = 1$ comparison with Garg & Rouleau (1972)

	Garg & Rouleau (1972)	**Current verification**
$m = 0$	$0.519989251733 + 0.02083549388i$	$0.519993072776 + 0.02083572516i$
$m = 1$	$0.535251083173 + 0.01722764397i$	$0.535256144106 + 0.01722682379i$

As Table 3.1 demonstrates, the most unstable eigenvalues appear to have an error ℓ^2 norm of $\mathcal{O}(10^{-6})$.

A more relevant set of spatial eigenvalues are tabulated by Tumin (1996). Similarly to Schmid & Henningson (1994), Tumin (1996) employs a Chebyshev spectral method to solve the spatial eigenvalue problem with 61 Chebyshev polynomials for flow conditions of $\mathrm{Re} = 2280,\ \omega = 0.96,\ m = 0,\ 1,\ 2,\ 3$. For comparison purposes, a uniform mesh consisting of 1001 points with a sixth-order central finite difference discretisation scheme was used. The focal point for the Arnoldi algorithm was set to be $\sigma = \omega + 0i$. For comparison purposes, the eigenvalues are plotted in Figures 3.2.

As Figure 3.2 demonstrates, the spatial eigenvalues appear to correspond well to the spectra of Tumin (1996). Spatial eigenvalue problems may yield spatially unstable eigenmodes ($\Im(k) < 0$) but these should be interpreted as disturbance waves belonging to the flowfield upstream of the disturbance source $z < 0$, as discussed previously. For the $m = 0$ case, the azimuthal velocity perturbation equations become decoupled from the axial and radial velocity perturbation equations (see Eqs. (2.16)). Consequently, there are two categories of solutions labelled meridional ($\hat{u}_\theta = 0$) and torsional ($\hat{u}_\theta \neq 0$) that are usually found close

to each other and can only be distinguished by solving for the eigenvectors. Additionally, $m = 0$ eigensolutions feature a pair of eigenvalues very close to the origin representing the incompressible asymptote of acoustic waves ($k = 0$) that propagate in both directions.

3.1.2 Non-Modal Stability Analysis

As described in Section 2.2, eigenvalues solely yield the long-time asymptotic behaviour of perturbations. For orthogonal (also known as normal) operators, this is sufficient. However, non-normal operators, such as those resulting from shear-dominated flows, the behaviour of the eigenvectors is important owing to the potential algebraic growth in the non-asymptotic limit triggering nonlinear phenomena.

3.1.2.1 Temporal analysis

To determine the temporal non-modal growth associated with Hagen-Poiseuille flow, we employed the same definition of the scalar product (Eq. (2.34)), flowfield decomposition (Eq. (2.36), and SVD-based optimal gain (Eq. (2.37)) as Schmid & Henningson (1994).

We also considered identical flow conditions: namely, $\mathrm{Re}_D = 3000$, $k = 0.0,\ 0.1,\ 1.0$ for azimuthal mode numbers $m = 1,\ 2,\ 3,\ 4$. Schmid & Henningson (1994) suggest that, in the best case scenario, only a few of the most unstable eigenvectors ($\lesssim 10$) are necessary to asymptotically reach the maximum possible non-modal gain. This scenario corresponded to the first helical mode with $k = 0$ and $\mathrm{Re} = 3000$. Our present study did indeed recover this finding for this case. However, the other cases required more than approximately 10 eigenmodes. This observation is consistent with the language of Schmid & Henningson (1994) because the $k = 0$, $m = 1$ scenario yielded the greatest transient amplification. The results are plotted simultaneously against digitised values of their non-modal gain, scaled by the square of the Reynolds number in Figure 3.3. Note that axisymmetric ($m = 0$) disturbances appear to have negligible non-modal growth, particularly compared against the

higher azimuthal modes. For this reason, the $m = 0$ scenario was not considered (Schmid & Henningson, 1994).

As Figure 3.3 demonstrates, the presently-obtained temporal non-modal energy gains compare favourably against those of Schmid & Henningson (1994) for a variety of flow conditions. In all scenarios, there is a collection of relatively non-normal eigenvectors that amplify the flow kinetic energy density within a brief time window. It is possible that these disturbances can grow to such an extent that they can no longer be considered small enough to be linear and thereby cause the flow to transition to turbulence (Schmid & Henningson, 2001; Chomaz, 2005). Therefore, the results from a non-modal stability analysis may potentially explain the apparent contradiction of all linear stability analyses predicting stability for fully-developed pipe flow for all Reynolds numbers against the experimental evidence of pipe flow transition at finite Reynolds numbers (Chomaz, 2005). By contrasting Figure 3.3(a-c), it is clear that the non-modal growth is generally more prominent as the wavenumber $k \to 0$ owing to the increasingly unstable modal growth rate ω_i. As wavenumbers decrease from Figure 3.3(c) to (a), the maximum non-modal growth magnitude appears to correspond to the lower azimuthal mode numbers but the higher azimuthal mode numbers appear to gain energy more quickly (a more ephemeral behaviour).

3.1.2.2 Spatial analysis

Verification of spatial non-modal growth associated with Hagen-Poiseuille flow is conducted in a similar manner. The scalar product, (Eq. (2.42)), flowfield decomposition (Eq. (2.43)), and SVD-based optimal gain (Eq. (2.45)) are the same as those used by Reshotko & Tumin (2001).

Identical flow conditions were considered: $\mathrm{Re}_D = 3000,\ \omega = 0.5$ for azimuthal modes $m = 1,\ 2,\ 3$ as well as $\mathrm{Re}_D = 7600,\ \omega = 0.356$ for azimuthal modes $m = 0,\ 1,\ 2,\ 3,\ 4,\ 6,\ 12$. All eigenvectors with spatial growth rates $\Im(k) < 6$ were used. Our resulting spatial non-normal gains are plotted with digitised values from Reshotko & Tumin (2001) in Figure 3.4.

Digitisation of the results incurred some error of approximately 5%.

Figure 3.4 demonstrates excellent correspondence between the results of Reshotko & Tumin (2001) and the results of the present study. Reminiscent of the temporal case in Section 3.1.2.1, axisymmetric $m = 0$ disturbances are not significantly amplified by non-normality. Additionally, the relatively low $m = 1$ perturbation does not have the dominant spatial non-modal growth for these relatively high frequencies ω. Instead, there is an 'optimal' azimuthal mode number $m = 2$ or $m = 3$ that features both the largest spatial amplification possible and the most rapid onset amplification.

Reshotko & Tumin (2001) also consider the optimal axial disturbance to yield the greatest kinetic energy density at $z = 8.6$ given a $\mathrm{Re} = 7600,\ \omega = 0.356$ flow to match the experiments of Kaskel (1961). Implementing the methodology of Eqs. (2.45)-(2.46), verification is possible, as shown in Figure 3.5

Demonstrated by the collapse of our data points upon the digitised $|u_z'|$ optimal disturbance plotted in Figure 3.5, the 1D spatial non-modal stability code has been verified. This suggests that a region of axial forcing near the pipe wall may be conducive to spatial non-modal growth in addition to a disturbance near the centerline of the pipe.

3.2 Axisymmetric Free Jet Flow

To further verify the robustness of our solver, we consider the modal and non-modal stability analyses of a free axisymmetric non-coaxial jet. The temporal formulation will be verified against Jiménez-González *et al.* (2015) while the spatial formulation will be verified against Boronin *et al.* (2013).

3.2.1 Modal Stability Analysis

Given the effective eigenvalue verification for the linear stability of axisymmetric Hagen-Poiseuille pipe flow in Section 3.1 and a dearth of reference studies concerning the temporal stability analysis of axisymmetric free jets, only the modal viscous spatial stability analysis will be verified.

3.2.1.1 Spatial analysis

Table 3.2: The four most unstable spatial eigenvalues k of an axisymmetric free jet at $\mathrm{Re} = 80,\ \omega = 0.2,\ m = 0$. Comparison with Morris (1976) and Boronin *et al.* (2013)

	Morris (1976)	**Boronin *et al.* (2013)**	**Current verification**
k_1	$0.2321 + 0.0665i$	$0.2322 + 0.0666i$	$0.2325 + 0.0666i$
k_2	$0.3839 + 0.3904i$	$0.3840 + 0.3904i$	$0.3839 + 0.3906i$
k_3	$0.4839 + 0.8973i$	$0.4842 + 0.8976i$	$0.4841 + 0.8977i$
k_4	$0.5634 + 1.5852i$	$0.5628 + 1.5850i$	$0.5637 + 1.5861i$

Morris (1976) produced a spatial modal stability analysis to identify the critical Reynolds number needed to induce convective instability of an equidensity free jet with a smoothened top-hat (Eq. (2.10); $\delta = 0.5$) and a farfield Schlichting velocity profile (Eq. (2.8)). Boronin *et al.* (2013), as mentioned, have created a spatial non-modal stability analysis routine but have also verified eigenvalues against Morris (1976). For verification purposes, then, the present study used a non-uniform mesh of $N_r = 1001$ with $\sigma = \omega + 0i$ with a sixth-order central finite difference discretisation scheme for a numerical domain extending to $r = 10$. The resultant eigenvalues of the farfield (Schlichting) velocity profile are presented in Table 3.1. Note that the reference values were taken from tables located in their respective papers and were only tabulated up to the fourth decimal figure.

As quantified by Table 3.1, the present study yields spatial eigenvalues that compare favourably with those of Morris (1976) and Boronin *et al.* (2013). The normalised absolute values of the corresponding four most unstable axial eigenvectors from the farfield (Schlichting) velocity profile also match that of Morris (1976) well qualitatively and quantitatively, as can be seen in Figure 3.6. Here, as in Table 3.1, k_1 corresponds to the most unstable eigenvalue, k_2 the second most unstable, and so on.

3.2.2 Non-Modal Stability Analysis

3.2.2.1 Temporal analysis

Unlike the SVD-based method described by Schmid & Henningson (1994) for temporal non-modal stability analysis, Jiménez-González *et al.* (2015) use adjoint-based optimisation of the initial condition through a Lagrange-multiplier formulation. The energy norm is identical to Eq. (2.42) except for a multiplicative factor of a half. The velocity profile is a hyperbolic-tangent from the Michalke family of profiles (Eq. (2.11)). Farrell (1988) has demonstrated that the optimal initial disturbance to maximise non-modal amplification at large timescales is the adjoint of the most unstable eigenmode. That provides the maximum asymptotic amplification. For any intermediate timescale amplification, Jiménez-González *et al.* (2015) use an adjoint-based optimisation method: An initial condition is time-marched to the target time τ to compute the kinetic energy density. The continuous adjoint problem is time-marched backwards to suggest how the initial disturbance should be modified to enhance the non-modal gain. The forward- and backward-time processes are repeated until the optimal disturbance that maximises the energy gain has converged. The associated waveform and non-modal gain are recorded. For the infinite-time limit, it is possible to express the non-modal contribution as an inner product between the most unstable eigenmode and its adjoint counterpart. As this jet can be unstable above a critical Reynolds number, the kinetic energy density can grow exponentially over time. To visualise the effect of non-normality-induced

growth compared to exponential induced by a modal instability, the energy is normalised by $\exp(2\omega_i t)$ where ω_i is the temporal growth rate of the unstable eigenmode.

Jiménez-González *et al.* (2015) have produced the temporal non-modal amplification of a Re = 1000 axisymmetric free jet with the most unstable wavenumbers for the azimuthal modes $m = 0$ ($k = 2.297$) and $m = 1$ ($k = 2.131$) with insets of the normalised transient growth. For verification purposes, we have studied the same flow conditions given the same energy norm and have presented for qualitative comparison in Figure 3.7. The top row displays the results of Jiménez-González *et al.* (2015) while the bottom row displays the present results. Note that all eigenvalues ω where $\Im(\omega) > -1$ where incorporated in the analysis. Generally, Jiménez-González *et al.* (2015) found that decreasing axial wavenumbers k corresponded to higher non-modal energy gains and that the non-modal growth mechanisms were reminiscent of the Orr or 'lift-up' mechanisms from planar flows.

As shown in Figure 3.7, the qualitative trends have been captured with the SVD-based approach. Namely, the asymmetric $m = 1$ mode exhibits the largest degree of non-modal amplification and the transient growth phase terminates at normalised time $t \approx 4$. The long-time behaviour is unambiguously dominated by the most unstable eigenvalue growing exponentially. Deviations in the quantitative values may be due to the differing methodologies between Jiménez-González *et al.* (2015) and the present study.

3.2.2.2 Spatial analysis

Unlike the SVD-based method described by Reshotko & Tumin (2001) for spatial non-modal stability analysis, Boronin *et al.* (2013) implement a more traditional optimisation problem to determine the optimal spatial non-modal disturbance for an axisymmetric free jet. To maximise their multiphase energy norm, they consider a Lagrangian-multiplier method of optimisation. Hence, quantitative comparison is not possible. However, comparing qualitative trends could possibly indicate the robustness of the currently-implemented SVD-based method. To that end, Boronin *et al.* (2013) use finite difference discretisation of the domain

$(0 \leq r \leq 50)$ with 20% of the mesh points located at $0 \leq r \leq 1$. Unlike for fully-developed pipe flow, axisymmetric free jets can become unstable (Batchelor & Gill, 1962). The kinetic energy of this unstable eigenvalue exponentially grows as the downstream station z increases. To account for this, Boronin *et al.* (2013) normalise the optimal non-modal gain E_{opt} with the energy associated with solely the unstable eigenmode E_{sg}. Unstable flow configurations, then, would have energy gains that appear to asymptotically tend to a plateau as z increases. For consistency, we have selected all eigenvalues k with $\Im(k) \leq 5$ including the sole unstable mode. The remaining spurious or non-dominant modes that exist in the unstable half-plane are neglected.

Boronin *et al.* (2013) also consider multiphase free jets, so they introduce an interfacial energy term in addition to the kinetic energy density as the total energy to be maximised. Note that homogeneous (viz., single phase) jets have a negligible interfacial energy owing to the very high Weber number. Consequently, it is possible that the qualitative trends could be similar. The results are shown in the bottom row of Figure 3.8 while the reported results of Boronin *et al.* (2013) are shown in the top row. Generally, Boronin *et al.* (2013) found that non-modal energy gain increased as the temporal frequency decreased.

Recalling that the method of optimisation and the definition of the energy norm are not identical between the two studies, we are only seeking qualitative comparisons. Remarkably, the qualitative trends and even the quantitative asymptotic limits appear to match the reference results very well. All unstable modes plateau after sufficient downstream propagation, as expected. Generally, perturbations with a lower temporal frequency have the highest maximum non-modal amplification. As seen for axisymmetric pipe flow, it appears that symmetry-breaking ($m \neq 0$) perturbations have significantly higher susceptibility to non-modal growth downstream. Perhaps unexpectedly, the most diffuse, parabolic velocity profile - the farfield self-similar solution derived by Schlichting - has the greatest potential of non-modal growth of the two velocity profiles. This velocity profile corresponds to the least modally unstable eigenmodes, typically (Morris, 1976). In summary, symmetry-breaking ini-

tial perturbations of an axisymmetric jet far upstream of the jet exit can yield the greatest amplification of the flow.

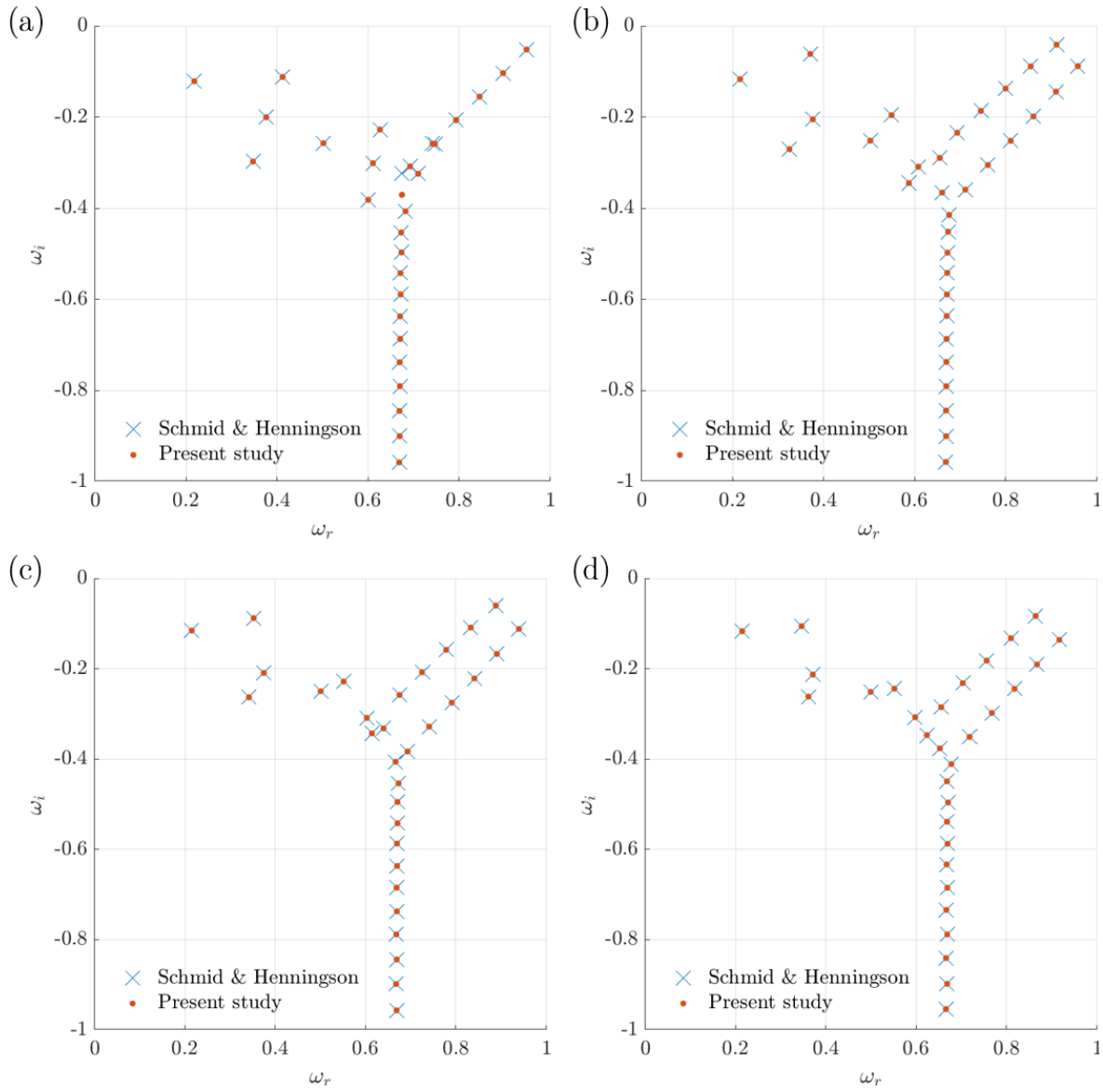

Figure 3.1: Temporal pipe Poiseuille flow eigenvalue spectrum verification against Schmid & Henningson (1994) for $\mathrm{Re}_D = 3000,\ k = 1$ for azimuthal mode numbers $m = 0,\ 1,\ 2,\ 3$ in (a), (b), (c), and (d), respectively.

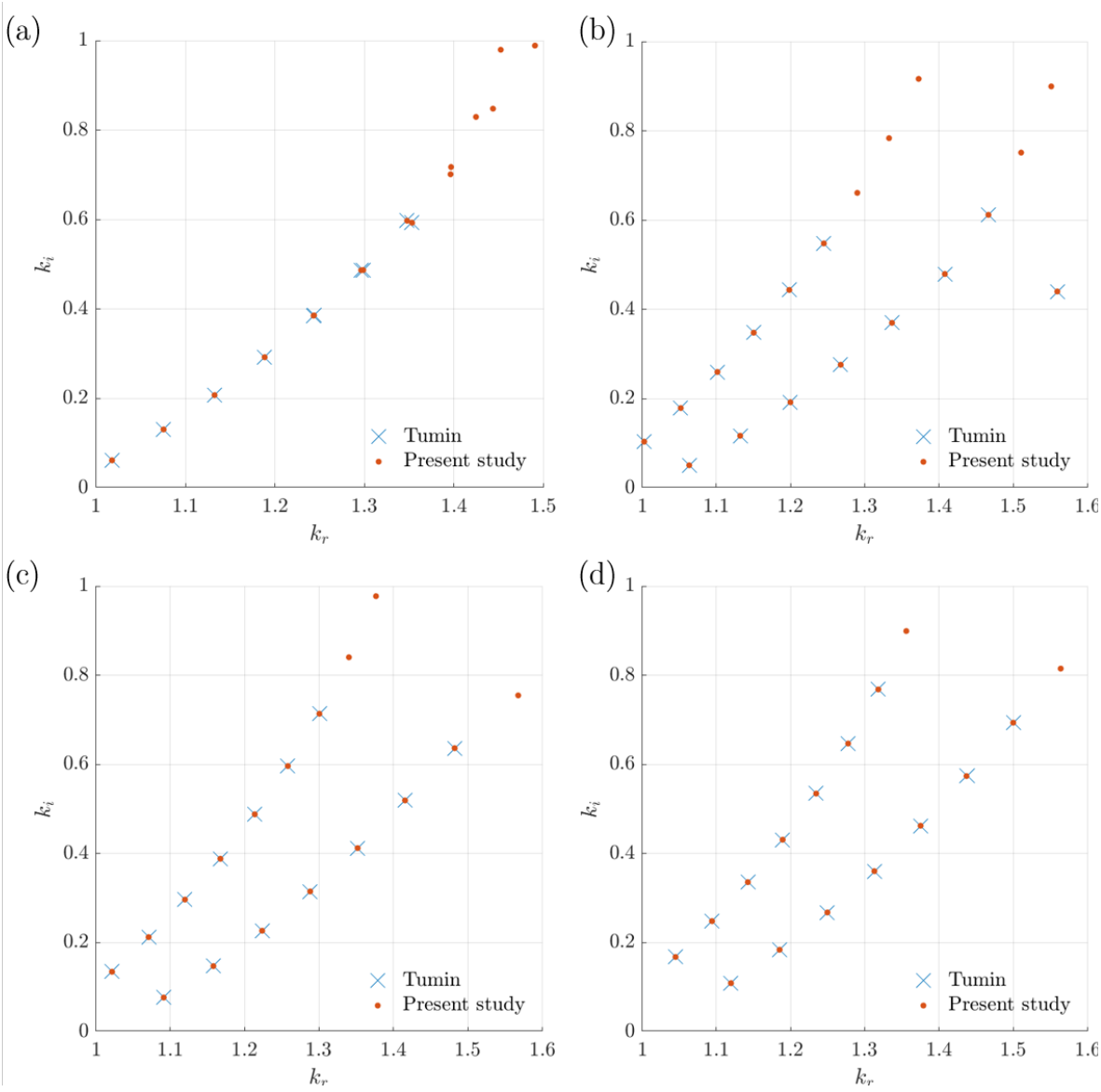

Figure 3.2: Spatial pipe Poiseuille flow eigenvalue spectrum verification against Tumin (1996) for $\mathrm{Re}_D = 2280,\ \omega = 0.96$ for azimuthal mode numbers $m = 0,\ 1,\ 2,\ 3$ in (a), (b), (c), and (d), respectively.

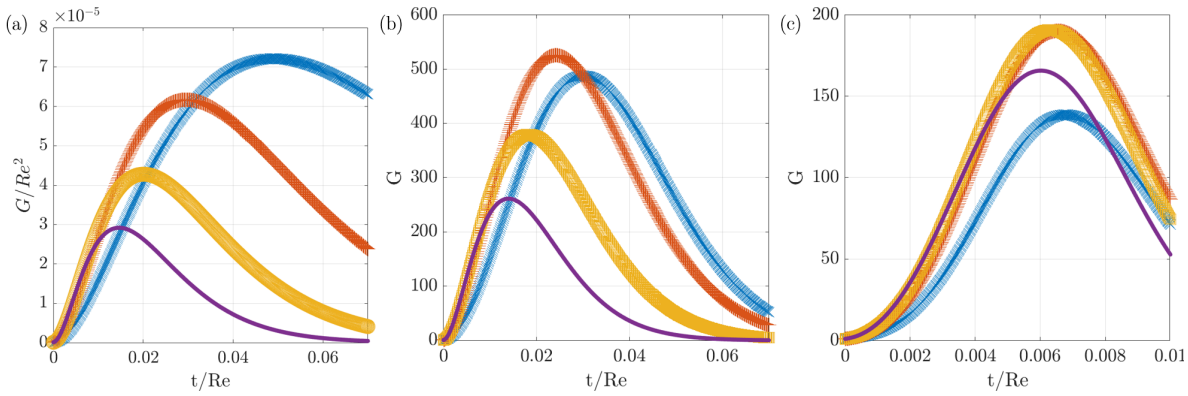

Figure 3.3: Temporal non-modal growth for pipe Poiseuille flow verification against Schmid & Henningson (1994) for $\mathrm{Re}_D = 3000$, $m = 1, 2, 3, 4$ (a) $k = 0$, (b) $k = 0.1$, (c) $k = 1.0$. Solid lines correspond to digitised values from Schmid & Henningson (1994) while markers correspond to our results. Blue '$\times$' indicates $m = 1$; orange '$+$': $m = 2$; yellow '$\square$': $m = 3$; purple '$\cdot$': $m = 4$.

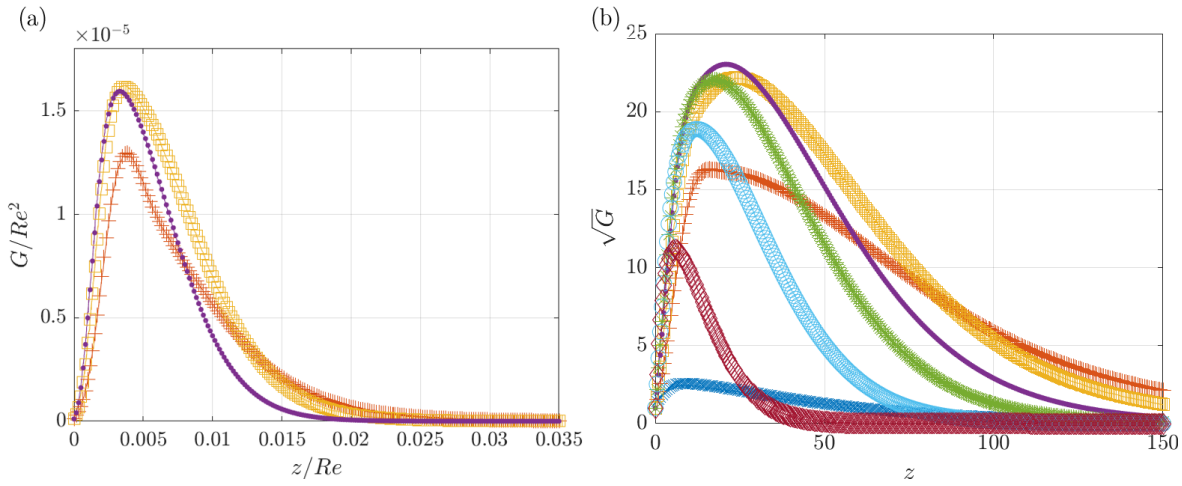

Figure 3.4: Spatial non-modal growth for pipe Poiseuille flow verification against Reshotko & Tumin (2001) for (a) $Re = 3000,\ \omega = 0.5,\ m = 1,\ 2,\ 3$ and for (b) $Re = 7600,\ \omega = 0.356,\ m = 0,\ 1,\ 2,\ 3,\ 4,\ 6,\ 12$. Solid lines correspond to digitised values from Reshotko & Tumin (2001) while markers correspond to our results. Blue '$\times$' indicates $m = 0$; orange '$+$': $m = 1$; yellow '$\square$': $m = 2$; purple '$\cdot$': $m = 3$; green '$*$': $m = 4$; teal '$\circ$': $m = 6$; burgundy $\Diamond$: $m = 12$.

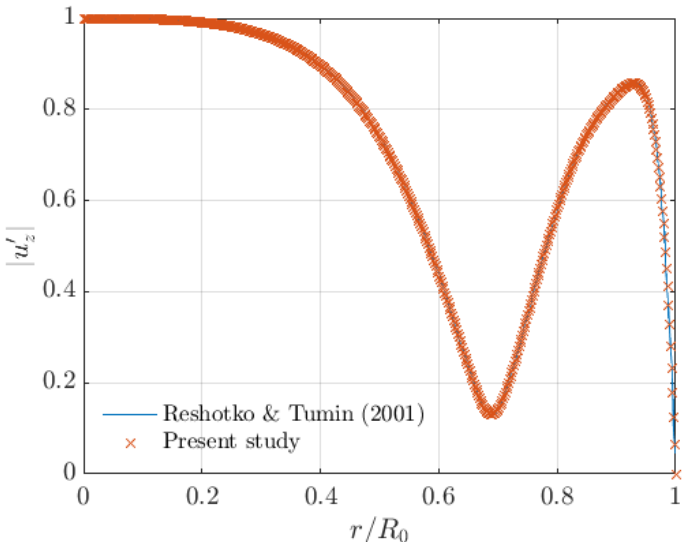

Figure 3.5: Optimal axial velocity disturbance to maximise spatial non-modal gain at $z = 8.6$ for Re $= 7600$, $\omega = 0.356$, $m = 0$ pipe Poiseuille flow. The solid blue line represents the digitised reference data from Reshotko & Tumin (2001) while the orange 'x' represents the results from our solver.

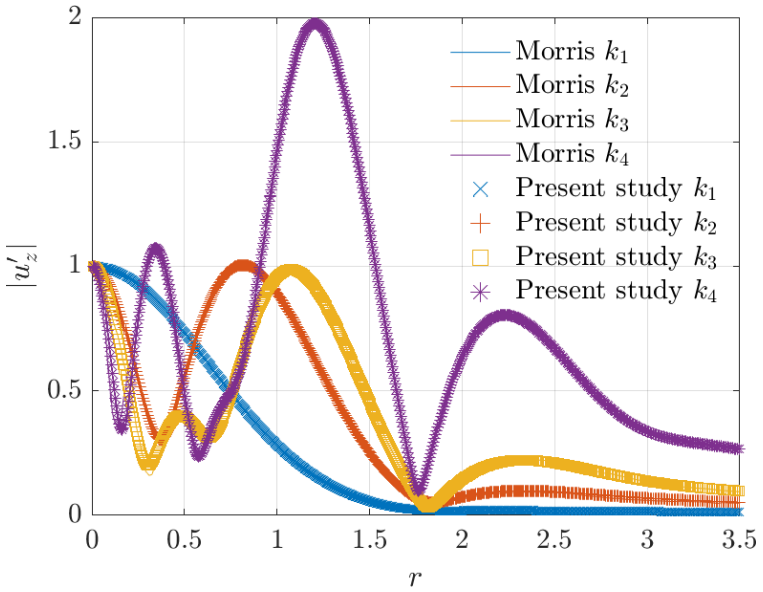

Figure 3.6: Normalised absolute values of the axial eigenvectors corresponding to the four most unstable eigenvalues of a Re $= 80,\ \omega = 0.2,\ m = 0$ axisymmetric free jet. Note that the comparison is with digitised eigenvectors from Morris (1976).

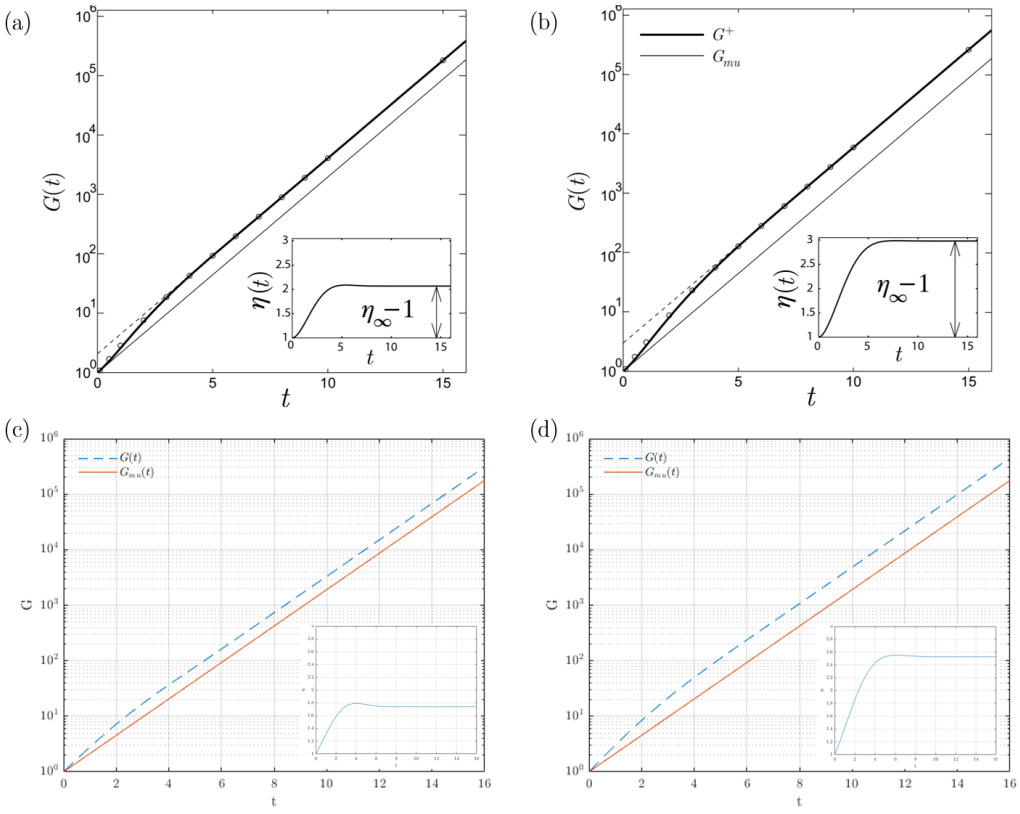

Figure 3.7: Temporal non-modal growth for a Re = 1000 free jet with a hyperbolic-tangent velocity profile with (a,c) $m = 0,\ k = 2.297$ and (b,d) $m = 1,\ k = 2.131$. Top row: Results from Jiménez-González *et al.* (2015); Bottom row: results from this present study.

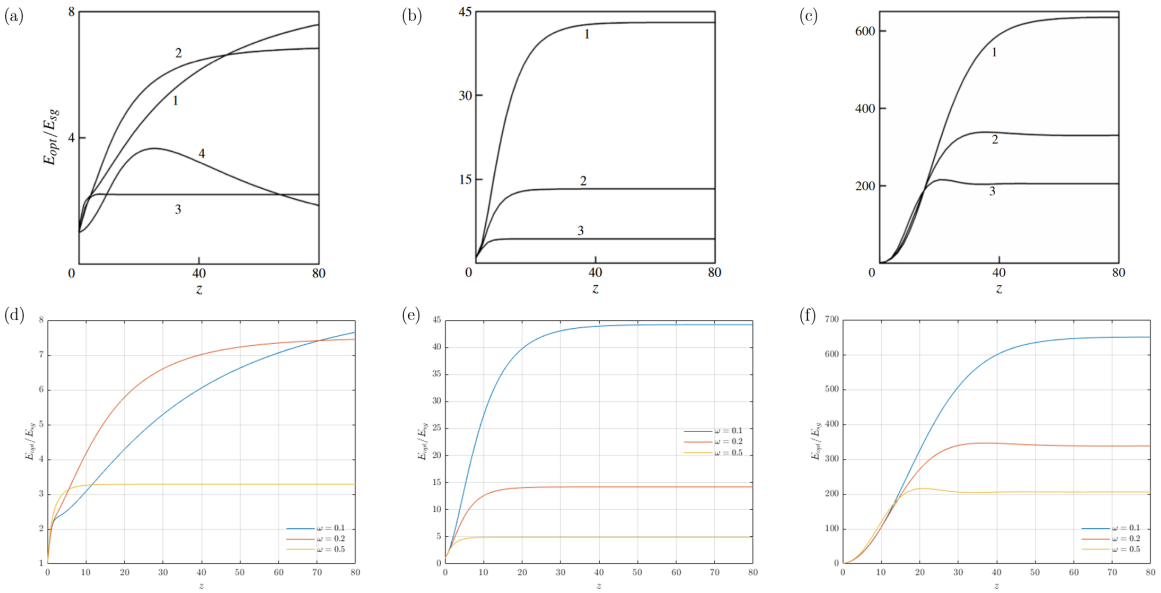

Figure 3.8: Normalised spatial non-modal growth of an axisymmetric free jet for Re = 1000 (a,d) $m = 0$ smooth top-hat velocity profile, (b,e) $m = 1$ smooth top-hat velocity profile, (c,f) $m = 1$ farfield profile. The labels 1, 2, 3, 4 correspond to $\omega = 0.1, 0.2, 0.5, 0.0$, respectively. Top row: results from Boronin *et al.* (2013); Bottom row: results from this present study.

CHAPTER 4

Governing equations and numerical methods for stability analysis for 2D base flows

After having considered and validated a one-dimensional linear stability analysis framework, we develop a two-dimensional local linear stability analysis for the jet-in-crossflow. This is not BiGlobal linear stability analysis, which considers a base flow that evolves in the streamwise direction. Rather, this is a 2D-local (or BiLocal or spanwise) stability analysis because we are employing a quasi-parallel flow approximation by stipulating that the jet-in-crossflow base flow does not evolve in the streamwise direction. This is in the spirit of linear stability analyses that employed the 1D (quasi-) parallel flow approximation that obtained physically-relevant instability characteristics despite the true base flow slowly evolving over space such as the planar mixing layer or the axisymmetric free jet. Streamwise, in the context of this present analysis of a jet-in-crossflow, refers to the direction of jet fluid issuance. However, crossflow perpendicular to the streamwise direction provides non-negligible convection of the jet fluid. This present analysis procedure can help to illustrate the coupling of the axisymmetric and various helical modes associated with the transverse jet, and insights that may relate to experimental observations.

4.1 Base flows considered

Here we consider base flows that vary in two inhomogeneous directions. The jet-in-crossflow base flows considered in this study have three velocity components that vary in two inhomo-

geneous directions.

4.2 Fully-coupled approach: Governing equations for spatial linear stability analysis for 2D base flows

For two-dimensional stability analysis, we linearise the nonlinear Navier-Stokes equations of Eq.(2.3) about a base flow with two inhomogeneous directions. Formulations in both polar and Cartesian coordinates have been used in this study, so their associated governing equations shall be elucidated in the following. The spatial formulation of the stability analysis is justified by excellent correspondence between modal spatial stability analyses and experimental measurements for weakly disturbed open shear flows but not with temporal stability analyses (Freymuth, 1966; Mattingly & Chang, 1974; Cohen & Wygnanski, 1987; Petersen & Samet, 1988; Criminale *et al.*, 2003; Gareev *et al.*, 2022). Examples where disturbances oscillate in time with a constant frequency but grow spatially include the boundary layer, mixing layer, free jets, wakes, and the jet-in-crossflow.

4.2.1 Polar coordinates

Linearisation of the nonlinear Navier-Stokes equations of Eq.(2.3) involves expanding each variable in terms of a Taylor series about a small disturbance in the base flow by ϵ as in Equation (2.13). Again, collection terms of $\mathcal{O}(\epsilon)$ led to the linear disturbance equations of Equation (2.14). The only differences between this analysis and that of Chapter 2 is the presumed form of the base flow and the normal Fourier mode decomposition.

Generally, a base flow non-dimensionalised with respect to a characteristic velocity scale in polar coordinates is assumed to take the form:

$$\vec{\bar{u}} \coloneqq \bar{u}_z(r,\theta)\hat{e}_z + \bar{u}_r(r,\theta)\hat{e}_r + \bar{u}_\theta(r,\theta)\hat{e}_\theta \tag{4.1}$$

The normal Fourier decomposition used for this local-2D analysis is:

$$u'_r = \hat{u}_r(r,\theta)\ \exp[i(kz-\omega t)] \tag{4.2a}$$

$$u'_\theta = \hat{u}_\theta(r,\theta)\ \exp[i(kz-\omega t)] \tag{4.2b}$$

$$u'_z = \hat{u}_z(r,\theta)\ \exp[i(kz-\omega t)] \tag{4.2c}$$

$$p' = \hat{p}(r,\theta)\ \exp[i(kz-\omega t)] \tag{4.2d}$$

Substitution of the Fourier modes of Eqs. (4.2) and the polar base flow of Eq. (4.1) into the linearised $\mathcal{O}(\epsilon)$ disturbance equations (Eqs. (2.14)) yields the following dispersion relation:

$$\frac{1}{r}\hat{u}_r + \frac{\partial \hat{u}_r}{\partial r} + \frac{1}{r}\frac{\partial \hat{u}_\theta}{\partial \theta} + ik\hat{u}_z = 0 \tag{4.3a}$$

$$\begin{aligned} -i\omega\hat{u}_r + \bar{u}_r\frac{\partial \hat{u}_r}{\partial r} + \hat{u}_r\frac{\partial \bar{u}_r}{\partial r} + \frac{\bar{u}_\theta}{r}\frac{\partial \hat{u}_r}{\partial \theta} + \frac{\hat{u}_\theta}{r}\frac{\partial \bar{u}_r}{\partial \theta} + ik\bar{u}_z\hat{u}_r - 2\frac{\bar{u}_\theta\hat{u}_\theta}{r} = \\ -\frac{\partial \hat{p}}{\partial r} + \frac{1}{Re}\left[\frac{1}{r}\frac{\partial \hat{u}_r}{\partial r} + \frac{\partial^2 \hat{u}_r}{\partial r^2} + \frac{1}{r^2}\frac{\partial^2 \hat{u}_r}{\partial \theta^2} - k^2\hat{u}_r - \frac{\hat{u}_r}{r^2} - \frac{2}{r^2}\frac{\partial \hat{u}_\theta}{\partial \theta}\right] \end{aligned} \tag{4.3b}$$

$$\begin{aligned} -i\omega\hat{u}_\theta + \bar{u}_r\frac{\partial \hat{u}_\theta}{\partial r} + \hat{u}_\theta\frac{\partial \bar{u}_\theta}{\partial r} + \frac{\bar{u}_\theta}{r}\frac{\partial \hat{u}_\theta}{\partial \theta} + \frac{\hat{u}_\theta}{r}\frac{\partial \bar{u}_\theta}{\partial \theta} + ik\bar{u}_z\hat{u}_\theta + \frac{\bar{u}_\theta\hat{u}_r}{r} + \frac{\bar{u}_r\hat{u}_\theta}{r} = \\ -\frac{1}{r}\frac{\partial \hat{p}}{\partial \theta} + \frac{1}{Re}\left[\frac{1}{r}\frac{\partial \hat{u}_\theta}{\partial r} + \frac{\partial^2 \hat{u}_\theta}{\partial r^2} + \frac{1}{r^2}\frac{\partial^2 \hat{u}_\theta}{\partial \theta^2} - k^2\hat{u}_\theta - \frac{\hat{u}_\theta}{r^2} + \frac{2}{r^2}\frac{\partial \hat{u}_r}{\partial \theta}\right] \end{aligned} \tag{4.3c}$$

$$\begin{aligned} -i\omega\hat{u}_z + \bar{u}_r\frac{\partial \hat{u}_z}{\partial r} + \hat{u}_r\frac{\partial \bar{u}_z}{\partial r} + \frac{\bar{u}_\theta}{r}\frac{\partial \hat{u}_z}{\partial \theta} + \frac{\hat{u}_\theta}{r}\frac{\partial \bar{u}_z}{\partial \theta} + ik\bar{u}_z\hat{u}_z = \\ -ik\hat{p} + \frac{1}{Re}\left[\frac{1}{r}\frac{\partial \hat{u}_z}{\partial r} + \frac{\partial^2 \hat{u}_z}{\partial r^2} + \frac{1}{r^2}\frac{\partial^2 \hat{u}_z}{\partial \theta^2} - k^2\hat{u}_z\right] \end{aligned} \tag{4.3d}$$

This dispersion relation can be formed into a generalised eigenvalue problem that is explicitly elucidated in Appendix B. Both viscous and inviscid analyses were performed in the present study. An inviscid analysis is possible by taking the limit of Re$\rightarrow \infty$ in Eq. (4.3) and may allow a reduction of the computational cost of the eigenproblem. However, an inviscid study is only warranted if a physical inviscid instability mechanism is suspected to exist

(Theofilis, 2003). Given that the jet-in-crossflow base flows considered in the present study contain inflexion points and that the prior simplified linear stability analyses of Alves *et al.* (2007) and Alves & Kelly (2008) indicate an inviscid instability exists, Rayleigh's theorem (applicable strictly only to 1D streamwise parallel flows) was invoked to justify the pursuit of an inviscid instability mechanism. Both inviscid and viscous analyses were performed in the present study. The polar spatial linear stability analysis presented as a generalised eigenproblem was solved via the Krylov-Schur algorithm of Stewart (2002) after having embedded the appropriate far-field boundary conditions.

Equations in polar, cylindrical, or spherical coordinates have a numerical coordinate singularity at the pole ($r = 0$) that is problematic when determining values multiplied by a factor of $1/r$ and when determining derivatives near the pole. Note that the physical solution of the equations do not have a true singularity at the pole. The one-dimensional linear stability analysis of Chapter 2 manages this singularity by prescribing a computational boundary condition at the pole derived from assuming axisymmetry, smoothness, and boundedness there (Khorrami *et al.*, 1989). This approach was not used to treat the coordinate singularity in two-dimensions because symmetry-breaking (induced by crossflow, for example) was of interest to obtain. Rather, the pole condition was treated with the method described by Mohseni & Colonius (2000). This involved (i) defining a coordinate transform from physical space $0 \leq \theta < 2\pi$ and $0 < r < R_{\max}$ to computational space $0 \leq \tilde{\theta} < \pi$ and $-R_{\max} < \tilde{r} < R_{\max}$, (ii) defining a numerical mesh that avoids the pole singularity, (iii) defining radial differentiation to be taken with respect to $\tilde{r}$ on the pole-less mesh, and (iv) propagating the Jacobian resulting from the coordinate transform of the multi-valued radial and azimuthal velocities throughout the governing equations. Further expounding can be found in Constantinescu & Lele (2002) as well as the development of series expansion solutions to the governing equations that are physically applicable to the region around the pole.

4.2.2 Cartesian coordinates

In order to co-verify the results obtained with the previous code formulated in polar coordinates, we construct a code framework in Cartesian coordinates as well. This Cartesian approach also obviates the need for any special treatment of the pole as there is no coordinate singularity.

The non-dimensional unforced Navier-Stokes equations are:

$$\frac{\partial u_x}{\partial x} + \frac{\partial u_y}{\partial y} + \frac{\partial u_z}{\partial z} = 0 \tag{4.4a}$$

$$\frac{\partial u_x}{\partial t} + u_x\frac{\partial u_x}{\partial x} + u_y\frac{\partial u_x}{\partial y} + u_z\frac{\partial u_x}{\partial z} = -\frac{\partial p}{\partial x} + \frac{1}{\mathrm{Re}}\left[\frac{\partial^2 u_x}{\partial x^2} + \frac{\partial^2 u_x}{\partial y^2} + \frac{\partial^2 u_x}{\partial z^2}\right] \tag{4.4b}$$

$$\frac{\partial u_y}{\partial t} + u_x\frac{\partial u_y}{\partial x} + u_y\frac{\partial u_y}{\partial y} + u_z\frac{\partial u_y}{\partial z} = -\frac{\partial p}{\partial y} + \frac{1}{\mathrm{Re}}\left[\frac{\partial^2 u_y}{\partial x^2} + \frac{\partial^2 u_y}{\partial y^2} + \frac{\partial^2 u_y}{\partial z^2}\right] \tag{4.4c}$$

$$\frac{\partial u_z}{\partial t} + u_x\frac{\partial u_z}{\partial x} + u_y\frac{\partial u_z}{\partial y} + u_z\frac{\partial u_z}{\partial z} = -\frac{\partial p}{\partial z} + \frac{1}{\mathrm{Re}}\left[\frac{\partial^2 u_z}{\partial x^2} + \frac{\partial^2 u_z}{\partial y^2} + \frac{\partial^2 u_z}{\partial z^2}\right] \tag{4.4d}$$

where u_x represents the streamwise velocity, u_y represents the spanwise velocity, and u_z represents the jet axial velocity. All parameters have been non-dimensionalised in the same manner as in Chapter 2, i.e., by the maximum axial velocity along the centreline and by the jet radius.

We assume that a two-dimensional base flow takes the following form:

$$\bar{\mathbf{u}} \coloneqq \bar{u}_x(x,y)\hat{\mathbf{e}}_x + \bar{u}_y(x,y)\hat{\mathbf{e}}_y + \bar{u}_z(x,y)\hat{\mathbf{e}}_z \tag{4.5}$$

Perturbing the non-dimensional Navier-Stokes equations of Eqs. (4.4) with a small disturbance as in Eq. (2.13) and collecting terms of $\mathcal{O}(\epsilon)$ led to the linear disturbance equations:

$$\frac{\partial u_x}{\partial x} + \frac{\partial u_y}{\partial y} + \frac{\partial u_z}{\partial z} = 0 \tag{4.6a}$$

$$\frac{\partial u_x}{\partial t} + \bar{u}_x\frac{\partial u_x}{\partial x} + u_x\frac{\partial \bar{u}_x}{\partial x} + \bar{u}_y\frac{\partial \bar{u}_x}{\partial y} + u_y\frac{\partial \bar{u}_x}{\partial y} + \bar{u}_z\frac{\partial u_x}{\partial z} + u_z\frac{\partial \bar{u}_x}{\partial z} = -\frac{\partial p}{\partial x} + \frac{1}{\mathrm{Re}}\left[\frac{\partial^2 u_x}{\partial x^2} + \frac{\partial^2 u_x}{\partial y^2} + \frac{\partial^2 u_x}{\partial z^2}\right] \tag{4.6b}$$

$$\frac{\partial u_y}{\partial t} + \bar{u}_x\frac{\partial u_y}{\partial x} + u_x\frac{\partial \bar{u}_y}{\partial x} + \bar{u}_y\frac{\partial \bar{u}_y}{\partial y} + u_y\frac{\partial \bar{u}_y}{\partial y} + \bar{u}_z\frac{\partial u_y}{\partial z} + u_z\frac{\partial \bar{u}_y}{\partial z} = -\frac{\partial p}{\partial y} + \frac{1}{\mathrm{Re}}\left[\frac{\partial^2 u_y}{\partial x^2} + \frac{\partial^2 u_y}{\partial y^2} + \frac{\partial^2 u_y}{\partial z^2}\right] \tag{4.6c}$$

$$\frac{\partial u_z}{\partial t} + \bar{u}_x\frac{\partial u_z}{\partial x} + u_x\frac{\partial \bar{u}_z}{\partial x} + \bar{u}_y\frac{\partial \bar{u}_z}{\partial y} + u_y\frac{\partial \bar{u}_z}{\partial y} + \bar{u}_z\frac{\partial u_z}{\partial z} + u_z\frac{\partial \bar{u}_z}{\partial z} = -\frac{\partial p}{\partial z} + \frac{1}{\mathrm{Re}}\left[\frac{\partial^2 u_z}{\partial x^2} + \frac{\partial^2 u_z}{\partial y^2} + \frac{\partial^2 u_z}{\partial z^2}\right] \tag{4.6d}$$

The normal Fourier mode decomposition used for this 2D-local analysis in Cartesian coordinates is:

$$u'_x = \hat{u}_x(x,y)\exp\left[i(kz-\omega t)\right] \tag{4.7a}$$

$$u'_y = \hat{u}_y(x,y)\exp\left[i(kz-\omega t)\right] \tag{4.7b}$$

$$u'_z = \hat{u}_z(x,y)\exp\left[i(kz-\omega t)\right] \tag{4.7c}$$

$$p' = \hat{p}(x,y)\exp\left[i(kz-\omega t)\right] \tag{4.7d}$$

Specialising the linearised Navier-Stokes equations of Eqs. (4.6) to the 2D Cartesian base flow of Eq. (4.5) and the normal Fourier mode decomposition of Eqs. (4.7), we obtain the following dispersion relation:

$$\frac{\partial \hat{u}_x}{\partial x} + \frac{\partial \hat{u}_y}{\partial y} + ik\hat{u}_z = 0 \tag{4.8a}$$

$$-i\omega\hat{u}_x + \bar{u}_x\frac{\partial \hat{u}_x}{\partial x} + \hat{u}_x\frac{\partial \bar{u}_x}{\partial x} + \bar{u}_y\frac{\partial \hat{u}_x}{\partial y} + \hat{u}_y\frac{\partial \bar{u}_x}{\partial y} + ik\bar{u}_z\hat{u}_x = -\frac{\partial \hat{p}}{\partial x} + \frac{1}{\mathrm{Re}}\left[\frac{\partial^2 \hat{u}_x}{\partial x^2} + \frac{\partial^2 \hat{u}_x}{\partial y^2} - k^2\hat{u}_x\right] \tag{4.8b}$$

$$-i\omega\hat{u}_y + \bar{u}_x\frac{\partial \hat{u}_y}{\partial x} + \hat{u}_x\frac{\partial \bar{u}_y}{\partial x} + \bar{u}_y\frac{\partial \hat{u}_y}{\partial y} + \hat{u}_y\frac{\partial \bar{u}_y}{\partial y} + ik\bar{u}_z\hat{u}_y = -\frac{\partial \hat{p}}{\partial y} + \frac{1}{\mathrm{Re}}\left[\frac{\partial^2 \hat{u}_y}{\partial x^2} + \frac{\partial^2 \hat{u}_y}{\partial y^2} - k^2\hat{u}_y\right] \tag{4.8c}$$

$$-i\omega\hat{u}_z+\bar{u}_x\frac{\partial\hat{u}_z}{\partial x}+\hat{u}_x\frac{\partial\bar{u}_z}{\partial x}+\bar{u}_y\frac{\partial\hat{u}_z}{\partial y}+\hat{u}_y\frac{\partial\bar{u}_z}{\partial y}+ik\bar{u}_z\hat{u}_z=-ik\hat{p}+\frac{1}{\mathrm{Re}}\left[\frac{\partial^2\hat{u}_z}{\partial x^2}+\frac{\partial^2\hat{u}_z}{\partial y^2}-k^2\hat{u}_z\right] \quad (4.8d)$$

We perform spatial linear stability analysis by creating the following generalised eigenproblem formulated using the companion matrix approach of Bridges & Morris (1984):

$$\begin{pmatrix} \mathcal{L}_c & -\frac{\partial\bar{u}_z}{\partial x} & \frac{\partial\bar{u}_z}{\partial y} & 0 & 0 & 0 & 0 \\ 0 & \mathcal{L}_c+\frac{\partial\bar{u}_x}{\partial x} & \frac{\partial\bar{u}_x}{\partial y} & \frac{\partial}{\partial x} & 0 & 0 & 0 \\ 0 & \frac{\partial\bar{u}_y}{\partial x} & \mathcal{L}_c+\frac{\partial\bar{u}_y}{\partial y} & \frac{\partial}{\partial y} & 0 & 0 & 0 \\ 0 & \frac{\partial}{\partial x} & \frac{\partial}{\partial y} & 0 & 0 & 0 & 0 \\ 0 & 0 & 0 & 0 & \mathbf{I} & 0 & 0 \\ 0 & 0 & 0 & 0 & 0 & \mathbf{I} & 0 \\ 0 & 0 & 0 & 0 & 0 & 0 & \mathbf{I} \end{pmatrix} \vec{\hat{q}}_c = k \begin{pmatrix} -i\bar{u}_z & 0 & 0 & -i & \frac{1}{\mathrm{Re}} & 0 & 0 \\ 0 & -i\bar{u}_z & 0 & 0 & 0 & \frac{1}{\mathrm{Re}} & 0 \\ 0 & 0 & -i\bar{u}_z & 0 & 0 & 0 & \frac{1}{\mathrm{Re}} \\ -i & 0 & 0 & 0 & 0 & 0 & 0 \\ \mathbf{I} & 0 & 0 & 0 & 0 & 0 & 0 \\ 0 & \mathbf{I} & 0 & 0 & 0 & 0 & 0 \\ 0 & 0 & \mathbf{I} & 0 & 0 & 0 & 0 \end{pmatrix} \vec{\hat{q}}_p \quad (4.9)$$

where $\mathcal{L}_c$ was defined as: $\mathcal{L}_c \coloneqq -i\omega+\bar{u}_x\frac{\partial}{\partial x}+\bar{u}_y\frac{\partial}{\partial y}-\frac{1}{\mathrm{Re}}\left[\frac{\partial^2}{\partial x^2}+\frac{\partial^2}{\partial y^2}-k^2\right]$ and the eigenvector $\hat{\mathbf{q}}_c$ was defined as $\hat{\mathbf{q}}_c \coloneqq \begin{pmatrix} \hat{u}_x(x,y) & \hat{u}_y(x,y) & \hat{u}_z(x,y) & \hat{p}(x,y) & k\hat{u}_x(x,y) & k\hat{u}_y(x,y) & k\hat{u}_z(x,y) \end{pmatrix}^T$. Note that an inviscid analysis is possible by taking the limit of $\mathrm{Re}\to\infty$ in Eq. (4.8). The Cartesian spatial linear stability analysis presented as a generalised eigenproblem was solved via the Krylov-Schur algorithm (Stewart, 2002) after having embedded the appropriate far-field boundary conditions. The companion matrix approach (Bridges & Morris, 1984) was used to enable numerical solution of this nonlinear spatial eigenvalue problem at the cost of increasing the leading dimension of the matrices by a factor of 7/4. The temporal viscous eigenvalue problem is strictly linear, so a companion matrix approach is unnecessary. The Jacobi-Davidson algorithm of Sleijpen & der Vorst (2000) can solve polynomial eigenvalue problems of the form $\mathbf{A}_0\mathbf{x}+\lambda\mathbf{A}_1\mathbf{x}+\lambda^2\mathbf{A}_2\mathbf{x}+\cdots=0$, where $\mathbf{x}$ is the direct eigenfunction-vector and $\mathbf{A}_0,\mathbf{A}_1,\ldots$ are pre-specified matrices. However, the Jacobi-Davidson algorithm scales superquadratically with memory whereas the Arnoldi algorithm scales quadratically (Heeg & Geurts, 1997).

Note that a tremendous simplification of Eq. (4.8a) is possible if the base flow $\bar{\mathbf{u}} \coloneqq 0\hat{\mathbf{e}}_x + 0\hat{\mathbf{e}}_y + \bar{u}_z(x,y)\hat{\mathbf{e}}_z$ and if only inviscid disturbances are considered. It is possible to condense Eq. (4.8a) to obtain a single equation: the generalised 2D Rayleigh pressure disturbance equation, which substantially reduces computational cost (Hall & Horseman, 1991; Balachandar & Malik, 1995; Otto & Denier, 1999). The remaining velocity eigenfunctions can be obtained from the pressure eigenfunction.

$$\left[\frac{\partial^2}{\partial x^2} + \frac{\partial^2}{\partial y^2} - k^2\right]\hat{p} - \frac{2}{\bar{u} - \omega/k}\frac{\partial \bar{u}_z}{\partial x}\frac{\partial \hat{p}}{\partial x} - \frac{2}{\bar{u} - \omega/k}\frac{\partial \bar{u}_z}{\partial y}\frac{\partial \hat{p}}{\partial y} = 0 \tag{4.10}$$

4.2.3 Novel upwind treatment for the convective term

The governing equations presented in Section 4.2 are discretised using a finite difference approach. Spectral discretisation (spectral collocation) schemes have been used for BiGlobal stability analyses, such as for airfoils, lid-driven cavities, backward-facing steps, etc. (Theofilis, 2011), owing their exponential accuracy convergence with respect to mesh size allowing for savings in memory requirements. Mesh design is more challenging, however, with spectral collocation. An alternative strategy is to reduce memory is to use time-stepping, but the solution requires more time to obtain. Merle *et al.* (2010) have demonstrated that a finite difference approach, specifically the dispersion-relation-preserving (DRP) scheme by Tam & Webb (1993), can lead to a good balance between accuracy, memory, and time requirements for the eigensolution of a global stability analysis. The present study uses a standard finite difference scheme (LeVeque, 2007). Prior direct numerical simulations, such as that of Mohan Rai & Moin (1991), have found that finite difference schemes were less restrictive in their grid point placement. The corresponding loss of exponential accuracy convergence may be compensated for by using higher-order schemes, even with upwind-biased finite difference stencils (Mohan Rai & Moin, 1991). Both co-located and staggered grid (Merle & Robinet, 2010; Macaraeg *et al.*, 1988; Theofilis & Colonius, 2004) approaches were developed in the Cartesian coordinate system; a co-located grid approach was developed in the polar

coordinate system. Co-located refers to the placement of all velocity and pressure eigenfunctions at the same location in numerical grid whereas staggered refers to the placement of velocity and pressure eigenfunctions in the manner of Harlow & Welch (1965). Note that the typical second order finite difference discretisation of a staggered grid (Harlow & Welch, 1965) is known to conserve kinetic energy (Morinishi *et al.*, 1998). Consequently, the present staggered grid only employed second-order accurate central finite difference schemes on a uniform Cartesian mesh.

The velocity, but not the pressure, eigenfunctions obtained from both inviscid and viscous spatial linear stability analysis formulated in both polar and Cartesian coordinates were contaminated with non-physical oscillations concentrated downstream of the jet potential core and could extend to the upstream and downstream numerical boundaries, irrespective of jet momentum thickness, jet-to-crossflow velocity ratio R, and numerical solver parameters. Examples of these non-physical oscillations are in Figure 4.1. These oscillations were *not* of the chequerboard type (also known as sawtooth, π, 2Δ waves or odd-even or pressure-velocity grid decoupling) that are common in incompressible flows (Rhie & Chow, 1983; Harlow & Welch, 1965; Zang *et al.*, 1994; Perić *et al.*, 1988; Ferziger & Perić, 2002). Artificial compressibility, described by Khorrami *et al.* (1989) for stability analyses, was also introduced and had negligible effect. Rotating the base flow and its derivatives while changing nothing else in the stability codes led to the non-physical oscillations rotating along with the eigenfunctions. In fact, the non-physical oscillations emerged from both co-located and staggered Cartesian grid formulations in the present study. The staggered grid formulation of Harlow & Welch (1965) is designed to avoid chequerboard oscillations by directly coupling the pressure and velocity variables, therefore providing additional evidence that pressure-velocity decoupling is not the origin of these non-physical oscillations. Note that a non-uniform co-located grid, even using second-order central finite difference discretisation schemes, also coupled the velocity and pressure eigenfunctions. Additionally, higher-order central finite difference schemes, namely the fourth- and sixth-order schemes, were also used and obtained

the same non-physical oscillations with higher amplitudes. Moreover, the extent of the numerical domain had negligible effect; the non-physical oscillations extended all the way to the downstream and sometimes the upstream boundary. The presence of non-physical oscillations in the present study impugned the validity of the computed eigenvalues even though said eigenvalues were insensitive to changes in grid resolution.

Interestingly, non-physical oscillations only occurred in the velocity eigenfunctions pertaining to the *jet-in-crossflow*; other base flows considered in this study for 2D-local linear stability code verification purposes such as the (asymmetric) coaxial free jet, (rotating) pipe Poiseuille flow, and Batchelor q-vortex did not yield velocity eigenfunctions that exhibited any such non-physical oscillations. Note that the (asymmetric) coaxial free jet was studied using an inviscid stability analysis using central finite differences on a slowly-stretched non-uniform grid, meaning that there was no physical dissipation and only a small amount of numerical dissipation present. This observation indicated that a stability problem where convection is physically significant (such as for a jet-in-crossflow but not for the other 2D base flows considered here) was potentially the cause of the non-physical oscillations. Indeed, synthetically deleting all linearised convective terms in the eigenproblem removed the non-physical oscillations entirely and produced a set of smooth disturbance eigenfunctions, whereas deleting any other term had no effect.

The convective term has been known to be the origin of unusual or erroneous results in flow simulations in the past, particularly for inviscid and incompressible flows in the asymptotic long-time limit (Morinishi *et al.*, 1998; Nicoud, 2000; Arakawa, 1966), which is relevant for eigenvalue problems. This observation was made in the context of unsteady simulations of turbulent flow using direct numerical simulation (DNS) or large eddy simulation (LES); a numerically stable and more physically representative solution is obtained if the kinetic energy is conserved, which is related to the convective term (Morinishi *et al.*, 1998). Morinishi *et al.* (1998) also note that fourth-order accurate schemes using a staggered grid can produce non-physical results at sufficiently high-Reynolds numbers if the schemes do not conserve

kinetic energy.

Refining the numerical grid in either polar or Cartesian coordinates increased the amplitude of the non-physical oscillations with both uniform and non-uniform grids. Particularly, a smooth and gradually-varying non-uniform mesh that aimed to improve the resolution of the sharpest gradients in the base flow and hence the disturbance eigenfunctions (viz., the shear layer region) simply aggrandised the non-physical oscillations much in a manner resembling Gibbs phenomenon (Gibbs, 1898; Boyd, 2001). By contrast, under-resolution could mitigate the oscillation amplitude. These observations stand contrary to the general observation that increased grid resolution is sufficient to remove non-physical oscillations (Xu & Yang, 2021; Ferziger & Perić, 2002). This is typically justified by the well-known observation that a local grid Péclet number of $\mathrm{Pe} \coloneqq \frac{\rho u L}{\Gamma} \leq 2$ is a necessary condition for avoiding all non-physical oscillations of a 1D convection-diffusion equation discretised using a finite difference method (Ferziger & Perić, 1980, 2002; Moin, 2010). The Péclet number quantifies the balance between the convection and the diffusion - Γ represents the diffusivity.

A viscous study found that use of the Orr-Sommerfeld equations with lower Reynolds numbers reduced the amplitude of the oscillations compared to when the Rayleigh equations were used. $\mathrm{Re}_D \approx 2000$, for example, generally produced oscillation-free eigenfunctions even when using central finite differences that have no numerical dissipation. This result indicated that physical dissipation could produce smoother eigenfunctions. Therefore, we introduced numerical dissipation for high spatial frequency or wavenumber phenomena in the form of upwinding for the convective term. To balance the amount of dissipation and dispersion introduced by the choice of finite difference scheme, the convective term is treated with a hybrid central-upwind approach. This is an approach for linear stability analyses of convection-dominated flows that allows tailored suppression of numerical oscillations with minimal numerical dissipation.

An upwinded treatment of the convective term has been conducted in prior direct numerical simulations such as those of Hosseinverdi & Fasel (2023) and Ghosh & Baeder (2010),

among others, to provide numerical dissipation for high-frequency or wavenumber phenomena. Mohan Rai & Moin (1991) found that an upwind finite difference scheme could control aliasing errors while not requiring kinetic energy conservation in their direct numerical simulation of incompressible fully-developed turbulent channel flow. Ghosh & Baeder (2010) found that upwinding the convective term was essential to obtain non-oscillatory solutions at high Reynolds numbers. Flow solutions obtained from simulations using an upwinded convective term have also been employed as base flows in stability analyses, such as that of Bhoraniya & Vinod (2017), who considered the global stability of a boundary layer along an axisymmetric cone.

The BiGlobal (temporal) stability analyses of plasma actuated boundary layers by Riherd (2013) used Chevyshev collocation (Boyd, 2001) to discretise the wall-normal direction and finite difference for the streamwise direction. Their convective term was treated with third-order accurate upwinded schemes generally and a layer of first-order accurate upwinding near the outlet. This was because they found that their outlet boundary conditions (interpolation-type or Gaster-type) permitted reflections to re-enter the domain. The layer of first-order upwinding near the outlet was also the prevent reflections contaminating the domain. It must also be noted that the framework of Hosseinverdi & Fasel (2023) was also capable of performing stability analyses.

A small aside regarding boundary conditions now follows. All boundary value problems require appropriate boundary conditions to (i) close the problem and (ii) impart the relevant/desirable physical behaviour in the problem/solution. For eigenproblems, the boundary conditions are typically homogeneous. Most stability analyses use homogeneous Dirichlet ($\hat{q} \equiv 0$) or homogeneous Neumann ($\frac{\partial \hat{q}}{\partial \hat{n}} \equiv 0$) boundary conditions because the disturbance $\hat{q}$ is expected to decay exponentially far from the region of interest (Theofilis, 2011). The Tollmein-Schlichting waves are such an example (Baines *et al.*, 1996). Inflow and outflow boundary conditions, particularly where the base flow continues to evolve, can be more challenging for both flow simulations (Peyret & Taylor, 1983; Fletcher, 1991; Ferziger & Perić,

2002; Rempfer, 2006) and stability analyses (Groot *et al.*, 2015; Sipp & Lebedev, 2007). Generally, the idea is to permit the disturbance to smoothly transit through the numerical domain while satisfying the conservation equations, to prevent any reflections from contaminating the interior (Colonius, 2004), as well as the prescribing the desired or expected behaviour of the solution. For stability problems, it is possible to use Gaster's transformation (Gaster, 1962) to prescribe a particular travelling wave that satisfies the eigenproblem at the inflow/outflow (Alizard & Robinet, 2007). That radiation or Robin boundary condition is not necessarily reflective of the overall eigenfunction throughout the domain, however. Other treatments of the boundary conditions, especially the outflow region, include use of the linearised pressure Poisson equation (Theofilis, 2017; Appel *et al.*, 2019; Chauvat, 2020), sponges (Bodony, 2006; Ran *et al.*, 2017), linear extrapolation (Bhoraniya & Vinod, 2018), the perfectly matched layer (Berenger, 1994; Appel, 2020; Appel *et al.*, 2019), or by stipulating traction-free behaviour (Shaabani-Ardali *et al.*, 2020).

Presently, the Dirichlet, Neumann, Robin, linearised pressure Poisson equation, and linear extrapolation have been employed as inflow and outflow boundary conditions with little effect on the non-physical oscillations and eigenvalues. Notably, extrapolation could reduce the non-physical oscillation amplitudes slightly, indicating possibly the presence of reflections from the outflow boundary. Still, the bulk of the non-physical oscillations are concentrated around the downstream portion of the jet flow. Inflow/outflow in this context pertains to the in and outflow of the crossflow along the x direction. Application of various boundary conditions for the spanwise boundaries had negligible effect. Although the jet-in-crossflow base flows presently used for stability analysis do not spatially evolve as much as, say, cylinder wakes or boundary layers, it is possible from the present boundary condition exploration study that this 2D-local stability analysis contains an element of inflow/outflow complexity.

For the present upwind treatment of the convective term, recall that central finite difference schemes on uniform grids only have phase or dispersion errors because the leading local truncation error term is an odd-order derivative (LeVeque, 2007). Dispersive errors

for, say, a one dimensional advection-diffusion equation, yield non-physical oscillations that resemble non-synchronised travelling waves. Dissipative errors, by contrast, occur if the leading local truncation error is an even-order derivative (LeVeque, 2007), and cause non-physical smoothing or amplitude damping of the solution. This is also known as artificial/numerical viscosity. Consequently, central finite difference schemes are not generally suitable for convection-dominated flows, wherein advection is significantly greater than diffusion. Adding numerical dissipation via e.g., upwinding may be necessary to stabilise the simulations of convection-dominated flows (Zhong, 1998). Upwind finite difference schemes account for the flow convection direction in obtaining the derivative. Zhong (1998) introduced a generalised framework to obtain upwind-biased finite difference schemes that are one order lower in accuracy than their central scheme counterpart in order to introduce a customisable degree of numerical dissipation through controlling the leading truncation error term.

For example, a second-order accurate central finite difference scheme for the first derivative applied to a uniform grid with grid spacing Δx discretised about grid point x_i of the function $f(x)$ may be written as:

$$\left.\frac{\mathrm{d}f}{\mathrm{d}x}\right|^{\text{central}} = \frac{f_{i+1} - f_{i-1}}{2\Delta x} - (\Delta x)^2 \frac{f'''(x)}{3!} + \dots \tag{4.11}$$

where f_{i+1} corresponds to the value of $f(x)$ at grid point x_{i+1} and f_{i-1} corresponds to the value of $f(x)$ at grid point x_{i-1}. The leading local truncation error includes the third derivative of $f(x)$, $f'''(x)$, which is an odd-order derivative. Hence, this second-order accurate central finite difference scheme contains only dispersion errors and no dissipative errors. The corresponding upwind scheme that is one order less accurate may be written as:

$$\left.\frac{\mathrm{d}f}{\mathrm{d}x}\right|^{\text{upwind}} = \frac{f_i - f_{i-1}}{\Delta x} + \Delta x \frac{f''(x)}{2!} - (\Delta x)^2 \frac{f'''(x)}{3!} + \dots \tag{4.12}$$

for a prevailing convection velocity that is positive. That is, the flow convects from lower

to higher values of x. The scheme is upwinded in the sense that it allocates more stencil points upstream rather than downstream. This may also be known as a backward finite difference scheme. Downwinding involves allocating more stencil points downstream rather than upstream. Note that the leading local truncation error includes the second derivative of $f(x)$, $f''(x)$, which is an even-order derivative. Hence, this first-order accurate upwind finite difference scheme contains dissipative errors. The next order truncation error is the same dispersion error as for the second-order accurate central scheme.

Acquisition of a finite difference scheme with a customisable degree of numerical dissipation may be derived in the manner outlined by Zhong (1998), or equivalently from the linear combination of a central and an upwind finite difference scheme that is one order less accurate using the same stencil points:

$$\left.\frac{\mathrm{d}f}{\mathrm{d}x}\right|_i^{\text{hybrid}} \approx (1-\alpha)\left.\frac{\mathrm{d}f}{\mathrm{d}x}\right|_i^{\text{central}} + \alpha\left.\frac{\mathrm{d}f}{\mathrm{d}x}\right|_i^{\text{upwind}} \tag{4.13}$$

where $\alpha \in \mathbb{R}$ is a user-defined free variable that sets the degree of numerical dissipation. This hybrid upwind scheme offers a customisable degree of numerical dissipation while retaining the same dispersion error of the central finite difference scheme. Specifically for the hybrid 2nd-1st order accurate scheme, we have:

$$\left.\frac{\mathrm{d}f}{\mathrm{d}x}\right|_i^{\text{hybrid,2nd}-\text{1st}} \approx \frac{\frac{1}{2}(1-\alpha)f_{i+1} + \alpha f_i - \frac{1}{2}(1+\alpha)f_{i-1}}{\Delta x} + \alpha(\Delta x)\frac{f''(x)}{2!} - (\Delta x)^2\frac{f'''}{3!} + \dots \tag{4.14}$$

where $\alpha = 0$ recovers the standard second-order central scheme in Equation (4.11) and $\alpha = 1$ recovers the first-order upwinded scheme in Equation (4.12). By inspection, the dispersion error of the hybrid 2^{nd}-1^{st}-order upwind scheme is the same as that of the central second-order accurate scheme. α may also be considered as a free variable to provide a reduced level of numerical dissipation compared to the typical first-order accurate upwind scheme. Additionally, this hybrid scheme also couples neighbouring grid points, thereby obviating any velocity-pressure decoupling when $\alpha \neq 0$, even for uniform grids. The hybrid scheme

generation formula, presented in Equation (4.13), is also applicable to finite difference stencils for non-uniform grids as well as for higher-order finite difference schemes.

The direction of biasing was determined by the local direction of the base flow that multiplied that derivative. This approach may be considered as a version of TVD-style flux-limiting. For example, the term $\bar{u}_x \frac{\partial}{\partial x}$ was upwinded at that location if the streamwise base flow term $\bar{u}_x > 0$ and downwinded if $\bar{u}_x < 0$. Not every location in the numerical mesh needed to be winded; generally only the near-wake region of the jet-in-crossflow exhibited numerical oscillations and therefore only the user-customised wake region needed damping. Note that the convective terms in polar coordinates also needed to be winded with respect to the local base flow direction; the azimuthal direction was discretised with periodic finite difference rather than Fourier discretisation to allow for this. Owing to the use of the Mohseni & Colonius (2000) coordinate transformation to treat the pole, the radial base flow $\bar{u}_r$ was upwinded with respect to $\tilde{r}$ in $0 < \theta < \pi/2$ and $\pi < \theta < 3\pi/2$ while $\bar{u}_r$ was downwinded with respect to $\tilde{r}$ in $\pi/2 < \theta < \pi$ and $3\pi/2 < \theta < 2\pi$.

For the present study, the Cartesian scheme was solved with 4^{th}-order central finite difference schemes for the non-convective terms while the convective terms were discretised with a hybrid 2^{nd}-1^{st}-order winded scheme for the near-wake region and a hybrid 4^{th}-3^{rd}-order winded scheme elsewhere. To avoid any discontinuity at the interface of the two types of winded discretisation schemes, a linear activation function was employed. Homogeneous Neumann boundary conditions were imposed on all of the disturbance eigenfunctions at the same order of accuracy as the non-convective scheme (Zhong, 1998). This necessitated biasing (i.e., winding) the finite difference stencil for the grid points close to the boundary. So as not to interfere with any boundary conditions, the region of where the 2^{nd}-1^{st}-order winded scheme applied was selected to terminate far from any boundary.

Given that grid resolution affected the oscillation magnitude and therefore the degree of numerical dissipation necessary in the convective terms, it was especially necessary to perform a grid convergence study. Table 4.1 displays the the axisymmetric and first (anti-)

symmetric helical inviscid eigenvalues for the $R = 10$, $\theta_0/R_0 = 1/15$ UVAS jet-in-crossflow as for $\mathrm{St}_D = 0.51, 0.70, 0.83$ as the number of Cartesian grid points $N_x = N_y$ increased from 300 to 600. Eigenvalues from grid sizes $N_x = N_y$ of 100 and 200 were also obtained but are not reported here owing to their non-convergence. The values of St_D were selected because they bracket the St_D associated with the dominant eigenvalue at $3 \leq R < \infty$. Similarly, Table 4.2 displays the grid convergence of the same base flow and frequency settings except for $\mathrm{Re}_D = 2000$. Depending on the St_D considered, the numerical domain generally extended from $-10 \leq x_{\min} \leq -5$ to $15 \leq x_{\max} \leq 20$ and $-15 \leq y_{\min} = y_{\max} \leq 15$ to ensure that the eigenfunctions could satisfy the homogeneous Neumann boundary conditions. Other numerical domains up to $x_{\max} \approx 100$ were also explored. The present grid choice offered a compromise between grid resolution, domain extent, and computational complexity. The numerical mesh was tailored for each case considered to ensure that the shear layer gradients were well-resolved and therefore the numerical dissipation strength was varied; generally the lower frequency eigenfunctions featured sharper shear layers. The zone where additional numerical dissipation brought about by the hybrid 2^{nd}-1^{st}-scheme generally lay $1.2 \lesssim x \lesssim 5$ and $-1 \lesssim y \lesssim +1$, although this too was tailored for each particular case to minimise the numerical dissipation deployed. Generally, increasing the degree of numerical dissipation smoothed the eigenfunctions while minimally affecting the eigenvalues. Eventually, both the eigenvalues and eigenfunctions stop varying with α. Just as spurious eigenvalues are sensitive to small changes in parameters, non-physical oscillations generally responded to small changes in the degree of numerical dissipation. Physical eigenstructures were generally indifferent to upwinding. At that point, the degree of numerical dissipation was considered the minimal necessary to ensure the eigenfunctions were smooth. In other words, both grid convergence and 'upwinding' convergence were sought and obtained.

As both Tables 4.1 and 4.2 indicate, this scheme does indeed converge eigenvalues to the 3^{rd} significant figure for the lower range of St_D values considered and up to the 5^{th} significant figure for the higher range of St_D values considered for the axisymmetric ($m = 0$), first anti-

k	300	400	500	600
$k^{m=0}_{\mathrm{St}_D=0.51}$	$2.2536 - 1.3316i$	$2.2536 - 1.3314i$	$2.2539 - 1.3305i$	-
$k^{m=1\mathrm{AS}}_{\mathrm{St}_D=0.51}$	$2.5005 - 1.0981i$	$2.5004 - 1.0981i$	$2.5013 - 1.0974i$	-
$k^{m=1\mathrm{S}}_{\mathrm{St}_D=0.51}$	$2.5609 - 1.1033i$	$2.5621 - 1.1024i$	$2.5643 - 1.0937$	-
$k^{m=0}_{\mathrm{St}_D=0.70}$	$3.7305 - 1.3084i$	$3.7305 - 1.3084i$	$3.7305 - 1.3082i$	-
$k^{m=1\mathrm{AS}}_{\mathrm{St}_D=0.70}$	$3.7875 - 1.1132i$	$3.7876 - 1.1133i$	$3.7878 - 1.1129i$	-
$k^{m=1\mathrm{S}}_{\mathrm{St}_D=0.70}$	$3.7939 - 1.0896i$	$3.7937 - 1.0900i$	$3.7933 - 1.0797i$	-
$k^{m=0}_{\mathrm{St}_D=0.83}$	$4.5552 - 1.1203i$	$4.5552 - 1.1203i$	$4.5553 - 1.1203i$	$4.5552 - 1.1203i$
$k^{m=1\mathrm{AS}}_{\mathrm{St}_D=0.83}$	$4.5503 - 0.9577i$	$4.5503 - 0.9578i$	$4.5506 - 0.9576i$	$4.5503 - 0.9578i$
$k^{m=1\mathrm{S}}_{\mathrm{St}_D=0.83}$	$4.5047 - 0.9411i$	$4.5044 - 0.9416i$	$4.5035 - 0.9289i$	$4.5044 - 0.9416i$

Table 4.1: Grid convergence study for the inviscid spatial eigenvalues given various values of $N_x = N_y$

k	300	400	500	600
$k^{m=0}_{\mathrm{St}_D=0.51}$	$2.3523 - 1.2212i$	$2.3523 - 1.2211i$	$2.3524 - 1.2210i$	-
$k^{m=1\mathrm{AS}}_{\mathrm{St}_D=0.51}$	$2.5834 - 0.9887i$	$2.5833 - 0.9887i$	$2.5833 - 0.9887i$	-
$k^{m=1\mathrm{S}}_{\mathrm{St}_D=0.51}$	$2.6216 - 0.9940i$	$2.6228 - 0.9928i$	$2.6236 - 0.9921$	-
$k^{m=0}_{\mathrm{St}_D=0.70}$	$3.7978 - 1.1238i$	$3.7978 - 1.1238i$	$3.7978 - 1.1238i$	-
$k^{m=1\mathrm{AS}}_{\mathrm{St}_D=0.70}$	$3.8381 - 0.9392i$	$3.8381 - 0.9392i$	$3.8381 - 0.9392$	-
$k^{m=1\mathrm{S}}_{\mathrm{St}_D=0.70}$	$3.8231 - 0.9313i$	$3.8231 - 0.9313i$	$3.8233 - 0.9312i$	-
$k^{m=0}_{\mathrm{St}_D=0.83}$	$4.5943 - 0.9092i$	$4.5943 - 0.9092i$	$4.5943 - 0.9092i$	$4.5943 - 0.9092i$
$k^{m=1\mathrm{AS}}_{\mathrm{St}_D=0.83}$	$4.5722 - 0.7591i$	$4.5722 - 0.7591i$	$4.5722 - 0.7591i$	$4.5722 - 0.7591i$
$k^{m=1\mathrm{S}}_{\mathrm{St}_D=0.83}$	$4.5106 - 0.7695i$	$4.5109 - 0.7692i$	$4.5110 - 0.7690i$	$4.5110 - 0.7691i$

Table 4.2: Grid convergence of the viscous spatial eigenvalues ($\mathrm{Re}_D = 2000$) for various values of $N_x = N_y$

symmetric helical ($m = 1$AS), and first symmetric helical $m = 1$S) modes. (Anti-)symmetry is defined about the theoretical plane of symmetry that bisects the jet-in-crossflow base flow. Given the approximate nature of the jet-in-crossflow base flows considered and given that the preferred St_D generally increases as R decreases, this was considered sufficient to demonstrate eigenvalue convergence with respect to both the grid size and the numerical dissipation. As a compromise between computational expense and eigenvalue accuracy, $N_x = N_y = 400$ generally, ensuring convergence to the 3$^{\mathrm{rd}}$ significant figure for both inviscid and viscous eigenvalues.

4.3 Verification of 2D linear stability analysis results

4.3.1 Axisymmetric round coaxial jet

A round coaxial free jet was modelled by Michalke & Hermann (1982) as:

$$\bar{u}_z(r,\theta) \coloneqq \frac{1}{2}(U_j + U_\infty) - \frac{1}{2}(U_j - U_\infty)\tanh\left[\frac{1}{4}\frac{R_0}{\theta_0}\left(\frac{r}{R_0} - \frac{R_0}{r}\right)\right] \tag{4.15a}$$

$$\bar{u}_r \coloneqq 0 \tag{4.15b}$$

$$\bar{u}_\theta \coloneqq 0 \tag{4.15c}$$

where U_j is the peak axial jet velocity, U_∞ is the axial external flow velocity, R_0 is the jet exit radius, and θ_0 is the jet momentum thickness. If $U_\infty = 0$, then the flowfield is that of an axisymmetric free jet with no co-flow or counterflow as considered by Michalke (1971, 1984).

To partly verify the two-dimensional Cartesian and polar linear stability solvers, spatial linear stability of the axisymmetric round coaxial jet defined by Eqs. (4.15) was performed and compared against the results reported by Michalke & Hermann (1982). Michalke & Hermann (1982) performed a one-dimensional inviscid spatial linear stability analysis composed of a pressure disturbance Rayleigh equation that was solved using the Runge-Kutta

algorithm with modified Bessel functions as asymptotic boundary conditions.

For verification, both axisymmetric and first helical modes of the coaxial jet were obtained using the polar coordinate formulation with sixth-order central finite difference discretisation in the radial direction with $N_r = 140$, Fourier discretisation in the azimuthal direction with $N_\theta = 36$, and a non-uniform radial mesh that refined the shear layer region well but stretched to $r_{max} = 15$. The following linear stability analysis verification considered an axisymmetric coaxial jet with $\theta_0/R_0 \coloneqq 1/10$ and $U_\infty/\Delta U \coloneqq U_\infty/(U_j - U_\infty) = 0, 0.1, 0.3, 0.5$. As Figure 4.2 demonstrates, the correspondence between our results and those of Michalke & Hermann (1982) is excellent for the axisymmetric and first helical modes for a range of $U_\infty/\Delta U$ values.

4.3.1.1 Asymmetric round coaxial jet

The asymmetric coaxial free jet base flow is defined as the superposition of a symmetric and an asymmetric component to the overall axial base flow by Freitas (2019) as:

$$\bar{u}_z(r,\theta) \coloneqq U_{\text{symmetric}}(r) + \delta U_{\text{asymmetric}}(r,\theta) \tag{4.16a}$$

$$\bar{u}_r \coloneqq 0 \tag{4.16b}$$

$$\bar{u}_\theta \coloneqq 0 \tag{4.16c}$$

where

$$\begin{aligned} U_{\text{symmetric}}(r) \coloneqq & \frac{1}{2}\left\{1 - \tanh\left[\frac{1}{4\theta_i}\left(r - \frac{1}{r}\right)\right]\right\} \\ & - \frac{\text{VR}}{2}\left\{\tanh\left[\frac{\text{DR}}{4\theta_i}\left(\frac{r}{\text{DR}} - \frac{\text{DR}}{r}\right)\right] - \tanh\left[\frac{1}{4\theta_i}\left(r - \frac{1}{r}\right)\right]\right\} \end{aligned} \tag{4.17}$$

$$U_{\text{asymmetric}}(r,\theta) \coloneqq -\frac{1}{2}\sin(M_\theta\ \theta)\left\{\tanh\left[\frac{\text{DR}}{4\theta_o}\left(\frac{r}{\text{DR}} - \frac{\text{DR}}{r}\right)\right] - \tanh\left[\frac{1}{4\theta_i}\left(\frac{1}{r} - r\right)\right]\right\} \tag{4.18}$$

where θ_i is the momentum thickness of the inner jet, θ_o is the momentum thickness of the annulus flow, M_θ is an integer that determines the azimuthal behaviour of the symmetry-breaking component ($M_\theta = 0$ ensures that the coaxial jet is symmetric), and $\delta \ll 1$ is amplitude of the asymmetric term. Note that both θ_i and θ_0 have been non-dimensionalised with respect to the inner jet radius: $\theta_i \coloneqq \frac{\tilde{\theta}_i}{R_i}$ and $\theta_o \coloneqq \frac{\tilde{\theta}_o}{R_i}$, where $\tilde{\theta}_i$ and $\tilde{\theta}_o$ are dimensional quantities. VR $\coloneqq \frac{\tilde{u}_{z,o}}{\tilde{u}_{z,i}}$ is the ratio between the maximum outer jet axial velocity and the maximum inner jet axial velocity. DR $\coloneqq \frac{D_o}{D_i}$ is the ratio between the outer and inner jet diameters. The resulting axial velocity field resembles a jet with a sinusoidal net co-flow and counter-flow annulus that break axisymmetry. Additional details can be found in Freitas (2019).

As part of a verification effort, spatial linear stability of the coaxial free jet was performed and compared against the results reported by Freitas (2019). They used a matrix-forming, centred finite difference approach to discretise the governing equations with iterative methods to solve the generalised eigenproblem. This base flow was chosen because (i) it had two inhomogeneous directions, (ii) a coaxial jet with (localised) suction or blowing issuing perpendicularly into a crossflow was experimentally investigated by Harris (2020), (iii) a jet with small tabs issuing perpendicularly into crossflow was experimentally investigated by Harris *et al.* (2021), (iv) previous linear stability analysis have found that coaxial free jets have absolute/convective stability behaviour, and (v) eigenvalue degeneracy-breaking was possible because the base flow was asymmetric.

Note that both the polar and Cartesian formulations of linear stability analysis were verified against the asymmetric coaxial jet. This means that polar base flow was converted to a Cartesian equivalent: $\bar{\mathbf{u}} \coloneqq \bar{u}_x\hat{\mathbf{e}}_x + \bar{u}_y\hat{\mathbf{e}}_y + \bar{u}_z\hat{\mathbf{e}}_z$. The derivatives of the base flow in both polar and Cartesian coordinates were obtained analytically as well as numerically, with negligible difference. For verification here, $\theta_o = \theta_i \coloneqq \frac{1}{10}$, $M_\theta \coloneqq 1$, VR $\coloneqq 0$, and DR $\coloneqq 2$. As Figures 4.3 and 4.4 demonstrate, the correspondence between our results and those of Freitas (2019) is excellent for the axisymmetric, first helical, and second helical modes, for

a range of δ values. Additional eigenvalue comparisons can be found in Appendix A.

As Figure 4.3 demonstrates, the effect of a more prominent asymmetry in the annular flow is to weaken the axisymmetric mode. The results from the present study align well quantitatively with the results of Freitas (2019), indicating a verification of the code. As Figure 4.4 demonstrates, the introduction of any amount of asymmetry in the base flow breaks the degeneracy of the first and second helical modes. The eigenfunctions indicate that there is an anti-symmetric and a symmetric mode, about the plane of symmetry introduced by the annular flow. Figure 4.4a indicates that the first symmetric mode de-stabilises as δ increases while the first anti-symmetric mode stabilises for $0.1 \leq \delta \leq 0.2$ and starts to de-stabilise for $\delta = 0.3$. Figure 4.4b indicates that the second symmetric mode stabilises as δ increases while second anti-symmetric mode initially de-stabilises for $0 \leq \delta \leq 0.2$ but then stabilises for $\delta = 0.3$. The results from the present study align well quantitatively with the results of Freitas (2019), indicating a verification of the code. Interestingly, the eigenspectrum appears to diverge for the first symmetric mode as δ increases from 0.2 to 0.3. This is an indication of a transition from convective to absolute instability. This suggests that the present code could be capable of capturing this transition.

4.3.1.2 Rotating pipe Poiseuille flow:

A canonical problem is the rotating pipe Poiseuille flow which has a base flow that is defined as follows:

$$\bar{u}_r(r) \coloneqq 0 \tag{4.19a}$$

$$\bar{u}_\theta(r) \coloneqq \Omega r \tag{4.19b}$$

$$\bar{u}_z(r) \coloneqq 1 - r^2 \tag{4.19c}$$

where Ω represents the non-dimensional pipe angular velocity. This base flow was selected

Ω	MO-1973 ω_i	KMA-1989 ω_i	Present ω_i	Present ω_r
0	$-1.57781649i$	$-1.57781649i$	$-1.57781649i$	0.666764346
0.1	$-1.5796i$	$-1.5796i$	$-1.57963734i$	0.666512921
1	$-1.795i$	$-1.795i$	$-1.79530789i$	0.618291551
10	$-2.29i$	$-2.29i$	$-2.28704781i$	5.42521225
50	$-2.72i$	$-2.72i$	$-2.71887590i$	24.9832221

Table 4.3: Temporal eigenvalues of the rotating pipe Poiseuille flow

because it had two components of the base flow $\bar{u}_z$ and $\bar{u}_z$ rather than just one (as is the case for the axisymmetric free jet), and because it is a canonical hydrodynamic stability problem (Metcalfe & Orszag, 1973; Khorrami *et al.*, 1989).

For verification, a round pipe of radius unity was discretised in polar coordinates with Fourier differentiation in the azimuthal θ direction and 6^{th}-order finite difference in the radial r direction on a uniform radial grid. Specifically, $N_r = 100$ and $N_\theta = 56$ with homogeneous Dirichlet boundary conditions for the velocity eigenfunctions and homogeneous Neumann boundary conditions for the pressure eigenfunctions at the pipe wall. The pole coordinate singularity was treated with the method described by Mohseni & Colonius (2000).

Firstly, viscous temporal linear stability analysis of the rotating pipe base flow defined by Eqs. (4.19) was performed with a Reynolds number of 10 and a wavenumber of unity, and the axisymmetric modes were obtained. As Table 4.3 demonstrates, there is excellent correspondence between the imaginary components of the eigenvalues (viz., the temporal growth rates) up to the available precision where MO-1973 (KMA-1989) is an abbreviation for the results reported by Metcalfe & Orszag (1973) (Khorrami *et al.* (1989)). Corresponding temporal frequency information were not available.

Given that the Reynolds number of the rotating pipe considered was $\mathrm{Re} = 10$, we perform temporal linear stability analysis of a static pipe (viz., $\Omega = 0$) for higher Reynolds numbers.

Re	m	MO-1973 ω_i	KMA-1989 ω_i	Present ω_i	Present ω_r
1000	5	$-0.180604i$	$-0.180604i$	$-0.180603518i$	0.300556905
1000	7	$-0.207943i$	$-0.207943i$	$-0.207941368i$	0.294876769
1000	9	$-0.245645i$	$-0.245645i$	$-0.245641308i$	0.286439258

Table 4.4: Temporal eigenvalues for the static pipe Poiseuille flow

The radial direction was discretised with 6^{th}-order central finite difference with $N_r = 100$ distributed in a non-uniform manner and with Fourier discretisation with $N_\theta = 80$ in a uniform grid. As Table 4.4 indicates, the temporal growth rates of eigenmodes of various azimuthal mode numbers m compare favourably. Note again that MO-1973 (KMA-1989) is an abbreviation for the results reported by Metcalfe & Orszag (1973) (Khorrami *et al.* (1989)). The corresponding temporal frequencies were not reported by Metcalfe & Orszag (1973) or Khorrami *et al.* (1989).

4.3.1.3 Batchelor q-vortex:

The Batchelor q-vortex is a canonical base flow defined in Eqs .(4.20) that has been used to investigate vortex breakdown in swirling jets and wakes as well as to represent slowly-evolving trailing line vortices (Olendraru *et al.*, 1999; Paredes *et al.*, 2011).

$$\bar{u}_z(r) \coloneqq a + \exp\left[-(r^2)\right] \tag{4.20a}$$

$$\bar{u}_r(r) \coloneqq 0 \tag{4.20b}$$

$$\bar{u}_\theta(r) \coloneqq \frac{q}{r}$$

where q is the swirl that the azimuthal velocity component of the base flow provides and a describes the external ambient flow in the axial direction. Olendraru *et al.* (1999) performed

Case	Olendraru *et al.* (1999)	Present study
$a \coloneqq 0$, $q \coloneqq 0.7$, $\omega \coloneqq 0.0425$	$0.6 + 0i$	$0.600059107 - 0.00027052i$
$a \coloneqq -1.268$, $q \coloneqq 0.6$, $\omega \coloneqq -0.78$	$0.454 + 1.276i$	$0.45442553 + 1.275676733i$
$a \coloneqq 0.01$, $q \coloneqq 0.6$, $\omega \coloneqq 0.2$	$0.761 - 0.336i$	$0.76143091 - 0.336421521i$
$a \coloneqq 0$, $q \coloneqq 0.1$, $\omega \coloneqq 0.01$	$0.506 - 0.139i$	$0.50640250 - 0.13929708i$

Table 4.5: Spatial eigenvalues of the Batchelor q-vortex compared.

one-dimensional spatiotemporal linear stability analysis formulated as two first-order ordinary differential equation with asymptotic boundary conditions near the pole and far from the jet solved via a numerical integration procedure paired with Newton-Raphson iteration.

As part of the verification process, the two-dimensional spatial linear stability equations in polar coordinates were discretised with 6^{th}-order central finite differnce in the radial direction and with Fourier discretisation in the azimuthal direction. The numerical grid consisted of a 400-point non-uniform radial grid extending to 30 radii and a 36-point uniform grid in the azimuthal direction.

As Figures 4.5 indicate, there is excellent correspondence between the normalised eigenfunction amplitudes obtained from the polar formulation and from Olendraru *et al.* (1999). $|F|$, $|G|$, $|H|$, and $|P|$ correspond to the normalised axial, radial, azimuthal, and pressure eigenfunctions, respectively. Note that all eigenfunctions have been normalised with respect to the L_∞ norm of the absolute value of the axial eigenfunction $|F|$ except for Figure 4.5c, which was normalised by the L_∞ norm of the absolute value of the radial eigenfunction $|G|$. Additionally, the corresponding eigenvalues compare favourably with the present two-dimensional polar coordinate approach, as tabulated in Table 4.5.

4.4 Jet-in-crossflow base flow models

To perform linear stability analysis, it is necessarily to linearise the Navier-Stokes equations about a steady-state base flow. As no analytical solution of the Navier-Stokes equations exists that yields a jet-in-crossflow, there have been numerous simplified mathematical models and numerical simulations used as base flows. Coelho & Hunt (1989) obtained an inviscid vortex-sheet model valid for the nearfield of an asymptotically strong jet encountering a weak crossflow. An inviscid base flow is unable to capture the physically-present viscous shear layer and the subsequent entrainment of crossflow fluid by the jet. The nearfields of higher velocity ratio R JICFs are dominated by the effect of viscous entrainment Coelho & Hunt (1989).

Alves *et al.* (2008) extended the inviscid flowfield of Coelho & Hunt (1989) to model a viscous jet-in-crossflow in two ways. Firstly, he considered a hyperbolic-tangent jet axial velocity profile, commonly used to model axisymmetric viscous free jets, perturbed by a weak crossflow. This is the 'tanh' model. The tanh model did not satisfy conservation of momentum, but did satisfy conservation of mass as well as far-field boundary conditions as established by Coelho & Hunt (1989). The second model is the UVAS (uniformly valid asymptotic solution) by Alves & Kelly (2008). This was formed as the asymptotic perturbation of the time-independent Navier-Stokes equations by a weak crossflow and by a non-zero boundary layer thickness. The resultant boundary-layer type equations were reformulated in a similarity solution as there was no natural physical length scale present. In the farfield, the inviscid solution of Coelho & Hunt (1989) was valid and close to the jet, the boundary-layer solution was valid. The smooth matching between the two solutions was achieved by the method of matched asymptotic expansions.

Firstly, Coelho & Hunt (1989) assume that an inviscid vortex-sheet model of the jet-in-crossflow can be asymptotically expanded in terms of $\lambda \coloneqq \frac{1}{R}$, where $R \coloneqq \frac{U_j}{U_\infty}$ is the jet-to-crossflow velocity ratio, and that the flowfield distortions caused by the crossflow have

the following azimuthal dependencies in the limit that $z > 1/3$ to avoid effects caused by proximity to the jet exit:

$$\bar{u}_z \coloneqq U_0(r) + \lambda^2 U_2(r)\cos(2\theta) \tag{4.21a}$$

$$\bar{u}_r \coloneqq \lambda V_1(r)\cos(\theta) + \lambda^2 V_2(r)\cos(2\theta) \tag{4.21b}$$

$$\bar{u}_\theta \coloneqq \lambda W_1(r)\sin(\theta) + \lambda^2 W_2(r)\sin(2\theta) \tag{4.21c}$$

where

$$U_0 = \begin{cases} 1, & \text{if } r > 1 \\ 0, & \text{if } r < 1 \end{cases} \qquad U_2 = \begin{cases} -\,r^2, & \text{if } r > 1 \\ r^{-2}, & \text{if } r < 1 \end{cases} \tag{4.22}$$

$$V_1 = \begin{cases} 0, & \text{if } r > 1 \\ 1 - r^{-2}, & \text{if } r < 1 \end{cases} \qquad V_2 = \begin{cases} 2(C_2 - z)\ r, & \text{if } r > 1 \\ 2(C_2 - z)\ r^{-3}, & \text{if } r < 1 \end{cases} \tag{4.23}$$

$$W_1 = \begin{cases} 0, & \text{if } r > 1 \\ -(1 + r^{-2}), & \text{if } r < 1 \end{cases} \qquad W_2 = \begin{cases} 2(z - C_2)\ r, & \text{if } r > 1 \\ 2(C_2 - z)\ r^{-3}, & \text{if } r < 1 \end{cases} \tag{4.24}$$

where z is the non-dimensionalised axial coordinate and r is the non-dimensionalised radial coordinate. Note that the $\mathcal{O}(\lambda)$ base flow is identical to that of potential flow around a two-dimensional cylinder. The $\mathcal{O}(\lambda^2)$ base flow introduces a symmetric hyperboloid-like non-uniformity in the jet flow that distorts the vortex sheet trajectory. C_2 is found to satisfy the following systems of linear equations:

$$C_2 = \lim_{N\to\infty} \sum_{n=1}^{N} B_n\ J_2(\tau_n) \tag{4.25a}$$

$$\lim_{N\to\infty} \sum_{n=1}^{N} \frac{B_n \tau_n\ J_2(\tau_n)}{(\sigma_m - \tau_n)} = -\frac{1}{\sigma_m} \tag{4.25b}$$

N	C_2
30	-0.212813316470310
100	-0.216379953683426
200	-0.217164541049491
300	-0.217427715406723
500	-0.217638852402732
1000	-0.217797555238058

Table 4.6: Values of C_2 for various values of N.

where J_2 is the Bessel function of the first kind at second order, τ_n and σ_n are the n$^{\text{th}}$ roots of J_2 and J_2', respectively, and A_n, B_n, and C_n are real scalar coefficients used to define the inviscid base flow of Coelho & Hunt (1989). To calculate C_2, they fixed the number of terms in the summation series N to be 100 after having determined negligible variation of B_n beyond 100 terms and fixed the maximum value of m to be N. Coelho & Hunt (1989) calculate that $C_2 = -0.2164$ within their accepted degree of accuracy and use that value throughout their analysis. They note that they could not prove that Eqs. 4.25 was convergent but did graphically demonstrate that an upper bound of $1/n^2$ exists.

More accurate calculations of C_2 are tabulated in Table 4.6. τ_n and σ_n were obtained via the secant method with a tolerance of 10^{-12}. The system of linear equations described by Eq. (4.25b) is solved via LU-decomposition in `MATLAB`. For consistency and to enable better comparison with the results of Alves *et al.* (2008) and Alves & Kelly (2008), the value $C_2 = -0.2164$ was selected.

4.4.1 Hyperbolic-tangent jet-in-crossflow base flow model

The question is now: How do we extend the inviscid base flow as defined in Eqs. (4.21) and (4.24) to now exhibit a jet velocity field that has an associated boundary layer as well as a boundary layer caused by the crossflow shearing around the jet core?

Using the same base flow expansion as Coelho & Hunt (1989), Alves *et al.* (2008) assumes the unperturbed jet can be approximated by a hyperbolic-tangent axial velocity profile as in Eq.(4.26a). This profile has been used by Michalke (1984) and Morris (1976), for example, to model viscous axisymmetric jets. It should be noted that the hyperbolic-tangent velocity profile of Eq. (4.26a) compares favourably with the experimentally-measured velocities obtained by Crow & Champagne (1971) around two diameters downstream of the jet exit. Crighton & Gaster (1976) suggest that the hyperbolic-tangent profile should be valid for modelling axisymmetric free jets up to six diameters downstream, beyond which the fully-developed jet velocity profile is more appropriate.

The remaining terms of Eq. (4.21) are determined from the constraints of (i) mass conservation at all orders of λ, (ii) the asymptotic limiting base flow defined in Eqs. (4.24), and (iii) the use of the hyperbolic-tangent profile of Eq.(4.26a) as a generalised smoothing function for the superposition of the inviscid velocity profiles of Coelho & Hunt (1989). It is important the note that this ad-hoc viscous base flow, shown in Eqs. (4.26) does not necessarily satisfy the momentum conservation equations, but is guaranteed to satisfy the mass conservation equation by definition.

$$U_0(r) \coloneqq \frac{1}{2}\left\{1 - \tanh\left[\frac{1}{4\theta_0}\left(r - \frac{1}{r}\right)\right]\right\} \tag{4.26a}$$

$$U_2(r) \coloneqq U_0(r)(-\,r^2) + (1 - U_0(r))\; r^{-2} \tag{4.26b}$$

$$W_1(r) \coloneqq (1 - U_0(r))\;(1 + r^{-2}) \tag{4.26c}$$

$$V_1(r) \coloneqq \frac{1}{2r}\left((1 + r_0 r)\left(\frac{1}{r_0} - \frac{1}{r}\right) + 4\theta_0 \log\left[\cosh\left(\frac{r^2 - 1}{4r\theta_0}\right) / \cosh\left(\frac{r_0^2 - 1}{4r_0\theta_0}\right)\right]\right) \tag{4.26d}$$

$$V_2(r) \coloneqq 2(C_2 - z_0)(rU_0(r) + (1 - U_0(r))\ r^{-3}) \tag{4.26e}$$

$$W_2(r) \coloneqq 2(C_2 - z_0)\left[-\ r^{-3} + (r + r^{-3})U_0(r) + \frac{1}{2}(r - r^{-2})\frac{\mathrm{d}U_0}{\mathrm{d}r} \right] \tag{4.26f}$$

where θ_0 is the non-dimensionalised local momentum thickness for the free jet in the absence of any crossflow and r is the non-dimensionalised radial coordinate. Additionally, $0 < r_0 \ll 1$ is the lower limit of the integration domain in r and z_0 represents the axial station of the base flow. z_0 is be related to the free jet-equivalent local momentum thickness θ_0 by the empirical correlation established by Crighton & Gaster (1976) that is valid for axisymmetric free jets.

$$\theta_0 = \frac{3}{100}\left(z_0 + \frac{4}{3}\right) \tag{4.27}$$

For visualisation and future verification purposes, Figures 4.6 display radial slices of the hyperbolic-tangent base flow for $\theta_0/R_0 = 1/10, 1/15, 1/20$. Contour plots of the axial and streamwise base flow velocity field for $R = 5$, $\lambda = 1/5$, $\theta_0/R_0 = 1/15$ are displayed in Figure 4.7. All velocities have been non-dimensionalised with respect to the peak axial velocity at the centreline.

The integrated upstream shear layer momentum thickness of the hyperbolic-tangent jet-in-crossflow at $z = 1$ is shown in Fig. (4.12a) for various jet-to-crossflow velocity ratios R and for several free jet-equivalent momentum thicknesses. By observation, the hyperbolic-tangent base flow becomes increasingly thick as R decreases, motivating the need to consider a range of momentum thicknesses to better match experimental conditions.

4.4.2 Uniformly valid asymptotic solution (UVAS)

The hyperbolic-tangent-based model for the viscous jet-in-crossflow is limited in that it does not generally satisfy conservation of momentum and the viscous shear layer is modelled by a hyperbolic-tangent function. Therefore, Alves & Kelly (2008) solved the asymptotically-expanded steady incompressible Navier-Stokes equations subject to the azimuthal form and

far-field conditions as implied by Coelho & Hunt (1989). Moreover, the viscous shear layer was assumed to be asymptotically small so as to enable the transformation to boundary layer-type equations and therefore allows a similarity solution to be found. The resultant boundary layer was merged with the far-field inviscid solution of Coelho & Hunt (1989) via the method of matched asymptotic expansions (see Van Dyke (1964)).

Specifically, the solution to the steady and incompressible Navier-Stokes equations was stipulated to be:

$$\bar{u}_z \coloneqq U_0(z,r) + \lambda U_1(z,r,\theta) + \lambda^2 U_2(z,r,\theta) \tag{4.28a}$$

$$\bar{u}_r \coloneqq V_0(z,r) + \lambda V_1(z,r,\theta) + \lambda^2 V_2(z,r,\theta) \tag{4.28b}$$

$$\bar{u}_\theta \coloneqq \quad + \lambda W_1(z,r,\theta) + \lambda^2 W_2(z,r,\theta) \tag{4.28c}$$

$$\bar{p} \coloneqq P_0(z,r) + \lambda P_1(z,r,\theta) + \lambda^2 P_2(z,r,\theta) \tag{4.28d}$$

It is significant to observe that $U_1(z,r,\theta) = 0$ in Coelho & Hunt (1989), whereas it is permitted to be nonzero in the UVAS base flow solution. Additionally, $W_0 \coloneqq 0$ as the solution at $\mathcal{O}(\lambda^0)$ should correspond to that of a viscous axisymmetric free jet and therefore should not have any azimuthal velocity.

The shear layer of the jet δ is assumed to be thin ($\delta \ll 1$) so as to allow further Taylor series expansions. Additionally, the governing equation are recast so that the shear layer lies at $r = 1 \coloneqq \tilde{r} = 0$ using the following transformation:

$$r = 1 + \delta\tilde{r} \tag{4.29}$$

where

$$\delta \coloneqq \mathrm{Re}^{-1/2} = U_j R_0/\nu_j \tag{4.30}$$

just as in the derivation for the Prandtl boundary layer equations. Indeed, the base flow components are at each order of λ are additionally expanded in terms of δ. Note that the $\mathcal{O}(\lambda^0)$ solution physically corresponds to the viscous axisymmetric jet flow in the absence of crossflow and therefore the governing equations at $\mathcal{O}(\lambda^0)$ were constrained with $\partial/\partial\theta = 0$.

$$U_0(z,r) \coloneqq \tilde{U}_0^0(z,\tilde{r}) + \delta\tilde{U}_0^1(z,\tilde{r}) + \mathcal{O}(\delta^2) \tag{4.31a}$$

$$V_0(z,r) \coloneqq \tilde{V}_0^0(z,\tilde{r}) + \delta\tilde{V}_0^1(z,\tilde{r}) + \delta^2\tilde{V}_0^2(z,\tilde{r}) + \mathcal{O}(\delta^3) \tag{4.31b}$$

$$V_1(z,r) \coloneqq \tilde{V}_1^0(z,\tilde{r}) + \delta\tilde{V}_1^1(z,\tilde{r}) + \mathcal{O}(\delta^2) \tag{4.31c}$$

$$W_1(z,r) \coloneqq \tilde{W}_1^0(z,\tilde{r},\theta) + \delta\tilde{W}_1^1(z,\tilde{r},\theta) + \mathcal{O}(\delta^2) \tag{4.31d}$$

where $\tilde{V}_0^0 = \tilde{V}_1^0 = 0$ to satisfy conservation of mass. Note that U_1 was not expanded in terms of δ.

After having inserted the asymptotic expansions in terms of λ and δ (defined by Eqs. (4.28) and (4.31), respectively) in the steady Navier-Stokes equations, terms with the same order of both λ and δ are collected up to $\mathcal{O}(\delta^1)$ and $\mathcal{O}(\lambda^1)$. These equations, with the far field boundary conditions implied by the Coelho & Hunt solution, lead to the following governing equations.

At $\mathcal{O}(\lambda^0\delta^0)$:

$$\frac{\partial\tilde{U}_0^0}{\partial z} + \frac{\partial\tilde{V}_0^1}{\partial\tilde{r}} = 0 \tag{4.32a}$$

$$\tilde{U}_0^0\frac{\partial\tilde{U}_0^0}{\partial z} + \tilde{V}_0^1\frac{\partial\tilde{U}_0^0}{\partial\tilde{r}} = \frac{\partial^2\tilde{U}_0^0}{\partial\tilde{r}^2} \tag{4.32b}$$

subject to the boundary conditions:

$$\lim_{\tilde{r}\to-\infty}\tilde{U}_0^0 = 1 \quad \text{and} \quad \lim_{\tilde{r}\to\infty}\tilde{U}_0^0 = 0 \tag{4.33}$$

This corresponds to the governing equations and boundary conditions of the planar mixing layer. As a result, $\tilde{U}_0^1 = \tilde{V}_0^2 = 0$. Therefore, the $\mathcal{O}(\lambda^0\delta^1)$ governing equations are ignored.

At $\mathcal{O}(\lambda^1\delta^0)$:

$$\frac{\partial \tilde{U}_1}{\partial z} + \frac{\partial \tilde{V}_1^1}{\partial \tilde{r}} + \frac{\partial \tilde{W}_1^0}{\partial \theta} = 0 \tag{4.34a}$$

$$\tilde{U}_0^0 \frac{\partial \tilde{U}_1}{\partial z} + \tilde{U}_1 \frac{\partial \tilde{U}_0^0}{\partial z} + \tilde{V}_0^1 \frac{\partial \tilde{U}_1}{\partial \tilde{r}} + \tilde{V}_1^1 \frac{\partial \tilde{U}_0^0}{\partial \tilde{r}} = \frac{\partial^2 \tilde{U}_1}{\partial \tilde{r}^2} \tag{4.34b}$$

$$\tilde{U}_0^0 \frac{\partial \tilde{W}_1^0}{\partial z} + \tilde{V}_0^1 \frac{\partial \tilde{W}_1^0}{\partial \tilde{r}} = \frac{\partial^2 \tilde{W}_1^0}{\partial \tilde{r}^2} \tag{4.34c}$$

subject to the boundary conditions

$$\lim_{\tilde{r}\to-\infty} \tilde{U}_1 = 0 \text{ and } \lim_{\tilde{r}\to\infty} \tilde{U}_1 = 0 \tag{4.35a}$$

$$\lim_{\tilde{r}\to-\infty} \tilde{V}_1^1 = 0 \text{ and } \lim_{\tilde{r}\to\infty} \tilde{V}_1^1 = 2\tilde{r}\cos\theta \tag{4.35b}$$

$$\lim_{\tilde{r}\to-\infty} \tilde{W}_1^0 = 0 \text{ and } \lim_{\tilde{r}\to\infty} \tilde{W}_1^1 = -2\sin\theta \tag{4.35c}$$

At $\mathcal{O}(\lambda^1\delta^1)$, only the azimuthal momentum equation is necessary to solve for $\tilde{W}_1^1$.

$$\tilde{U}_0^0 \frac{\partial \tilde{W}_1^1}{\partial z} + \tilde{V}_0^1 \frac{\partial \tilde{W}_1^1}{\partial \tilde{r}} + \tilde{V}_0^1 \tilde{W}_1^0 = \frac{\partial^2 \tilde{W}_1^1}{\partial \tilde{r}^2} + \frac{\tilde{W}_1^0}{\partial \tilde{r}} \tag{4.36}$$

subject to the boundary conditions

$$\lim_{r\to\tilde{-}\infty} \tilde{W}_1^1 = 0 \text{ and } \lim_{r\to\tilde{+}\infty} \tilde{W}_1^1 = 2\tilde{r}\sin\theta \tag{4.37}$$

Note that the asymptotic expansions in terms of λ and δ (defined by Eqs. (4.28) and (4.31), respectively) in the steady Navier-Stokes equations lead to the result that $\partial P_0/\partial \tilde{r}$, $\partial P_1/\partial \tilde{r} \sim \mathcal{O}(\delta^2)$ and $\partial P_0/\partial z = P_1 = 0$.

In order to solve the governing equations of Eqs. (4.32), (4.34), and (4.36) with a similarity solution, the similarity variable was defined as:

$$\eta \coloneqq (r-1)\sqrt{\frac{\mathrm{Re}}{z}} = \frac{\tilde{r}}{z} \tag{4.38}$$

Similarity functions $f_0(\eta)$, $f_1(\eta)$, $g_1^0(\eta)$, $g_1^1(\eta)$, and $h_1(\eta)$ were defined as:

$$\tilde{U}_0^0 \coloneqq \frac{df_0}{d\eta} \text{ and } \tilde{V}_0^1 \coloneqq \frac{1}{2\sqrt{z}}\left(\eta\frac{df_0}{d\eta} - f_0\right) \tag{4.39a}$$

$$\tilde{W}_1^0 = -2\ \sin\theta\ g_1^0(\eta) \tag{4.39b}$$

$$\tilde{V}_1^1 = 2\ \sqrt{z}\ \cos\theta\ h_1(\eta) \tag{4.39c}$$

$$\tilde{U}_1 = 2\ z\ \cos\theta\ f_1(\eta) \tag{4.39d}$$

$$\tilde{W}_1^1 = 2\ \sqrt{z}\ \sin\theta\ g_1^1(\eta) \tag{4.39e}$$

The similarity variables defined in Eqs. (4.39) were inserted into governing equations Eqs. (4.32), (4.34), (4.37) , and (4.36) to re-derive the ordinary differential equations at each order of λ and δ. Particular attention was paid on re-deriving the asymptotic boundary conditions from Eqs. (4.33), (4.35), and (4.37) into similarity form.

At $\mathcal{O}(\lambda^0\delta^0)$:

$$2f_0''' + f_0 f_0'' = 0 \tag{4.40}$$

subject to the asymptotic boundary conditions:

$$\begin{aligned} f_0^{\eta\to-\infty} =& a_1 + \eta + a_2 \exp\left(-\frac{\eta(2a_1+\eta)}{4}\right) \\ &\times\left\{2 + \sqrt{\pi}\exp\left[\frac{(a_1+\eta)^2}{4}\right](a_1+\eta)\left(1+\mathrm{erf}\left[\frac{a_1+\eta}{2}\right]\right)\right\} \end{aligned} \tag{4.41a}$$

$$f_0^{\eta\to+\infty} = a_3 + 4\frac{a_4}{a_3^2}\exp\left(-\frac{a_3\eta}{2}\right) \tag{4.41b}$$

At $\mathcal{O}(\lambda^1\delta^0)$:

The azimuthal velocity term can be solved separately as follows:

$$2g_1^{0\,\prime\prime} + f_0 g_1^{0\,\prime} = 0 \tag{4.42}$$

subject to the asymptotic boundary conditions:

$$g_1^{0,\ \eta\to-\infty} = b_1\sqrt{\pi}\exp\left(\frac{a_1^2}{4}\right)\left[1+\operatorname{erf}\left(\frac{a_1+\eta}{2}\right)\right] \tag{4.43a}$$

$$g_1^{0,\ \eta\to+\infty} = 1 - 2\frac{b_2}{a_3}\exp\left(-\frac{a_3\eta}{2}\right) \tag{4.43b}$$

The remaining axial and radial velocity components at this order must be solved through a coupled system of ordinary differential equations:

$$f_1'' + \frac{1}{2}f_0 f_1' - \left(f_0' - \frac{1}{2}\eta f_0''\right)f_1 - f_0'' h_1 = 0 \tag{4.44a}$$

$$h_1' - \frac{1}{2}\eta f_1' + f_1 = g_1^0 \tag{4.44b}$$

subject to the asymptotic boundary conditions:

$$\begin{aligned} f_1^{\eta\to-\infty} =& \frac{b_3}{16}\exp\left(-\frac{\eta(2a_1+\eta)}{4}\right)\Bigg\{-2(a_1+\eta) \\ &+\sqrt{\pi}\exp\left[\frac{(a_1+\eta)^2}{4}\right](2+(a_1+\eta)^2)\left[-2+\operatorname{erfc}\left(\frac{a_1+\eta}{2}\right)\right]\Bigg\} \end{aligned} \tag{4.45a}$$

$$h_1^{\eta\to-\infty} = b_4 \tag{4.45b}$$

$$f_1^{\eta\to+\infty} = 2\frac{b_5}{a_3}\exp\left(-\frac{a_3\eta}{2}\right) \tag{4.45c}$$

$$h_1^{\eta\to+\infty} = \eta - b_6 \tag{4.45d}$$

It is important to note that the asymptotic boundary condition for f_1 as $\eta \to -\infty$, $f_1^{\eta\to-\infty}$, differs from that in Alves (2006) due to a transcription error. As a result, the definition as well as final numerical value of the unknown constant b_3 is different in the present study compared to that of Alves (2006). This difference was discovered after having re-derived the analytical asymptotic boundary condition using `Mathematica`.

At $\mathcal{O}(\lambda^1\delta^1)$:

The azimuthal velocity component is determined by the governing equation:

$$2g_1^{1,\,\prime\prime} + f_0 g_1^{1,\prime} - f_0' g_1^1 = (f_0 - \eta f_0')g_1^0 + 2g_1^{0,\,\prime} \tag{4.46}$$

subject to the asymptotic boundary conditions:

$$\begin{aligned} g_1^{1,\,\eta\to-\infty} =& \frac{b_7}{2}\Bigg\{ -2\ \exp\left[-\frac{\eta(2a_1+\eta)}{4}\right] \\ &+ \sqrt{\pi}\left[\exp\left(\frac{a_1^2}{4}\right)\right](a_1+\eta)\left[-2+\operatorname{erfc}\left(\frac{a_1+\eta}{2}\right)\right]\Bigg\} \end{aligned} \tag{4.47a}$$

$$g_1^{1,\,\eta\to+\infty} = \eta - 2\frac{b_8}{a_3}\exp\left(-\frac{a_3\eta}{2}\right) \tag{4.47b}$$

It is important to note that the asymptotic boundary condition for g_1^1 as $\eta \to -\infty$, $g_1^{1,\,\eta\to-\infty}$, differs from that in Alves (2006) due to a transcription error. As a result, the definition as well as final numerical value of the unknown constant b_7 is different in the present study compared to that of Alves (2006). This difference was unearthed after having

re-derived the analytical asymptotic boundary condition using `Mathematica`. It was found that the asymptotic boundary condition for g_1^1 as $\eta \to -\infty$ stated by Alves (2006) did not satisfy the governing equation Eq. (4.46).

The two-sided boundary value problems established by the ordinary differential equations outlined in Eqs. (4.40) (4.42), (4.44), and (4.46) were considered as two initial value problems wrapped within a root-finding framework for the unknown constants. The ostensibly infinite analytical domain was truncated to lie within $-9 \leq \eta \leq 36$ as the numerical domain to be consistent with Alves & Kelly (2008). The asymptotic boundary conditions were initialised with a guess for the unknown constants using symbolic arithmetic to avoid catastrophic cancellation from the use of floating-point arithmetic (Goldberg, 1991). This was particularly important to solve for $f_1^{\eta \to -\infty}$. The ODEs were then integrated from both extents of the domain to terminate at $\eta = 0$ using adaptive step-size Runge-Kutta schemes of at least fourth-order accuracy with a tolerance of $\sim 10^{-14}$ to be two orders of magnitude above machine precision to avoid round-off errors (Press *et al.*, 2007). Broyden's method (Broyden, 1965) was used to optimise the values of the constants until the mismatch between the similarity variables and their derivatives integrated from the two domain limits at $\eta = 0$ was minimised. The case of obtaining f_0 was unique in that the cost function instead incorporated the boundary condition of $f(0) = 0$. Note that $b_4 \coloneqq 0$ on physical grounds and therefore did not need to be solved for (Alves, 2006). This solution procedure was performed in both `MATLAB` and `Mathematica` and yielded the same results.

The governing equations were solved sequentially from the lowest orders of λ, δ with high resolution to be used as the basis for linear interpolation to solve the equations at higher orders of λ, δ. Table 4.7 tabulates the values of the constants compared against those used by Alves & Kelly (2008). The computed values compare favourably against those of Alves & Kelly (2008) except for b_3 and b_7, which are defined differently in Eqs. (4.45a) and (4.47a) compared to Alves (2006), due to the differences in the associated asymptotic boundary conditions (Eqs. (4.45a) and (4.47a), respectively). The values of the constants are reported

Constant	Alves value	present value
a_1	0.52886	0.52886332493764
a_2	-0.15375	-0.15374862197005
a_3	1.2385	1.23849432823400
a_4	-0.62633	-0.62632669210705
b_1	0.15375	0.153748621994112
b_2	0.62633	0.626326667296181
b_3	151.74	-0.65884306448
b_4	0	0
b_5	312.18	313.464874761
b_6	4.5029	4.50290267099
b_7	0.17100	5.88069
b_8	0.66945	0.669448

Table 4.7: Asymptotic boundary condition constants for the UVAS base flow compared.

with the number of significant figures that were converged. The higher order equations in λ and δ could not be converged to the same degree of accuracy as the lower order equations despite using higher-order polynomial and spline interpolation schemes.

To visualise these similarity solutions as well as verify their accuracy, they were plotted in Figure 4.8. By inspection, there is excellent correspondence between the present results and those of Alves & Kelly (2008). Additionally, f_0 and f_0' corresponded to the solution of a planar mixing layer and thus could be also compared against Lock (1951).

Finally, the viscous boundary layer solution obtained thus far is merged with the inviscid far-field solution of Coelho & Hunt (1989) by the method of matched asymptotic expansions to produce the 'uniformly valid asymptotic solution' base flow. U_0 and U_1 were not corrected because they intrinsically matched the inviscid far-field behaviour. However, V_1 and W_1 were

corrected in the following manner:

$$V_1(\eta) \coloneqq V_1^{\text{inv}}(\eta) + V_1^{\text{bl}}(\eta - b_6) + V_1^{\text{cor}}(\eta) \tag{4.48a}$$

$$W_1(\eta) \coloneqq W_1^{\text{inv}}(\eta) + W_1^{\text{bl}}(\eta) + W_1^{\text{cor}}(\eta) \tag{4.48b}$$

where the 'inv' superscript indicates the inviscid solution of Coelho & Hunt (1989) defined in Eqs. (4.24), the 'bl' superscript indicates the boundary layer solution described in Eqs. (4.28) - (4.47), and the 'cor' superscript indicates the correction terms needed for the method of matched asymptotic solutions defined in Eq. (4.49). It is important that the boundary layer solution for V_1 must be translated inboard to account for the displacement of the reference planar mixing layer streamline Lock (1951). As a result, U_1 must also be translated inboard by b_6.

$$V_1^{\text{cor}} \coloneqq \cos(\theta) \begin{cases} 0, & \text{if } \; r < 1 \\ -2(r-1), & \text{if } r > 1 \end{cases} \tag{4.49a}$$

$$W_1^{\text{cor}} \coloneqq \sin(\theta) \begin{cases} 0, & \text{if } \; r < 1 \\ 2 - 2(r-1), & \text{if } r > 1 \end{cases} \tag{4.49b}$$

Therefore, the overall UVAS base flow can be described most compactly as:

$$U \coloneqq f_0'(\eta) + \lambda[2z\cos(\theta) f_1(\eta - b_6)] \tag{4.50a}$$

$$V \coloneqq \lambda[V_1^{\text{inv}}(r)\cos(\theta) + 2\sqrt{z}\cos(\theta) h_1(\eta - b_6) + V_1^{\text{cor}}(r,\theta)] \tag{4.50b}$$

$$W \coloneqq \lambda\Big[W_1^{\text{inv}}(r)\sin(\theta) + \Big(-2\sin(\theta) g_1^0(\eta) + \delta 2\sqrt{z}\sin(\theta) g_1^1(\eta)\Big) + W_1^{cor}(r,\theta)\Big] \tag{4.50c}$$

Generally, the momentum thickness of the UVAS base flow is established implicitly by setting the Reynolds number Re defined in Eq. (4.30). Table 3.1 of Alves (2006) tabulates a correlation between Reynolds number and momentum thickness for a UVAS base flow located one radius downstream of the jet exit obtained from a free jet equivalency.

To visualise the UVAS base flow as well as verify their accuracy, they were plotted in Figure 4.9. By inspection, there is excellent correspondence between the present results and those of Alves & Kelly (2008). Contour plots of the axial and streamwise base flow velocity field for $R = 5$, $\lambda = 1/5$, $\theta_0/R_0 = 1/15$ are displayed in Figure 4.10. Note that there is a small localised region of counterflow near the upstream shear layer without a recirculation region in the wake of the jet.

Additionally, the integrated upstream shear layer momentum thickness of the UVAS jet-in-crossflow at $z = 1$ is shown in Fig. 4.12b for various jet-to-crossflow velocity ratios R and for several free jet-equivalent momentum thicknesses. By observation, the UVAS base flow remains approximately the same momentum thickness as R decreases, unlike the hyperbolic-tangent base flow. There is a complex interplay between the prescribed momentum thickness, prescribed downstream location of the base flow, and the R value necessary to best match experimental measurements.

4.4.3 Verification of base flows

Finally, to visualise the hyperbolic-tangent and UVAS base flows as well as verify their accuracy, they were plotted in Figure 4.11 with the correspondence velocity profiles obtained the DNS described in the PhD thesis of Alves (2006). By inspection, there is excellent correspondence between the present results and those of Alves (2006). A comparison of the streamwise velocity component of the tanh and UVAS base flows against the experimental measurements of Harris *et al.* (2021) is presented in Figure 4.13. Note that, for better comparison, the velocity has been normalised by the maximum axial velocity, which may not lie at the origin.

4.5 Numerical eigenproblem solver methodology in 2D

The discretised governing equations with embedded boundary conditions built using a matrix forming approach. That is to say, the matrices associated with the generalised eigenproblem $Ax = kBx$ were formed and saved in memory explicitly in sparse form. The eigenproblem was iteratively solved using a shift-and-invert Krylov-Schur algorithm of Stewart (2002) with a convergence tolerance of 10^{-14}. One code was written in `MATLAB` and implicitly used the ARPACK toolbox to solve the eigenproblem (R. B. Lehoucq & Yang, 1998). This implementation is multi-threaded but was found to be not amenable to multi-node operation on a high-performance computer. Hence, another code was written using to leverage the PETSc (Balay *et al.*, 2023) and SLEPc (Hernandez *et al.*, 2005) libraries via the Python wrappers PETSc4py (Dalcin *et al.*, 2011) and SLEPc4py for using on the shared high-performance computing resources of Hoffman2 at UCLA. A small note is that balancing the generalised eigenproblem was performed through the SLEPc implementation in order to reduce the condition number and hence improve the accuracy of the eigenproblem. The non-physical oscillations were insensitive to this balancing and the eigenvalues changed negligibly. Therefore, the eigenproblem was not numerically balanced. This insensitivity may be because the B matrix is inherently singular.

4.5.1 Data-driven eigenmode classification

Unlike one-dimensional linear stability analysis, the present two-dimensional linear stability analyses yield the entire eigenspectrum simultaneously because there are no simplifying symmetry conditions that constrain the resulting eigensolutions. The various eigenvalues can have similar values in the complex domain, meaning that a simple polynomial extrapolation method to identify eigenmodes is not possible. Additionally, the eigenspectrum can be contaminated by spurious (non-physical) solutions that are highly sensitive to changes in numerical settings such as the mesh, the discretisation, or the solver. To obviate any manual

classification, a convolutional neural network (CNN) (Goodfellow *et al.* (2016); Bishop & Nasrabadi (2006)) was trained on manually-tagged jet-in-crossflow eigenfunctions to classify eigenfunctions as axisymmetric, first (anti-) symmetric helical, second (anti-) symmetric helical, third (anti-) symmetric helical, or spurious eigenmodes.

A convolutional neural network is an example of supervised learning, a machine learning paradigm where a dataset consisting of labelled input-output pairs is used to train a model that best infers the underlying correlation that converts input to output. k-nearest-neighbours, linear discriminant analysis, and support vector machines are additional examples of supervised learning algorithms (Hastie *et al.*, 2009). Trigonometric regression of data in the azimuthal direction was inadequate owing to the non-negligible distortion of the eigenfunctions caused by the crossflow, particularly at low R values.

A convolutional neural network was selected because (i) interpretability of the model/results was unnecessary, (ii) CNNs are can manage spatio-temporally correlated and contiguous high-dimensional data, and (iii) CNNs can tolerate nonlinear and possibly noisy data. From a numerical perspective, the convolutional neural network is well-known to be relatively parsimonious on memory, is time efficient, and highly accurate for image classification tasks.

To obtain the lowest feature dimension possible (as constrained by the curse of dimensionality (Hastie *et al.*, 2009)), to minimise the amount of training data needed, and to ensure that trained CNN could be agnostic to the choice of polar or Cartesian coordinate formulations, the velocity eigenfunctions were neglected in the training of the CNN. Further data compression was obtained by using only the absolute value of the pressure eigenfunction lying on a circle centred at the origin with a radius of unity. This is justified by the mathematical constraint that the eigenfunctions depend on the azimuthal direction θ as $\exp(im\theta)$ in the limit of $\lambda \to 0$, where m represents the azimuthal mode number. Owing to the symmetry-breaking distortion introduced by the crossflow, the resultant eigenfunctions are heavily influenced the $\exp(im\theta)$ relationship but do not exactly follow it. To ensure that the trained CNN classifier could be agnostic to the mesh used in the linear stability

analysis, the pressure eigenfunctions were interpolated in two dimensions ((x, y) or (r, θ)) by cubic splines with not-a-knot endpoint treatments (de Boor, 1978) onto a circle centred at the origin with a radius of unity discretised over 200 azimuthal locations $\theta \in (0, \pi)$. The relatively high value of 200 was selected to clearly avoid the Nyquist limit associated with even high azimuthal mode number physical eigenmode while remaining sensitive to the features associated with non-physical eigenfunctions, such as sawtooth oscillations. This yields a set of labelled training data where the input $\mathbf{x} \in \mathbb{R}^{200}$ is the interpolated pressure eigenfunction arranged as a vector and the output $y \in \mathbb{Z}$ is the associated azimuthal 'mode' of the eigenfunction (such as axisymmetric, first (anti-) symmetrical helical, or spurious) represented by discrete categories. The input x was mean-subtracted and L^∞-normalised such that the maximum absolute value of x was unity.

For a particular value of the momentum thickness, θ_0/R_0, a fully-connected convolutional neural network architecture was selected to accept an input $\mathbf{x} \in \mathbb{R}^{200}$, to a hidden two-dimensional convolution layer of size 10×8, then to a second hidden two-dimensional convolutional layer of size 20×16, and then to a final classification layer. Both hidden layers contained a batch normalisation step and a ReLU nonlinear activation function (Agarap, 2018). A softmax layer preceded the classification layer to obtain probabilities. The Adam optimiser (adaptive moment estimator by Kingma & Ba (2014)) was employed to obtain the gradients of the weights with respect to the overall L^2 cost function, while backpropagation was used to update the CNN weights. An initial learning rate of 10^{-3} was set and the network was trained for up to 35 epochs.

To provide coordinate system-independence, both the $\theta_0/R_0 = 1/10$ and $\theta_0 = 1/15$ scenarios contained processed data obtained from the Cartesian and polar linear stability analysis. There were 2014 and 2040 total data points to train the $\theta_0/R_0 = 1/10$ and $\theta_0 = 1/15$ CNNs, respectively.

The prediction accuracy of the CNN model as well as its generalisability can depend on the choice of the data used to train the model (Goodfellow *et al.*, 2016). Stratified K-fold

K	$\epsilon_{\theta_0/R_0=1/10}$	$\epsilon_{\theta_0/R_0=1/15}$
5	99.7%	99.95%
10	99.8%	99.90%
20	99.8%	99.95%
N	N/A	100%

Table 4.8: Stratified K-fold cross-validation accuracy for different values of N as applied to the UVAS JICF with momentum thicknesses $\theta_0/R_0 = 1/10$ and $1/15$.

cross-validation, with K set to be $5, 10, 20$, was used to select a model, more accurately estimate the prediction error associated with the CNN, to minimise the testing variance, and to avoid any overly-optimistic prediction bias causing overfitting. This was done by randomly subdividing the total training data available into K non-overlapping cross-validation folds, then training a CNN with all data except that belonging to one fold, and quantifying the prediction error by testing the CNN with unseen data from the fold not used in the training. Stratification ensured that the training and the testing datasets in each fold contained approximately evenly-distributed data from each class as in the original dataset. This process was repeated for all K folds and then averaged to yield an overall cross-validation prediction error. As the maximum number of epochs was selected such that the learning rate would stagnate, the model with the highest prediction accuracy trained on one of the $K = 5$ folds was selected to act as the eigenmode classifier. $K = 5$ is a commonly-used value that is known to balance the estimator bias against variance adequately for most applications (Hastie *et al.*, 2009; Goodfellow *et al.*, 2016). The limiting case of when $K = N$ (known as leave-one-out cross validation), the number of training data available, was also performed once for the UVAS JICF with a momentum thickness of $\theta_0/R_0 = 1/15$ owing to the computational expense. Table 4.8 enumerates the average cross-validation error ϵ for each of the K and θ_0/R_0 values considered.

4.6 The asymptotic inviscid linear stability analysis of Alves

Given that the tanh and UVAS base flows were both asymptotically expanded in terms of λ, the linear stability analysis of Alves *et al.* (2008) and Alves & Kelly (2008) was also expanded in terms of λ. Specifically, the disturbance eigenfunctions (defined in Eqs. (4.2)) were expanded in terms of λ to be:

$$\hat{u}_z(r,\theta) \coloneqq \hat{u}^+_{z,0}(r)\mathrm{e}^{im\theta} + \hat{u}^-_{z,0}(r)\mathrm{e}^{-im\theta} + \lambda\hat{u}_{z,1}(r,\theta) + \lambda^2\hat{u}_{z,2}(r,\theta) \tag{4.51a}$$

$$\hat{u}_r(r,\theta) \coloneqq \hat{u}^+_{r,0}(r)\mathrm{e}^{im\theta} + \hat{u}^-_{r,0}(r)\mathrm{e}^{-im\theta} + \lambda\hat{u}_{r,1}(r,\theta) + \lambda^2\hat{u}_{r,2}(r,\theta) \tag{4.51b}$$

$$\hat{u}_\theta(r,\theta) \coloneqq \hat{u}^+_{\theta,0}(r)\mathrm{e}^{im\theta} + \hat{u}^-_{\theta,0}(r)\mathrm{e}^{-im\theta} + \lambda\hat{u}_{\theta,1}(r,\theta) + \lambda^2\hat{u}_{\theta,2}(r,\theta) \tag{4.51c}$$

$$\hat{p}(r,\theta) \coloneqq \hat{p}^+_0(r)\mathrm{e}^{im\theta} + \hat{p}^-_0(r)\mathrm{e}^{-im\theta} + \lambda\hat{p}_1(r,\theta) + \lambda^2\hat{p}_2(r,\theta) \tag{4.51d}$$

where $m \in \mathbb{Z}$ is the azimuthal mode number.

The complex wavenumber k and frequency ω were also expanded up to $\mathcal{O}(\lambda^2)$:

$$k \coloneqq k_0 + \lambda k_1 + \lambda^2 k_2 \tag{4.52a}$$

$$\omega \coloneqq \omega_0 + \lambda\omega_1 + \lambda^2\omega_2 \tag{4.52b}$$

It is important to remark that the fully-coupled linear stability analysis described in Chapter 4.2 did not perform the expansions of Eqs. (4.51) or (4.52). Rather, the eigenfunctions and eigenvalues could be considered be as the extension of Eqs. (4.51) and (4.52), respectively, over an infinite sum of λ terms.

After having inserted Eqs. (4.51) and (4.52) into the linear stability dispersion relation of Eq. (4.3) and using the expanded base flows defined in Eqs. (4.26) or (4.28), terms of

the same order of λ were collected to form governing equations at order $\mathcal{O}(\lambda^0)$, $\mathcal{O}(\lambda^1)$, and $\mathcal{O}(\lambda^2)$ for specified azimuthal mode numbers m. Higher-order equations in λ were neglected.

At $\mathcal{O}(\lambda^0)$, it was found that

$$\hat{u}^+_{z,0}(r) = \hat{u}^+_{z,0}(r) \coloneqq \hat{u}_{z,0}(r) \tag{4.53a}$$

$$\hat{u}^+_{r,0}(r) = \hat{u}^+_{r,0}(r) \coloneqq \hat{u}_{r,0}(r) \tag{4.53b}$$

$$\hat{u}^+_{\theta,0}(r) = \hat{u}^+_{\theta,0}(r) \coloneqq \hat{u}_{\theta,0}(r) \tag{4.53c}$$

$$\hat{u}^+_{z,0}(r) = \hat{u}^+_{z,0}(r) \coloneqq \hat{u}_{z,0}(r) \tag{4.53d}$$

and the governing equations at $\mathcal{O}(\lambda^0)$ are the same as the axisymmetric free jet.

At $\mathcal{O}(\lambda^1)$, it was found that ω_1 and k_1 were agnostic to the base flow perturbations caused by the crossflow. This is because ω_1 and $k_1 \sim \mathrm{e}^{\pm im\theta}$ whereas the inhomogeneous base flow terms associated with the crossflow at $\mathcal{O}(\lambda^1)$ were orthogonal by $\mathrm{e}^{\pm i\theta}$. As the study was interested exclusively in how the ω_1 and k_1 were affected by the crossflow and it turned out that ω_1 and k_1 were independent of the crossflow, $\omega_1 = k_1 = 0$ for all values of m. In order to obtain the $\mathcal{O}(\lambda^2)$ linear stability equations, the perturbation eigenfunctions were modelled as:

$$\hat{u}_{z,1}(r,\theta) \coloneqq \breve{u}_{z,1}(r)\cos(\theta) \tag{4.54a}$$

$$\hat{u}_{r,1}(r,\theta) \coloneqq \breve{u}_{r,1}(r)\cos(\theta) \tag{4.54b}$$

$$\hat{u}_{\theta,1}(r,\theta) \coloneqq \breve{u}_{\theta,1}(r)\sin(\theta) \tag{4.54c}$$

$$\hat{p}_1(r,\theta) \coloneqq \breve{p}_1(r)\cos(\theta) \tag{4.54d}$$

for the axisymmetric $m = 0$ mode, as

$$\hat{u}_{z,1}(r,\theta) \coloneqq \breve{u}^{0}_{z,1}(r) + \breve{u}^{+2}_{z,1}(r)\mathrm{e}^{2i\theta} + \breve{u}^{-2}_{z,1}(r)\mathrm{e}^{-2i\theta} \tag{4.55a}$$

$$\hat{u}_{r,1}(r,\theta) \coloneqq \breve{u}^{0}_{r,1}(r) + \breve{u}^{+2}_{r,1}(r)\mathrm{e}^{2i\theta} + \breve{u}^{-2}_{z,1}(r)\mathrm{e}^{-2i\theta} \tag{4.55b}$$

$$\hat{u}_{\theta,1}(r,\theta) \coloneqq \breve{u}^{+2}_{\theta,1}(r)\mathrm{e}^{2i\theta} + \breve{u}^{-2}_{\theta,1}(r)\mathrm{e}^{-2i\theta} \tag{4.55c}$$

$$\hat{p}_{1}(r,\theta) \coloneqq \breve{p}^{0}_{1}(r) + \breve{p}^{+2}_{1}(r)\mathrm{e}^{2i\theta} + \breve{p}^{-2}_{1}(r)\mathrm{e}^{-2i\theta} \tag{4.55d}$$

for the first helical $m = \pm 1$ mode, and as

$$\hat{u}_{z,m}(r,\theta) \coloneqq \breve{u}^{\pm m\pm 1}_{z,m}(r)\mathrm{e}^{i(\pm m\pm 1)\theta} \tag{4.56a}$$

$$\hat{u}_{r,m}(r,\theta) \coloneqq \breve{u}^{\pm m\pm 1}_{r,m}(r)\mathrm{e}^{i(\pm m\pm 1)\theta} \tag{4.56b}$$

$$\hat{u}_{\theta,m}(r,\theta) \coloneqq \breve{u}^{\pm m\pm 1}_{\theta,m}(r)\mathrm{e}^{i(\pm m\pm 1)\theta} \tag{4.56c}$$

$$\hat{p}_{m}(r,\theta) \coloneqq \breve{p}^{\pm m\pm 1}_{m}(r)\mathrm{e}^{i(\pm m\pm 1)\theta} \tag{4.56d}$$

for the $|m| > 1$ helical modes. Note that the superscript '$\pm m \pm 1$' indicates that there should a sum over the 4 eigenmodes present: $+m+1$, $+m-1$, $-m+1$, and $-m-1$.

Similarly, the governing equations at $\mathcal{O}(\lambda^2)$ were found to allow crossflow-eigenfunction interaction to influence ω_2, k_2 and so those generally non-zero complex unknowns must be solved for. The linear stability analysis was only expanded to obtain eigenvalues up to $\mathcal{O}(\lambda^2)$ and the θ-dependence of the $\mathcal{O}(\lambda^2)$ eigenfunctions was only necessary to determine the eigenvalues at $\mathcal{O}(\lambda^3)$. Therefore, the eigenfunctions at $\mathcal{O}(\lambda^2)$ were modelled to depend on θ precisely as ω_2 and k_2 depended on θ. For example, the axial and radial velocity and pressure eigenfunctions for the axisymmetric $m = 0$ mode were modelled as θ-independent and the azimuthal mode was modelled to be identically zero owing to its independence to ω_2 and k_2. Generally, the eigenfunctions can be written as:

$$\hat{u}_{z,2}(r,\theta) \coloneqq \breve{u}_{z,2}(r) \tag{4.57a}$$

$$\hat{u}_{r,2}(r,\theta) \coloneqq \breve{u}_{r,2}(r) \tag{4.57b}$$

$$\hat{u}_{\theta,2}(r,\theta) \coloneqq 0 \tag{4.57c}$$

$$\hat{p}_{2}(r,\theta) \coloneqq \breve{p}_{2}(r) \tag{4.57d}$$

for the axisymmetric $m = 0$ mode, as

$$\hat{u}_{z,2}(r,\theta) \coloneqq \breve{u}_{z,2}^{+1}(r)\mathrm{e}^{i\theta} + \breve{u}_{z,2}^{-1}(r)\mathrm{e}^{-i\theta} \tag{4.58a}$$

$$\hat{u}_{r,2}(r,\theta) \coloneqq \breve{u}_{r,2}^{+1}(r)\mathrm{e}^{i\theta} + \breve{u}_{r,2}^{-1}(r)\mathrm{e}^{-i\theta} \tag{4.58b}$$

$$\hat{u}_{\theta,2}(r,\theta) \coloneqq \breve{u}_{\theta,2}^{+1}(r)\mathrm{e}^{i\theta} + \breve{u}_{\theta,2}^{-1}(r)\mathrm{e}^{-i\theta} \tag{4.58c}$$

$$\hat{p}_{2}(r,\theta) \coloneqq \breve{p}_{2}^{+1}(r)\mathrm{e}^{i\theta} + \breve{p}_{2}^{-1}(r)\mathrm{e}^{-i\theta} \tag{4.58d}$$

for the first helical $m = \pm 1$ mode, and as

$$\hat{u}_{z,2}(r,\theta) \coloneqq \breve{u}_{z,2}^{\pm m}(r)\mathrm{e}^{\pm im\theta} \tag{4.59a}$$

$$\hat{u}_{r,2}(r,\theta) \coloneqq \breve{u}_{r,2}^{\pm m}(r)\mathrm{e}^{\pm im\theta} \tag{4.59b}$$

$$\hat{u}_{\theta,2}(r,\theta) \coloneqq \breve{u}_{\theta,2}^{\pm m}(r)\mathrm{e}^{\pm im\theta} \tag{4.59c}$$

$$\hat{p}_{2}(r,\theta) \coloneqq \breve{p}_{2}^{\pm m}(r)\mathrm{e}^{\pm im\theta} \tag{4.59d}$$

for the $|m| > 1$ helical modes. Note that the superscript '$\pm m$' indicates that there should be a sum over the two eigenfunctions present: $+m$ and $-m$.

All of the coupled boundary-value problems at $\mathcal{O}(\lambda^0)$, $\mathcal{O}(\lambda^1)$, and $\mathcal{O}(\lambda^2)$ were synthesised into one pressure disturbance equation at each order of λ_i for a given azimuthal mode number m. These were recast as initial value problems with accompanying asymptotic boundary conditions in the limits of $r \to 0$ and $r \to \infty$. Therefore, the pressure disturbance equations, given an initial guess for the wavenumber k_i at that order of λ, were integrated using iterative schemes from both extremes to meet at $r = 1$. A secant method optimised the value of k_i to ensure the continuity of pressure and its derivatives at $r = 1$. At $\mathcal{O}(\lambda^2)$, the eigenvalues were obtained instead by requiring the homogeneous pressure disturbance $\breve{p}_2(r)$ be orthogonal to the inhomogeneous term of the Hermitian version of the pressure disturbance equation at $\mathcal{O}(\lambda^2)$. Note that $\mathcal{O}(\lambda^0)$ terms interact with $\mathcal{O}(\lambda^2)$ terms when solving for the first helical mode $m = \pm 1$, a phenomenon termed subharmonic resonance. Owing to the absence of $\mathcal{O}(\lambda^2)$ terms in the UVAS base flow model, it was not possible to obtain $m = \pm 1$ eigenvalues in that case.

By asymptotically expanding the linear stability analysis in terms of λ, as in Eqs. (4.51) and (4.52), in addition to the asymptotically-expanded base flows, the azimuthal mode couplings between eigenfunctions were restricted. Therefore, an asymptotic expansion approach to a linear stability analysis may have affected the resultant eigenvalues, particularly as λ increased.

The complete azimuthal dependencies of the eigenfunctions at $\mathcal{O}(\lambda^2)$ are explicated as:

$$\hat{u}_{z,2}(r,\theta) \coloneqq \breve{u}_{z,2}^{+1}(r)\mathrm{e}^{i\theta} + \breve{u}_{z,2}^{-1}(r)\mathrm{e}^{-i\theta} + \breve{u}_{z,2}^{+3}(r)\mathrm{e}^{3i\theta} + \breve{u}_{z,2}^{-3}(r)\mathrm{e}^{-3i\theta} \tag{4.60a}$$

$$\hat{u}_{r,2}(r,\theta) \coloneqq \breve{u}_{r,2}^{+1}(r)\mathrm{e}^{i\theta} + \breve{u}_{r,2}^{-1}(r)\mathrm{e}^{-i\theta} + \breve{u}_{r,2}^{+3}(r)\mathrm{e}^{3i\theta} + \breve{u}_{r,2}^{-3}(r)\mathrm{e}^{-3i\theta} \tag{4.60b}$$

$$\hat{u}_{\theta,2}(r,\theta) \coloneqq \breve{u}_{\theta,2}^{+1}(r)\mathrm{e}^{i\theta} + \breve{u}_{\theta,2}^{-1}(r)\mathrm{e}^{-i\theta} + \breve{u}_{\theta,2}^{+3}(r)\mathrm{e}^{3i\theta} + \breve{u}_{\theta,2}^{-3}(r)\mathrm{e}^{-3i\theta} \tag{4.60c}$$

$$\hat{p}_2(r,\theta) \coloneqq \breve{p}_2^{+1}(r)\mathrm{e}^{i\theta} + \breve{p}_2^{-1}(r)\mathrm{e}^{-i\theta} + \breve{p}_2^{+3}(r)\mathrm{e}^{3i\theta} + \breve{p}_2^{-3}(r)\mathrm{e}^{-3i\theta} \tag{4.60d}$$

for the axisymmetric $m = 0$ mode, as

$$\hat{u}_{z,2}(r,\theta) \coloneqq \breve{u}_{z,2}^{+1}(r)\mathrm{e}^{i\theta} + \breve{u}_{z,2}^{-1}(r)\mathrm{e}^{-i\theta} + \breve{u}_{z,2}^{+3}(r)\mathrm{e}^{3i\theta} + \breve{u}_{z,2}^{-3}(r)\mathrm{e}^{-3i\theta} \tag{4.61a}$$

$$\hat{u}_{r,2}(r,\theta) \coloneqq \breve{u}_{r,2}^{+1}(r)\mathrm{e}^{i\theta} + \breve{u}_{r,2}^{-1}(r)\mathrm{e}^{-i\theta} + \breve{u}_{r,2}^{+3}(r)\mathrm{e}^{3i\theta} + \breve{u}_{r,2}^{-3}(r)\mathrm{e}^{-3i\theta} \tag{4.61b}$$

$$\hat{u}_{\theta,2}(r,\theta) \coloneqq \breve{u}_{\theta,2}^{+1}(r)\mathrm{e}^{i\theta} + \breve{u}_{\theta,2}^{-1}(r)\mathrm{e}^{-i\theta} + \breve{u}_{\theta,2}^{+3}(r)\mathrm{e}^{3i\theta} + \breve{u}_{\theta,2}^{-3}(r)\mathrm{e}^{-3i\theta} \tag{4.61c}$$

$$\hat{p}_{2}(r,\theta) \coloneqq \breve{p}_{2}^{+1}(r)\mathrm{e}^{i\theta} + \breve{p}_{2}^{-1}(r)\mathrm{e}^{-i\theta} + \breve{p}_{2}^{+3}(r)\mathrm{e}^{3i\theta} + \breve{p}_{2}^{-3}(r)\mathrm{e}^{-3i\theta} \tag{4.61d}$$

for the first helical mode $m = \pm 1$, and as:

$$\hat{u}_{z,2}(r,\theta) \coloneqq \breve{u}_{z,2}^{\pm m\pm 2}(r)\mathrm{e}^{i(\pm m\pm 2)\theta} + \breve{u}_{z,2}^{\pm m}(r)\mathrm{e}^{\pm im\theta} \tag{4.62a}$$

$$\hat{u}_{r,2}(r,\theta) \coloneqq \breve{u}_{r,2}^{\pm m\pm 2}(r)\mathrm{e}^{i(\pm m\pm 2)\theta} + \breve{u}_{r,2}^{\pm m}(r)\mathrm{e}^{\pm im\theta} \tag{4.62b}$$

$$\hat{u}_{\theta,2}(r,\theta) \coloneqq \breve{u}_{\theta,2}^{\pm m\pm 2}(r)\mathrm{e}^{i(\pm m\pm 2)\theta} + \breve{u}_{\theta,2}^{\pm m}(r)\mathrm{e}^{\pm im\theta} \tag{4.62c}$$

$$\hat{p}_{2}(r,\theta) \coloneqq \breve{p}_{2}^{\pm m\pm 2}(r)\mathrm{e}^{i(\pm m\pm 2)\theta} + \breve{p}_{2}^{\pm m}(r)\mathrm{e}^{\pm im\theta} \tag{4.62d}$$

for $|m| > 1$ helical modes. Note that the superscript '$\pm m \pm 2$' indicates that there is a sum over four eigenfunctions present: $m + 2$, $m - 2$, $-m + 2$, and $-m - 2$.

With an asymptotic expansion of the linear stability analysis in terms of λ with Eqs. (4.51) and (4.52), the higher azimuthal couplings between eigenfunctions have been neglected, as can be observed by comparing Eqs. (4.58) against Eqs. (4.61). Specifically, $\mathrm{e}^{\pm 2i\theta}$ eigenfunctions are absent in Eqs. (4.58), which may affect the determination of the eigenvalues. Additionally, higher helical modes were also determined without the higher azimuthal couplings between eigenfunctions present. Indeed, it is possible that, by expanding the linear stability analysis up to $\mathcal{O}(\lambda^2)$, all but a few eigenfunction-base flow interactions were permitted in the process of obtaining the eigenvalues.

4.7 Fourier-based LSA approach

To further investigate the effect of limiting the eigenfunction-base flow azimuthal mode couplings, a discrete Fourier transformation was applied to the linearised Navier-Stokes equations so that the azimuthal mode couplings could be strategically determined.

The 2D-local dispersion relation of Eqs. (4.3) was made inviscid and then integral-transformed presuming that the eigenfunctions could be written as a truncated orthogonal series solution. To better match the expanded linear stability analysis described in Chapter 4.6 the eigenfunctions $\hat{q}$ were decomposed in terms of a finite number of orthonormal exponential bases as:

$$\hat{q}(r,\theta) \coloneqq \sum_{n=-N_f}^{n=+N_f} q^n(r)\mathrm{e}^{in\theta} \tag{4.63}$$

where $q^n(r)$ is the unknown function-coefficient corresponding to the n^{th} term in the series solution. Just as in the discrete Fourier series, $q^n(r)$ is determined by an inner product of Eq. (4.63) with a basis $\mathrm{e}^{in\theta}$ over the domain $[-\pi,\pi[$. Therefore, $q^n(r)$ is defined as:

$$q^n(r) \coloneqq \frac{1}{2\pi}\int_{-\pi}^{\pi} \hat{q}(r,\theta)\mathrm{e}^{-in\theta}d\theta \tag{4.64}$$

The dispersion relation of Eq. (4.3) undergoes an inner product in the same manner to compose a system of governing equations that solve for the unknown functions $u_z^n, u_r^n, u_\theta^n, p^n$. In this case, the base flow was expanded in exponential form rather than trigonometric form in the following manner:

$$\bar{u}_z = U_z^0(r) + U_z^{+1}(r)\mathrm{e}^{+i\theta} + U_z^{-1}\mathrm{e}^{-i\theta} + U_z^{+2}\mathrm{e}^{+2i\theta} + U_z^{-2}\mathrm{e}^{-2i\theta} \tag{4.65a}$$

$$\bar{u}_r = U_r^{+1}(r)\mathrm{e}^{+i\theta} + U_r^{-1}\mathrm{e}^{-i\theta} + U_r^{+2}\mathrm{e}^{+2i\theta} + U_r^{-2}\mathrm{e}^{-2i\theta} \tag{4.65b}$$

$$\bar{u}_\theta = U_\theta^{+1}(r)\mathrm{e}^{+i\theta} + U_\theta^{-1}\mathrm{e}^{-i\theta} + U_\theta^{+2}\mathrm{e}^{+2i\theta} + U_\theta^{-2}\mathrm{e}^{-2i\theta} \tag{4.65c}$$

After integrating by parts and simplifying, the governing equations for $u_z^n, u_r^n, u_\theta^n, p^n$ for a particular value of n are:

$$\left(\frac{\mathrm{d}}{\mathrm{d}r}+\frac{1}{r}\right)u_r^n+\frac{in}{r}u_\theta^n=iku_z^n \tag{4.66a}$$

$$\mathcal{L}_{\text{conv}}(u_z^n)+\mathcal{L}_1(u_r^n)+\frac{i}{r}\mathcal{L}_3(u_\theta^n)=-ik\mathcal{L}_4(u_z^n)-ikp^n \tag{4.66b}$$

$$(\mathcal{L}_{\text{conv}}+\mathcal{L}_5)(u_r^n)+\mathcal{L}_6(u_\theta^n)+\frac{\mathrm{d}p^n}{\mathrm{d}r}=-ik\mathcal{L}_4(u_r^n) \tag{4.66c}$$

$$(\mathcal{L}_{\text{conv}}+\mathcal{L}_7)(u_\theta^n)+\mathcal{L}_8(u_r^n)+\frac{im}{r}p^n=-ik\mathcal{L}_4(u_r^n) \tag{4.66d}$$

where

$$\begin{aligned}\mathcal{L}_{\text{conv}}(q^n) \coloneqq -i\omega q^n+\left[U_r^{+1}\frac{\mathrm{d}q^{n-1}}{\mathrm{d}r}+U_r^{+2}\frac{\mathrm{d}q^{n-2}}{\mathrm{d}r}+u_r^{-1}\frac{\mathrm{d}q^{n+1}}{\mathrm{d}r}+U_r^{-2}\frac{\mathrm{d}q^{n-2}}{\mathrm{d}r}\right]\\ +\frac{i}{r}\left[(n-1)U_\theta^{+1}q^{n-1}+(n-2)U_\theta^{+2}q^{n-2}+(n+1)U_\theta^{-1}q^{n+1}+(n+2)U_\theta^{-2}q^{n+2}\right]\end{aligned} \tag{4.67}$$

$$\mathcal{L}_1(q^n) \coloneqq \left[\frac{\mathrm{d}U_z^0}{\mathrm{d}r}q^n+\frac{\mathrm{d}U_z^{+1}}{\mathrm{d}r}q^{n-1}+\frac{\mathrm{d}U_z^{+2}}{\mathrm{d}r}q^{n-2}+\frac{\mathrm{d}U_z^{-1}}{\mathrm{d}r}q^{n+1}+\frac{\mathrm{d}U_z^{-2}}{\mathrm{d}r}q^{n+2}\right] \tag{4.68}$$

$$\mathcal{L}_3(q^n) \coloneqq \left[U_z^{+1}q^{n-1}+2U_z^{+2}q^{n-2}-U_z^{-1}q^{n+1}-2U_z^{-2}q^{n+2}\right] \tag{4.69}$$

$$\mathcal{L}_4(q^n) \coloneqq \left[U_z^0q^n+U_z^{+1}q^{n-1}+U_z^{+2}q^{n-2}+U_z^{-1}q^{n+1}+U_z^{-2}q^{n+2}\right] \tag{4.70}$$

$$\mathcal{L}_5(q^n) \coloneqq \left[\frac{\mathrm{d}U_r^{+1}}{\mathrm{d}r}q^{n-1}+\frac{\mathrm{d}U_r^{+2}}{\mathrm{d}r}q^{n-2}+\frac{\mathrm{d}U_r^{-1}}{\mathrm{d}r}q^{n+1}+\frac{\mathrm{d}U_r^{-2}}{\mathrm{d}r}q^{n+2}\right] \tag{4.71}$$

$$\mathcal{L}_6(q^n) \coloneqq \frac{1}{r}\Bigg[i\Bigg(U_r^{+1}q^{n-1} + 2U_r^{+2}q^{n-2} - U_r^{-1}q^{n+1} - 2U_r^{-2}q^{n+2}\Bigg) \\ -2\Bigg(U_\theta^{+1}q^{n-1} + U_\theta^{+2}q^{n-2} + U_\theta^{-1}q^{n+1} + U_\theta^{-2}q^{n+2}\Bigg)\Bigg] \tag{4.72}$$

$$\mathcal{L}_7(q^n) \coloneqq \frac{1}{r}\Bigg[i\Bigg(U_\theta^{+1}q^{n-1} + 2U_\theta^{+1}q^{n-2} - U_\theta^{-1}q^{n+1} - 2U_\theta^{-2}q^{n+2}\Bigg) \\ +\Bigg(U_r^{+1}q^{n-1} + U_r^{+2}q^{n-2} + U_r^{-1}q^{n+1} + U_r^{-2}q^{n+2}\Bigg)\Bigg] \tag{4.73}$$

$$\mathcal{L}_8(q^n) \coloneqq \Bigg[\Bigg(\frac{\mathrm{d}U_\theta^{+1}}{\mathrm{d}r}q^{n-1} + \frac{\mathrm{d}U_\theta^{+2}}{\mathrm{d}r}q^{n-2} + \frac{\mathrm{d}U_\theta^{-1}}{\mathrm{d}r}q^{n+1} + \frac{\mathrm{d}U_\theta^{-2}}{\mathrm{d}r}q^{n+2}\Bigg) \\ +\frac{1}{r}\Bigg(U_\theta^{+1}q^{n-1} + U_\theta^{+2}q^{n-2} + U_\theta^{-1}q^{n+1} + U_\theta^{-2}q^{n+2}\Bigg)\Bigg] \tag{4.74}$$

Clearly, there is eigenfunction-base flow coupling induced by the presence of $\mathcal{O}(\lambda^1)$ and $\mathcal{O}(\lambda^2)$ base flow terms. This means that obtaining a particular eigenfunction q^n necessitates the simultaneous coupled solution of $2N_f + 1$ eigenfunctions. Additionally, it means the eigenvalue k is particular to the choice of N_f eigenfunctions represented. As $N_f \gg 1$, k should approach the value obtained from the fully-coupled linear stability analysis of Chapter 4.2. Therefore it is possible to limit the azimuthal mode couplings to most closely mimic those of Alves *et al.* (2008) and to study the effect of increased azimuthal mode coupling on the eigenvalue with the fully-coupled results as a reference. Note that the eigenvalue k and eigenfunctions used in Eqs. (4.66) have not been expanded in terms of λ as was performed in Eq. (4.52) and Eq. (4.51) and therefore a direct comparison is not possible.

By inspection of Eqs. (4.53), (4.54), and (4.57), it is clear that Alves (2006) modelled the eigenfunctions of the axisymmetric mode as:

$$\hat{u}_z(r,\theta) = \begin{cases} \breve{u}_{z,0}(r) \\ +\lambda\left[\breve{u}_{z,1}^{+1}\mathrm{e}^{i\theta} + \breve{u}_{z,1}^{-1}\mathrm{e}^{-i\theta}\right] \\ +\lambda^2\,\breve{u}_{z,2}^{0}(r) \end{cases} \tag{4.75a}$$

$$\hat{u}_r(r,\theta) = \begin{cases} \breve{u}_{r,0}(r) \\ +\lambda\left[\breve{u}_{r,1}^{+1}\mathrm{e}^{i\theta} + \breve{u}_{r,1}^{-1}\mathrm{e}^{-i\theta}\right] \\ +\lambda^2\,\breve{u}_{r,2}^{0}(r) \end{cases} \tag{4.75b}$$

$$\hat{u}_\theta(r,\theta) = \begin{cases} 0 \\ +\lambda\left[\breve{u}_{\theta,1}^{+1}\mathrm{e}^{i\theta} + \breve{u}_{\theta,1}^{-1}\mathrm{e}^{-i\theta}\right] \\ +0 \end{cases} \tag{4.75c}$$

$$\hat{p}(r,\theta) = \begin{cases} \breve{p}_0(r) \\ +\lambda\left[\breve{p}_1^{+1}\mathrm{e}^{i\theta} + \breve{p}_1^{-1}\mathrm{e}^{-i\theta}\right] \\ +\lambda^2\,\breve{p}_2^{0}(r) \end{cases} \tag{4.75d}$$

To reproduce these azimuthal mode couplings as closely as possible, Eqs. (4.66) were solved with $N_f = 1$ and $u_\theta^0 = 0$. All eigenfunction-base flow interaction terms that required higher-order eigenfunctions (such as $U_r^{+2}\frac{dq^{n-2}}{dr}$ in Eq. (4.67)) were neglected, effectively establishing that all eigenfunctions $q^n = 0$ if $|n| > 1$.

4.7.1 Numerical methods for Fourier-based LSA

Again, it was found that the eigenfunctions exhibited non-physical oscillations in the radial direction stemming from the convective terms, particularly as R decreased. To maintain co-location of the disturbance velocity and pressure eigenfunctions, the non-convective terms were discretised by a 4^{th}-order central finite difference schemes while the radial convective derivative was discretised with the hybrid 2^{nd}-1^{st}-order winded scheme for the near-wake

region and a hybrid 4^{th}-3^{rd}-order winded scheme elsewhere. A linear activation function smoothed the interface between the two types of convective schemes. The direction of winding was contigent on the sign of $\bar{u}_r$ at that location; the radial derivative was upwinded with respect to $\tilde{r}$ in $0 < \theta < \pi/2$ and $\pi < \theta < 3\pi/2$ while the radial derivative was downwinded with respect to $\tilde{r}$ in $\pi/2 < \theta < \pi$ and $3\pi/2 < \theta < 2\pi$. Again, the coordinate transform of Mohseni & Colonius (2000) was employed to treat the pole condition. Homogeneous Neumann boundary conditions were established for all disturbance velocity and pressure eigenfunctions.

The eigenproblem of Eqs. (4.66a) was formed for a particular value of N and then solved using the Krylov-Schur algorithm in `MATLAB`. Any eigenfunction-base flow azimuthal coupling was artificially destroyed, as needed, prior to solving the eigenproblem.

4.8 Spatial kinetic energy budget analysis

It is necessary to obtain a physical cause of an instability beyond obtaining the dominant frequency or eigenfunction shape, particularly in scenarios where results are unexpected. One black-box approach is to conduct a perturbation sensitivity analysis of the relevant parameters of the problem. However, this primarily provides interpretation of the stability results rather than an explanation. A kinetic energy budget analysis (Hama *et al.*, 1980) is one approach to quantify the contribution of various physical mechanisms on a resultant eigenvalue. One treatise of a non-disturbance kinetic energy budget analysis for incompressible flows is that of Batchelor (2000). Note the momentum and energy equations are decoupled for incompressible flows, meaning that the velocity field is invariant of thermal phenomena. This means that pressure takes on a mechanical meaning and has no thermodynamic interpretation (Panton, 2013). As a result, the incompressible flow energy conservation equation is considered as 'derived' (Coppola *et al.*, 2019).

Kinetic energy budget analyses are most commonly performed for incompressible tem-

poral stability problems (Schmid & Henningson, 2001; Criminale *et al.*, 2003), where the procedure may also be known as obtaining the Reynolds-Orr equation, because the temporal eigenvalue ω is equal to the superposition of linearised physical mechanisms with individually clear interpretations as stated in Eq. (4.76):

$$\omega = \int_\Omega \mathbf{u}'^* \cdot \left((\bar{\mathbf{u}} \cdot \nabla)\mathbf{u}' \right) \frac{\mathrm{d}\Omega}{|N|^2} + \int_\Omega \mathbf{u}'^* \cdot \left((\mathbf{u}' \cdot \nabla)\bar{\mathbf{u}} \right) \frac{\mathrm{d}\Omega}{|N|^2} + \int_\Omega -\mathbf{u}'^* \cdot \left(\frac{1}{\mathrm{Re}} \nabla^2 \mathbf{u}' \right) \frac{\mathrm{d}\Omega}{|N|^2} \quad (4.76)$$

after having substituted the appropriate normal Fourier mode ansatz (e.g., from Eq. (2.15) or Eq. (4.2)) to replace $\vec{u'}$ and made the appropriate algebraic simplifications. Ω represents the entire domain of integrated considered and is independent of coordinate system or dimensionality. Therefore, $\mathrm{d}\Omega$ represents the integral over the entire domain considered; Eigenfunction boundary conditions are implicitly assumed to be present and valid at the boundaries. $\mathbf{u}' = (u_1', u_2', u_3')^T$ represents the vector of disturbance velocities, $\mathbf{u}'^* = (u_1'^*, u_2'^*, u_3'^*)^T$ represents the vector of disturbance velocities after having underwent a complex conjugation, and $|N|^2$ represents the scalar normalisation factor which is typically $\int_\Omega \mathbf{u}'^* \cdot \mathbf{u}' \, \mathrm{d}\Omega$. ω is a complex scalar representing the temporal eigenvalue. A derivation of such a temporal kinetic energy budget analysis in one dimension may be found in Criminale *et al.* (2003).

The first, second, and third integrals in Eq. (4.76) correspond to the 'Advection', 'Production', and 'Viscous dissipation' terms, respectively. Each may be interpreted as scalar contributions to the eigenvalue that comprise of functions of the eigenfunction integrated over all space considered. Note that 'Production' is also known as 'Reynolds stress' terms owing to their resemblance to the Reynolds stresses upon linearisation and that 'Viscous dissipation' is typically a negative contribution to the temporal growth rate. Some explicit formulations of the Reynolds-Orr equation may be in Lagrangian form such as in Schmid & Henningson (2001), but this form obscures the 'Advection' term; the Euler form does not have this issue. It is important to note that the incompressible continuity equation $\nabla \cdot \mathbf{u} = 0$ is typically accounted for in the 'Viscous dissipation' term. Temporal kinetic energy budget

analyses (where the wavenumber $k \in \mathbb{R}$) eradicate the pressure terms by using the continuity equation and boundary conditions. For more details, refer to Sections 4.8.1 - 4.8.3.

Mathematically, the nonlinear advection term present in the Navier-Stokes equations is $(\mathbf{u} \cdot \nabla)\mathbf{u}$. This embeds the physical interpretation of momentum flux being transported by the surrounding fluid spatially. Upon linearisation with the ansatz $u \coloneqq \bar{u} + \epsilon u'$ into $(\mathbf{u} \cdot \nabla)\mathbf{u}$ and retaining only the $\mathcal{O}(\epsilon)$ terms, one obtains:

$$(\bar{\mathbf{u}} \cdot \nabla)\mathbf{u}' + (\mathbf{u}' \cdot \nabla)\bar{\mathbf{u}} \tag{4.77}$$

where the first term physically represents the base flow advecting a disturbance while the second term represents the disturbance advecting the base flow. Conventionally in kinetic budget analysis, upon performing an inner product with the disturbance velocity (as shown in Sections 4.8.1 for example), the former is termed 'Advection' while the latter is termed 'Production'. Note that 'Production' terms often resemble linearised Reynolds stresses, but this should not be used as a criterion for classification in cylindrical or spherical coordinates.

Physically, recall that the linearised disturbance is periodic in the inhomogeneous spatial direction. Temporal growth of the kinetic energy of the disturbances is considered within a volume of one spatial wavelength in the inhomogeneous direction and the entire domain in the homogeneous direction(s). The 'Advection' term (e.g., $\bar{u}_x \frac{\partial u'_x}{\partial x}$) indicates the disturbance energy growth associated with advecting the disturbances. The 'Production' term (e.g., $u'_x \frac{\partial \bar{u}_x}{\partial x}$) represents the Reynolds stress work or the production of disturbance kinetic energy. The 'Viscous dissipation' term is related to the energy that is irreversibly converted to internal energy. For further discussion, see Hama & de la Veaux (1980).

Spatial kinetic energy budget analysis is somewhat less common, especially for linear stability analyses, though there are several relevant studies which employ such analysis in linear stability analyses, as will be discussed below. One key difference with respect to the temporal approach is that the spatial approach obfuscates the direct contribution of each physical mechanism to the eigenvalue, k, due to a new term present in the spatial analysis

that is absent in the temporal analysis: The pressure-velocity correlation (Eq. (4.78)). Rather, indirect inferences can be made through the spatial growth of the kinetic energy as observed from a particular station for all time, as sketched in Eq. (4.78).

$$\begin{aligned}\text{Spatial KE growth rate}(k) =& \text{Advection} + \text{Production} \\ &+ \text{Pressure-velocity correlation}(k) \\ &+ \text{Viscous dissipation}\end{aligned} \tag{4.78}$$

Both the pressure-velocity correlation and the total spatial kinetic energy growth rates are functions of the eigenvalue k. Again, the viscous dissipation term is typically a negative contribution to the spatial kinetic energy growth rate. Explicit examples of such a spatial kinetic energy budget analysis may be found in Sections 4.8.1-4.8.3 or in Hama *et al.* (1980) in one dimension.

Physically, a spatial kinetic energy budget analysis considers the spatial growth of kinetic energy of the disturbances within one time period and as they pass through a station in space. The 'Spatial KE growth rate' is the time-averaged spatial growth of disturbance kinetic energy in the inhomogeneous direction considered at a station in the flowfield. The 'pressure-velocity correlation' is the transport of the disturbance pressure by the fluctuating inhomogeneous velocity, or the work done by pressure transport.

According to the seminal spatial kinetic energy budget analysis of Hama *et al.* (1980) applied to a 1D parallel incompressible boundary layer, the pressure-velocity correlation is a significant term because it is 'always opposite to the trend of the [disturbances]; it suppresses the energy when [the disturbance is destabilising] and supplies the energy when [the disturbance is stabilising].' Additionally, Gmelin & Rist (2001) note that the spatial distribution of the integrands indicate that 'the pressure term always acts to counteract the production term' for an actively spanwise vorticity-controlled 2D parallel incompressible Blasius boundary layer. The viscous linearised parabolised stability analysis of a hypersonic

yawed cone of Patel *et al.* (2022) also indicate that the production term has the opposite trend as the pressure-velocity term.

To explore this further, it is necessary to obtain a normalised comparison of kinetic energy terms from eigenfunctions that correspond to different tuning parameters by considering the percentage contribution of each term to the total spatial kinetic energy growth rate.

The data corresponding to Figure 21 of Hama *et al.* (1980) are displayed in Fig. 4.14a and have been converted a percentage format in Fig. 4.14b. They performed a spatial 1D local linear stability analysis of the Blasius boundary layer with a parallel-flow assumption for a range of Reynolds numbers. From the resultant eigenvalues and eigenfunctions, Hama *et al.* (1980) were able to calculate the value of the 'Spatial KE growth rate', 'Production', 'Pressure-velocity correlation', and the 'Viscous dissipation' terms in spatial kinetic energy balance Eq. (4.78) for a range of Reynolds numbers $300 \lesssim \mathrm{Re}^* \leq 1000$. Note that Hama *et al.* (1980) The abscissa is restricted to $650 \leq \mathrm{Re}^* = U_\infty \delta^* / \nu \leq 750$ to focus on the spatially unstable values while avoiding the locations where the total spatial kinetic energy growth is zero. It is important to note that maximum spatial growth rate corresponds to approximately $\mathrm{Re}^*_{\mathrm{crit}} \approx 700$ (Hama *et al.*, 1980). The Reynolds number Re^* is defined with the displacement thickness δ^* as the characteristic length scale.

Referring to Fig. 4.14b, as the Reynolds number approaches $\mathrm{Re}^*_{\mathrm{crit}}$ (i.e., as the flow increasingly destabilises), the pressure-velocity correlation term provides more energy as a percentage of the total kinetic energy. The absolute contribution (Fig. 4.14a) of the pressure-velocity correlation is always negative irrespective of flow stability, but does provide less energy in absolute terms as the flow destabilises. In both formulations, the 'Production' terms played a smaller role as the boundary layer stabilised, contrary to what typically occurs for temporal analyses.

Indeed, the notion that the pressure-velocity correlation is a significant indicator of flow (in)stability can be found in Aadhishwaran & Diwan (2021), who reported that, as a 1D hyperbolic-tangent mixing layer increasingly become more spatially unstable, the pressure-

velocity correlation provided more of the overall energy in percentage terms. Additionally, they remarked that the pressure-velocity correlation dominated the spatial kinetic energy budget as the mixing layer approached absolute instability. Hence it is of interest to explore the spatial kinetic energy budget for the jet-in-crossflow problem to enable interpretation of the present results.

One important note is that non-parallelism in a Blasius boundary layer has been found to be always adding to the total kinetic energy growth rate by Hama & de la Veaux (1980) because the displacement thickness continues to grow in the streamwise direction. The present linear stability analyses are considered '2D-local', whereby the flowfield is prevented from evolving downstream of the jet exit. Experimental measurements indicate that the potential core of a jet-in-crossflow diminishes further from the jet exit, indicating that the shear layer momentum thickness increases downstream (see Getsinger *et al.* (2014), for example).

4.8.1 Cartesian formulation

Generally, the spatial kinetic energy budget equations can be derived from an inner product of the momentum equations over one time period and over the domain considered. There are equivalent approaches as can be seen in Aadhishwaran & Diwan (2021); Hama *et al.* (1980); Gmelin & Rist (2001), but the derivation presented below starts from the linearised momentum equations of Eqs. (4.8) which has incorporated the normal mode decomposition ansatz in Eq. (4.7). The linearised momentum equations undergo a inner product by the complex conjugate of the eigenfunctions and are then integrated over x and y, the in-plane domain (Groot, 2018).

For example, the z-momentum (z being the axial coordinate) equation Eq. (4.8d) in the inviscid limit becomes:

$$\iint_\Omega \hat{u}_z^*\left(-i\omega\hat{u}_z + \bar{u}_x\frac{\partial\hat{u}_z}{\partial x} + \bar{u}_y\frac{\partial\hat{u}_z}{\partial y}\right)\,\mathrm{d}x\,\mathrm{d}y + \iint_\Omega \hat{u}_z^*\left(\hat{u}_x\frac{\partial\bar{u}_z}{\partial x} + \hat{u}_y\frac{\partial\bar{u}_z}{\partial y}\right)\,\mathrm{d}x\,\mathrm{d}y + \iint_\Omega \hat{u}_z^*\left(ik\hat{p}\right)\,\mathrm{d}x\,\mathrm{d}y = -ik\iint_\Omega \bar{u}_z\hat{u}_z^*\hat{u}_z\,\mathrm{d}x\,\mathrm{d}y \tag{4.79}$$

where $\hat{u}_z^*$ is the complex conjugate of the $\hat{u}_z$ eigenfunction and the double integral is taken over the entire domain Ω. Ostensibly, this is $-\infty < x, y < \infty$, but computational limitations mean that the eigenfunction can only be represented on a finite domain. However, the eigenfunctions are taken to decay at an exponential rate far from the shear layer and jet exit, so a sufficiently large computational domain will permit the eigenfunctions to approach zero amplitude. Allow $|\hat{q}|^2 \coloneqq \hat{q}^*\hat{q}$ and note that $|\hat{q}|$ is strictly real and non-negative, where $\hat{q}$ represents an eigenfunction term.

After performing a similar procedure for the x- and y-momentum equations, the resulting three equations are summed into one equation:

$$\begin{aligned}
-k\iint_\Omega \bar{u}_z\Big(|\hat{u}_x|^2 + |\hat{u}_y|^2 + |\hat{u}_z|^2\Big)\,\mathrm{d}x\,\mathrm{d}y = \\
&- i\iint_\Omega\Bigg[-i\omega\Big(|\hat{u}_x|^2 + |\hat{u}_y|^2 + |\hat{u}_z|^2\Big) \\
&+ \bar{u}_x\hat{u}_x^*\frac{\partial\hat{u}_x}{\partial x} + \bar{u}_y\hat{u}_x^*\frac{\partial\hat{u}_x}{\partial y} + \bar{u}_x\hat{u}_y^*\frac{\partial\hat{u}_z}{\partial x} + \bar{u}_y\hat{u}_y^*\frac{\partial\hat{u}_z}{\partial y} + \bar{u}_x\hat{u}_z^*\frac{\partial\hat{u}_z}{\partial x} + \bar{u}_y\hat{u}_z^*\frac{\partial\hat{u}_z}{\partial y}\Bigg]\,\mathrm{d}x\,\mathrm{d}y \\
&- i\iint_\Omega\left[\hat{u}_z^*\hat{u}_x\frac{\partial\bar{u}_z}{\partial x} + \hat{u}_z^*\hat{u}_y\frac{\partial\bar{u}_z}{\partial y} + \hat{u}_x^*\hat{u}_x\frac{\partial\bar{u}_x}{\partial x} + \hat{u}_x^*\hat{u}_y\frac{\partial\bar{u}_x}{\partial y} + \hat{u}_y^*\hat{u}_x\frac{\partial\bar{u}_y}{\partial x} + \hat{u}_y^*\hat{u}_y\frac{\partial\bar{u}_y}{\partial y}\right]\,\mathrm{d}x\,\mathrm{d}y \\
&+ k\iint_\Omega \hat{u}_z^*\hat{p}\,\mathrm{d}x\,\mathrm{d}y \\
&- i\iint_\Omega\left[\hat{u}_x\frac{\partial\hat{p}}{\partial x} + \hat{u}_y\frac{\partial\hat{p}}{\partial y}\right]\,\mathrm{d}x\,\mathrm{d}y
\end{aligned} \tag{4.80}$$

To enforce continuity, we consider the inner product of the continuity equation Eq. (4.8a) with the complex conjugate of the disturbance pressure eigenfunction $\hat{p}^*$ as:

$$\iint_{\Omega} \left[i\hat{p}^* \left(\frac{\partial \hat{u}_x}{\partial x} + \frac{\partial \hat{u}_y}{\partial y} \right) \right] \mathrm{d}x \; \mathrm{d}y = +k \iint_{\Omega} \hat{p}^* \hat{u}_z \; \mathrm{d}x \; \mathrm{d}y \tag{4.81}$$

By using integration by parts and by imposing homogeneous Dirichlet boundary conditions in the farfield, the continuity equation becomes:

$$-i \iint_{\Omega} \frac{\partial \hat{p}^*}{\partial x} \hat{u}_x \; \mathrm{d}x \; \mathrm{d}y - i \iint_{\Omega} \frac{\partial \hat{p}^*}{\partial y} \hat{u}_y \; \mathrm{d}x \; \mathrm{d}y = k \iint \hat{p}^* \hat{u}_z \; \mathrm{d}x \; \mathrm{d}y \tag{4.82}$$

The homogeneous Dirichlet boundary conditions ensure that the boundary terms resulting from integration by parts vanish.

Applying complex conjugation of Eq. (4.82) and using the identity $(fg)^* = f^* g^*$, the form of the continuity equation that is most useful is:

$$i \iint_{\Omega} \frac{\partial \hat{p}}{\partial x} \hat{u}_x^* \; \mathrm{d}x \; \mathrm{d}y + i \iint_{\Omega} \frac{\partial \hat{p}}{\partial y} \hat{u}_y^* \; \mathrm{d}x \; \mathrm{d}y = k^* \iint_{\Omega} \hat{p} \hat{u}_z^* \; \mathrm{d}x \; \mathrm{d}y \tag{4.83}$$

Applying Eq. (4.83) to Eq. (4.80) enforces conservation of mass to conceptually yield the following energy balance:

$$E = A + P + PV \tag{4.84}$$

where E denotes the spatial kinetic energy growth rate, A represents advection (see Eq. (4.77)), P, represents production or linearised Reynolds stress terms (see Eq. (4.77)), and PV denotes the pressure-velocity correlation contribution to the overall kinetic energy budget. Eq. (4.84) is the inviscid limit of Eq. (4.78). The explicit definitions of each of the aforementioned terms are:

$$E \coloneqq -k \iint_{\Omega} \bar{u}_z \Big(|\hat{u}_x|^2 + |\hat{u}_y|^2 + |\hat{u}_z|^2 \Big) \; \mathrm{d}x \; \mathrm{d}y \tag{4.85a}$$

$$A \coloneqq -i \iint_\Omega \Bigg[- i\omega\Big(|\hat{u}_x|^2 + |\hat{u}_y|^2 + |\hat{u}_z|^2\Big) + \bar{u}_x \hat{u}_x^* \frac{\partial \hat{u}_x}{\partial x} + \bar{u}_y \hat{u}_x^* \frac{\partial \hat{u}_x}{\partial y} + \bar{u}_x \hat{u}_y^* \frac{\partial \hat{u}_z}{\partial x} + \bar{u}_y \hat{u}_y^* \frac{\partial \hat{u}_z}{\partial y} + \bar{u}_x \hat{u}_z^* \frac{\partial \hat{u}_z}{\partial x} + \bar{u}_y \hat{u}_z^* \frac{\partial \hat{u}_z}{\partial y} \Bigg] \, \mathrm{d}x \, \mathrm{d}y \tag{4.85b}$$

$$P \coloneqq -i \iint_\Omega \Bigg[\hat{u}_z^* \hat{u}_x \frac{\partial \bar{u}_z}{\partial x} + \hat{u}_z^* \hat{u}_y \frac{\partial \bar{u}_z}{\partial y} + \hat{u}_x^* \hat{u}_x \frac{\partial \bar{u}_x}{\partial x} + \hat{u}_x^* \hat{u}_y \frac{\partial \bar{u}_x}{\partial y} + \hat{u}_y^* \hat{u}_x \frac{\partial \bar{u}_y}{\partial x} + \hat{u}_y^* \hat{u}_y \frac{\partial \bar{u}_y}{\partial y} \Bigg] \, \mathrm{d}x \, \mathrm{d}y \tag{4.85c}$$

$$PV \coloneqq +(k - k^*) \iint_\Omega \hat{u}_z^* \hat{p} \, \mathrm{d}x \, \mathrm{d}y \tag{4.85d}$$

Note that $k - k^*$ yields an imaginary number even though k is complex in general. By inspection, only the total spatial kinetic energy growth rate integrand is known to be real a priori. All other terms are complex in general, and therefore can only be analysed a posteriori.

4.8.2 Polar formulation

For completeness and to assist in the derivation of the discrete Fourier-based formulation of the spatial kinetic energy budget analysis, the polar form of the spatial kinetic energy budget analysis is derived here.

Again, the linearised momentum equations (Eqs. (4.3)) undergo a inner product by the complex conjugate of the eigenfunctions and are then integrated over r and θ, the in-plane domain.

For example, the z-momentum equations Eq. (4.3d) in the inviscid limit becomes:

$$\iint_\Omega \hat{u}_z^* \left(- i\omega \hat{u}_z + \bar{u}_r \frac{\partial \hat{u}_z}{\partial r} + \frac{\bar{u}_\theta}{r} \frac{\partial \hat{u}_z}{\partial \theta} \right) r \, \mathrm{d}r \, \mathrm{d}\theta + \iint_\Omega \hat{u}_z^* \left(\hat{u}_r \frac{\partial \bar{u}_z}{\partial r} + \frac{\hat{u}_\theta}{r} \frac{\partial \bar{u}_z}{\partial \theta} \right) r \, \mathrm{d}r \, \mathrm{d}\theta + ik \iint_\Omega \hat{u}_z^* \hat{p} \, r \, \mathrm{d}r \, \mathrm{d}\theta = -ik \iint_\Omega \bar{u}_z \hat{u}_z^* \hat{u}_z \, r \, \mathrm{d}r \, \mathrm{d}\theta \tag{4.86}$$

where $\hat{u}_z^*$ is the complex conjugate of the $\hat{u}_z$ eigenfunction and the double integral is taken over the entire domain. Ostensibly, this is $0 \leq r < \infty$, but computational limitations mean that the eigenfunction can only be represented on a finite domain. However, the eigenfunctions are taken to decay at an exponential rate far from the shear layer, so a sufficiently large computational domain will permit the eigenfunctions to approach zero amplitude. On physical grounds, the eigenfunctions are expected to be periodic in the θ direction. Allow $|\hat{q}|^2 \coloneqq \hat{q}^*\hat{q}$ and note that $|\hat{q}|^2$ is strictly real and non-negative.

After performing a similar procedure for the r- and θ-momentum equations, the resulting three equations are summed into one equation as follows:

$$\begin{aligned}
-k \iint_\Omega \bar{u}_z \Big(|\hat{u}_z|^2 + |\hat{u}_r|^2 + |\hat{u}_\theta|^2 \Big) \; r \; \mathrm{d}r \; \mathrm{d}\theta = \\
- i \iint_\Omega \Bigg[- i\omega \Big(|\hat{u}_z|^2 + |\hat{u}_r|^2 + |\hat{u}_\theta|^2 \Big) + \hat{u}_r^* \left(\bar{u}_r \frac{\partial \hat{u}_r}{\partial r} + \frac{\bar{u}_\theta}{r} \frac{\partial \hat{u}_r}{\partial \theta} - \frac{\bar{u}_\theta}{r} \hat{u}_\theta \right) \\
+ \hat{u}_\theta^* \left(\bar{u}_r \frac{\partial \hat{u}_\theta}{\partial r} + \frac{\bar{u}_\theta}{r} \frac{\partial \hat{u}_\theta}{\partial \theta} + \frac{\bar{u}_\theta}{r} \hat{u}_r \right) + \hat{u}_z^* \left(\bar{u}_r \frac{\partial \hat{u}_z}{\partial r} + \frac{\bar{u}_\theta}{r} \frac{\partial \hat{u}_z}{\partial \theta} \right) \Bigg] \; r \; \mathrm{d}r \; \mathrm{d}\theta \\
- i \iint_\Omega \Bigg[\hat{u}_r^* \left(\hat{u}_r \frac{\partial \bar{u}_r}{\partial r} + \frac{\hat{u}_\theta}{r} \frac{\partial \bar{u}_r}{\partial \theta} - \frac{\hat{u}_\theta}{r} \bar{u}_\theta \right) \\
+ \hat{u}_\theta^* \left(\hat{u}_r \frac{\partial \bar{u}_\theta}{\partial r} + \frac{\hat{u}_\theta}{r} \frac{\partial \bar{u}_\theta}{\partial \theta} + \frac{\hat{u}_\theta}{r} \bar{u}_r \right) + \hat{u}_z^* \left(\hat{u}_r \frac{\partial \bar{u}_z}{\partial r} + \frac{\hat{u}_\theta}{r} \frac{\partial \bar{u}_z}{\partial \theta} \right) \Bigg] \; r \; \mathrm{d}r \; \mathrm{d}\theta \\
+ k \iint_\Omega \hat{u}_z^* \hat{p} \; r \; \mathrm{d}r \; \mathrm{d}\theta - i \iint_\Omega \left[\hat{u}_r^* \frac{\partial \hat{p}}{\partial r} + \hat{u}_\theta^* \frac{\partial \hat{p}}{\partial \theta} \right] \; r \; \mathrm{d}r \; \mathrm{d}\theta
\end{aligned} \tag{4.87}$$

To enforce continuity, we consider the inner product of the continuity equation Eq. (4.3a) with the complex conjugate of the disturbance pressure eigenfunction $\hat{p}^*$ as:

$$\begin{aligned}
i \iint_\Omega \hat{p}^* \left(\frac{\hat{u}_r}{r} + \frac{\partial \hat{u}_r}{\partial r} + \frac{1}{r} \frac{\partial \hat{u}_\theta}{\partial \theta} \right) \; r \; \mathrm{d}r \; \mathrm{d}\theta = \\
k \iint_\Omega \hat{p}^* \hat{u}_z \; r \; \mathrm{d}r \; \mathrm{d}\theta
\end{aligned} \tag{4.88}$$

By using integration by parts and by imposing homogeneous Dirichlet boundary conditions for $r \to \infty$ and periodic boundary conditions in the θ direction, the continuity equation becomes:

$$-i \iint_{\Omega} \left(\frac{\partial \hat{p}^*}{\partial r} \hat{u}_r + \frac{\partial \hat{p}^*}{\partial \theta} \hat{u}_\theta \right) \, r \, \mathrm{d}r \, \mathrm{d}\theta = k \iint_{\Omega} \hat{p}^* \hat{u}_z \, r \, \mathrm{d}r \, \mathrm{d}\theta \tag{4.89}$$

assuming that boundary terms at $r \to 0$ will disappear. This is empirically reasonable given that the single-valued pressure eigenfunctions and their derivatives do not become singular at the origin and that the pressure terms are multiplied by r. The remaining boundary conditions ensure that the other boundary terms resulting from integration by parts also vanish.

Applying complex conjugation to Eq. (4.89) and using the identity $(fg)^* = f^* g^*$, the form of the continuity equation that is most useful is:

$$i \iint_{\Omega} \left(\frac{\partial \hat{p}}{\partial r} \hat{u}_r^* + \frac{\partial \hat{p}}{\partial \theta} \hat{u}_\theta^* \right) \, r \, \mathrm{d}r \, \mathrm{d}\theta = k^* \iint \hat{p} \hat{u}_z^* \, r \, \mathrm{d}r \, \mathrm{d}\theta \tag{4.90}$$

Substituting Eqs. (4.90) into Eq. (4.87) enforces conservation of mass and yields:

$$E = A + P + PV \tag{4.91}$$

where E denotes the spatial kinetic energy growth rate, A represents advection (see Eq. (4.77)), P, represents production or linearised Reynolds stress terms (see Eq. (4.77)), and PV denotes the pressure-velocity correlation contribution to the overall kinetic energy budget. Eq. (4.84) is the inviscid limit of Eq. (4.78). The explicit definitions of each of the aforementioned terms are:

$$E \coloneqq -k \iint_{\Omega} \bar{u}_z \Big(|\hat{u}_z|^2 + |\hat{u}_r|^2 + |\hat{u}_\theta|^2 \Big) \, r \, \mathrm{d}r \, \mathrm{d}\theta \tag{4.92a}$$

$$A \coloneqq -i \iint_{\Omega} \Bigg[-i\omega\Big(|\hat{u}_z|^2 + |\hat{u}_r|^2 + |\hat{u}_\theta|^2\Big) + \hat{u}_r^* \left(\bar{u}_r \frac{\partial \hat{u}_r}{\partial r} + \frac{\bar{u}_\theta}{r} \frac{\partial \hat{u}_r}{\partial \theta} - \frac{\bar{u}_\theta}{r} \hat{u}_\theta \right) + \hat{u}_\theta^* \left(\bar{u}_r \frac{\partial \hat{u}_\theta}{\partial r} + \frac{\bar{u}_\theta}{r} \frac{\partial \hat{u}_\theta}{\partial \theta} + \frac{\bar{u}_\theta}{r} \hat{u}_r \right) + \hat{u}_z^* \left(\bar{u}_r \frac{\partial \hat{u}_z}{\partial r} + \frac{\bar{u}_\theta}{r} \frac{\partial \hat{u}_z}{\partial \theta} \right) \Bigg] \, r \, \mathrm{d}r \, \mathrm{d}\theta \tag{4.92b}$$

$$P \coloneqq -i \iint_{\Omega} \Bigg[\hat{u}_r^* \left(\hat{u}_r \frac{\partial \bar{u}_r}{\partial r} + \frac{\hat{u}_\theta}{r} \frac{\partial \bar{u}_r}{\partial \theta} - \frac{\hat{u}_\theta}{r} \bar{u}_\theta \right) + \hat{u}_\theta^* \left(\hat{u}_r \frac{\partial \bar{u}_\theta}{\partial r} + \frac{\hat{u}_\theta}{r} \frac{\partial \bar{u}_\theta}{\partial \theta} + \frac{\hat{u}_\theta}{r} \bar{u}_r \right) + \hat{u}_z^* \left(\hat{u}_r \frac{\partial \bar{u}_z}{\partial r} + \frac{\hat{u}_\theta}{r} \frac{\partial \bar{u}_z}{\partial \theta} \right) \Bigg] \, r \, \mathrm{d}r \, \mathrm{d}\theta \tag{4.92c}$$

$$PV \coloneqq +(k - k^*) \iint_{\Omega} \hat{u}_z^* \hat{p} \, r \, \mathrm{d}r \, \mathrm{d}\theta \tag{4.92d}$$

Note that $k - k^*$ yields an imaginary number even though k is complex in general. By inspection, only the total spatial kinetic energy growth rate integrand is known to be real a priori. All other terms are complex in general, and therefore can only be analysed a posteriori.

4.8.3 Discrete Fourier based formulation

Applying the derivation illustrated in 4.8.2 to the discrete Fourier-transformed system of linear stability equations of Eqs. (4.66) must be done for each particular value of n individually until all values of $|n| \leq N_f$ have been completed. Note that it is possible to recover the entire polar kinetic energy budget of Section 4.8.2 by superposing all the equations associated with each value of n until N_f is reached.

The discrete Fourier transformed linearised momentum equations Eqs. (4.3) (which have incorporated a base flow that has been expanded in exponential form as in Eqs. (4.65)) undergo a inner product by the complex conjugate of the eigenfunctions and are then integrated over r.

For example, the z-momentum equations Eq. (4.66b) in the inviscid limit embedded with the continuity equation (4.66a) and concerning only the UVAS base flow for $N_f \coloneqq 1$ and

$n = 0$ becomes:

$$
\begin{aligned}
-k\int_\Omega \bar{u}_z^0\left(|u_z^0|^2\right)\,r\,\mathrm{d}r \qquad\qquad &= -i\int_\Omega\Bigg[-i\omega\left(|u_z^0|^2\right)\\
-k\int_\Omega u_z^{0*}\left(\bar{u}_z^{-1}u_z^{+1}+\bar{u}_z^{+1}u_z^{-1}\right)\,r\,\mathrm{d}r \qquad &\quad +u_z^{0*}\left(\bar{u}_r^{+1}\frac{\mathrm{d}u_z^{-1}}{\mathrm{d}r}+\bar{u}_r^{-1}\frac{\mathrm{d}u_z^{+1}}{\mathrm{d}r}\right)\\
&\quad +u_z^{0*}\left(-\frac{i}{r}\bar{u}_\theta^{+1}u_z^{-1}+\frac{i}{r}\bar{u}_\theta^{-1}u_z^{+1}\right)\Bigg]\,r\,\mathrm{d}r\\
&\quad -i\int_\Omega\Bigg[u_z^{0*}\left(\frac{\mathrm{d}\bar{u}_z^0}{\mathrm{d}r}u_r^0+\frac{\mathrm{d}\bar{u}_z^{-1}}{\mathrm{d}r}u_r^{+1}+\frac{\mathrm{d}\bar{u}_z^{+1}}{\mathrm{d}r}u_r^{-1}\right)\\
&\quad +u_z^{0*}\frac{i}{r}\left(\bar{u}_z^{+1}u_\theta^{-1}-\bar{u}_z^{-1}u_\theta^{+1}\right)\Bigg]\,r\,\mathrm{d}r\\
&\quad +(k-k^*)\int_\Omega u_z^{0*}p^0\,r\,\mathrm{d}r
\end{aligned}
\tag{4.93}
$$

Similarly, the spatial kinetic energy budget equation for $N_f \coloneqq 1$ and $n = +1$ becomes:

$$
\begin{aligned}
-k\int_\Omega \bar{u}_z^0\left(|u_z^{+1}|^2\right)\,r\,\mathrm{d}r \qquad &= -i\int_\Omega\Bigg[-i\omega\left(|u_z^{+1}|^2\right)\\
-k\int_\Omega u_z^{+1*}\left(\bar{u}_z^{+1}u_z^0\right)\,r\,\mathrm{d}r \qquad &\quad +u_z^{+1*}\left(\bar{u}_r^{+1}\frac{\mathrm{d}u_z^0}{\mathrm{d}r}\right)\Bigg]\,r\,\mathrm{d}r\\
&\quad -i\int_\Omega\Bigg[u_z^{+1*}\left(\frac{\mathrm{d}\bar{u}_z^0}{\mathrm{d}r}u_r^{+1}+\frac{\mathrm{d}\bar{u}_z^{+1}}{\mathrm{d}r}u_r^0\right)\\
&\quad +u_z^{+1*}\frac{i}{r}\left(\bar{u}_z^{+1}u_\theta^0\right)\Bigg]\,r\,\mathrm{d}r\\
&\quad +(k-k^*)\int u_z^{+1*}p^{+1}\,r\,\mathrm{d}r
\end{aligned}
\tag{4.94}
$$

For completeness, the spatial kinetic energy budget equation for $N_f \coloneqq 1$ and $n = -1$ is:

$$
\begin{aligned}
-k\int_\Omega \bar{u}_z^0\left(|u_z^{-1}|^2\right)\,r\,\mathrm{d}r \quad &= -i\int_\Omega\Bigg[-i\omega\left(|u_z^{-1}|^2\right)\\
-k\int_\Omega u_z^{-1*}\left(\bar{u}_z^{-1}u_z^0\right)\,r\,\mathrm{d}r \quad &\qquad + u_z^{-1*}\left(\bar{u}_r^{-1}\frac{\mathrm{d}u_z^0}{\mathrm{d}r}\right)\Bigg]\,r\,\mathrm{d}r\\
&\quad -i\int_\Omega\Bigg[u_z^{-1*}\left(\frac{\mathrm{d}\bar{u}_z^0}{\mathrm{d}r}u_r^{-1}+\frac{\mathrm{d}\bar{u}_z^{-1}}{\mathrm{d}r}u_r^0\right)\\
&\qquad\quad - u_z^{-1*}\frac{i}{r}\left(\bar{u}_z^{-1}u_\theta^0\right)\Bigg]\,r\,\mathrm{d}r\\
&\quad +(k-k^*)\int_\Omega u_z^{-1*}p^{-1}\,r\,\mathrm{d}r
\end{aligned}
\tag{4.95}
$$

where, for Eqs. (4.93) (4.94), and (4.95), the first integral on the left-hand side is the total spatial kinetic energy growth rate associated with self-interaction and the second integral is the total spatial kinetic energy growth rate associated with inter-mode coupling for the u_z^n eigenmode. For the right-hand side, the first integral is the 'Advection' term, the second integral is the 'Production' term, and the third integral is the 'Pressure-velocity correlation' term for the u_z^n eigenmode.

This procedure illustrated above for the z-momentum equation is repeated for the r- and $\theta-$momentum equations (Eq. (4.66c) and Eq. (4.66d), respectively). Just as in Section 4.8.2, the resultant equations are summed to yield the overall spatial kinetic energy budget equation for a particular eigenfunction azimuthal number n. For brevity, the equations are not displayed in this section. The same procedure is applied to $N_f \coloneqq 2$, yielding 5 kinetic energy budget equations, and $N_f \coloneqq 3$, yielding 7 kinetic energy budget equations, which are elucidated in Appendix C.

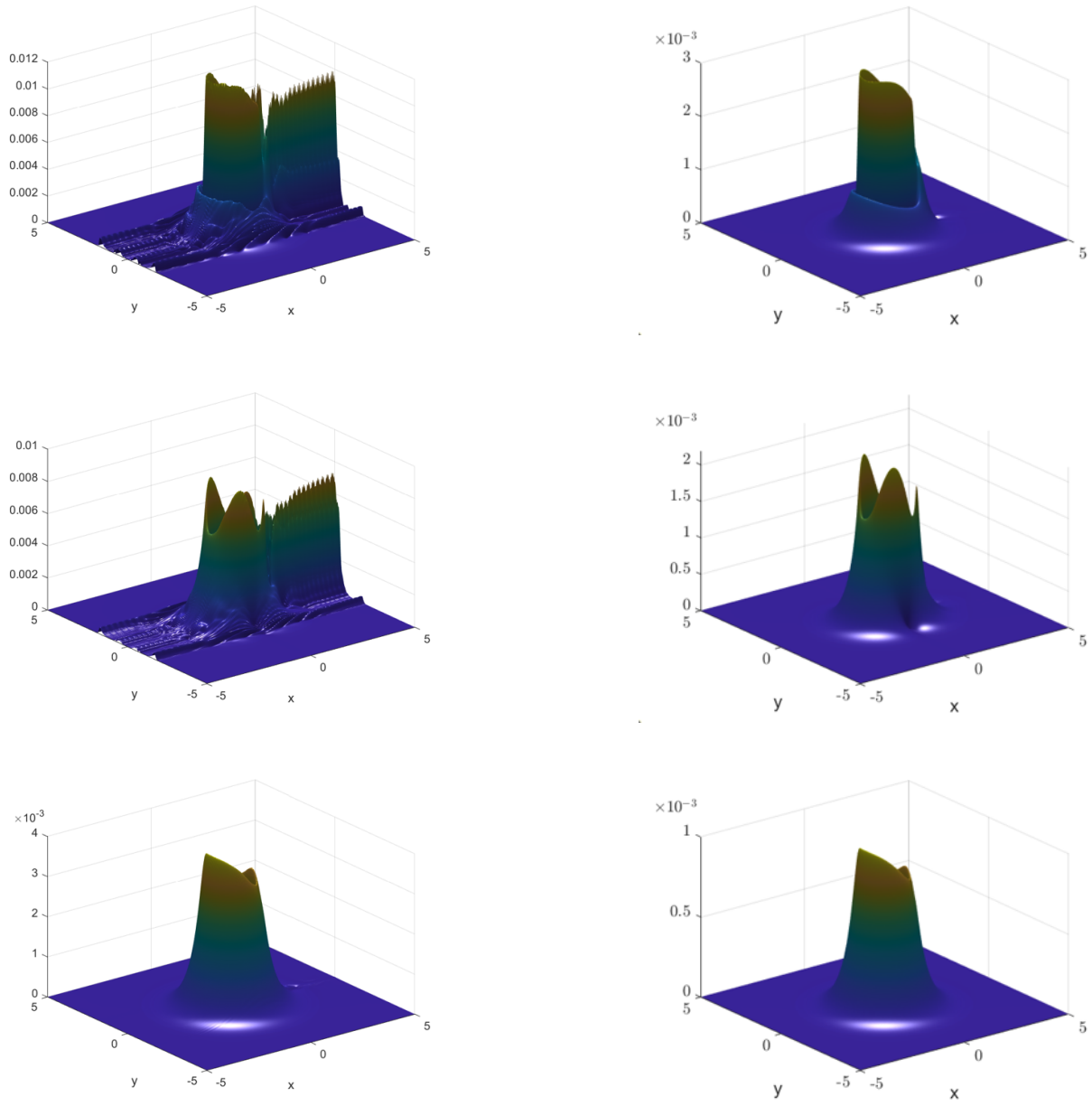

(a) From central finite difference

(b) From upwinded finite difference

Figure 4.1: Examples of non-physical oscillations in the eigenfunctions of the axisymmetric mode of the $R = 4$, $\theta_0/R_0 = 1/15$ UVAS base flow. Left column corresponds to using central finite difference. Right column corresponds to using the present upwind approach.

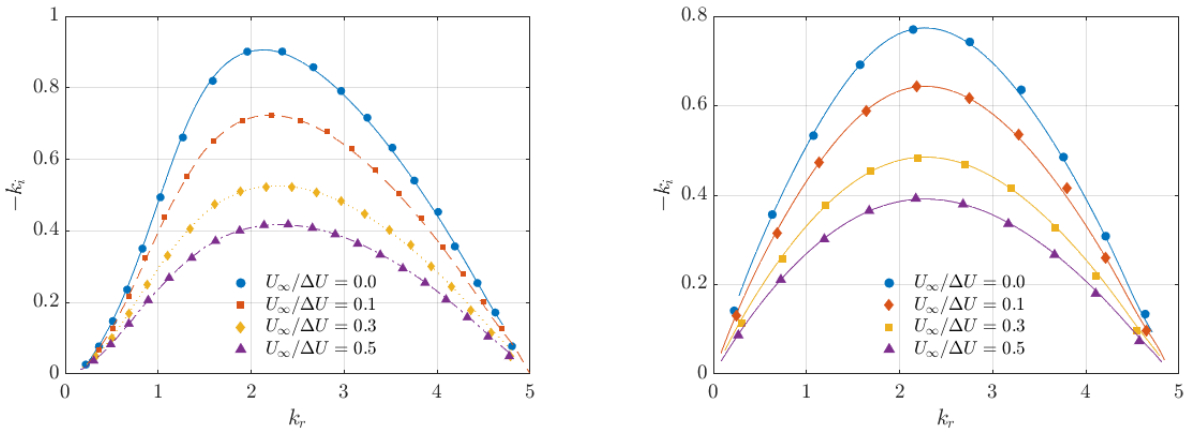

(a) Axisymmetric mode

(b) First helical mode

Figure 4.2: Spatial growth rates plotted against wavenumbers for the (a) axisymmetric and (b) first helical modes of the axisymmetric round coaxial jet. Symbols correspond to results reported by Michalke & Hermann (1982) while lines correspond to the present results for the velocity ratios indicated in the legends.

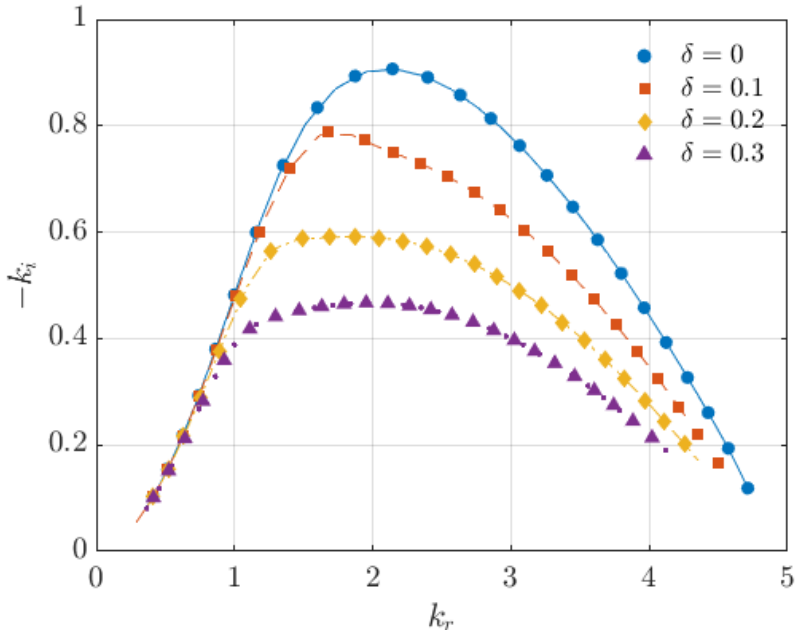

Figure 4.3: Spatial growth rates plotted against wavenumbers for the axisymmetric mode of the asymmetric coaxial jet. Lines correspond to results reported by Freitas (2019) while symbols correspond to the present results for various values of δ, the amplitude of the asymmetric term.

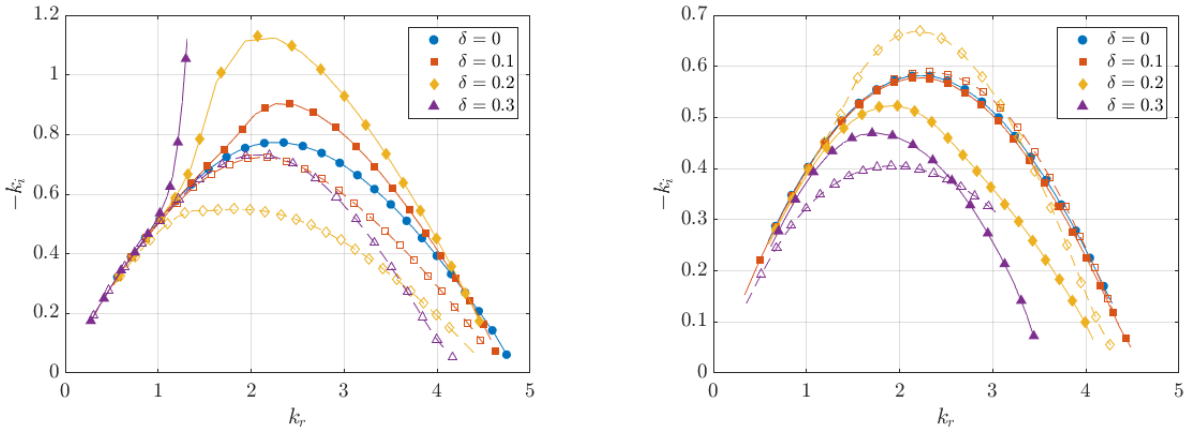

(a) First helical mode

(b) Second helical mode

Figure 4.4: Spatial growth rates plotted against wavenumbers for the (a) first and (b) second helical modes of the asymmetric coaxial jet. Lines correspond to results reported by Freitas (2019) while symbols correspond to the present results for various values of δ, the amplitude of the asymmetric term. Filled symbols correspond to the symmetric mode and empty symbols correspond to the anti-symmetric mode.

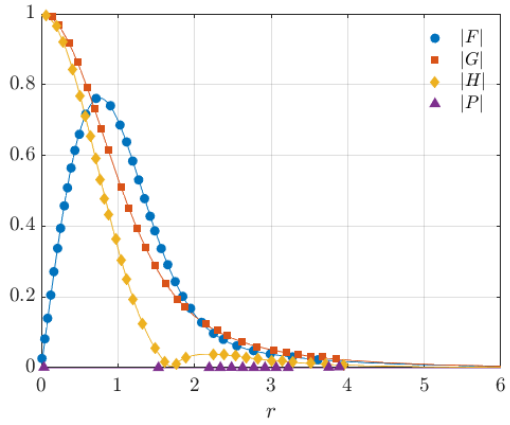

(a) $m \coloneqq 1$, $a \coloneqq 0$, $q \coloneqq 0.7$, $\omega \coloneqq 0.0425$

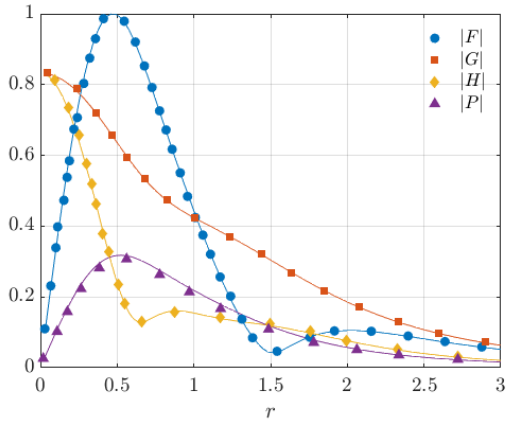

(b) $m \coloneqq -1$, $a \coloneqq -1.268$, $q \coloneqq 0.6$, $\omega \coloneqq -0.78$

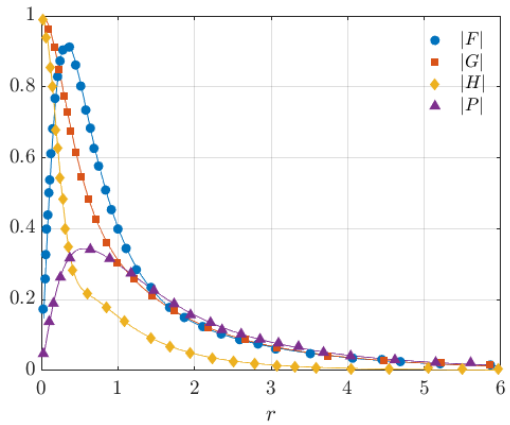

(c) $m \coloneqq -1$, $a \coloneqq 0.01$, $q \coloneqq 0.6$, $\omega \coloneqq 0.2$

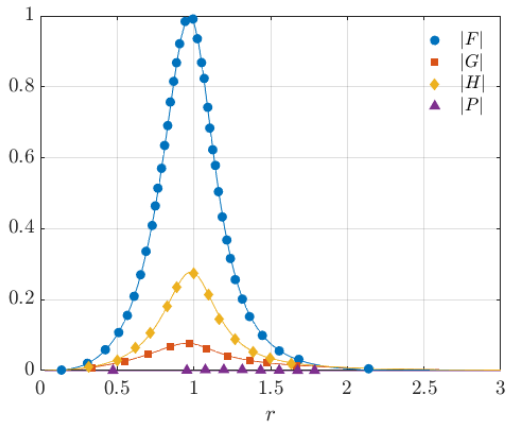

(d) $m \coloneqq 3$, $a \coloneqq 0$, $q \coloneqq 0.1$, $\omega \coloneqq 0.01$

Figure 4.5: Normalised spatial eigenfunction amplitudes for the Batchelor q-vortex corresponding to different conditions as indicated. Symbols correspond to the results of Olendraru *et al.* (1999) while the lines correspond to the present results for various conditions.

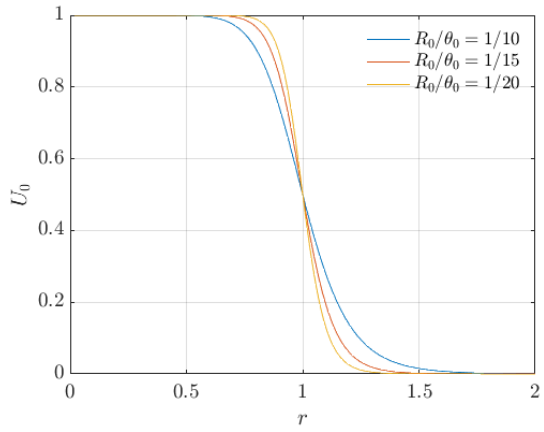

(a) $U_0(r)$

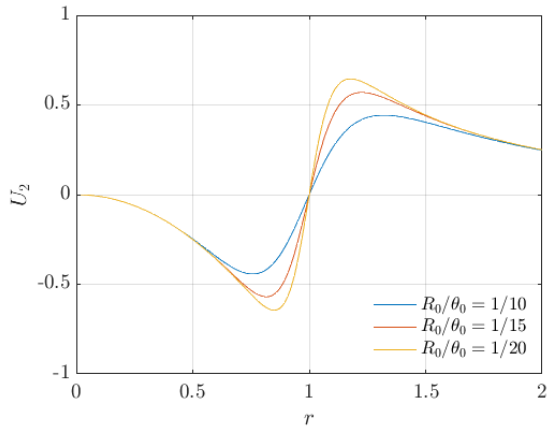

(b) $U_2(r)$

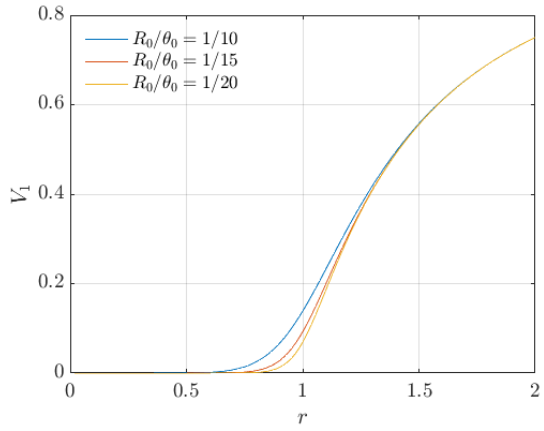

(c) $V_1(r)$

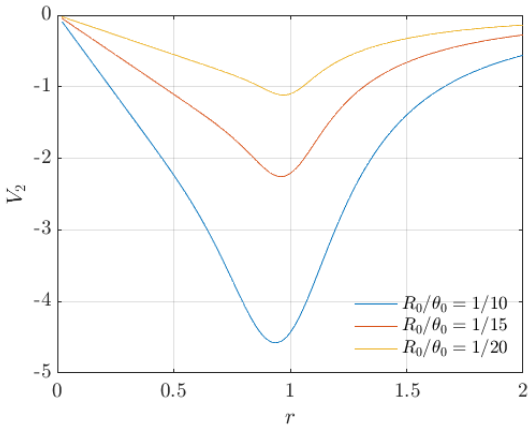

(d) $V_2(r)$

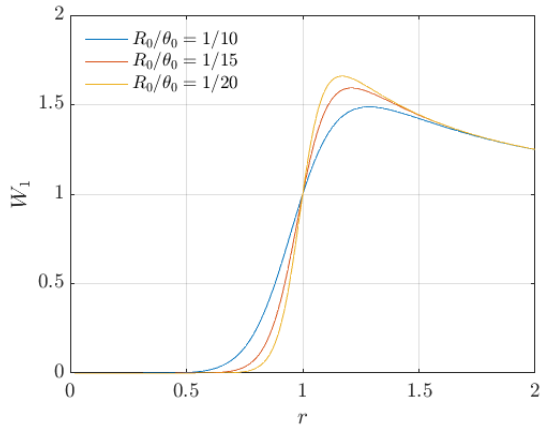

(e) $W_1(r)$

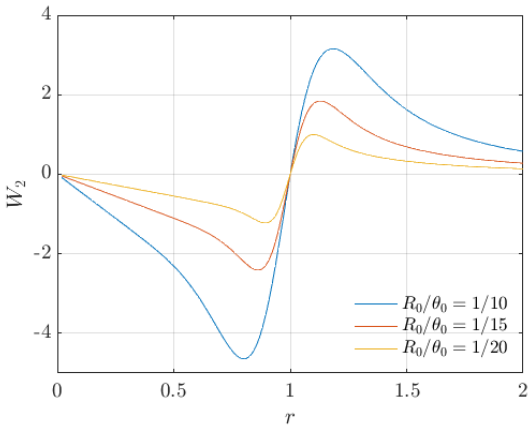

(f) $W_2(r)$

Figure 4.6: Radial slices of the hyperbolic-tangent base flow for $\theta_0/R_0 = 1/10, 1/15, 1/20$.

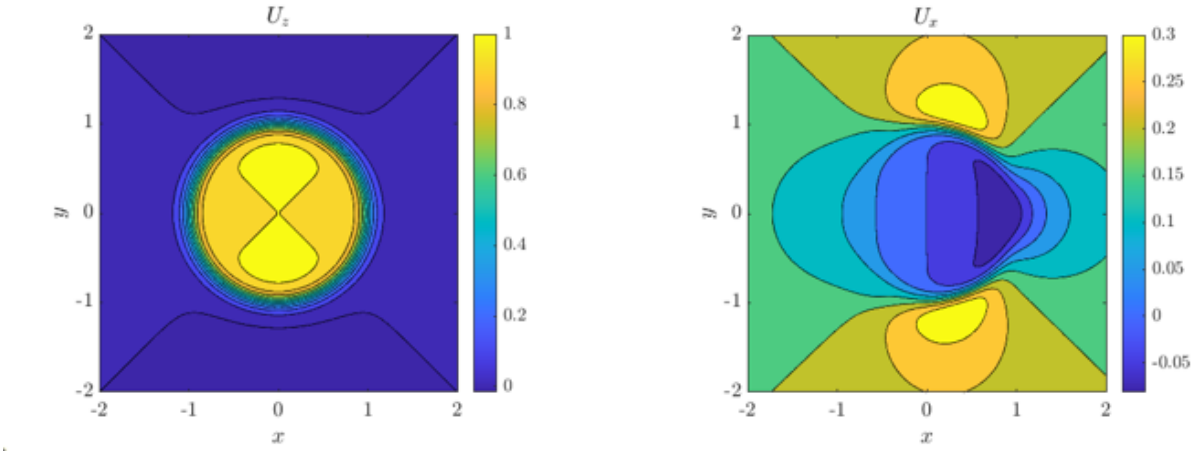

(a) $\bar{u}_z(r)$ (b) $\bar{u}_x(r)$

Figure 4.7: Contour plots of the (a) axial and (b) streamwise velocity fields for the $R = 5$, $\theta_0/R_0 = 1/15$ hyperbolic-tangent base flow.

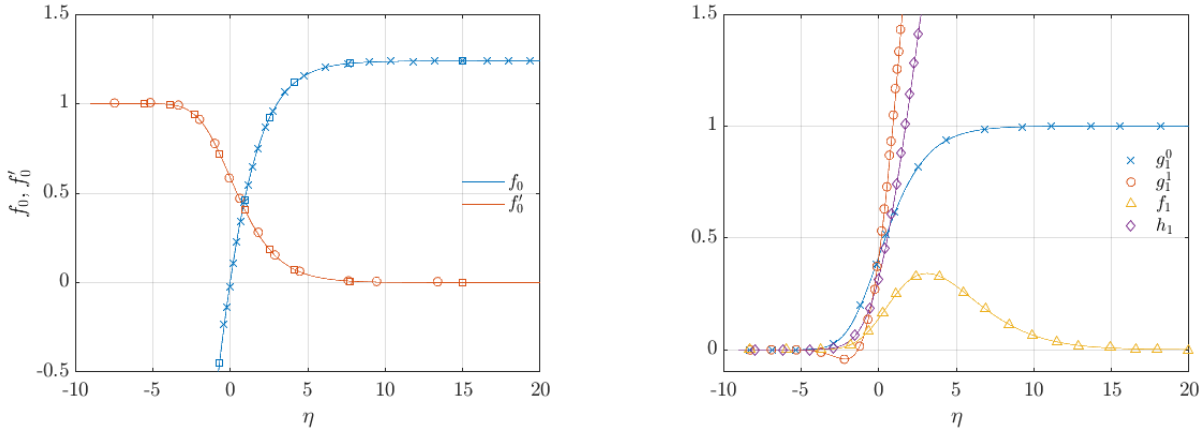

(a) f_0 and f_0' (b) g_1^0, g_1^1, f_1, and h_1

Figure 4.8: Similarity solutions $f_0, f_0', g_1^0, g_1^1, f_1, h_1$ plotted against η. Lines correspond to the present results while the square symbols correspond the results of Lock (1951) and all other symbols correspond to the results of Alves & Kelly (2008).

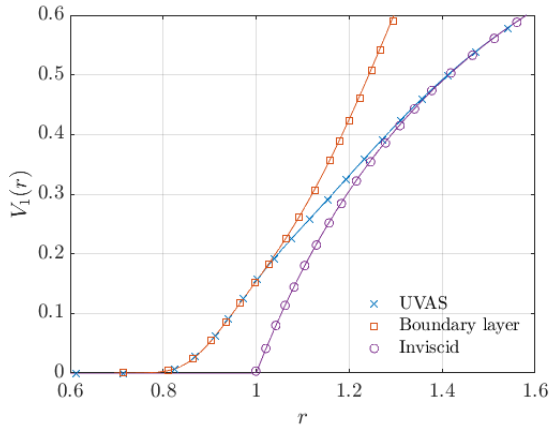

(a) UVAS $V_1(r)$

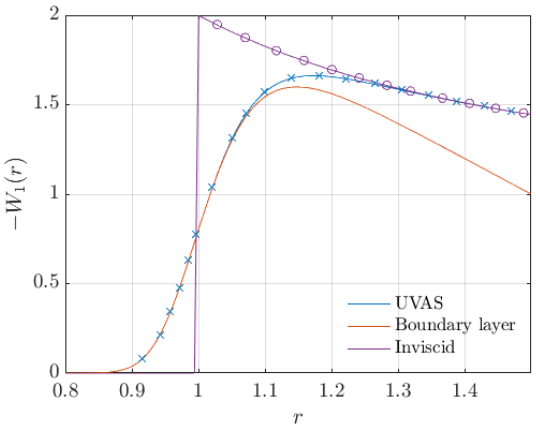

(b) UVAS $W_1(r)$

Figure 4.9: UVAS base flow for Re = 1000, $z = 1$ plotted against r. Lines correspond to the present results while the symbols correspond the results of Alves & Kelly (2008).

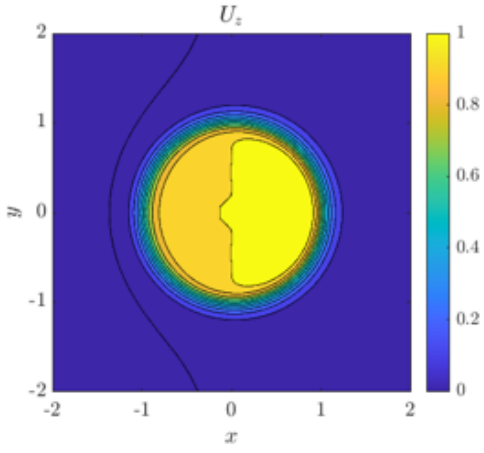

(a) $\bar{u}_z$

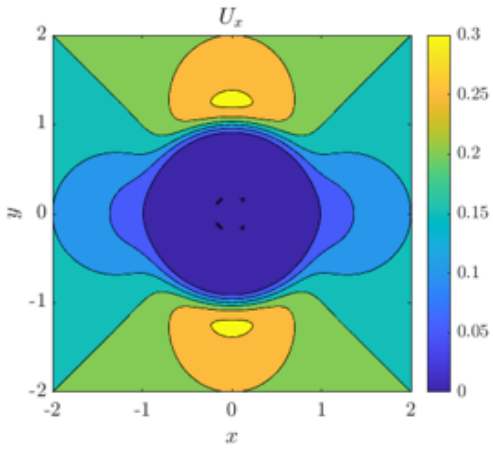

(b) $\bar{u}_x$

Figure 4.10: Contour plots of the (a) axial and (b) streamwise velocity fields for the $R = 5$, $\theta_0/R_0 = 1/15$ UVAS base flow.

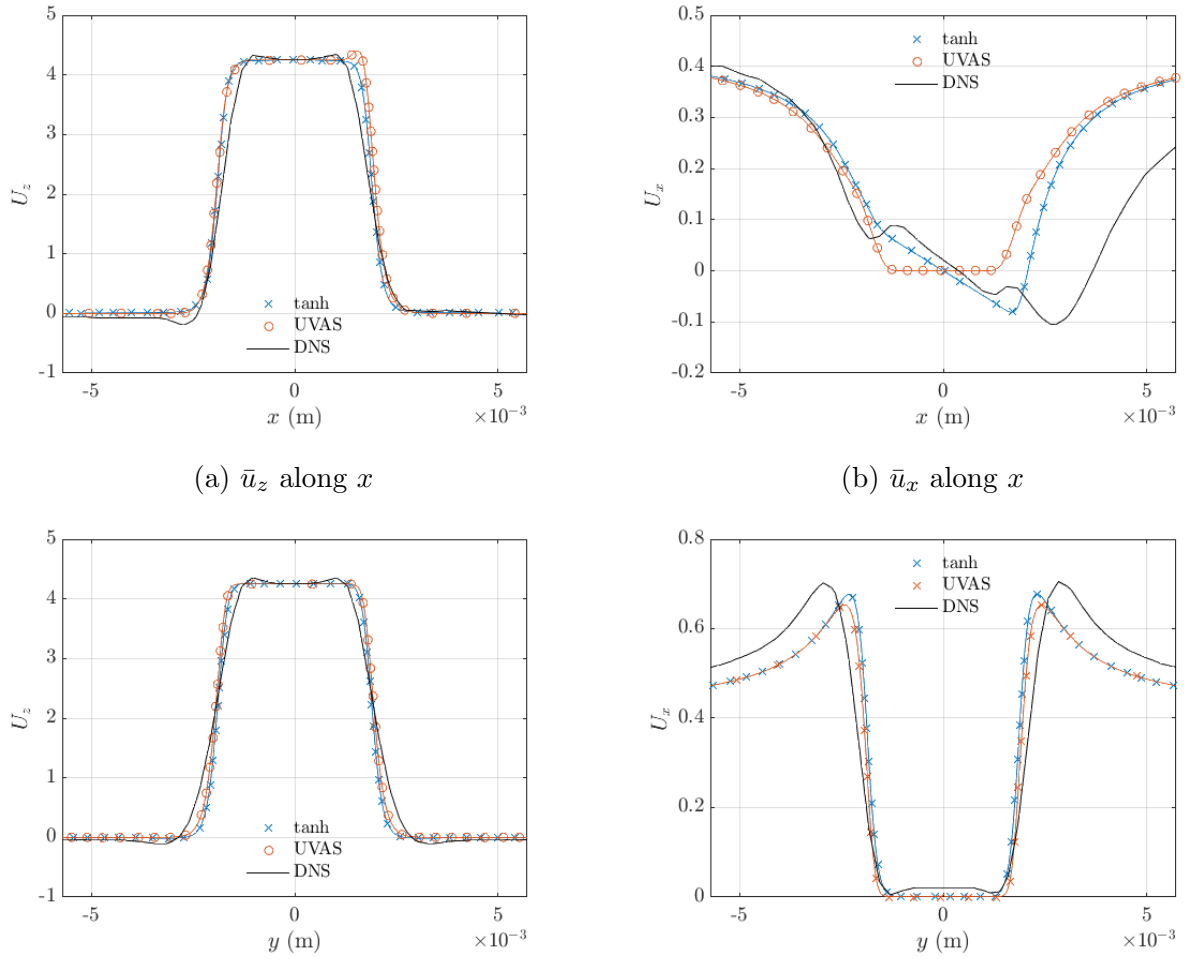

(a) $\bar{u}_z$ along x

(b) $\bar{u}_x$ along x

(c) $\bar{u}_z$ along y

(d) $\bar{u}_x$ along y

Figure 4.11: Hyperbolic-tangent, UVAS, and DNS-derived velocity profiles plotted in the streamline x and spanwise y directions for jet-to-crossflow velocity ratio $R \coloneqq 10$. Lines correspond to the present profiles while the symbols correspond to the profiles of Alves (2006) for hyperbolic-tangent, UVAS. The black lines correspond to the direct numerical simulations (DNS) by Alves (2006).

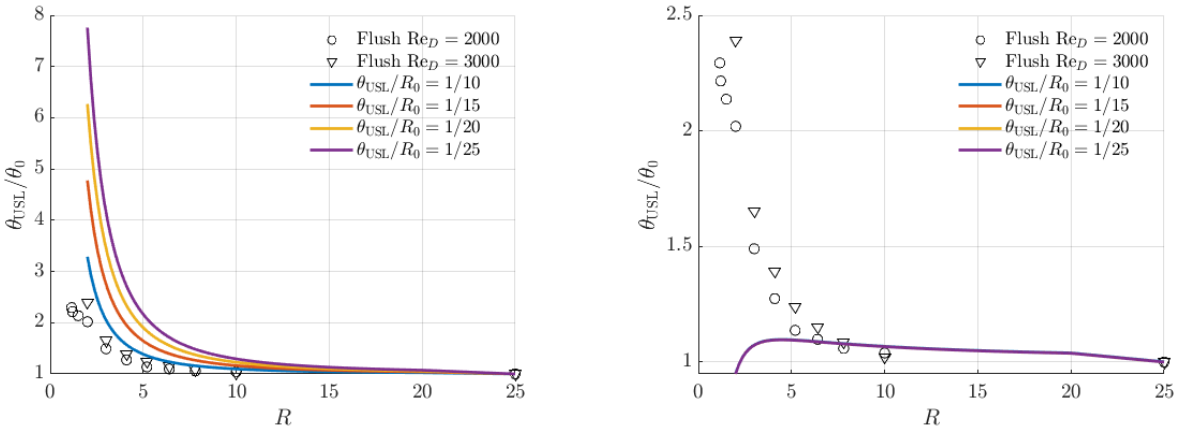

(a) tanh (b) UVAS

Figure 4.12: Upstream shear layer momentum thicknesses θ_{USL} normalised by the free jet equivalent momentum thickness θ_0 for various values of velocity ratio R for the (a) hyperbolic-tangent and (b) UVAS jet-in-crossflow base flow models. Symbols correspond to the experimental measurements of Megerian *et al.* (2007).

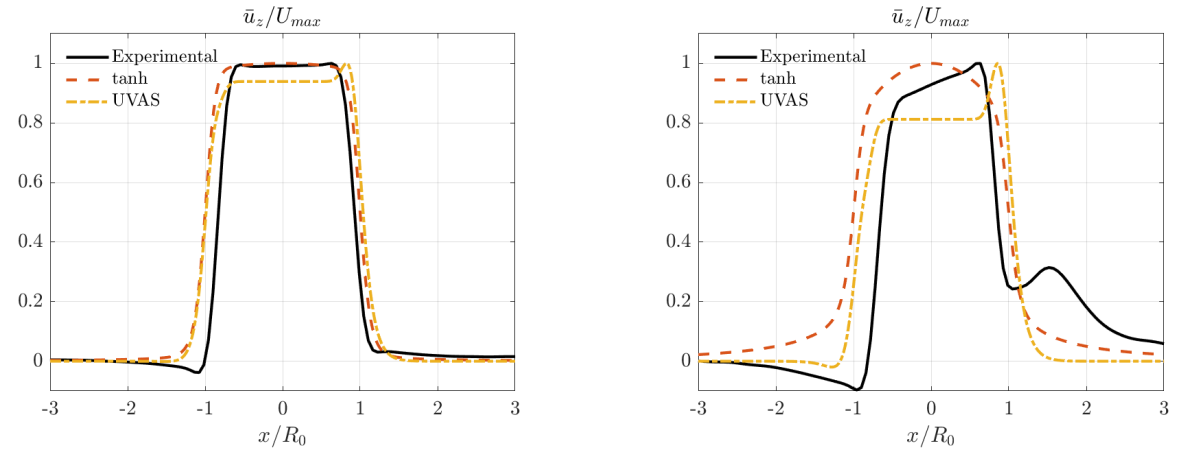

(a) $R = 6.4$ (b) $R = 2.2$

Figure 4.13: Normalised axial velocity fields $\bar{u}_z/U_{\mathrm{max}}$ of the tanh, UVAS, and experiments of Harris *et al.* (2021) taken along the centreplane.

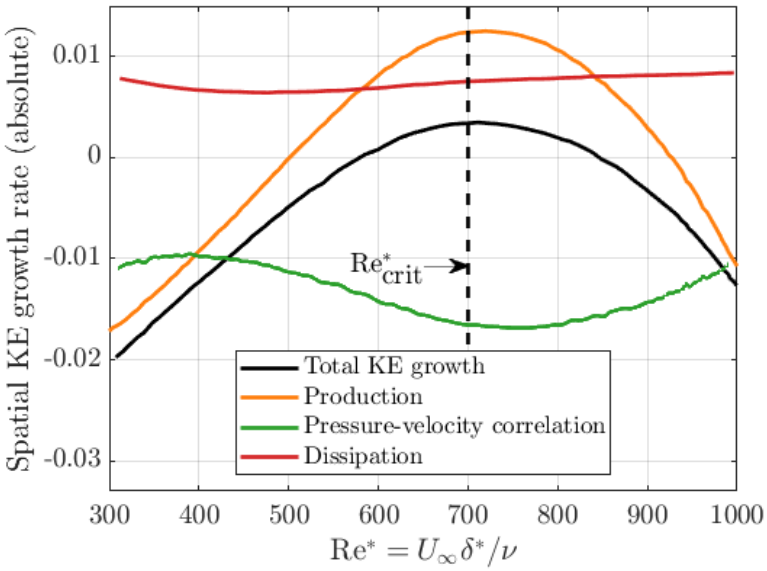

(a) In absolute terms

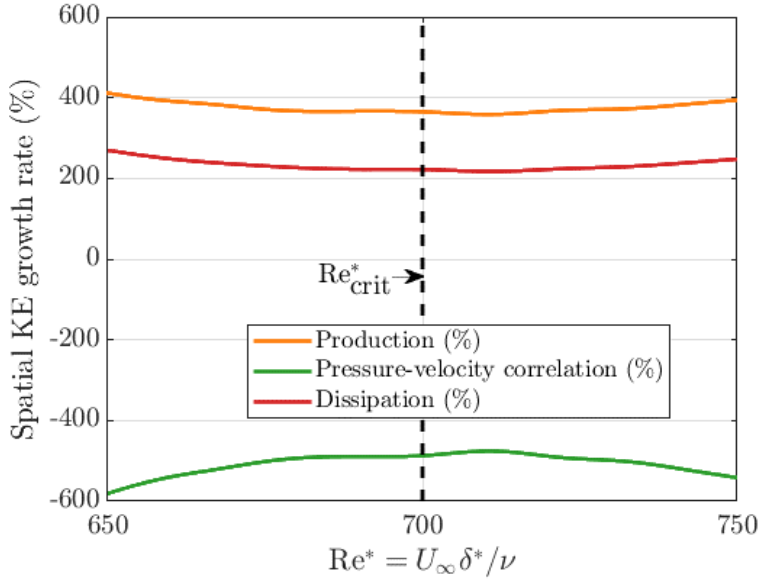

(b) In percentage terms

Figure 4.14: The spatial kinetic energy budget results of Hama *et al.* (1980) for a range of Reynolds numbers Re^* with the maximum spatial growth rate corresponding to $\mathrm{Re}^*_{\mathrm{crit}}$.

CHAPTER 5

Results and discussion for jet-in-crossflow linear stability

The governing equations, jet-in-crossflow base flows, and numerical solution procedure outlined in Section 4 have been used and their results are presented in the following.

5.1 Fully-coupled results: Cartesian and polar grids

The inviscid linear stability results of the viscous UVAS base flow with momentum thicknesses $\theta_0/R_0 = 1/15$ and $1/10$ from both the Cartesian grid and the polar grid formulations are presented below. Comparisons against experiments and the prior asymptotic expansion-based inviscid linear stability analysis of the same base flow by Alves & Kelly (2008) are made whenever possible. The experimental Strouhal numbers corresponding to the flush nozzle with $\mathrm{Re}_D = 1900$ are from Shoji *et al.* (2020*a*) whereas those corresponding to the flush nozzle at $\mathrm{Re}_D = 2000, 3000$ are from Megerian *et al.* (2007). The experimental spatial growth rates were obtained from Alves *et al.* (2008). The experimentally-measured upstream shear layer momentum thickness is approximately $1/16.5 \lesssim \theta_0/R_0 \lesssim 1/15$.

As Fig. 5.1 indicates, the experimentally-measured spatial growth rate of the axisymmetric mode destabilises as the crossflow becomes stronger. The prior asymptotic expansion-based linear stability analysis of Alves & Kelly (2008) qualitatively aligns with this experimental observation. However, as Fig. 5.1c clearly demonstrates, the present fully-coupled approaches from both Cartesian and polar frameworks yield spatial stabilisation as the cross-

flow becomes stronger for both momentum thicknesses considered - a behaviour that diverges from both prior experimental and linear stability analyses performed with an asymptotic expansion approach.

By contrast, the present predictions of Strouhal numbers (Fig. 5.1a) and wavenumbers (Fig. 5.1b) qualitatively match the past asymptotic expansion-based linear stability results of Alves & Kelly (2008) as well as the general trend of the experimental results reasonably well. Indeed, the present Strouhal numbers feature an inflection point for $R \lesssim 3$, similar to experimental observations; this inflection is not observed at lower R values (larger λ) by the asymptotic expansion-based linear stability analysis of Alves & Kelly (2008). Yet the present results show lower Strouhal numbers and wavenumbers than those predicted by Alves & Kelly (2008) and of experimental measurements. This deviation occurs at lower R values; for R greater than approximately 12; in this range, approaching the free jet, the quantitative correspondence between the present and prior asymptotic expansion-based linear stability analysis is excellent.

It is possible that, perhaps, the pursuit of an inviscid stability mechanism is contributing to the non-physical stabilisation of the axisymmetric mode as R decreases. Therefore, viscous stability mechanisms were included in the eigenproblem through finite $\mathrm{Re}_D = 2 \times 10^3, 2 \times 10^4$ when considering the UVAS base flow with $\theta_0/R_0 = 1/15$. Figure 5.5a displays the spatial growth rate of the axisymmetric mode for $R = 10$ plotted against the Strouhal number for three Reynolds numbers: $\mathrm{Re}_D = \infty, 2 \times 10^3, 2 \times 10^4$. The figure clearly indicates that, as Re_D decreases, the eigenspectrum shifts downwards. The subsequent decrease of spatial growth rate for that and for other values of R can be seen in Figure 5.5b. Indeed, the effect of physical viscosity is to weaken the axisymmetric mode. Therefore, viscosity is not the cause of non-physical trends in the spatial growth rate of the axisymmetric mode. Note that less numerical dissipation was necessary as Re_D decreased.

Thinner momentum thicknesses are also known to contribute to spatial destabilisation (Morris, 1976). Figure 5.6 presents the eigenspectrum of the axisymmetric mode of the

UVAS base flow for momentum thicknesses $\theta_0/R_0 = 1/20, 1/15, 1/10$. The thinnest momentum thickness, $\theta_0/R_0 = 1/20$, exhibits a spatial growth rate that slightly destabilises as R decreases. However, this destabilisation is not commensurate with experimental trends. Therefore, the momentum thickness is not the sole cause of the non-physical trends in growth rate.

Hitherto, only the eigenspectra of the UVAS base flow have been displayed. The spatial eigenvalues of the tanh base flow were more challenging to obtain because the non-physical oscillations were more challenging to eliminate. Therefore, only $R \geq 8$ results could be obtained. The spatial eigenvalues of the troublesome axisymmetric mode are presented with comparison against those from the UVAS base flow (Alves & Kelly, 2008), experiments (Megerian *et al.*, 2007), and prior asymptotic expansion-based stability analysis (Alves *et al.*, 2008) in Figure 5.7. From this figure, it is evident that the spatial growth rate stabilises as R deceases. Therefore, both of the asymptotic base flows, the UVAS and the tanh, have axisymmetric modes that stabilise as R decreases. Hence, the choice of base flow by itself is not the sole cause of the non-physical stabilisation of growth rate.

Generally, the results obtained from Cartesian and polar frameworks for a range of symmetric and anti-symmetric helical modes are quantitatively similar. This is some additional evidence to verify the correctness of the stability codes used, though the differences in the most spatially-unstable axisymmetric mode with respect to the prior asymptotic expansion-based LSA and experimental trends requires further exploration using the kinetic energy budget analysis in Section 5.3.

The present analysis indicates that the axisymmetric mode of the UVAS base flow is the most unstable, with the higher helical modes being increasingly weak. This aligns with the observations from a Fourier-transformed local linear stability analysis of an inviscid base flow of the jet-in-crossflow by Alves *et al.* (2007). Both the present and prior analysis of Alves *et al.* (2007) were able to distinguish between symmetric (S) and anti-symmetric (AS) helical modes to identify any degeneracy-breaking about the plane of symmetry of the base

flow along the centreplane ($y = 0$). The present viscous linear stability analysis using the viscous UVAS base flow may be considered as an extension of Alves *et al.* (2007). The results are shown presently refer to the first anti-symmetric mode as 1AS, the first symmetric mode as 1S, and so forth for the higher helical modes. Figs. 5.2- 5.4 indicate that all helical modes stabilise as the crossflow becomes stronger with the thicker momentum thickness case $\theta_0/R_0 = 1/10$ being most stable.

The behaviour of the second helical mode as R varies obtained from the present fully-coupled inviscid linear stability analysis is displayed in Fig. 5.3. For comparison, results obtained from the asymptotic expansion-based inviscid linear stability analysis of Alves (2006) is also presented. Note that these prior results were reconstructed from linear interpolation of spline-fitted digitised values of α_0 and α_2 from Alves (2006) - indicating approximately a 10% error and explaining the relatively jagged contours. By inspection, there is an excellent quantitative comparison of the behaviour of the second helical mode for $R \gtrsim 8$. For smaller velocity ratios R (or larger crossflow velocities), both the current fully-coupled for either Cartesian or polar coordinate representation and prior asymptotic expansion-based linear stability analyses indicate spatial stabilisation of the second helical mode with qualitatively good agreement. The fact that the spatial growth rate trends agree for the second helical mode is interesting because the trends for the spatial growth rate of the axisymmetric mode substantially and non-physically. Moreover, the two analyses differ on the qualitative behaviour of the Strouhal number and wavenumber. The presently-captured degeneracy-breaking of the second helical mode indicates that the second anti-symmetric helical (2AS) mode is slightly more spatially unstable than the second symmetric (2S) mode and prefer distinct Strouhal numbers. The asymptotic expansion-based linear stability analysis of the UVAS base flow by Alves (2006) was not able to capture any degeneracy breaking. This result may have implications for control and actuation strategies of the jet-in-crossflow that will be discussed in more detail later in this section.

Due to a special resonance occurring for the first helical mode, Alves & Kelly (2008) did

not report results for the first helical mode for the UVAS base flow. This special resonance also occurred with the inviscid stability analysis of an inviscid base flow of Alves *et al.* (2007). Additionally, Alves & Kelly (2008) did not report any results for the third or higher helical modes owing to the axisymmetric mode being more spatially unstable.

It is important to note that eigenspectra obtained from local linear stability analyses of fundamentally nonlocal flow fields are well-known to be less accurate at low frequencies (or wavenumbers) due to the locality approximation (Crighton & Gaster, 1976; Tam & Morris, 1980; Suzuki & Colonius, 2006; Gudmundsson & Colonius, 2019; Alves *et al.*, 2007). A local stability analysis presumes that the base flow does not evolve in space, that the flow field is invariant to the initial condition, and cannot account for the effect of disturbances that propagate up- or downstream which may affect the base flow (Juniper *et al.*, 2014). Consequently, the computed eigenspectra embed a memorylessness quality - the frequencies, wavenumbers, and growth rates must be interpreted as applicable locally only (Crighton & Gaster, 1976). Capturing the stability characteristics at various streamwise stations using a local stability analysis is typically performed by varying the base flow (Coenen *et al.*, 2008; Crighton & Gaster, 1976). A local stability analysis may provide sufficiently accurate results when the base flow spatially evolves very slowly compared to the disturbance wavelength (Schmid & Henningson, 2001). However, if it is found that lower frequency St_D disturbance waves are associated with small wavenumbers and thus large disturbance wavelengths, then the disturbance is exposed to more base flow evolution. Hence, the parallel-flow approximation is violated and therefore a local stability analysis is expected to yield less accurate results (Suzuki & Colonius, 2006). Accounting for the nonlocal (i.e., slowly-evolving) nature of the base flow can improve eigenspectra calculations as compared against experiments, as illustrated by the linearised parabolised stability analysis of Gudmundsson & Colonius (2019) for an axisymmetric free jet. Notably, the eigenvalues associated with the axisymmetric mode of the jet improved more than the helical modes in the low-frequency regime. This may be explained by the experimental observation that axisymmetric disturbance waves

have longer wavelengths (smaller wavenumbers) than their higher helical mode counterparts (Suzuki & Colonius, 2006). Hence, the parallel-flow approximation is least applicable to the axisymmetric mode.

Given that both the present fully-coupled and prior asymptotic expansion-based linear stability analyses of Alves *et al.* (2007, 2008); Alves & Kelly (2008) are local while the base flow evolves in the streamwise direction, it is important to regard all such eigenspectra for any azimuthal mode associated with the low frequency regime are less trustworthy. Indeed, Alves (2006) reported 'odd' behaviour at low frequencies for both the inviscid and the viscous base flows considered. Supporting the hypothesis that a local linear stability analysis of an evolving base flow is responsible for such odd behaviour at low frequency is the fact that the eigenspectra in the low frequency regime behaved unusually over a wider range of frequencies (and hence wavenumbers) as R decreased (Alves, 2006). This decrease of R (increase of λ) is associated with the increasing significance of the nonlocality of the base flow because the crossflow velocity and associated distortion of the jet are increasing (Alves *et al.*, 2007). It is important to comment that the local linear stability analysis of Alves *et al.* (2007) and Alves *et al.* (2008) found that the range of frequencies over which the eigenspectra behaved unusually widened for the higher helical modes (Alves, 2006). Therefore, any comparisons made between eigenspectra avoided the low-frequency regime.

One possibility to obtain eigenspectra in the low-frequency regime may be to consider an inviscid base flow, as was performed by Alves *et al.* (2007). Open shear flows have been modelled with base flows that feature a discontinuity to represent the inviscid limit e.g., Batchelor & Gill (1962). Corresponding linear stability analyses are known to yield growth rates that increase monotonically with frequency or wavenumber, depending on if the analysis is spatial or temporal, respectively. Examples include the planar mixing layer, jets, and wakes (Lin, 1955; Chandrasekhar, 1961; Drazin & Reid, 1981; Crow & Champagne, 1971; Schmid & Henningson, 2001). By contrast, linear stability analyses using smooth base flows representing a finite momentum thickness typically have a maximum growth rate

(Criminale *et al.*, 2003). However, stability analyses of inviscid and viscous base flows can yield similar eigenspectra in the limit of small frequencies that may align with experimental measurements. For example, one may compare the eigenspectra of a viscous axisymmetric free jet base flow of Morris (1976) against those of an inviscid cylindrical vortex sheet of Michalke (1970) in the low-frequency regime. Experimental comparisons may be found in Freymuth (1966); Michalke (1965); Crow & Champagne (1971); Michalke (1964). Hence, it is expected that results from any local linear stability analysis of a sufficiently evolving (i.e., nonlocal) base flow is likely to be unreliable at low frequencies for aforementioned reasons, but the behaviour from inviscid and viscous base flows should be comparable in the low-frequency regime.

Interestingly, degeneracy breaking is observed for all helical modes in the present analysis, where the AS and S modes have eigenspectra that are not identical to one another, which was not found in the asymptotic expansion-based linear stability analysis of viscous base flows in Alves *et al.* (2008); Alves & Kelly (2008) but was found in the multiple mode analysis of an inviscid base flow in Alves *et al.* (2007). Presently, there is a preference for the first symmetric helical mode, the second anti-symmetric mode, and the third symmetric helical mode while the axisymmetric mode remains the most spatially unstable of all azimuthal modes. Note that these modes are symmetric or anti-symmetric with respect to the plane of symmetry along $y = 0$ for the jet-in-crossflow base flows used. The anti-symmetric and symmetric first helical modes undergo the greatest degeneracy breaking while the second and third helical modes exhibit diminishing degeneracy breaking. However, for all helical modes obtained from the present study, any amount of crossflow causes degeneracy breaking. As R decreases, the two types of helical mode yield eigenspectra branches that increasingly diverge from each other. It is important to observe that the symmetric and the anti-symmetric modes have peak spatial growth rates that are generally associated with distinct Strouhal numbers. This implies that it may be possible for natural or artificial excitation to amplify the growth of a helical disturbance that can affect whether the jet-in-crossflow evolves asymmetrically

downstream.

Indeed, the present determination of the helical modes of the jet-in-crossflow of the viscous UVAS base flow may inform control or excitation strategies. For example, Corke & Kusek (1993) demonstrated that it was possible to amplify the growth of helical modes of an axisymmetric free jet by applying acoustic excitation near the jet exit. It is also possible to excite multiple modes simultaneously to create a desired flow field (Raman *et al.*, 1991; Danaila & Boersma, 2000; Tyliszczak & Boguslawski, 2007; Martin & Meiburg, 1991). Forcing both the $m = \pm 1$ helical modes simultaneously led to noticeably stronger vortex roll-up in a jet-in-crossflow (Alves, 2006). Besnard *et al.* (2022) demonstrated that asymmetric excitation of the crossflow could impact the structure, evolution, and mixing of the jet-in-crossflow.

Additionally, the unforced jet-in-crossflow has been experimentally demonstrated to have a naturally asymmetric flowfield evolution, particularly for high jet-to-crossflow velocity ratios R (Getsinger *et al.*, 2014; Gevorkyan *et al.*, 2016) and is generally challenging to make symmetric (Smith & Mungal, 1998). Even small-amplitude asymmetric disturbances experimentally imposed upon the crossflow can greatly impact the symmetry of the relatively high $R = 7.8$ ($J = 61$) and $R = 6.4$ ($J = 41$) jets-in-crossflow (see Figures 8 and 9, for example, in Besnard *et al.* (2022)). These flow conditions correspond to jets-in-crossflow that naturally feature asymmetric flow structures downstream, are convectively unstable, and have sufficiently high jet-to-crossflow velocity ratios to enable comparisons to the axisymmetric free jet. The axisymmetric free jet has been found to have linear stability helical modes that are degenerate - meaning that the positive and negative azimuthal modes $\pm m$ yield identical eigenspectra (Michalke, 1971; Morris, 1976). In principle, this means that the resulting flowfield should be geometrically symmetric assuming that the $\pm m$ helical disturbances are identically balanced (viz., equal and opposite) (Corke & Kusek, 1993; Mallier, 1998; Alves, 2006).

However, our present study as well as the asymptotic expansion-based analysis of an

inviscid base flow by Alves *et al.* (2007) find that any amount of crossflow applied to the jet base flow breaks degeneracy of the linear helical modes and that degeneracy breaking is most pronounced for the first helical mode. Moreover, Alves (2006) used a direct numerical simulation of the jet-in-crossflow to investigate low-amplitude helical forcing and found that forcing in a $m = +1$ manner generates different asymmetries than when forcing with $m = -1$. Given that the high R jet-in-crossflow is convectively unstable, one possible mechanism that may cause asymmetric evolution of a jet-in-crossflow is that low-amplitude ambient noise amplifies one of the symmetry-breaking helical modes that spatially grows in favour of its twin helical mode of opposite sign (Besnard, 2019; Alves, 2006). The helical modes would evolve in an unbalanced manner and therefore induce asymmetry.

With the possibility that non-degenerate linear helical modes may contribute to the asymmetry of the high R jet-in-crossflow as described above, it is important to point out that experimental evidence indicates the jet-in-crossflow typically evolves more symmetrically about the centreplane $y = 0$ when R is small (Fric & Roshko, 1994; Getsinger *et al.*, 2014; Gevorkyan *et al.*, 2016; Shoji *et al.*, 2020*a*). The present stability analysis indicates that, as R decreases, the symmetric and anti-symmetric helical modes have spatial growth rates that grow further apart from each other. This apparent contradiction may indicate that the degeneracy-breaking nature of the helical modes should in fact be most distinct at higher R values and then become less significant at lower R values. Perhaps this could be considered as evidence suggesting that the present asymptotic base flow is not sufficiently representative of reality in the low-R regime.

Alternatively, it may be that the axisymmetric mode remains the most spatially unstable compared to any of the helical modes and therefore overwhelms any symmetry-breaking disturbances from growing. After all, there is experimental evidence indicating a transition from convective to absolute instability for the axisymmetric mode of a jet-in-crossflow below $R \lesssim 3$ which is self-excited and therefore linearly insensitive to external forcing (Megerian *et al.*, 2007; Davitian *et al.*, 2010; Getsinger *et al.*, 2012). It must be noted that experimental

evidence (Alves *et al.*, 2008) indicates that the axisymmetric mode becomes increasingly more spatially unstable as R decreases whereas the present fully-coupled linear stability analysis finds that the axisymmetric mode becomes more stable at low R. Hence, the degeneracy breaking nature of the helical modes may be increasing as R decreases but the axisymmetric mode dominates the flowfield evolution. Again, this may be evidence suggesting that the present asymptotic base flow is not sufficiently representative of reality in the low-R regime. Separately, it may be that the fully-coupled nature of this present linear stability analysis which employed an asymptotically-expanded base flow in terms of λ has contributed - certainly with respect to the differences observed between the present study and the asymptotic expansion-based linear stability analysis of Alves & Kelly (2008).

5.2 Weakly-coupled results

As the results of Section 5.1 demonstrate, the axisymmetric linear stability mode stabilises as R decreases, contradicting experimental evidence as well as the prior asymptotic expansion-based linear stability analysis of Alves & Kelly (2008). As described in Section 4.6, the linear stability analysis of Alves & Kelly (2008) was asymptotically expanded in addition to the base flow considered. This resulted in a stability analysis framework with limited azimuthal base flow-eigenfunction coupling. However, the approach reduced the computational cost of the analysis and was informed by the correspondence between the asymptotically-expanded base flow with the azimuthal dependence from direct numerical simulations (Alves, 2006). To clarify the meaning of base flow-eigenfunction coupling, recall that the base flow was asymptotically expanded in terms of θ implicitly it was expanded in terms of λ, as in Eqs. (4.26) or (4.28) based on the functional form of Coelho & Hunt (1989). That is, $\bar{u} \sim \lambda^0\bar{u}_0^0 + \lambda^1(\bar{u}_1^{+1}\mathrm{e}^{+i\theta} + \bar{u}_1^{-1}\mathrm{e}^{-i\theta}) + \lambda^2(\bar{u}_1^{+2}\mathrm{e}^{+2i\theta} + \bar{u}_1^{-2}\mathrm{e}^{-2i\theta}) + \ldots$. The eigenfunctions in the asymptotic expansion-based analysis of Alves & Kelly (2008) were expanded in terms of λ as in Eqs. (4.51) and that implicitly conveys an expansion in terms of θ in a similar manner.

When base flow and eigenfunction terms mingle in the linearised Navier-Stokes equations and are segregated at different orders of λ, the resultant terms all have an associated dependence of θ. This is the base flow-eigenfunction azimuthal coupling. For example, a base flow term of $\mathcal{O}(\mathrm{e}^{+i\theta})$ may be multiplied with an eigenfunction term of $\mathrm{O}(\mathrm{e}^{-i\theta})$ to yield a coupling of $\sim \mathrm{e}^{0}$.

As Eqs. (4.75) elucidate, the base flow-eigenfunction couplings associated with the axisymmetric mode were the most severely restricted; these eigenvalues depended only on the base flow-eigenfunction couplings as $\mathcal{O}(1)$ and $\mathcal{O}(\mathrm{e}^{\pm i\theta})$ (see Eqs. (4.75)). By contrast, the present fully-coupled linear stability analysis permitted as many base flow-eigenfunction couplings as the numerical grid could support. It is significant to point out that the UVAS and tanh base flows are still asymptotic expansions i.e., they are modelled up to $\sim \mathrm{e}^{\pm 1\theta}$ and $\sim \mathrm{e}^{\pm 2\theta}$, respectively. Even with a fully-coupled analysis, base flow-eigenfunction azimuthal couplings are still neglected - increasingly so as the grid is resolved in the azimuthal direction. For example, a coupling of order $\exp(+10i\theta)$ is possible to achieve with $\exp(+1i\theta) \times \exp(+9i\theta)$ but not with $\exp(+5i\theta) \times \exp(+5i\theta)$ because the base flow is not modelled with $\exp(+5i\theta)$ terms.

It is possible that the computed eigenvalues are sensitive to the set of base flow-eigenfunction couplings that are modelled in the linearised governing equations - particularly for the axisymmetric mode. Therefore, to better understand why the present fully-coupled results appeared to contradict experimental observations, it was necessary to artificially remove most of the base flow-eigenfunction couplings via a weakly-coupled analysis. To obtain the best match with the asymptotic linear stability analysis of Alves & Kelly (2008), the systems of equations implied by Eqs. (4.75), Eqs. (4.66) were first solved with $N_f \coloneqq 1$ and $u_\theta^0(r) \coloneqq 0$. These equations are not exactly the same as those which Alves & Kelly (2008) solved, but represent a very similar approach that is more extensible to higher orders of azimuthal couplings by increasing the number of Fourier modes. Therefore, there is no expectation that the eigenvalues or eigenfunctions will align exactly with those reported by Alves & Kelly

(2008), but the qualitative trend should be similar. In this manner, this approach may be considered a type of "reduced-order model". The corresponding results are presented in Fig. 5.8.

As Fig. 5.8 clearly shows, artificially removing most of the base flow-eigenfunction azimuthal couplings have yielded axisymmetric eigenvalues that align well with the past results of Alves & Kelly (2008). Specifically, the spatial growth rate trend indicates an increasing spatial destabilisation as the crossflow strengthens and quantitatively compares favourably with that of Alves & Kelly (2008) and is well within the range of experimental measurements. The only trend that was not consistent when compared with the results of Alves & Kelly (2008) related to the wavenumbers at very low R for the case with $\theta_0/R_0 = 1/10$. It is expected that eigenvalues obtained from thicker momentum thicknesses should be less accurate because the UVAS base flow is a modification of the inviscid vortex sheet solution of Coelho & Hunt (1989) to produce a finite vorticity thickness. Indeed, the UVAS base flow is formulated in a manner that may be considered as mapping a round jet solution to a planar mixing layer. Hence, a larger momentum thickness represents a greater deviation from the planar mixing layer and from the inviscid vortex sheet.

For completeness, Eqs. 4.66 were solved with $N_f \coloneqq 1$ and $u_\theta^0(r) \neq 0$ to yield Figs. 5.9. By comparing Figs. 5.9 and 5.8, one observes that there is negligible difference between the eigenspectra. Indeed, the u_θ^0 eigenfunction obtained has a very small amplitude compared to the other eigenfunctions, indicating that the presence of an axisymmetric eigenmode with symmetry-breaking crossflow is not correlated with any 'swirling' velocity component. Note that causality is challenging to establish for elliptic problems.

Figs. 5.10 and 5.11 illustrate the eigenvalue behaviour as the number of Fourier modes (and therefore the number of base flow-eigenfunction interactions) increase to $N_f = 2$ and $N_f = 3$, respectively. Higher values of N_f were not possible to solve owing to the complexity of establishing both grid and upwind-damping convergence for these more heavily-coupled systems of equations. Figure 5.10 indicates more aggressively spatially destabilising eigen-

values as the crossflow strengthens, where as Fig. 5.11 is less destabilising, though the differences are not large.

In summary, the weakly-coupled linear stability analysis of the axisymmetric mode found that a small set of base flow-eigenfunction couplings led to (i) a growing spatial destabilisation as R decreased, (ii) excellent agreement with the prior asymptotic expansion-based linear stability analysis of Alves & Kelly (2008), and (iii) reasonable correspondence with experimental measurements. Increasing the number of base flow-eigenfunction couplings by increasing the number of Fourier modes N_f produces less aggressively spatially destabilising eigenvalues but are still in line with the the prior results of Alves & Kelly (2008).

We speculate that the spatial stabilisation trend observed with $N_f = 1, 2, 3$ continues as the number of permitted base flow-eigenfunction couplings grows - until the fully-coupled results in Fig. 5.1 (representative of the asymptotic limit of $N_f \gg 1$) are obtained. That is to say, increased base flow-eigenfunction interactions contribute to *stabilisation* as R decreases. This can be seen from comparing Figs. 5.8-5.11. Another piece of evidence to reinforce this view is the observation that the fully-coupled analysis yields a Strouhal number featuring an inflexion point around $R \approx 3$. The $N_f = 3$ analysis features such an inflexion point around $R \approx 4$ whereas the lower $N_f = 1, 2$ analyses do not. Additionally, the present weakly-coupled analysis appears to yield wavenumbers and Strouhal numbers that increase less aggressively as R decreases as N_f increases - asymptotically agreeing with the fully-coupled analysis. That being said, the behaviour of the Strouhal number, wavenumber, and spatial growth rate indicate a pattern of oscillatory convergence as the number of Fourier modes N increases towards the $N \gg 1$ limit represented by Fig. 5.1.

Given this behaviour, one potential mechanism that we are currently proposing to explain why the present fully-coupled linear stability analysis yields axisymmetric spatial growth rates than disagree with those of the asymptotic expansion-based linear stability analysis of Alves & Kelly (2008) is that an inadequately expanded asymptotic base flow leads to incomplete base flow-eigenfunction couplings that affect the eigenvalues. Fundamentally,

the UVAS base flow presently considered only has terms of $\sim e^0, e^{\pm 1}$. As discussed in the beginning of Section 5.2, the fact that the base flow is modelled to low orders of θ means that any stability analysis has limited base flow-eigenfunction azimuthal couplings. As we resolve higher orders of θ, either by increasing the number of Fourier modes or by increasing the azimuthal mesh resolution in a fully-coupled analysis, more and more of these base flow-eigenfunction couplings are neglected because there is no corresponding base flow term at that order of θ. Instead, the governing equations consist of a few high-order disturbance eigenfunctions coupled to low-order base flow terms; the intermediate and reverse combinations are absent. The asymptotic expansion-based linear stability analysis of Alves & Kelly (2008) employed a physical justification to neglect even more base flow-eigenfunction couplings as discussed in Section 4.6. Therefore, the absence of the complete set of base flow-eigenfunction azimuthal couplings affects the calculated eigenvalues. It is possible that the surviving coupling terms contribute to eigenvalue stabilisation while the missing terms contribute a balancing effect - an idea that we shall explore with spatial kinetic energy budget analysis described in Section 4.8 and conducted in Section 5.3.

A key piece of evidence here is that, by neglecting base flow-eigenfunction couplings as performed by the present weakly-coupled analysis, the eigenspectra of the axisymmetric mode better aligned with the asymptotic expansion analysis of Alves & Kelly (2008). It is only upon introducing more Fourier modes, which implies that more and more base flow-eigenfunction couplings are neglected, that the axisymmetric eigenspectra begin to deviate. Specifically, it seems that the additional base flow-eigenfunction couplings contribute to spatial stabilisation. Use of a base flow with higher order θ terms is hence likely to affect the eigenvalues also.

Another piece of evidence is that the second helical mode eigenspectra obtained from the present fully-coupled analysis align qualitatively well with the asymptotic expansion-based analysis of Alves (2006) - more so than the axisymmetric eigenspectra. As expounded in Section 4.6, Alves (2006) solved the higher helical modes $|m| \geq 2$ eigenspectra using

more base flow-eigenfunction couplings than for the axisymmetric mode. Converted to our formalism, Alves (2006) solved the $|m| = 2$ mode with $N_f = 4$, the $|m| = 1$ mode with $N_f = 3$, and the $m = 0$ mode with $N_f = 1$. Hence, the present fully-coupled analysis (many base flow-eigenfunction couplings are supported) yields eigenvalues that compare favourably with the results of Alves (2006), which employed a larger number of supported base flow-eigenfunction couplings. Given that the second helical mode seems to stabilise as R decreases, it is possible that the surviving base flow-eigenfunction couplings contribute to eigenvalue stabilisation.

The same inadequately expanded base flow may also cause the mismatch between the present fully-coupled axisymmetric spatial growth rates and the experimental measurements of Megerian *et al.* (2007); Alves *et al.* (2008). Using the same evidence from the axisymmetric and second helical modes and the hypothesis that the surviving base flow-eigenfunction azimuthal coupling terms contribute to eigenvalue stabilisation, it is possible that a more detailed base flow provides more physical couplings which may improve the alignment between the present linear stability analysis and against experimental measurements.

As an aside, it must be mentioned that any amount of crossflow leads to a divergence between the present fully-coupled and asymptotic expansion-based linear stability of Alves & Kelly (2008). One possible explanation is that the prior linear stability analysis was quadratic in λ and thus the eigenvalue behaviour as R varied could not have an inflexion point. If the initial gradient of growth rate with respect to R at near $R \to \infty$ is negative, then it will stay negative as R decreases. A cubic analysis, for example, may be able to provide an inflexion point in the eigenvalue trend.

5.3 Kinetic energy budget analysis results

As discussed in Section 4.8, a spatial kinetic energy budget analysis (SKEB) may illuminate why the fully-coupled results for the axisymmetric mode stabilise as the crossflow strengthens

while the weakly-coupled discrete Fourier-transformed results indicate destabilisation as the crossflow strengthens that appear to resemble the past asymptotic expansion-based linear stability analysis of Alves & Kelly (2008) and the experimental measurements of Megerian *et al.* (2007); Shoji *et al.* (2020*a*).

The present SKEB analysis is also an opportunity to explore the mechanism underlying the differences between the present fully-coupled and the prior asymptotic expansion-based linear stability analysis of Alves & Kelly (2008) proposed at the end of Section 5.2. A key point raised from that proposed mechanism is the effect of the surviving base flow-eigenfunction azimuthal couplings on the stability of the eigenvalues.

5.3.1 Fully-coupled Cartesian results

To that end, the spatial kinetic energy budget trends for the axisymmetric mode of the UVAS base flow obtained from a fully-coupled Cartesian analysis are presented in Figure 5.12. As Figure 5.12 indicates, the energy balance of the axisymmetric mode of the UVAS jet-in-crossflow base flow features a decreasing contribution from the pressure-velocity correlation, a comparably increasing contribution from the production term, and negligible variation of the advective term. In fact, as $R \to 2$, the relative contribution of the 'Production' term approaches 86% and 83% for momentum thicknesses $\theta_0/R_0 = 1/15$ and $\theta_0/R_0 = 1/10$, respectively. Recalling the stabilising trend of the spatial growth rates of the axisymmetric mode in Fig. 5.1c, we see that spatial stabilisation is correlated with a reduction of the relative contribution of the 'Pressure-velocity' term and an increase in the relative contribution of the 'Production' term. This is more evidence supporting the interpretation by Hama *et al.* (1980), where (as shown correspondingly in Fig. 4.14) the reduction in the relative contribution of the 'Pressure-velocity' term is associated with spatial stabilisation near the critical stability condition. Such a reduction in the 'Pressure-Velocity contribution' for the JICF occurs at lower velocity ratios R, where observations in experiments (Megerian *et al.*, 2007; Shoji *et al.*, 2020*a*) and direct numerical simulations (Iyer & Mahesh, 2016) demonstrate a

transition in the shear layer instability, eventually to global instability. Hence there appears to be a consistency for the kinetic energy balance exploration with the observations of Hama *et al.* (1980). The cause, then, of this unexpected spatial stabilisation in the present results, e.g., in Fig. 5.1, most likely relates to from the 'phase' interactions between the velocity and pressure eigenfunctions.

5.3.2 Weakly-coupled results

It is important, however, to consider the spatial kinetic energy budget of the axisymmetric mode of the UVAS base flow resulting from weakly-coupled analyses.

Firstly, the kinetic energy budget scenario for the UVAS base flow with $\theta_0/R_0 = 1/15$, $N_f \coloneqq$, and $u_\theta^0 \neq 0$, corresponding to the stability characteristics in Fig. 5.9 is shown in Fig. 5.13. In contrast to the fully-coupled SKEB results in Fig. 5.12, the relative contribution of 'Pressure-velocity' term for the $n = 0$ Fourier mode in Fig. 5.13a increases when $R \lesssim 4$, and that for the 'Production' term decreases, aligning with the destabilisation of the spatial growth rate observed in Fig. 5.9c. Hence the SKEB revealed that, for the axisymmetric mode for the weakly coupled analysis with $N_f \coloneqq 1$, growth in the instability could be tracked with the 'Pressure-velocity' term. The 'Advection' contribution remains negligible in this case.

Yet, the spatial kinetic energy budget for the $n = \pm 1$ Fourier modes indicate quite different behaviour. In contrast to the $n = 0$ results in Fig. 5.13a, for $n = +1$ and $n = -1$, respectively, Figs. 5.13b and 5.13c feature a decaying contribution of the 'Pressure-velocity' term, as R decreases, approaching 4%, while the 'Production' term dominates the energy balance. According to the interpretation of Hama *et al.* (1980), this implies that the $n = \pm 1$ Fourier eigenmodes are contributing to stabilisation of the spatial growth rate. However, caution must be taken in comparing the budgets for different Fourier modes such as $n = 0$ against $n = \pm 1$ because their absolute scale is not identical. The most pertinent comparison regarding the axisymmetric mode is for the $n = 0$ Fourier mode for different values of N_f.

An important observation is that the spatial growth of the kinetic energy is positive due to 'self-interaction' terms but 'mode coupling' terms curtail spatial growth. This trend is more emphasised for the $n = \pm 1$ modes, which appear to exhibit 'mode coupling' terms that dampen spatial kinetic energy growth even more strongly. An interpretation is that the velocity eigenfunctions from adjacent Fourier mode numbers become increasingly phase-decorrelated as the crossflow strengthens. Note that the $n = +1$ and the $n = -1$ results are identical due to the symmetry of the eigenproblem. Therefore, only the positive Fourier modes will be presented and discussed henceforth.

Now, consider the spatial kinetic energy budget of the UVAS base flow with $\theta_0/R_0 = 1/15$, $N_f \coloneqq 2$, and $u_\theta^0 \neq 0$ in Fig. 5.14. Recalling the eigenvalue trends presented in Fig. 5.10, permitting the number of discrete Fourier modes to be $N_f \coloneqq 2$ created more aggressive spatial growth rate destabilisation than for $N_f \coloneqq 1$. This may be explained by the observation that the 'Pressure-velocity' term for the $n = 0$ Fourier mode increases less aggressively at lower R values when comparing against that of the $N_f = 1$ case. Additionally, the $n = +1$ Fourier mode appears to feature a growing 'Pressure-velocity' contribution as $R \lesssim 5$ in contrast to when $N_f \coloneqq 1$. However, the $n = +2$ Fourier mode in Fig. 5.14 features a decaying 'Pressure-velocity' term, indicating that this Fourier mode is contributing a dampening effect to the overall spatial kinetic energy growth. For all $n = 0, +1, +2$, one observes that the total kinetic energy growth due to 'mode coupling' is increasingly negative as the Fourier modes increase.

Finally, we consider the spatial kinetic energy budget of the UVAS base flow with $\theta_0/R_0 = 1/15$, $N_f \coloneqq 3$, and $u_\theta^0 \neq 0$ in Fig. 5.15. Recalling the eigenvalue trends presented in Fig. 5.10, permitting the number of discrete Fourier modes to be $N_f \coloneqq 3$ created less aggressive spatial growth rate destabilisation than for $N_f \coloneqq 2$, which is an indication of oscillatory convergence. The $n = 0$ and $n = +1$ Fourier modes have similar trends to the $N_f \coloneqq 2$ scenario, indicating that the $n = 0$ and $n = +1$ eigenmodes are relatively unmodified upon the introduction of additional Fourier modes $|n| \geq 2$. Note that the 'Pressure-velocity' term

of the $n = 0$ Fourier mode again increases less aggressively at lower R values when compared against those of the $N_f = 1$ and $N_f = 2$ cases. However, the $n = +2$ Fourier mode features a strongly negative 'Pressure-velocity' term for $R \lesssim 4$, indicating that the $n = +2$ Fourier mode is overall stabilising. The $n = +3$ Fourier mode has a weakly increasing 'Pressure-velocity' contribution to the spatial kinetic energy, indicating that the third Fourier mode is weakly destabilising. Generally, the contribution to the kinetic energy growth from 'mode coupling' is negative for all the Fourier modes but is most negative for the $n = 2$ mode; the $n = 3$ mode is less aggressively negative as R decreases by comparison. Overall, this pattern is another indication of oscillatory (odd-even) convergence. Interestingly, the $|n| \geq 2$ Fourier eigenmodes feature a dominant 'Advection' contribution over both 'Production' and 'Pressure-velocity'. This may be due to the fact that the UVAS base flow is only expanded up to $e^{\pm i\theta}$.

From the present SKEB analysis, one observes that the 'mode coupling' terms all introduce stabilisation - providing evidence supporting the mechanism proposed in Section 5.2. Given also that the 'Advection' term unexpectedly dominates the spatial kinetic energy balance for the orders of θ that exceed that of the underlying UVAS base flow is another piece of evidence in support of the aforementioned mechanism. By contrast, having a base flow term defined at that particular order of θ is associated with a growing 'Pressure-velocity' term as R decreases, which correlates with increased spatial growth - as discussed in Section 5.3. Therefore, it is possible that the action of the absent base flow eigenfunction couplings neglected due to the inadequately expanded base flow contributes more to eigenvalue destabilisation as R decreases.

5.4 Summary and discussion of results

The overall results of the present linear stability analysis, kinetic energy budget analysis as well as a comparison against experimental and prior linear stability analyses are presented

Type of analysis	**Spatial growth rate trend as R decreases**	**Kinetic energy budget trend as R decreases**
Experimental	Destabilisation	-
Prior weakly-coupled	Destabilisation	-
Present fully-coupled	Stabilisation	Pressure-velocity term shrinks
Present weakly-coupled	Destabilisation	Pressure-velocity term grows

Table 5.1: Summary of spatial growth rate and pressure-velocity term behaviour as a percentage of the total kinetic energy as R decreases for the UVAS jet-in-crossflow base flow for experimental as well as prior and present linear stability analyses.

in Table 5.1. 'Prior weakly-coupled' refers to the prior asymptotic linear stability analysis of Alves & Kelly (2008), 'Present fully-coupled' refers to the analysis described in Section 4.2, and 'Present weakly-coupled' refers to the discrete Fourier-based analysis described in Section 4.7.

A fully-coupled analysis of an asymptotic base flow that has been expanded up to $\mathcal{O}(\lambda^2)$ yields spatial growth rates that destabilise as the crossflow strengthens. This is contradictory to both experimental evidence and the prior linear stability analysis of Alves & Kelly (2008), who used the same base flow. Only upon artificially removing the azimuthal coupling terms that the fully-coupled analysis supports does the spatial growth rate destabilise as the crossflow strengthens. A spatial kinetic energy budget of a fully-coupled analysis revealed that the relative contribution of the 'Pressure-velocity' correlation term decreased as R decreased. By contrast, the kinetic energy budget analysis of the weakly-coupled analysis indicated that the 'mode interaction' terms were typically negative contributors to overall kinetic energy growth. The higher Fourier modes were generally stabilising, possibly due to the fact that the base flow was only expanded up to $\mathrm{e}^{\pm i\theta}$ or $\mathcal{O}(\lambda^1)$.

Table 5.1 implies that weakly-coupled linear stability analyses of the UVAS jet-in-crossflow

base flow may exhibit increasing destabilisation of the spatial growth rate as R decreases owing the small number of Fourier modes (and therefore mode interactions) that such analyses permit. However, upon increasing the number of Fourier modes in the present weakly-coupled linear stability analysis, the spatial growth rate destabilised less aggressively as R decreased concomitantly with decreasing contributions of the 'Pressure-velocity' term in the spatial kinetic energy budget. Therefore, it is possible that increasing the number of Fourier modes in the weakly-coupled linear stability analysis may weaken eigenmode destabilisation enough to eventually yield stabilisation as R decreased. This would correspond to the fully-coupled linear stability analyses. A remedy may be to use a base flow that has been expanded asympotically in terms of λ with higher order terms in λ.

5.5 Comparisons of base flows against experimental measurements

One important feature to highlight, in the context of some inconsistencies between the present LSA trends and those of experiments and DNS as velocity ratio is reduced, is the approximate nature of the hyperbolic-tangent (tanh) and uniformly valid asymptotic solution (UVAS) base flow as models for the jet-in-crossflow. As the basis for base flow comparison, experimental velocity data were used. These data were obtained from particle image velocimetry (PIV) of an unforced equidensity jet-in-crossflow emerging from a flush nozzle at $J = 5, 8, 12, 20, 41 \rightarrow R = 2.2, 2.8, 3.5, 4.5, 6.4$ with an acetone mole fraction $\psi = 0.112$ and a jet Reynolds number $\mathrm{Re}_j = 1900$ based on the nozzle outlet diameter and the jet bulk velocity as documented for the "tabless insert" cases in Harris *et al.* (2021) and Harris (2020). These experimental velocity profiles have momentum thicknesses $1/16.5 \lesssim \theta_0/R_0 \lesssim 1/15$.

The comparisons among the experimental, UVAS, and tanh velocity profiles near the jet exit along the centreplane are presented in Figs. 5.16-5.20. All velocity components were normalised with respect to the maximum axial jet velocity $U_{\max}$ and by the nozzle exit radius R_0. The experimental streamwise and spanwise velocities (u_x and u_y, respectively)

were measured one radius downstream of the jet exit plane. Correspondingly, the numerical base flows were also generated one radius downstream using the correlation given in Eq. (4.27) . The numerical base flows have a momentum thickness of $\theta_0/R_0 = 1/15$.

As Figs. 5.16-5.20 demonstrate, both the tanh and UVAS base flows somewhat resemble the experimental velocity field, particularly the axial velocity. However, the local region of counterflow in the upstream shear layer is not properly represented in either the tanh or the UVAS base flows and the UVAS base flow has a prominent coflow region in the downstream shear layer. The normalised streamwise velocity, largely consisting of the crossflow, exhibits quantitative discrepancies between experimental and numerical values; the experimental streamwise velocity is slower than the numerical base flows impose and features reverse flow indicative of a wake region. The numerical spanwise velocity is identically zero along the centreplane due to the assumption of symmetry about the centreplane. However, experimental measurements indicate that this theoretical symmetry does not exist in practice. It must be noted that the experimental spanwise velocity measurement is derived from the out-of-plane component of stereo-PIV measurements, which is known to be more susceptible to error than the in-plane components.

As the crossflow velocity increases, indicated by the decreasing J or R value from $J = 41$ to $J = 5$, the mismatch between experimental velocity fields and numerical base flows become more pronounced. This was expected because both the tanh and the UVAS base flows were asymptotic solutions expanded with respect to $\lambda = 1/R$; as λ increased (R decreased), the tanh and UVAS solutions would become less accurate. To improve accuracy at lower R values, it would be necessary to increase the expansion order in terms of λ to include $\mathcal{O}(\lambda^3)$ or higher terms for the tanh base flow and $\mathcal{O}(\lambda^2)$ or higher terms for the UVAS base flow. It must also be mentioned that (i) the experimental axial velocity field features a localised region of counterflow near the upstream shear layer that slightly distorts the calculation of the upstream shear layer momentum thickness and (ii) the integrated momentum thickness of the numerical base flows at $z = 1$ presently considered do not vary with R as the experimental

momentum thicknesses do.

Hence, an improved base flow that better aligns with experimental measurements is expected to improve the accuracy of the subsequent linear stability analysis. Indeed, it may be that the present fully-coupled analysis yields axisymmetric growth rates that deviate with experimental measurements most strongly at low R values partially due to an inadequately-representative base flow. One may extend the UVAS base flow solution of Alves & Kelly (2008) to include $\mathcal{O}(\lambda^2)$ terms, for example, or use a base flow obtained from numerical simulations of a jet-in-crossflow.

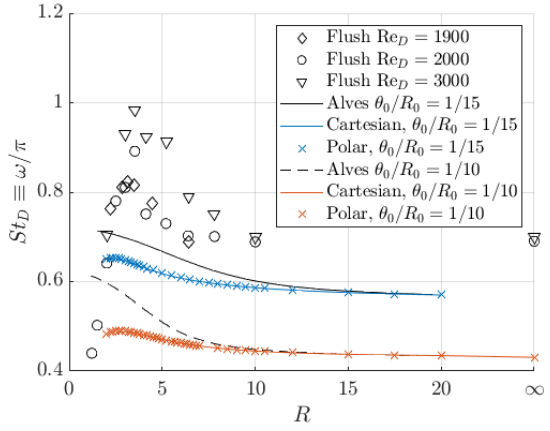

(a) $\mathrm{St}_D \coloneqq \omega/\pi$

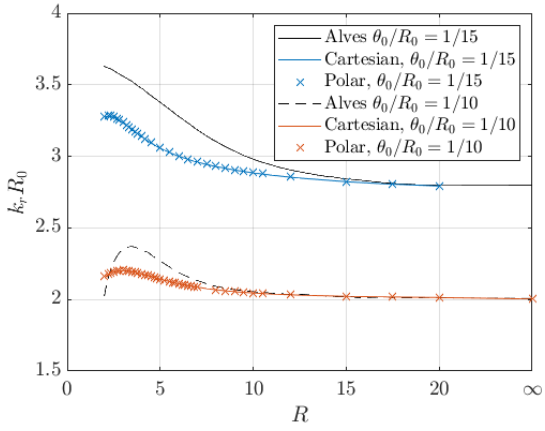

(b) $k_r R_0$

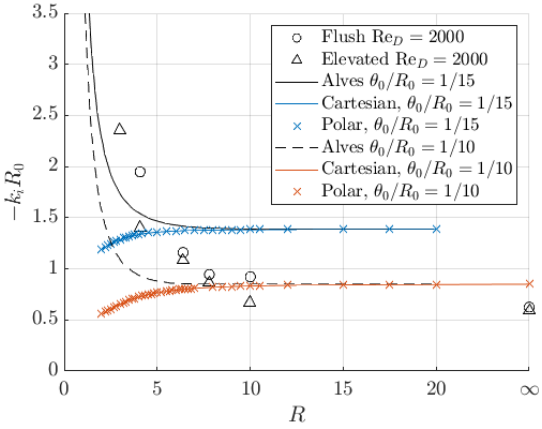

(c) $-k_i R_0$

Figure 5.1: Comparison of the predicted (a) Strouhal number, (b) wavenumber, and (c) spatial growth rate for the axisymmetric mode of the UVAS base flow, shown by the 'x' symbols and solid lines for the polar and Cartesian analyses, against experimental values (open symbols), and the prior linear stability analysis of Alves & Kelly (2008) for $\theta_0/R_0 = 1/15, 1/10$ in the inviscid limit.

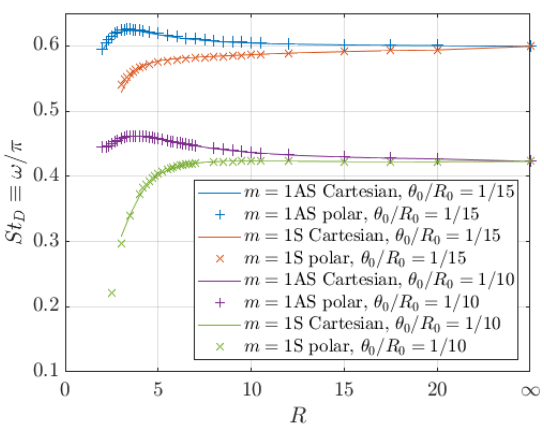

(a) $\mathrm{St}_D \coloneqq \omega/\pi$

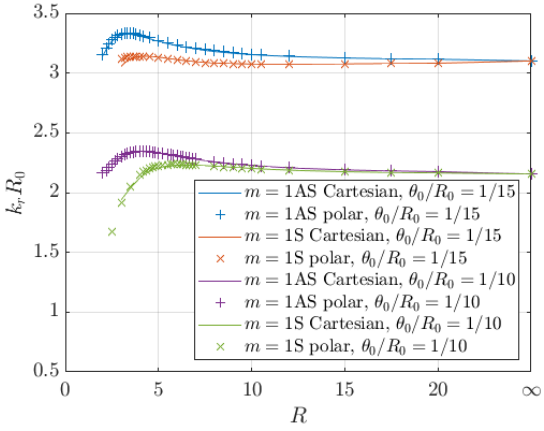

(b) $k_r R_0$

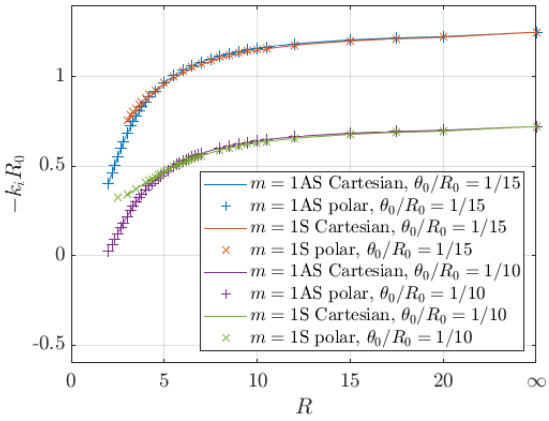

(c) $-k_i R_0$

Figure 5.2: The predicted (a) Strouhal number, (b) wavenumber, and (c) spatial growth rate for the first helical mode of the UVAS base flow for $\theta_0/R_0 = 1/15, 1/10$ in the inviscid limit.

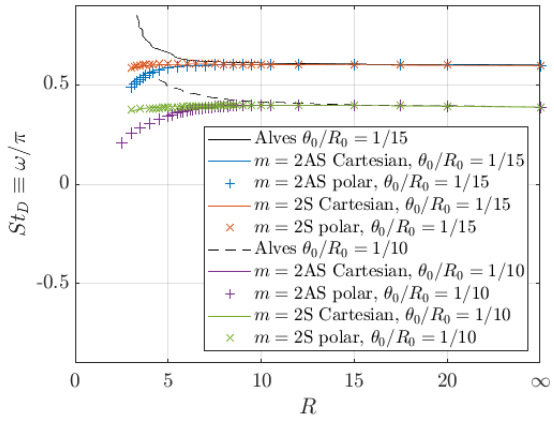

(a) $\mathrm{St}_D \coloneqq \omega/\pi$

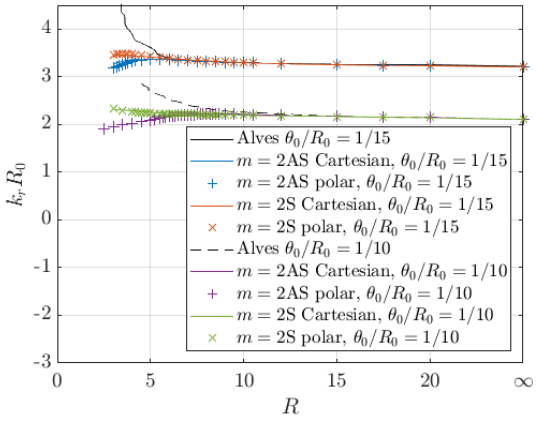

(b) $k_r R_0$

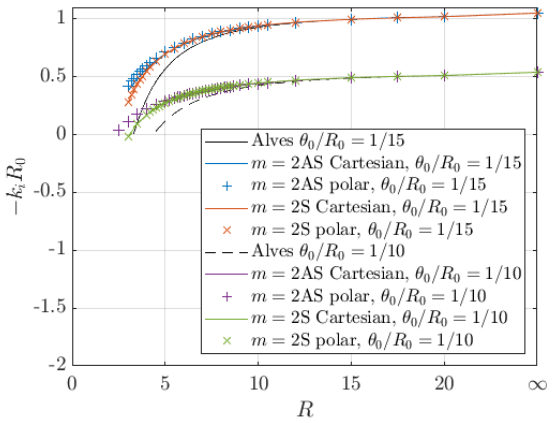

(c) $-k_i R_0$

Figure 5.3: Comparison of the dominant (a) Strouhal number, (b) wavenumber, and (c) spatial growth rate for the second helical mode of the UVAS base flow against the prior linear stability analysis of Alves & Kelly (2008) for $\theta_0/R_0 = 1/15, 1/10$ in the inviscid limit.

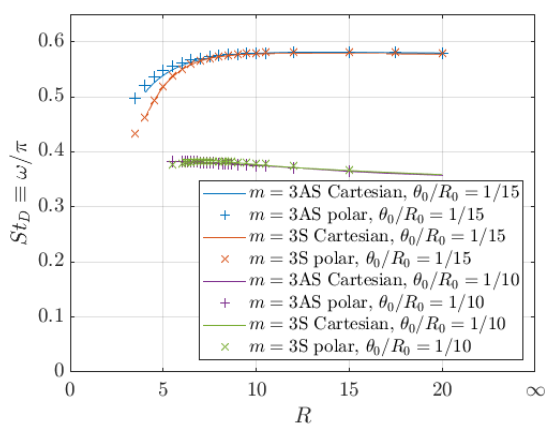

(a) $\mathrm{St}_D \coloneqq \omega/\pi$

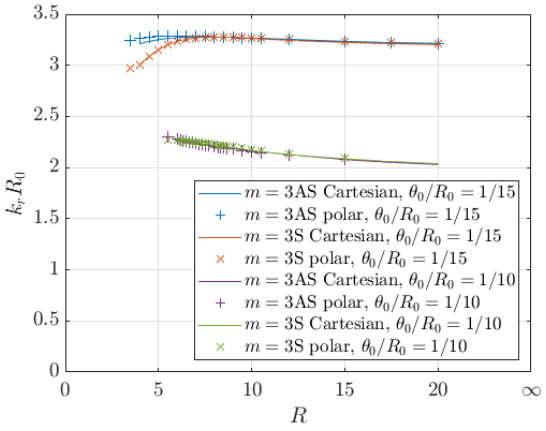

(b) $k_r R_0$

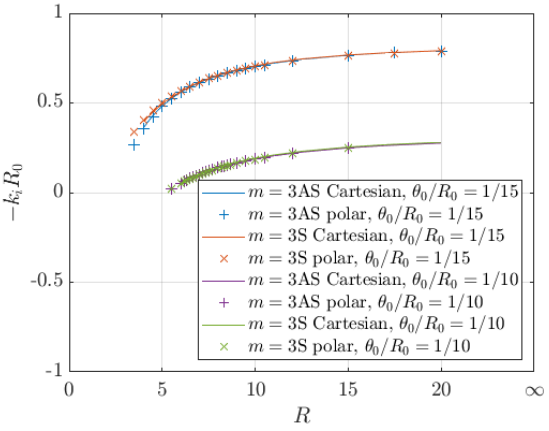

(c) $-k_i R_0$

Figure 5.4: The dominant (a) Strouhal number, (b) wavenumber, and (c) spatial growth rate for the third helical mode of the UVAS base flow for $\theta_0/R_0 = 1/15, 1/10$ in the inviscid limit.

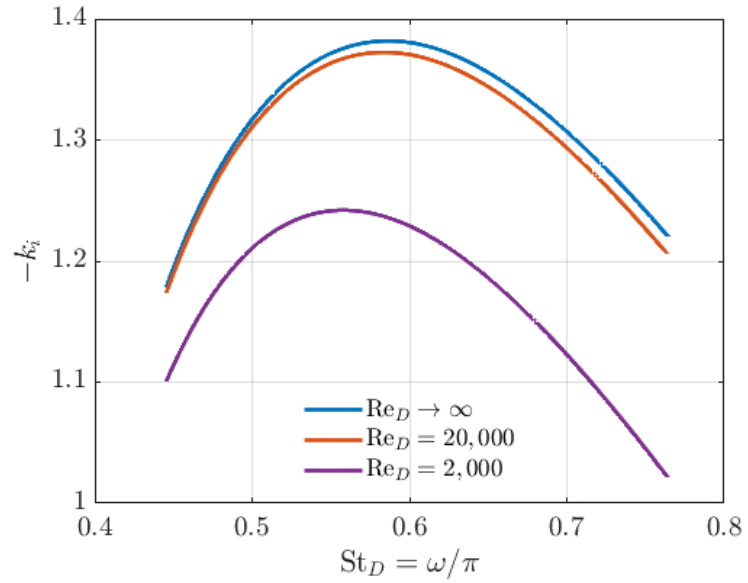

(a) Spatial growth rate over $\mathrm{St}_D \coloneqq \omega/\pi$

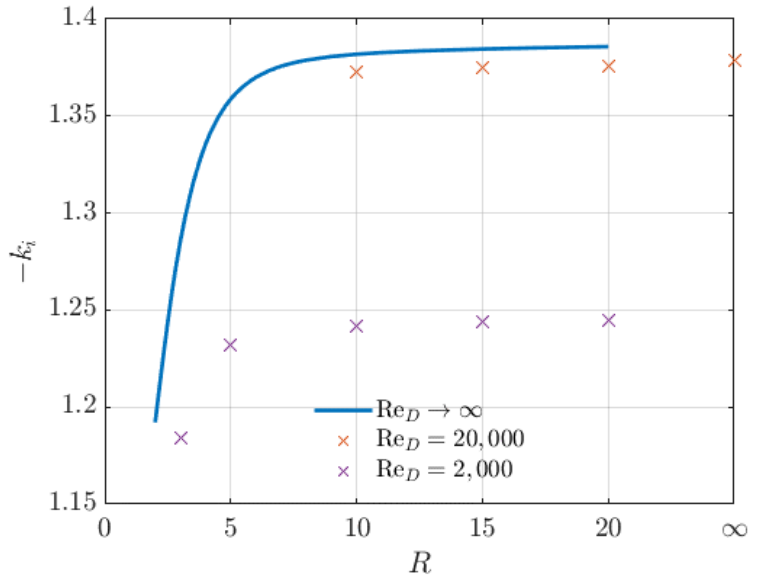

(b) Spatial growth rate over R

Figure 5.5: The (a) spatial growth rate over St_D for $R = 10$ and (b) dominant spatial growth rate over R for the axisymmetric mode of the UVAS base flow for $\theta_0/R_0 = 1/15$ for different Reynolds numbers Re_D.

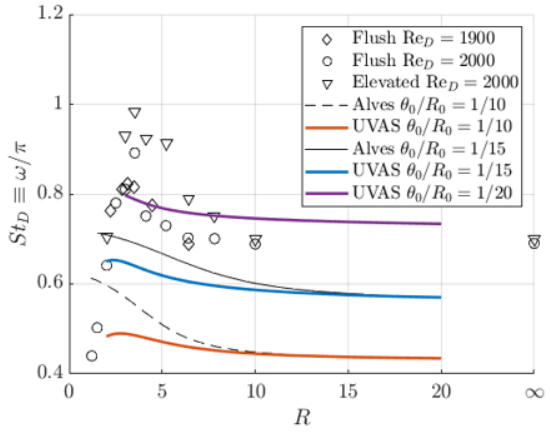

(a) $\mathrm{St}_D \coloneqq \omega/\pi$

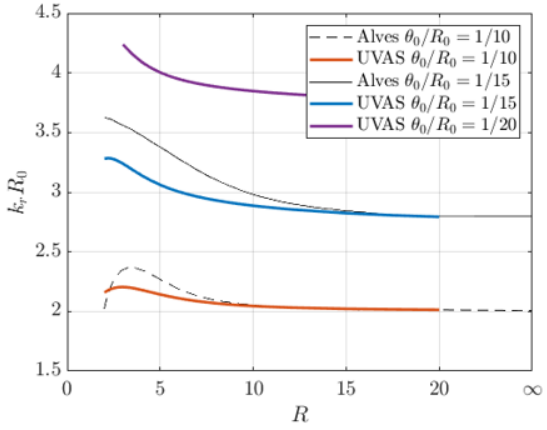

(b) $k_r R_0$

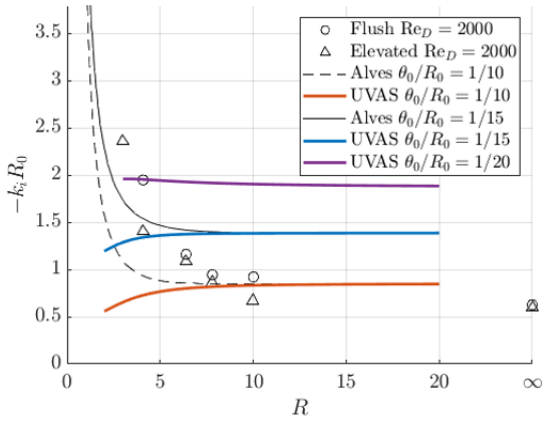

(c) $-k_i R_0$

Figure 5.6: Comparison of the predicted (a) Strouhal number, (b) wavenumber, and (c) spatial growth rate for the axisymmetric mode of the UVAS base flow, shown by the 'x' symbols and solid lines for the polar and Cartesian analyses, against experimental values (open symbols), and the prior linear stability analysis of Alves & Kelly (2008) for $\theta_0/R_0 = 1/20, 1/15, 1/10$ in the inviscid limit.

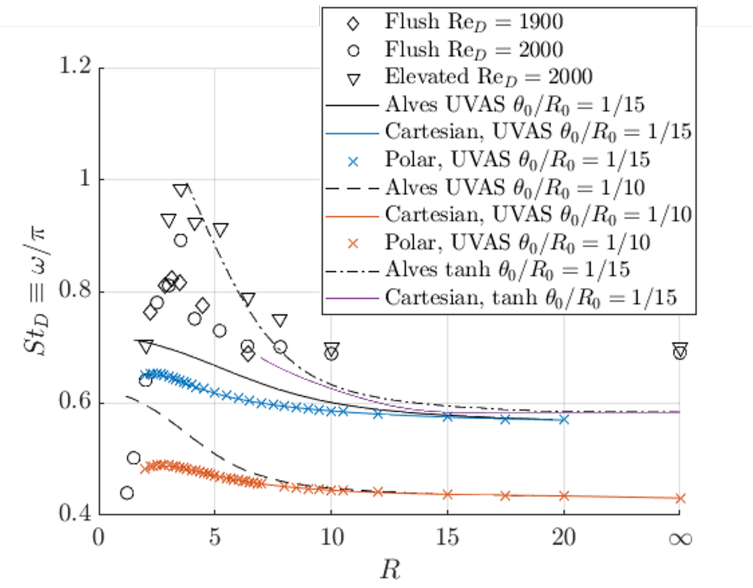

(a) $\mathrm{St}_D \coloneqq \omega/\pi$

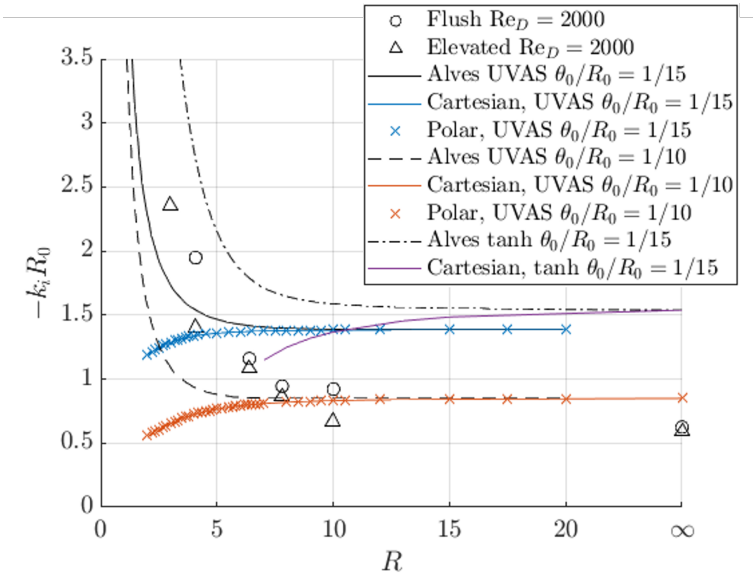

(b) $-k_i R_0$

Figure 5.7: Comparison of the predicted (a) Strouhal number, (b) wavenumber, and (c) spatial growth rate for the axisymmetric mode, shown by the 'x' symbols and solid lines for the polar and Cartesian analyses, against experimental values (open symbols), and the prior linear stability analysis of Alves & Kelly (2008) and Alves *et al.* (2008) for the UVAS base flow with $\theta_0/R_0 = 1/15, 1/10$ and the tanh base flow with $\theta_0/R_0 = 1/15$ in the inviscid limit.

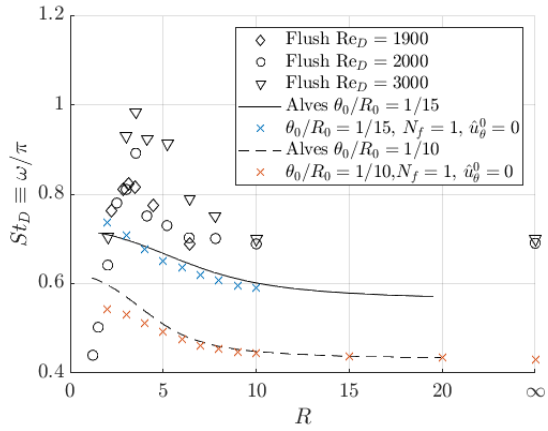

(a) $\mathrm{St}_D \coloneqq \omega/\pi$

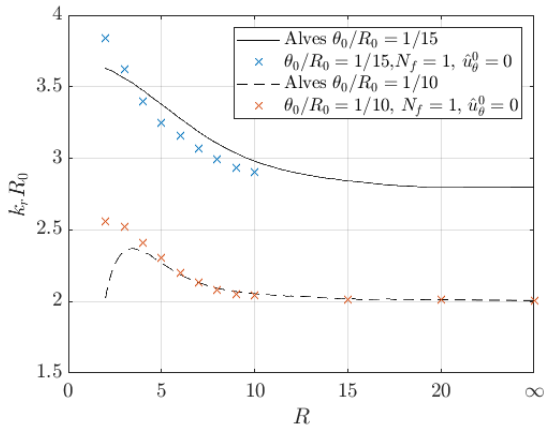

(b) $k_r R_0$

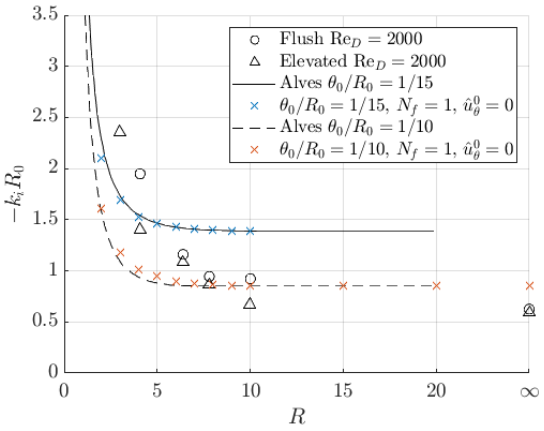

(c) $-k_i R_0$

Figure 5.8: Comparison of the predicted (a) Strouhal number, (b) wavenumber, and (c) spatial growth rate for the axisymmetric mode of the UVAS base flow with $N_f \coloneqq 1$ and $u_{\theta,0}(r) \coloneqq 0$, shown by the x symbols against experimental values (open symbols), and the prior linear stability analysis of Alves & Kelly (2008) (solid and dashed lines) for $\theta_0/R_0 = 1/15, 1/10$ in the inviscid limit.

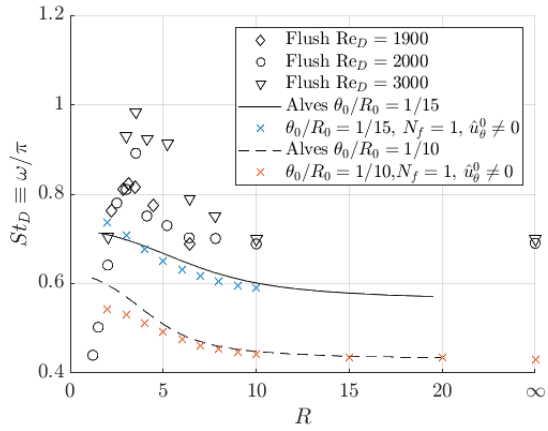

(a) $\mathrm{St}_D \coloneqq \omega/\pi$

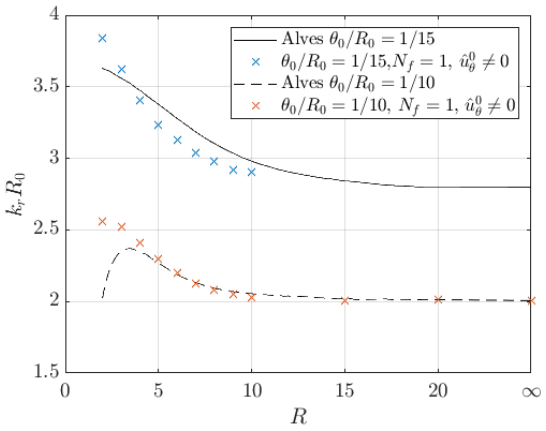

(b) $k_r R_0$

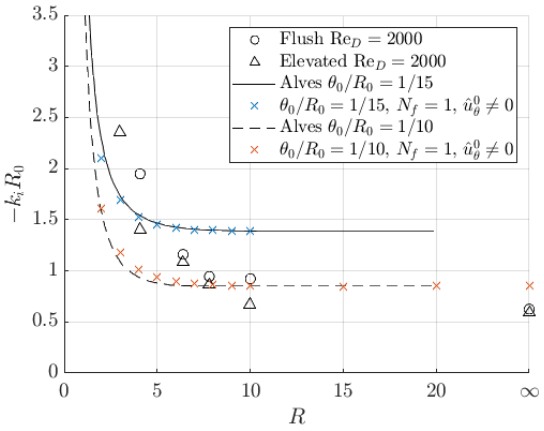

(c) $-k_i R_0$

Figure 5.9: Comparison of the predicted (a) Strouhal number, (b) wavenumber, and (c) spatial growth rate for the axisymmetric mode of the UVAS base flow with $N_f \coloneqq 1$ and $u_{\theta,0}(r) \neq 0$, shown by the x symbols against experimental values (open symbols), and the prior linear stability analysis of Alves & Kelly (2008) (solid and dashed lines) for $\theta_0/R_0 = 1/15, 1/10$ in the inviscid limit.

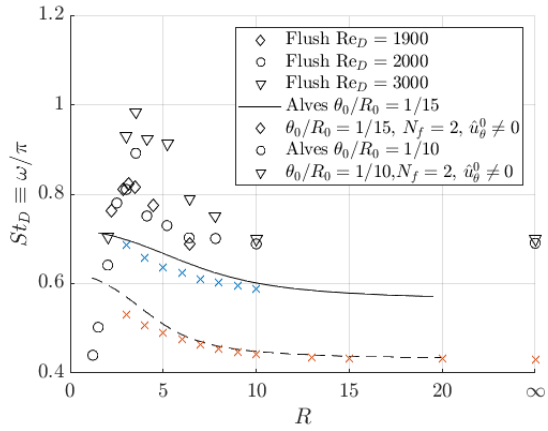

(a) $\mathrm{St}_D \coloneqq \omega/\pi$

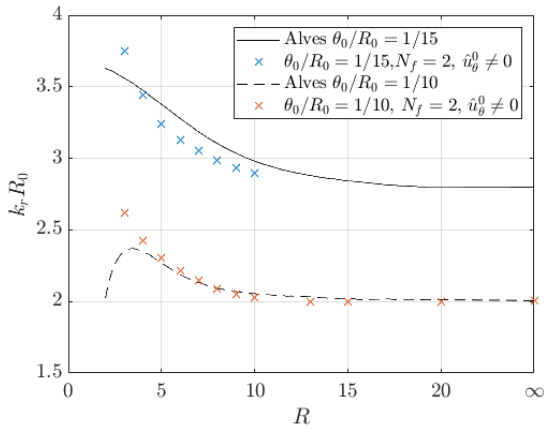

(b) $k_r R_0$

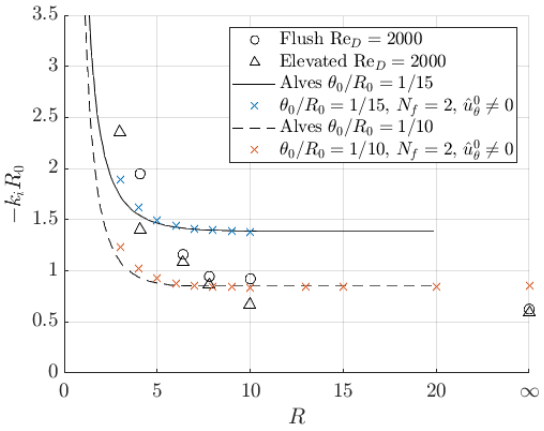

(c) $-k_i R_0$

Figure 5.10: Comparison of the predicted (a) Strouhal number, (b) wavenumber, and (c) spatial growth rate for the axisymmetric mode of the UVAS base flow with $N_f \coloneqq 2$ and $u_{\theta,0}(r) \neq 0$, shown by x symbols, against experimental values (open symbols), and the prior linear stability analysis of Alves & Kelly (2008) (solid and dashed lines) for $\theta_0/R_0 = 1/15, 1/10$ in the inviscid limit.

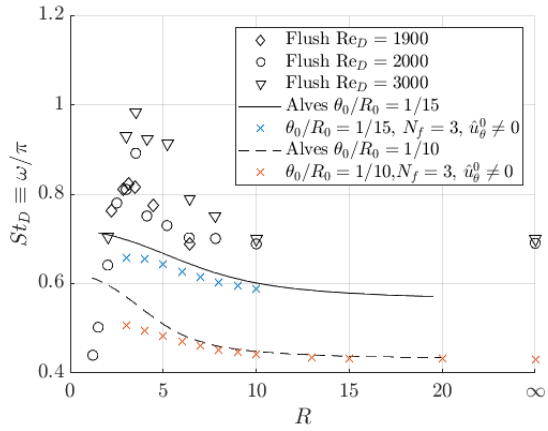

(a) $\mathrm{St}_D \coloneqq \omega/\pi$

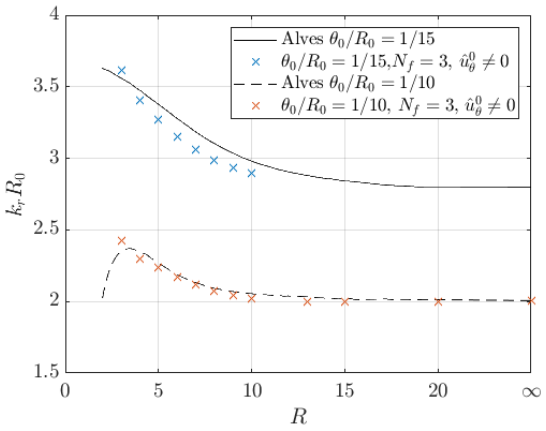

(b) $k_r R_0$

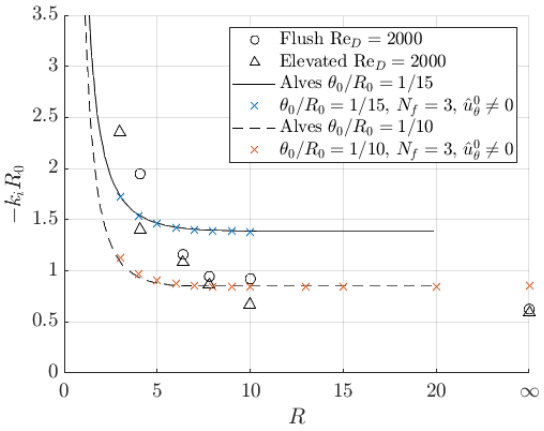

(c) $-k_i R_0$

Figure 5.11: Comparison of the predicted (a) Strouhal number, (b) wavenumber, and (c) spatial growth rate for the axisymmetric mode of the UVAS base flow with $N_f \coloneqq 3$ and $u_{\theta,0}(r) \neq 0$, shown by the x symbols, against experimental values (open symbols), and the prior linear stability analysis of Alves & Kelly (2008) (solid and dashed lines) for $\theta_0/R_0 = 1/15, 1/10$ in the inviscid limit.

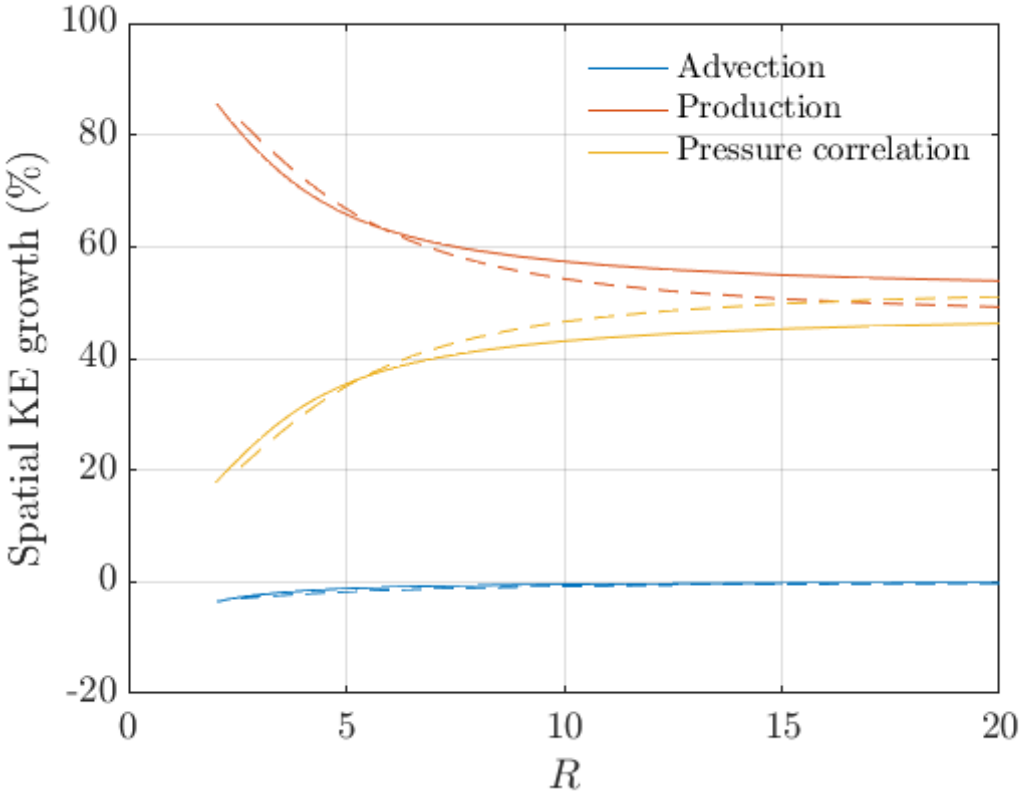

Figure 5.12: Spatial kinetic energy budget for the axisymmetric mode of the UVAS base flow for $\theta_0/R_0 = 1/15$ (solid lines) and $1/10$ (dashed lines) in the inviscid limit from a fully-coupled Cartesian analysis.

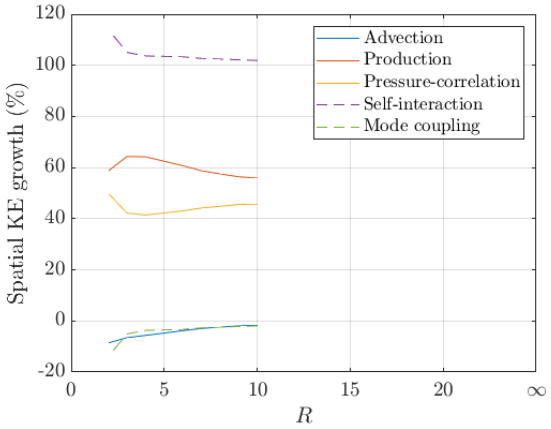

(a) $n = 0$

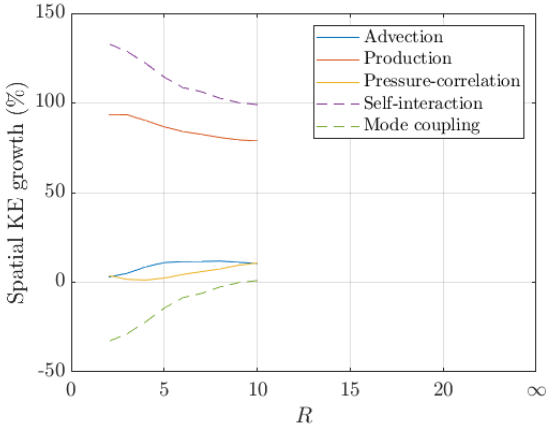

(b) $n = +1$

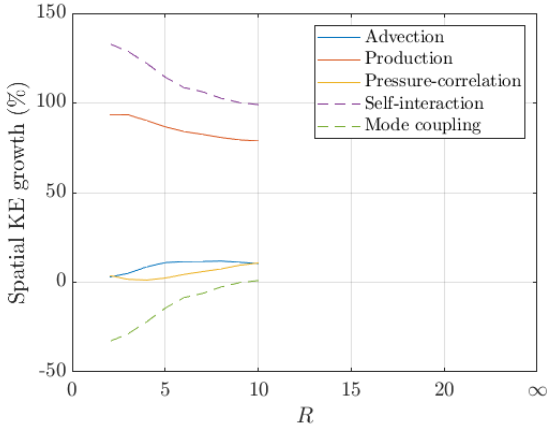

(c) $n = -1$

Figure 5.13: Spatial kinetic energy budget for the axisymmetric mode for $n = 0$ (a), $+1$ (b), and -1 (c), of the UVAS base flow for $\theta_0/R_0 = 1/15$ in the inviscid limit from a weakly-coupled analysis with $N_f \coloneqq 1$.

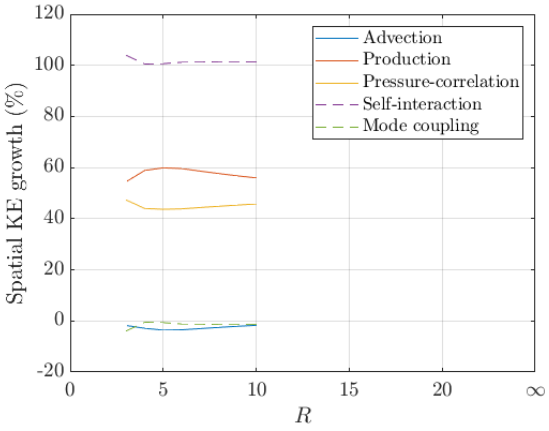

(a) $n = 0$

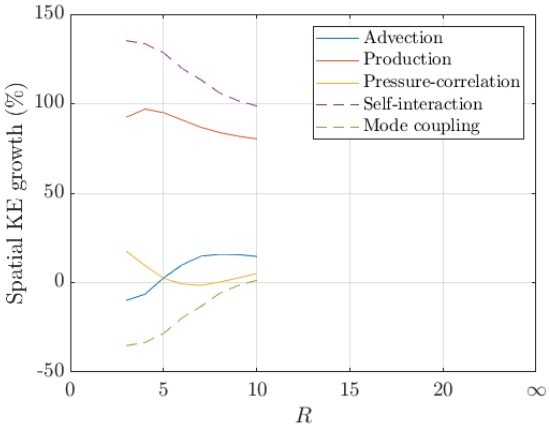

(b) $n = +1$

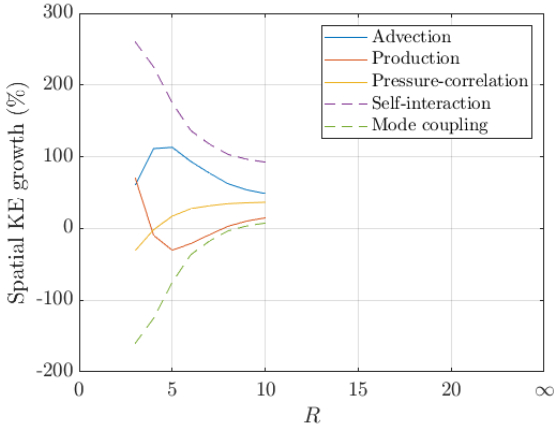

(c) $n = +2$

Figure 5.14: Spatial kinetic energy budget for the axisymmetric mode for $n = 0$ (a), $+1$ (b), and $+2$ (c), of the UVAS base flow for $\theta_0/R_0 = 1/15$ in the inviscid limit from a weakly-coupled analysis with $N_f \coloneqq 2$.

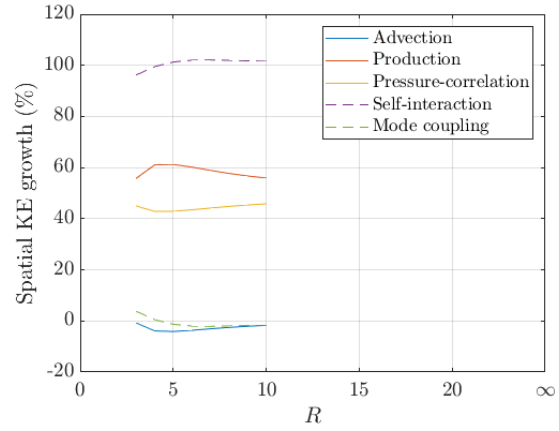

(a) $n = 0$

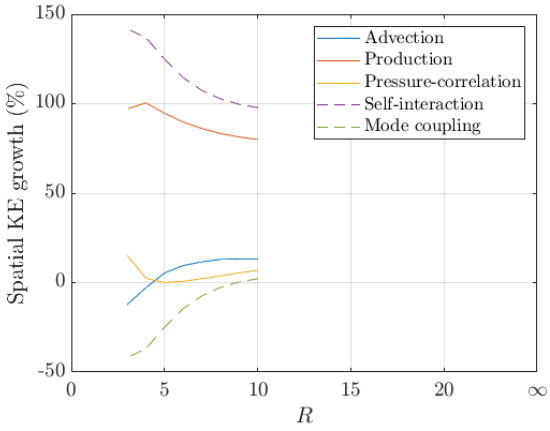

(b) $n = +1$

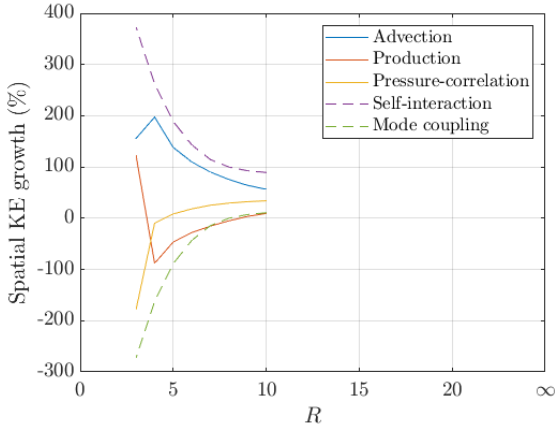

(c) $n = +2$

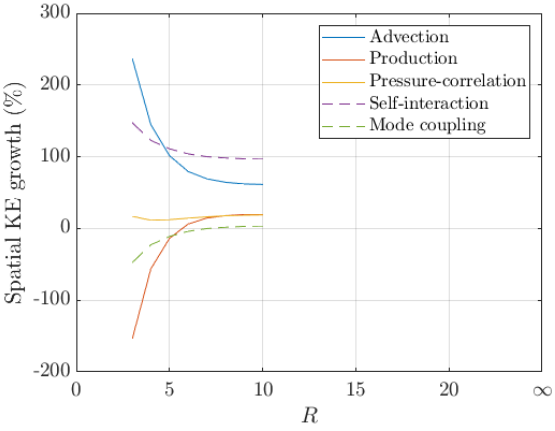

(d) $n = +3$

Figure 5.15: Spatial kinetic energy budget for the axisymmetric mode for $n = 0$ (a), $+1$ (b), $+2$ (c) and $+3$ (d), of the UVAS base flow for $\theta_0/R_0 = 1/15$ in the inviscid limit from a weakly-coupled analysis with $N_f := 3$.

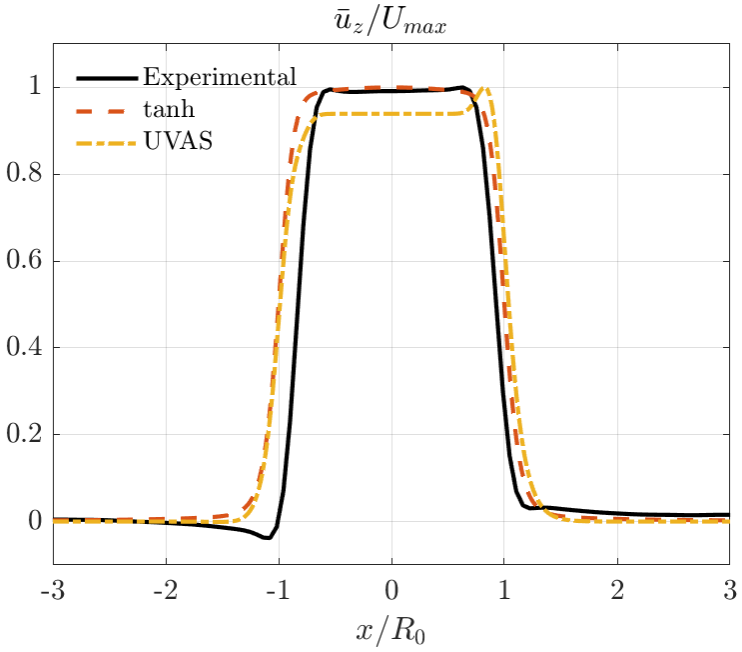

(a) $u_z/U_{\max}$

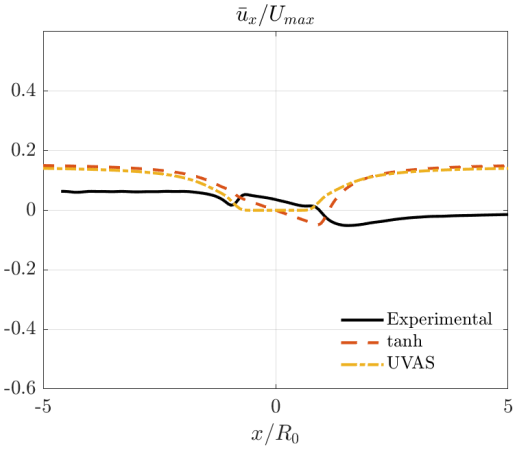

(b) $u_x/U_{\max}$

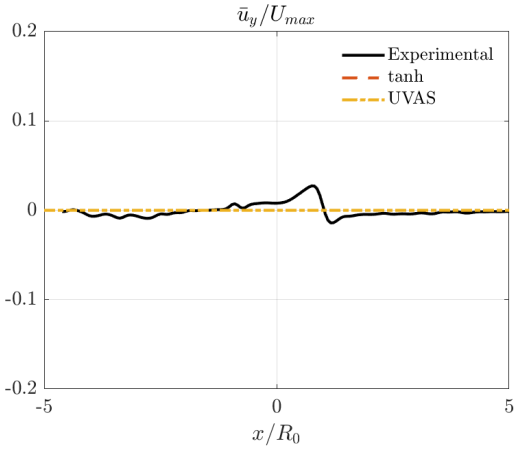

(c) $u_y/U_{\max}$

Figure 5.16: Comparison of the velocity field along centreplane between experimental data, the tanh model, and the UVAS model for $J = 41$, $R = 6.4$.

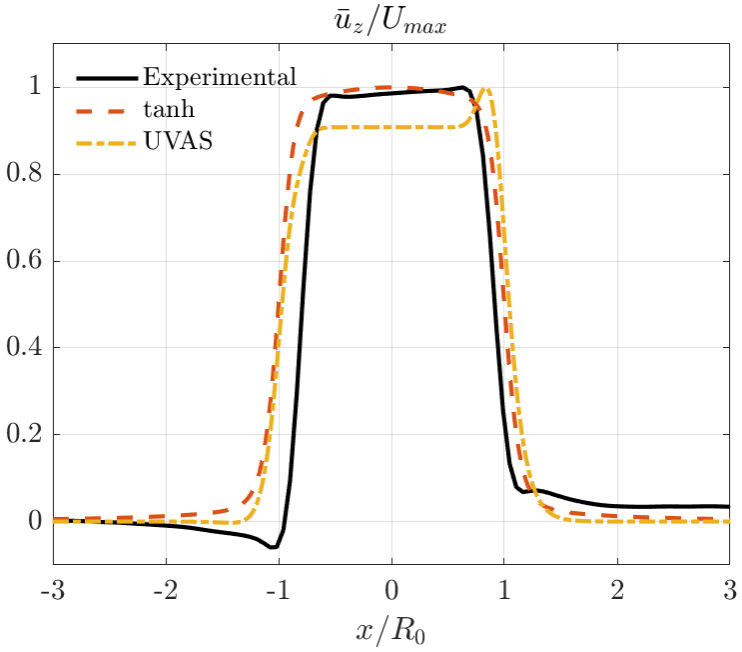

(a) u_z/U_{max}

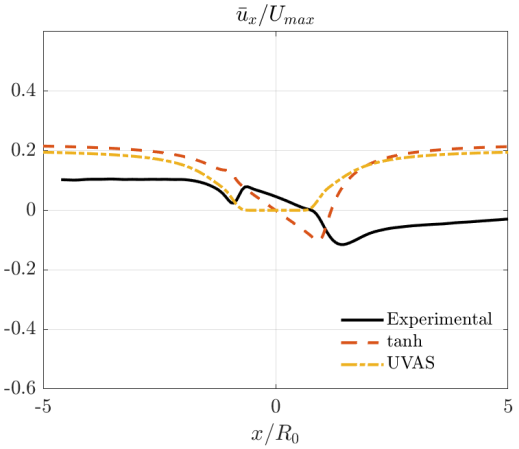

(b) u_x/U_{max}

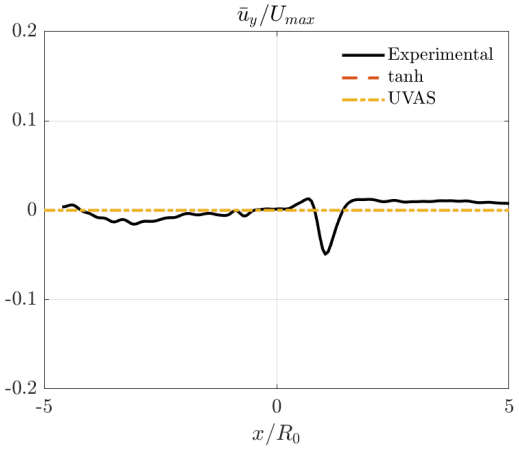

(c) u_y/U_{max}

Figure 5.17: Comparison of the velocity field along centreplane between experimental data, the tanh model, and the UVAS model for $J = 20$, $R = 4.5$.

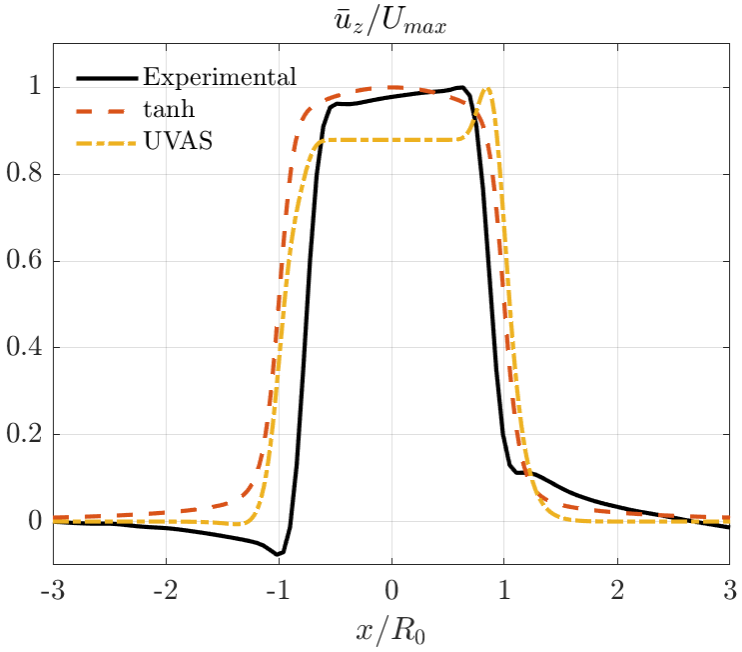

(a) u_z/U_{max}

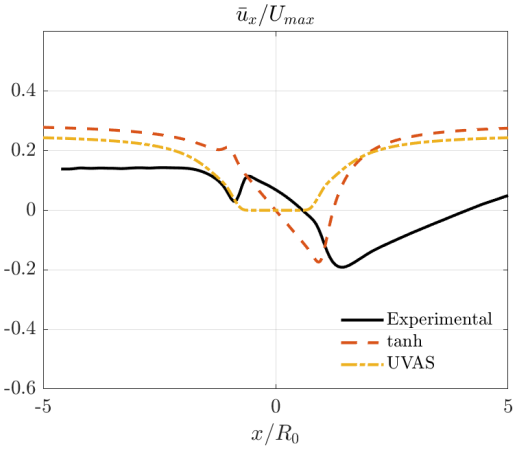

(b) u_x/U_{max}

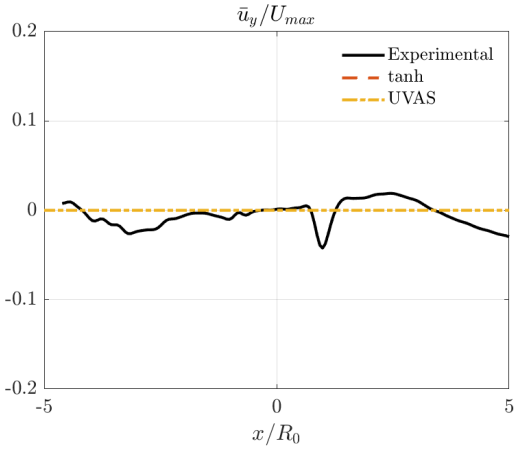

(c) u_y/U_{max}

Figure 5.18: Comparison of the velocity field along centreplane between experimental data, the tanh model, and the UVAS model for $J = 12$, $R = 3.5$.

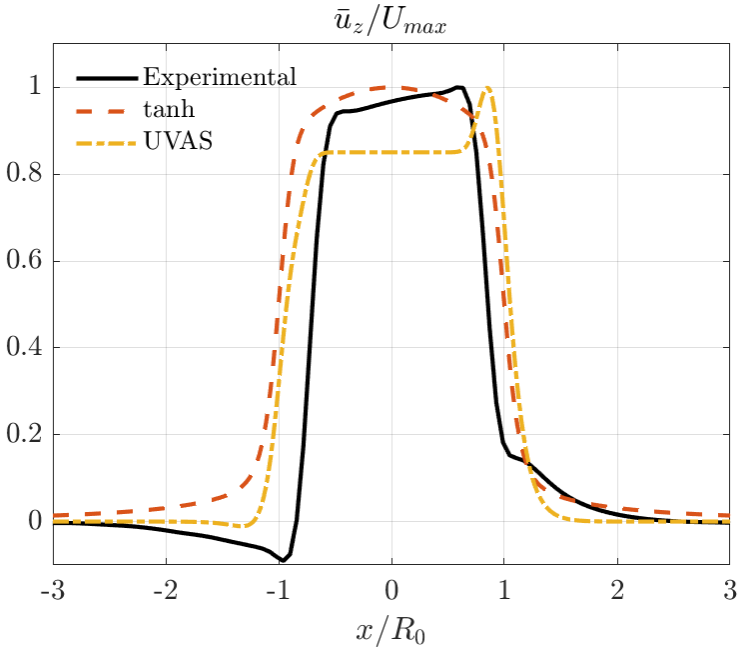

(a) u_z/U_{max}

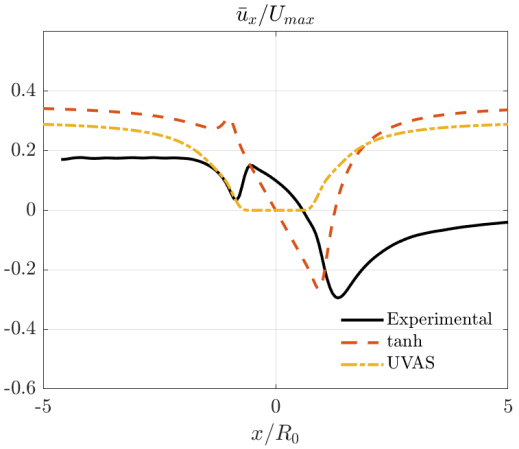

(b) u_x/U_{max}

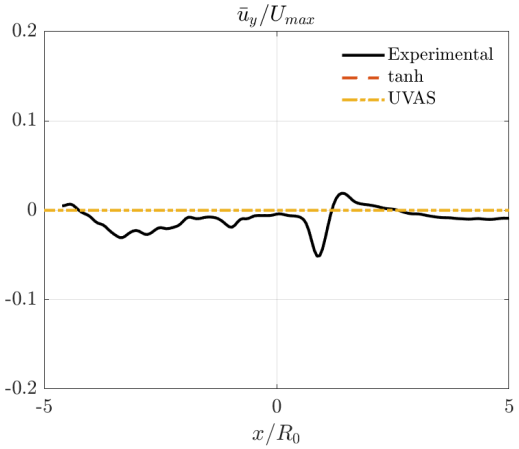

(c) u_y/U_{max}

Figure 5.19: Comparison of the velocity field along centreplane between experimental data, the tanh model, and the UVAS model for $J = 8$, $R = 2.8$.

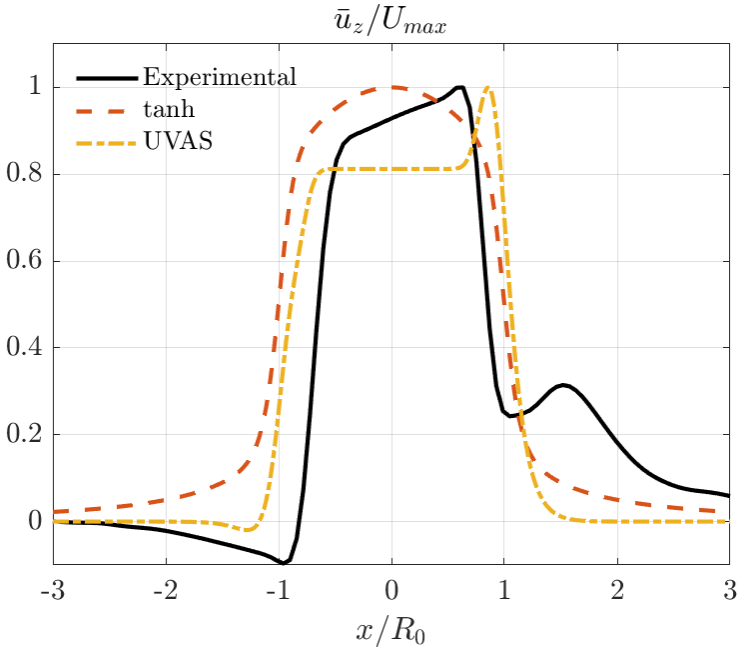

(a) u_z/U_{max}

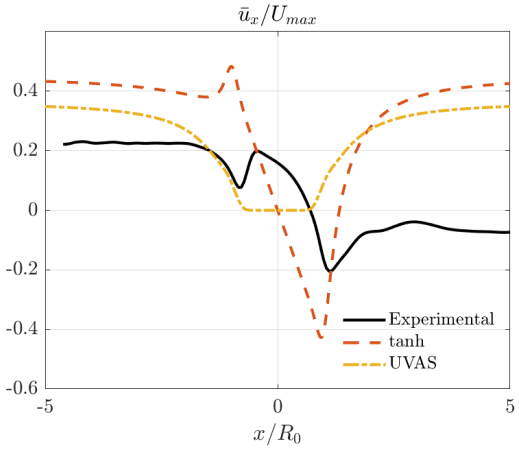

(b) u_x/U_{max}

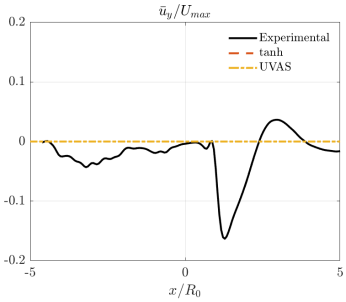

(c) u_y/U_{max}

Figure 5.20: Comparison of the velocity field along centreplane between experimental data, the tanh model, and the UVAS model for $J = 5$, $R = 2.2$.

CHAPTER 6

Conclusions and Future Recommendations

6.1 Present Conclusions

This present study initially aimed to complement experimental investigations of the incompressible jet-in-crossflow. The theoretical plane of symmetry that lies along the centreplane of the jet-in-crossflow is typically not realised in experimental conditions - particularly when the jet velocity is significantly greater than the crossflow velocity (high R values). In fact, the asymmetric forcing studies of Besnard *et al.* (2022) found that even low-amplitude disturbances applied asymmetrically to the jet-in-crossflow could reverse the asymmetry of the downstream flow field. Therefore, there may be a linear and perhaps even local origin to the natural asymmetry found in experimental jets-in-crossflow. The main strategy deployed in this study, then, was a 2D-local fully-coupled spatial linear stability analysis with the incorporation of viscous instability mechanisms. This may be considered an extension of the asymptotic expansion-based linear stability analysis of Alves & Kelly (2008) which only considered inviscid instability mechanisms. All such stability analyses considered the same asymptotically expanded viscous base flows of Alves *et al.* (2008) and Alves & Kelly (2008).

The fully-coupled linear stability analysis results unexpectedly indicated a *stabilising* axisymmetric mode spatial growth rate trend as R decreased that was contrary to the *destabilising* behaviour that both experimental measurements (Megerian *et al.*, 2007; Davitian *et al.*, 2010; Shoji *et al.*, 2019) and the prior asymptotic expansion-based linear stability analyses of Alves & Kelly (2008) captured. This unexpected result was especially puzzling

given that codes formulated in Cartesian and polar coordinates yielded the same eigenvalues, variations in physical and numerical hyperparameters yielded the same eigenvalues as one another, and the code was able to recover the same eigenvalues from other 1D or 2D base flows such as an asymmetric coaxial round free jet.

One potential cause of the unexpected behaviour of the axisymmetric mode spatial growth rate obtained from the present inviscid stability analysis was postulated to be the non-physical oscillations that contaminated the velocity eigenfunctions near the downstream shear layer of the jet-in-crossflow. However, we developed a novel upwind treatment of the linearised convection term provided the necessary numerical dissipation to ensure that the eigenfunctions were smooth while not substantially affecting the eigenvalues. Hence, the unexpected stabilisation behaviour was not caused by the non-physical eigenfunction oscillations, as they were eliminated via the novel upwinding technique.

Given that the principal difference between the present fully-coupled and the prior asymptotic expansion-based linear stability analyses is the range of supported base flow-eigenfunction azimuthal couplings, a weakly-coupled linear stability analysis was developed to explore the effect of base flow-eigenfunction azimuthal coupling on the stability analysis. It was found that restricting the base flow-eigenfunction azimuthal couplings in a manner that resembled that of Alves & Kelly (2008) yielded very quantitatively comparable eigenvalues - including the destabilisation trend. Permitting increase base flow-eigenfunction couplings, particularly when beyond the order of the azimuthal coordinate θ for which the underlying base flow was defined, seems to contribute a stabilising effect on the spatial growth rate and may possibly to converge towards the fully-coupled results with more coupling terms.

Therefore, it was proposed that an inadequately azimuthally expanded base flow leads to a set of incomplete base flow-eigenfunction couplings that improperly affect the eigenvalues. The surviving subset of base flow-eigenfunction couplings may in fact contribute to eigenvalue stabilisation - particularly the higher order θ terms where there is no corresponding base flow term.

A spatial kinetic energy budget analysis using results from the fully-coupled approach was utilised to explore this hypothesis. It was found that the 'Pressure-velocity' correlation term contributed less energy as R decreased while the 'Production' term behaved in the opposite manner. This is indicative of eigenvalue growth rate stabilisation and aligned with the results from linear stability analysis. By contrast, spatial kinetic energy budget analyses using results from the weakly-coupled approach that best matched the asymptotic expansion-based analysis of Alves & Kelly (2008) found that the 'Pressure-velocity' correlation term contributed energy when $R \lesssim 4$, suggestive of destabilisation, as seen in experiments, DNS, and prior LSA. Mode coupling terms always contributed to energy decreases while self-interaction terms generally grew. Interestingly, the higher base flow-eigenfunction couplings for $n \geq 2$ appear to alternately provide less and provide more to the spatial kinetic energy budget. Indeed, as the number of modelled base flow-eigenfunction couplings increased beyond the azimuthal order of the base flow, the 'Advection' term unexpected dominated the kinetic energy budget. This likely indicated that unexpected behaviour occurs when base flow-eigenfunction azimuthal couplings are modelled beyond those of the underlying UVAS base flow.

Asymptotic base flows were used because no analytical solution of the jet-in-crossflow hitherto is known but were amenable to 2D-local stability analysis. These base flows were asymptotically expanded in terms of $\lambda = 1/R$ and are only expected to be accurate to their model assumptions when the $R \gg 1$ and the shear layer is thin. Comparisons of the numerical base flows against experimental measurements indicate that both the tanh and UVAS base flows increasingly differ from experimental measurements as R decreases. The noticeable counterflow near the upstream shear layer is somewhat captured by the UVAS base flow but not by the tanh base flow while the coflow associated with the wake near the downstream shear layer is not present in either numerical base flow.

Given that the numerical base flows increasingly deviate from experimental measurements as R decreases, it is expected that spatial growth rates, wavenumbers, and preferred

frequencies from a linear stability analysis will better align with experimental measurements given a more representative base flow. Moreover, an asymptotically expanded base flow with more terms at higher orders of θ may contribute to more spatial destabilisation, to better align with experimental measurements.

6.2 Further Numerical-Theoretical Research

Given that the present 2D-local linear stability analysis framework is capable of reproducing eigenspectra corresponding to 1D and 2D base flows, it may be possible to obtain more representative jet-in-crossflow eigenspectra by using a more representative base flow using the existing framework. One approach to obtain a more representative base flow and to contribute evidence in favour of the aforementioned proposed mechanism is to extend the tanh and UVAS base flows to higher orders of θ. It is important to note that the distorted inviscid vortex sheet solution of Coelho & Hunt (1989), the basis of both the tanh and the UVAS base flows, was only solved up to $\mathcal{O}(\lambda^2)$ but the $\mathcal{O}(\lambda^3)$ equations were presented. However, these extended base flows may still yet provide inadequate base flow-eigenfunction azimuthal couplings in the fully-coupled asymptotic limit. Hence, a base flow may be alternatively obtained from time-averaged experimental or numerical simulation data. For example, stereo particle image velocimetry (PIV) using a laser sheet aligned parallel to the jet exit plane may provide the three components of velocity. If there was a density difference in the flowfield, perhaps due to thermal phenomena, stratification, or constituent inhomogeneity between the jet and the crossflow, then background-oriented schlieren may also provide the requisite velocity fields. This approach, however, would necessitate the consideration of density variation because the flow incompressibility assumption has been violated. This could be done using the Boussinesq approximation, the zero-Mach number Navier-Stokes equations with the Crocco-Busemann relationship, or the fully compressible Navier-Stokes equations. Finally, a 3D numerical simulation of the jet-in-crossflow may also provide the necessary

velocity fields. These could be direct numerical simulations (DNS) or could involve a turbulence model, such as Unsteady Reynolds-Averaged Navier-Stokes (URANS) or Large Eddy Simulation (LES) because the flowfield near the jet exit at $\mathrm{Re}_D \approx 1900$ is expected to be largely coherent.

The non-negligible non-physical oscillations that contaminated the velocity eigenfunctions near the wake region as R decreased when a high Reynolds number stability mechanism was sought led to the development of a novel upwinding discretisation scheme of the convection terms to provide targeted numerical dissipation in problematic regions. This approach may be extended to surgically provide just enough numerical dissipation to ensure eigenfunction smoothness by adaptively adjusting the scheme or by adaptively refining the numerical grid. Ideas from essentially non-oscillatory (ENO) schemes or weighted essentially non-oscillatory (WENO) schemes may be incorporated here due to their ability to provide smooth solutions for convection-dominated problems. Advances in this upwinding framework may be relevant for pursuing high Reynolds number instability mechanisms for 2D or 3D linear stability analysis using a finite difference discretisation approach.

An alternative strategy to address the non-physical oscillations in the velocity eigenfunctions is to implement numerical schemes that aim to preserve the underlying properties of either the conservation equations or the analytical operators. An inadequate conservation of kinetic energy originating from the nonlinear convection term has been shown to lead to erroneous results for incompressible flows at high Reynolds numbers in flow simulations (Morinishi *et al.*, 1998). Coppola *et al.* (2019) review prior applications of energy-conserving schemes that were able to remove non-physical oscillations at high Reynolds numbers without introducing numerical dissipation. This therefore improved the fidelity of solution. The mimetic finite difference approach aims to create discrete difference operators that preserve the properties of their analytical counterparts (Castillo & Miranda, 2013) and has been shown to yield solutions to the Navier-Stokes equations (Brzenski & Castillo, 2023).

Presuming that a sufficiently representative base flow can be found and a suitable nu-

merical scheme can be employed, then it may be possible to address the 'local' assumption in the present work. A 2D-local linear stability analysis presumes that the base flow negligibly evolves in the streamwise direction i.e., the disturbance wavelength is smaller than the length scale of base flow evolution. Not only does this assumption lead to inaccurate eigenspectra in the low-frequency/wavenumber regime, this assumption does not necessarily capture the reality of streamwise evolution effects on the stability characteristics. For example, the Batchelor vortex was found to have distinct stability characteristics depending on if the underlying base flow was permitted to evolve in the streamwise direction (Broadhurst *et al.*, 2006; Broadhurst & Sherwin, 2008). Therefore, if a suitable base flow can be found, then a parabolised stability equation (PSE) approach can be deployed to obtain stability characteristics that account for weakly-evolving base flow effects (Broadhurst & Sherwin, 2008; Paredes *et al.*, 2011; Li & Malik, 1996; Herbert, 1997).

A flow can be spatially decomposed into regions of perturbation amplification and perturbation generation. The latter, known as the wavemaker, is indicated by the largest eigenvalue sensitivity to disturbances introduced to the structure of the problem as well as the greatest modal response. The region most sensitive to external forcing for the $R = 2,\ 4$ equidensity jet-in-crossflow apparently extends from just inside the jet exit into the bent-over upstream shear layer (Regan & Mahesh, 2019*b*). Extending the existing computational framework to explore the wavemaker structure as the flow conditions are varied could potentially inform control strategies in future experiments via acoustic excitation, for example.

Similarly, the passive disturbance of the jet-in-crossflow base flow applied by a small cusp protruding into the jet exit has significant impact on the upstream shear layer dynamics as well as the downstream jet-in-crossflow structural evolution. Potentially, the outsized effectiveness of disturbing the upstream portion of the jet exit may be explained with the wavemaker study of Regan & Mahesh (2017). However, the more general problem of flow stability sensitivity to modifications of the base flow is relevant to our experimental studies. For example, perhaps experimentally-introduced asymmetries in the jet base flow are

sufficiently amplified downstream to be responsible for the generally-asymmetric counter-rotating vortex pair (CVP). Base flow sensitivity analysis, then, could form part of a passive control study for the jet-in-crossflow. Adjoint-accelerated optimisation could be part of such as a study owing to the computationally parsimonious nature of the adjoint approach.

A non-modal stability analysis may also be explored to understand if there are bypass mechanisms for any of the instabilities. The temporal non-modal stability analysis of R = 1.5, 1.6 jets-in-crossflow given symmetric base flows by Peplinski *et al.* (2015) indicates transient growth on the order of $\mathcal{O}(10^{12})$. Spatial analyses would be more relevant to our experimental forcing study, however. In-house analysis of non-modal growth of flow corresponding to our experimental conditions, then, could inform our forcing strategy to best leverage non-modal growth. For example, the optimal initial condition of a R = 1.5, 1.6 jet-in-crossflow that yielded maximal transient growth consisted of near-horizontal vortices upstream of the jet exit near the upstream shear layer paired with an angled wave packet directed towards the CVP (Peplinski *et al.*, 2015). Impulsively introducing this disturbance experimentally, then, could be the most parsimonious method to 'lock-in' the jet-in-crossflow. Additionally, the structure of optimal non-modal perturbations could explain the experimentally-observed preferences for intrinsic/extrinsic forcing.

Experiments have employed external acoustic excitation of the jet-in-crossflow e.g., Shapiro *et al.* (2006). Resolvent analysis of a $R = 0.3$ flush pipe-issued jet-in-crossflow has found that the optimal forcing structures resemble overlapping lobes emanating from the pipe exit that yield elongated wake-like structures (Chauvat *et al.*, 2020). There was a noticeable difference as the interrogated temporal frequency was varied from $\omega = 0.2$ to $\omega = 0.4$ - the lobe periodicity and the lobe origin within the pipe most notably. This may even better dictate and explain how experiments should harmonically force the jet-in-crossflow. Additionally, the resolvent norm gradient across a range of temporal frequencies ω may align with the asymmetries observed in lock-in diagrams of the free jet and the jet-in-crossflow. A physical understanding may emerge as resolvent optimal forcing indicates the action of

nonlinear advection.

Appendix A

Eigenvalues of the asymmetric coaxial jet

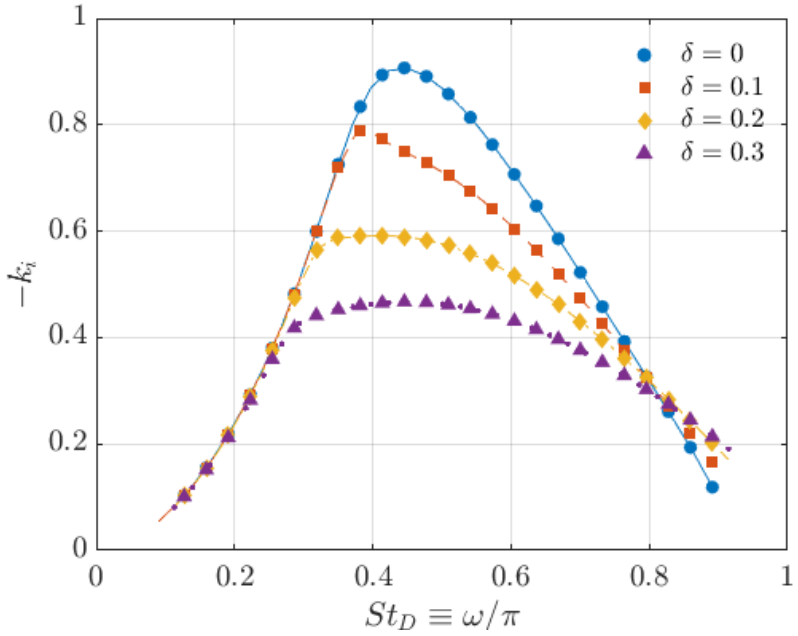

Figure A.1: Spatial growth rates plotted against Strouhal numbers ($\mathrm{St}_D \equiv \omega/\pi$) for the axisymmetric mode of the asymmetric coaxial jet with $\theta_o = \theta_i = \frac{1}{10}$, $N_\theta = 1$, VR $\coloneqq u_{z,o}/u_{z,i} = 0$, and DR $\coloneqq D_0/D_i = 2$. Lines correspond to results reported by Freitas (2019) while symbols correspond to the present results for various values of δ, the amplitude of the asymmetric term.

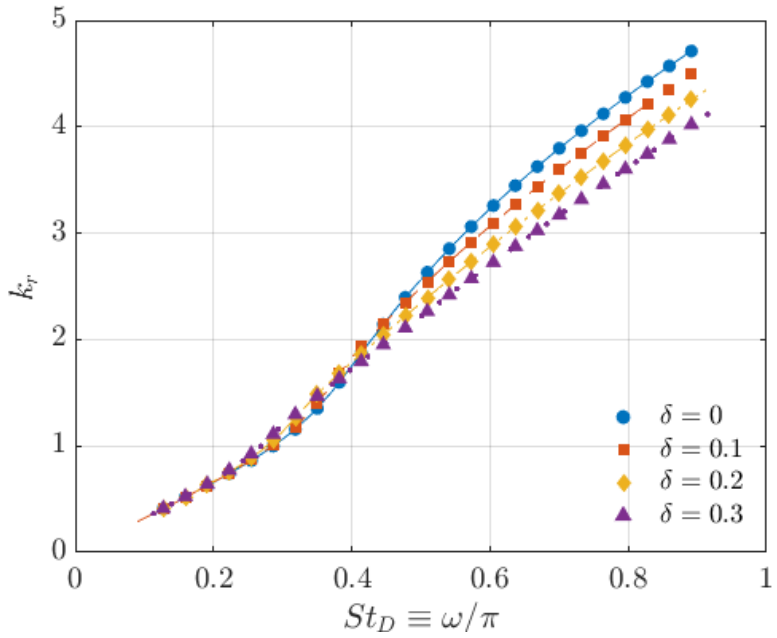

Figure A.2: Wavenumbers plotted against Strouhal numbers ($\mathrm{St}_D \equiv \omega/\pi$) for the axisymmetric mode of the asymmetric coaxial jet with $\theta_o = \theta_i = \frac{1}{10}$, $N_\theta = 1$, VR $\coloneqq u_{z,o}/u_{z,i} = 0$, and DR $\coloneqq D_0/D_i = 2$. Lines correspond to results reported by Freitas (2019) while symbols correspond to the present results for various values of δ, the amplitude of the asymmetric term.

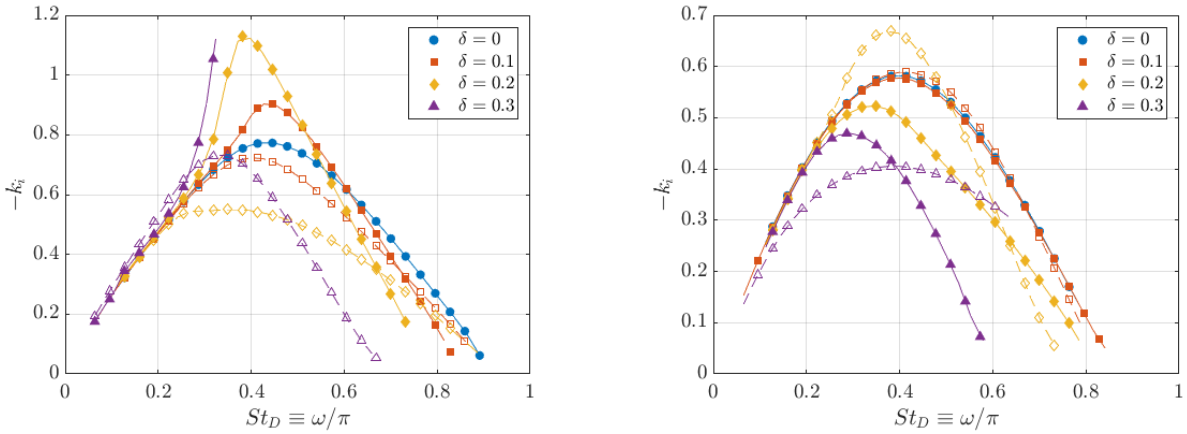

(a) First helical mode

(b) Second helical mode

Figure A.3: Spatial growth rates plotted against Strouhal number ($\mathrm{St}_D \equiv \omega/\pi$) for the (a) first and (b) second helical modes of the asymmetric coaxial jet with $\theta_o = \theta_i = \frac{1}{10}$, $N_\theta = 1$, VR $\coloneqq u_{z,o}/u_{z,i} = 0$, and DR $\coloneqq D_0/D_i = 2$. Lines correspond to results reported by Freitas (2019) while symbols correspond to the present results for various values of δ, the amplitude of the asymmetric term. Filled symbols correspond to the symmetric mode and empty symbols correspond to the anti-symmetric mode.

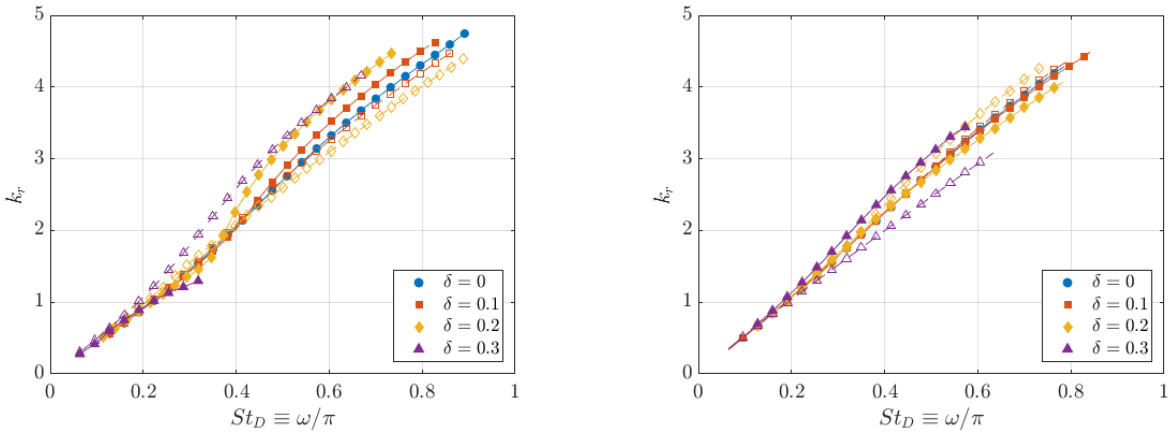

(a) First helical mode

(b) Second helical mode

Figure A.4: Wavenumbers plotted against Strouhal number ($\mathrm{St}_D \equiv \omega/\pi$) for the (a) first and (b) second helical modes of the asymmetric coaxial jet with $\theta_o = \theta_i = \frac{1}{10}$, $N_\theta = 1$, VR $\coloneqq u_{z,o}/u_{z,i} = 0$, and DR $\coloneqq D_0/D_i = 2$. Lines correspond to results reported by Freitas (2019) while symbols correspond to the present results for various values of δ, the amplitude of the asymmetric term. Filled symbols correspond to the symmetric mode and empty symbols correspond to the anti-symmetric mode.

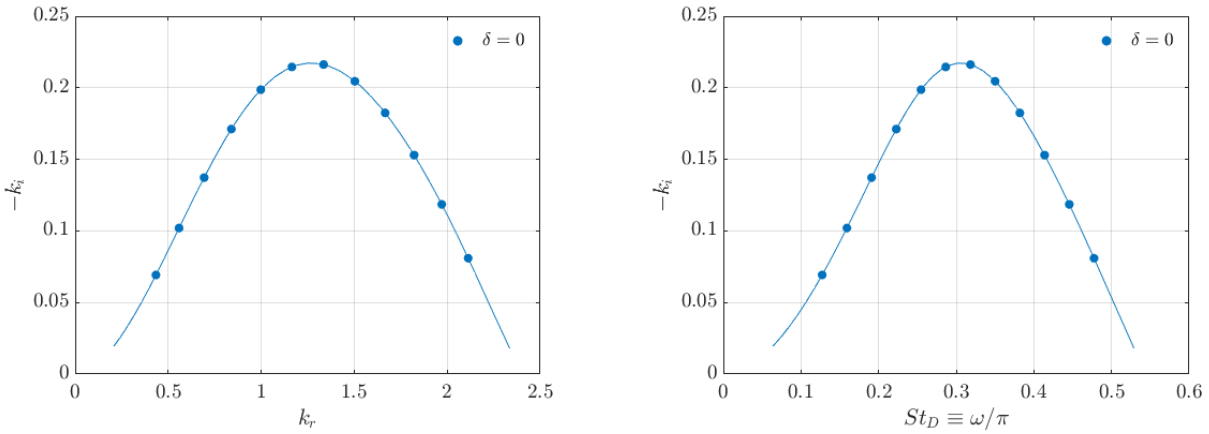

(a) Wavenumber

(b) Strouhal number

Figure A.5: Spatial growth rates of the axisymmetric mode of the asymmetric coaxial jet with $\theta_o = \theta_i = \frac{1}{5}$, $N_\theta = 1$, VR $\coloneqq u_{z,o}/u_{z,i} = 0$, and DR $\coloneqq D_0/D_i = 2$ plotted against (a) wavenumber k_r and (b) Strouhal number $\mathrm{St}_D \equiv \omega/\pi$. Lines correspond to results reported by Freitas (2019) while symbols correspond to the present results.

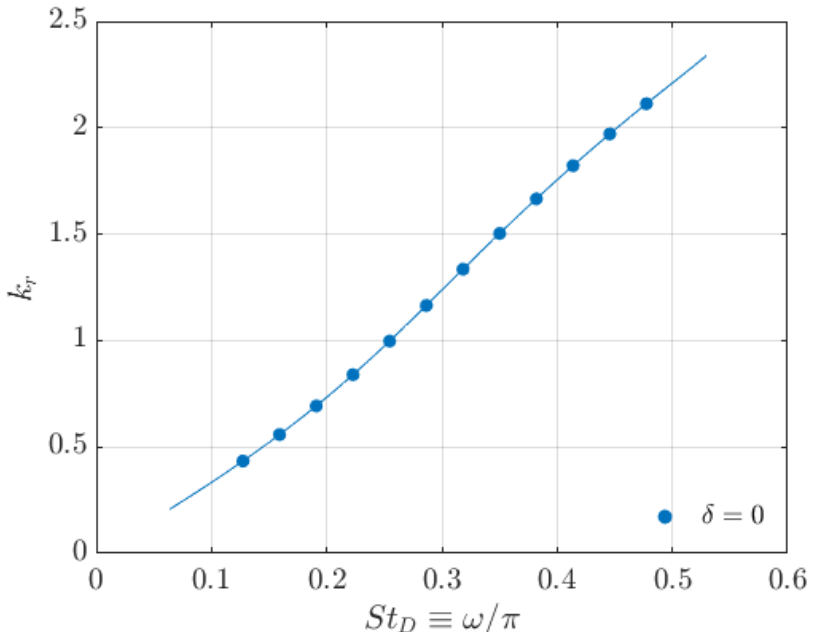

Figure A.6: Wavenumbers plotted against Strouhal numbers ($\mathrm{St}_D \equiv \omega/\pi$) for the axisymmetric mode of the asymmetric coaxial jet with $\theta_o = \theta_i = \frac{1}{5}$, $N_\theta = 1$, VR $\coloneqq u_{z,o}/u_{z,i} = 0$, and DR $\coloneqq D_0/D_i = 2$. Lines correspond to results reported by Freitas (2019) while symbols correspond to the present results.

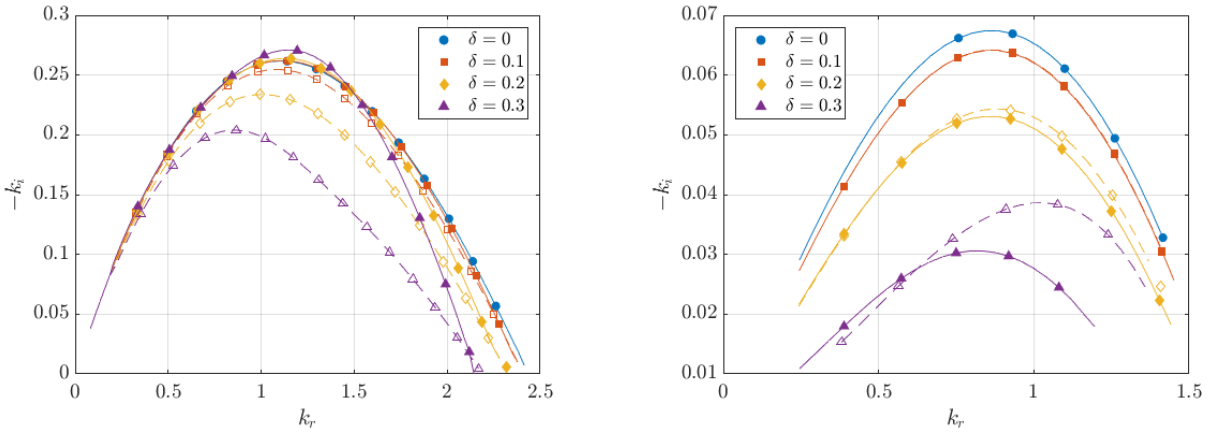

(a) First helical mode

(b) Second helical mode

Figure A.7: Spatial growth rate plotted against the wavenumber for the (a) first and (b) second helical modes of the asymmetric coaxial jet with $\theta_o = \theta_i = \frac{1}{5}$, $N_\theta = 1$, VR $\coloneqq u_{z,o}/u_{z,i} = 0$, and DR $\coloneqq D_0/D_i = 2$. Lines correspond to results reported by Freitas (2019) while symbols correspond to the present results for various values of δ, the amplitude of the asymmetric term. Filled symbols correspond to the symmetric mode and empty symbols correspond to the anti-symmetric mode.

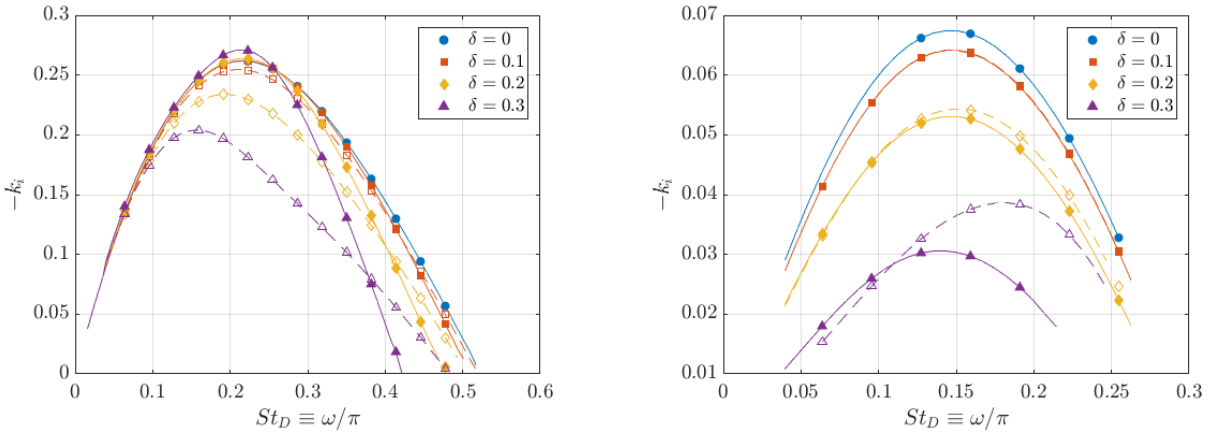

(a) First helical mode

(b) Second helical mode

Figure A.8: Spatial growth rate plotted against Strouhal number ($\mathrm{St}_D \equiv \omega/\pi$) for the (a) first and (b) second helical modes of the asymmetric coaxial jet with $\theta_o = \theta_i = \frac{1}{5}$, $N_\theta = 1$, VR $\coloneqq u_{z,o}/u_{z,i} = 0$, and DR $\coloneqq D_0/D_i = 2$. Lines correspond to results reported by Freitas (2019) while symbols correspond to the present results for various values of δ, the amplitude of the asymmetric term. Filled symbols correspond to the symmetric mode and empty symbols correspond to the anti-symmetric mode.

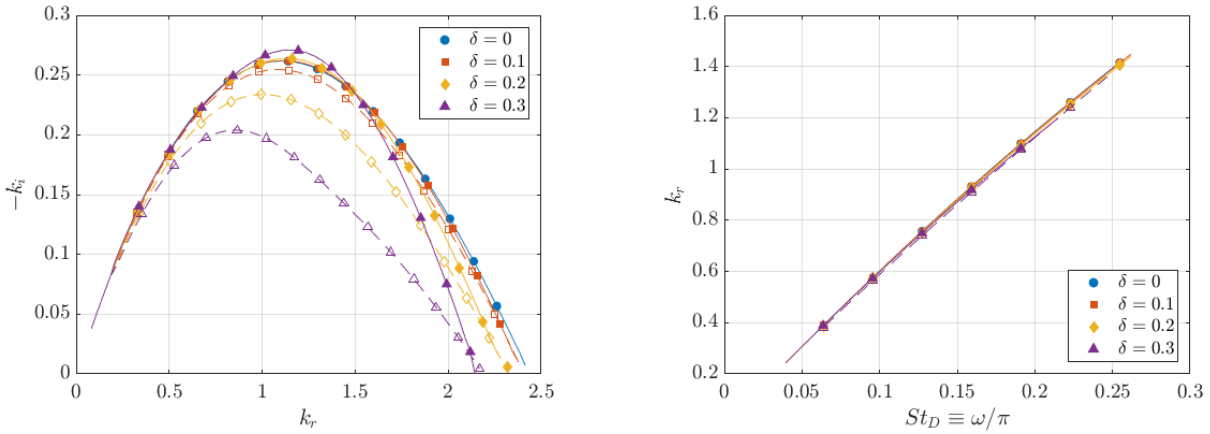

(a) First helical mode

(b) Second helical mode

Figure A.9: Wavenumbers plotted against Strouhal number ($\mathrm{St}_D \equiv \omega/\pi$) for the (a) first and (b) second helical modes of the asymmetric coaxial jet with $\theta_o = \theta_i = \frac{1}{5}$, $N_\theta = 1$, VR $\coloneqq u_{z,o}/u_{z,i} = 0$, and DR $\coloneqq D_0/D_i = 2$. Lines correspond to results reported by Freitas (2019) while symbols correspond to the present results for various values of δ, the amplitude of the asymmetric term. Filled symbols correspond to the symmetric mode and empty symbols correspond to the anti-symmetric mode.

Appendix B

2D linear stability analysis governing equations

B.1 Polar coordinates

Specialising to polar coordinates, 2D spatial linear stability analysis can be formulated as a generalised eigenvalue problem as follows:

$$A_p \vec{\hat{q}}_p = k B_p \vec{\hat{q}}_p \tag{B.1}$$

where A_p and B_p are the generalised eigenvalue pencil pair for the polar coordinates, $k \in \mathcal{C}$ is the spatial eigenvalue, and $\vec{\hat{q}}_p$ is the polar eigenvector defined as:

$$\vec{\hat{q}}_p \coloneqq \begin{pmatrix} \hat{u}_r(r,\theta) & \hat{u}_\theta(r,\theta) & \hat{u}_z(r,\theta) & \hat{p}(r,\theta) & k\hat{u}_r(r,\theta) & k\hat{u}_\theta(r,\theta) & k\hat{u}_z(r,\theta) \end{pmatrix}^T \tag{B.2}$$

.

$$A_p = \begin{pmatrix} \mathcal{L}_p & -\frac{\partial \bar{u}_z}{\partial r} & \frac{1}{r}\frac{\partial \bar{u}_z}{\partial \theta} & 0 & 0 & 0 & 0 \\ 0 & \mathcal{L}_p + \frac{\partial \bar{u}_r}{\partial r} - \frac{1}{Re}\left[\frac{1}{r^2} + \frac{2}{r^2}\frac{\partial}{\partial \theta}\right] & \frac{1}{r}\frac{\partial \bar{u}_r}{\partial \theta} - 2\frac{\bar{u}_\theta}{r} & \frac{\partial}{\partial r} & 0 & 0 & 0 \\ 0 & \frac{\partial \bar{u}_\theta}{\partial r} + \frac{\bar{u}_\theta}{r} & \mathcal{L}_p + \frac{1}{r}\frac{\partial \bar{u}_\theta}{\partial \theta} + \frac{\bar{u}_r}{r} - \frac{1}{Re}\left[\frac{1}{r^2} - \frac{2}{r^2}\frac{\partial}{\partial \theta}\right] & \frac{1}{r}\frac{\partial}{\partial \theta} & 0 & 0 & 0 \\ 0 & \frac{1}{r} + \frac{\partial}{\partial r} & \frac{1}{r}\frac{\partial}{\partial \theta} & 0 & 0 & 0 & 0 \\ 0 & 0 & 0 & 0 & \mathbf{I} & 0 & 0 \\ 0 & 0 & 0 & 0 & 0 & \mathbf{I} & 0 \\ 0 & 0 & 0 & 0 & 0 & 0 & \mathbf{I} \end{pmatrix} \tag{B.3}$$

$$B_p = \begin{pmatrix} -i\bar{u}_z & 0 & 0 & -i & -\frac{1}{Re} & 0 & 0 \\ 0 & -i\bar{u}_z & 0 & 0 & 0 & -\frac{1}{Re} & 0 \\ 0 & 0 & -i\bar{u}_z & 0 & 0 & 0 & -\frac{1}{Re} \\ -i & 0 & 0 & 0 & 0 & 0 & 0 \\ \mathbf{I} & 0 & 0 & 0 & 0 & 0 & 0 \\ 0 & \mathbf{I} & 0 & 0 & 0 & 0 & 0 \\ 0 & 0 & \mathbf{I} & 0 & 0 & 0 & 0 \end{pmatrix} \tag{B.4}$$

The operator $\mathcal{L}_p$ was defined as: $\mathcal{L}_p := -i\omega + \bar{u}_r\frac{\partial}{\partial r} + \frac{\bar{u}_\theta}{r}\frac{\partial}{\partial \theta} - \frac{1}{Re}\left[\frac{\partial^2}{\partial r^2} + \frac{1}{r}\frac{\partial}{\partial r} + \frac{1}{r^2}\frac{\partial^2}{\partial \theta^2} + \frac{\partial^2}{\partial z^2}\right]$. I represents the identity matrix.

Appendix C

Equations for the discrete Fourier transformed spatial kinetic energy budget analysis using the UVAS base flow

This appendix elucidates the the equations associated with the discrete Fourier transformed spatial kinetic energy budget analysis for $N_f = 2, 3$ for the z-momentum equations after having incorporated the continuity equation, just as was done for $N_f = 1$ in Section 4.8.3. These equations pertain to only the UVAS base flow. The r- and θ-momentum equations can be derived in the same manner.

C.1 $N_f \coloneqq 2$

After having incorporated the results of the inner product of the incompressible continuity with pressure for the z-momentum equation becomes with $N_f \coloneqq 2$, there are 5 resultant equations for $n = -2, -1, 0, +1, +2$. The $n = 0$ equation is:

$$
\begin{aligned}
-k\int_\Omega \bar{u}_z^0\left(|u_z^0|^2\right)\,r\,\mathrm{d}r \qquad & = -i\int_\Omega\Bigg[-i\omega\left(|u_z^0|^2\right)\\
-k\int_\Omega u_z^{0*}\left(\bar{u}_z^{-1}u_z^{+1}+\bar{u}_z^{+1}u_z^{-1}\right)\,r\,\mathrm{d}r \qquad & \qquad +u_z^{0*}\left(\bar{u}_r^{+1}\frac{\mathrm{d}u_z^{-1}}{\mathrm{d}r}+\bar{u}_r^{-1}\frac{\mathrm{d}u_z^{+1}}{\mathrm{d}r}\right)\\
& \qquad +u_z^{0*}\left(-\frac{i}{r}\bar{u}_\theta^{+1}u_z^{-1}+\frac{i}{r}\bar{u}_\theta^{-1}u_z^{+1}\right)\Bigg]\,r\,\mathrm{d}r\\
& -i\int_\Omega\Bigg[u_z^{0*}\left(\frac{\mathrm{d}\bar{u}_z^0}{\mathrm{d}r}u_r^0+\frac{\mathrm{d}\bar{u}_z^{-1}}{\mathrm{d}r}u_r^{+1}+\frac{\mathrm{d}\bar{u}_z^{+1}}{\mathrm{d}r}u_r^{-1}\right)\\
& \qquad +u_z^{0*}\frac{i}{r}\left(\bar{u}_z^{+1}u_\theta^{-1}-\bar{u}_z^{-1}u_\theta^{+1}\right)\Bigg]\,r\,\mathrm{d}r\\
& +(k-k^*)\int_\Omega u_z^{0*}p^0\,r\,\mathrm{d}r
\end{aligned}
\tag{C.1}
$$

The $n=+1$ equation is:

$$
\begin{aligned}
-k\int_\Omega \bar{u}_z^0\left(|u_z^{+1}|^2\right)\,r\,\mathrm{d}r \qquad & = -i\int_\Omega\Bigg[-i\omega\left(|u_z^{+1}|^2\right)\\
-k\int_\Omega u_z^{+1*}\left(\bar{u}_z^{+1}u_z^{0}+\bar{u}_z^{-1}u_z^{+2}\right)\,r\,\mathrm{d}r \qquad & \qquad +u_z^{+1*}\left(\bar{u}_r^{+1}\frac{\mathrm{d}u_z^{0}}{\mathrm{d}r}+\bar{u}_r^{-1}\frac{\mathrm{d}u_z^{+2}}{\mathrm{d}r}\right)\\
& \qquad +u_z^{+1*}\left(\frac{2i}{r}\bar{u}_\theta^{-1}u_z^{+2}\right)\Bigg]\,r\,\mathrm{d}r\\
& -i\int_\Omega\Bigg[u_z^{+1*}\left(\frac{\mathrm{d}\bar{u}_z^0}{\mathrm{d}r}u_r^{+1}+\frac{\mathrm{d}\bar{u}_z^{+1}}{\mathrm{d}r}u_r^{0}+\frac{\mathrm{d}\bar{u}_z^{-1}}{\mathrm{d}r}u_r^{+2}\right)\\
& \qquad +u_z^{+1*}\frac{i}{r}\left(\bar{u}_z^{+1}u_\theta^{0}-\bar{u}_z^{-1}u_\theta^{+2}\right)\Bigg]\,r\,\mathrm{d}r\\
& +(k-k^*)\int u_z^{+1*}p^{+1}\,r\,\mathrm{d}r
\end{aligned}
\tag{C.2}
$$

The $n=+2$ equation is:

$$
\begin{aligned}
-k\int_\Omega \bar{u}_z^0\left(|u_z^{+2}|^2\right)\,r\,\mathrm{d}r \qquad =& -i\int_\Omega\Bigg[-i\omega\left(|u_z^{+2}|^2\right)\\
-k\int_\Omega u_z^{+2*}\left(\bar{u}_z^{+1}u_z^{+1}\right)\,r\,\mathrm{d}r \qquad & +u_z^{+2*}\left(\bar{u}_r^{+1}\frac{\mathrm{d}u_z^{+1}}{\mathrm{d}r}\right)\\
& +u_z^{+2*}\left(\frac{i}{r}\bar{u}_\theta^{+1}u_z^{+1}\right)\Bigg]\,r\,\mathrm{d}r\\
& -i\int_\Omega\Bigg[u_z^{+2*}\left(\frac{\mathrm{d}\bar{u}_z^0}{\mathrm{d}r}u_r^{+2}+\frac{\mathrm{d}\bar{u}_z^{+1}}{\mathrm{d}r}u_r^{+1}\right)\\
& \qquad +u_z^{+2*}\frac{i}{r}\left(\bar{u}_z^{+1}u_\theta^{+1}\right)\Bigg]\,r\,\mathrm{d}r\\
& +(k-k^*)\int u_z^{+2*}p^{+2}\,r\,\mathrm{d}r
\end{aligned}
\tag{C.3}
$$

The $n=-1$ equation is:

$$
\begin{aligned}
-k\int_\Omega \bar{u}_z^0\left(|u_z^{-1}|^2\right)\,r\,\mathrm{d}r \qquad =& -i\int_\Omega\Bigg[-i\omega\left(|u_z^{-1}|^2\right)\\
-k\int_\Omega u_z^{-1*}\left(\bar{u}_z^{-1}u_z^0+\bar{u}_z^{+1}u_z^{-2}\right)\,r\,\mathrm{d}r \qquad & +u_z^{-1*}\left(\bar{u}_r^{-1}\frac{\mathrm{d}u_z^0}{\mathrm{d}r}+\bar{u}_r^{+1}\frac{\mathrm{d}u_z^{-2}}{\mathrm{d}r}\right)\\
& +u_z^{-1*}\left(-\frac{2i}{r}\bar{u}_\theta^{+1}u_z^{-2}\right)\Bigg]\,r\,\mathrm{d}r\\
& -i\int_\Omega\Bigg[u_z^{-1*}\left(\frac{\mathrm{d}\bar{u}_z^0}{\mathrm{d}r}u_r^{-1}+\frac{\mathrm{d}\bar{u}_z^{-1}}{\mathrm{d}r}u_r^0+\frac{\mathrm{d}\bar{u}_z^{+1}}{\mathrm{d}r}u_r^{-2}\right)\\
& \qquad +u_z^{-1*}\frac{i}{r}\left(\bar{u}_z^{+1}u_\theta^{-2}-\bar{u}_z^{-1}u_\theta^0\right)\Bigg]\,r\,\mathrm{d}r\\
& +(k-k^*)\int u_z^{-1*}p^{-1}\,r\,\mathrm{d}r
\end{aligned}
\tag{C.4}
$$

The $n=-2$ equation is:

$$
\begin{aligned}
-k\int_\Omega \bar{u}_z^0\left(|u_z^{-2}|^2\right)\,r\,\mathrm{d}r \qquad =& -i\int_\Omega\Bigg[-i\omega\left(|u_z^{-2}|^2\right)\\
-k\int_\Omega u_z^{-2*}\left(\bar{u}_z^{-1}u_z^{-1}\right)\,r\,\mathrm{d}r \qquad & \qquad +u_z^{-2*}\left(\bar{u}_r^{-1}\frac{\mathrm{d}u_z^{-1}}{\mathrm{d}r}\right)\\
& \qquad +u_z^{-2*}\left(-\frac{i}{r}\bar{u}_\theta^{-1}u_z^{-1}\right)\Bigg]\,r\,\mathrm{d}r\\
& -i\int_\Omega\Bigg[u_z^{-2*}\left(\frac{\mathrm{d}\bar{u}_z^0}{\mathrm{d}r}u_r^{-2}+\frac{\mathrm{d}\bar{u}_z^{-1}}{\mathrm{d}r}u_r^{-1}\right)\\
& \qquad +u_z^{+2*}\frac{-i}{r}\left(\bar{u}_z^{-1}u_\theta^{-1}\right)\Bigg]\,r\,\mathrm{d}r\\
& +(k-k^*)\int u_z^{-2*}p^{-2}\,r\,\mathrm{d}r
\end{aligned}
\tag{C.5}
$$

C.2 $N_f \coloneqq 3$

After having incorporated the results of the inner product of the incompressible continuity with pressure for the z-momentum equation becomes with $N_f \coloneqq 3$, there are 7 resultant equations for $n = -3, -2, -1, 0, +1, +2, +3$. The $n = 0$ equation is:

$$
\begin{aligned}
-k\int_\Omega \bar{u}_z^0\left(|u_z^0|^2\right)\,r\,\mathrm{d}r \qquad & = -i\int_\Omega\Bigg[-i\omega\left(|u_z^0|^2\right)\\
-k\int_\Omega u_z^{0*}\left(\bar{u}_z^{-1}u_z^{+1}+\bar{u}_z^{+1}u_z^{-1}\right)\,r\,\mathrm{d}r \qquad & \qquad +u_z^{0*}\left(\bar{u}_r^{+1}\frac{\mathrm{d}u_z^{-1}}{\mathrm{d}r}+\bar{u}_r^{-1}\frac{\mathrm{d}u_z^{+1}}{\mathrm{d}r}\right)\\
& \qquad +u_z^{0*}\left(-\frac{i}{r}\bar{u}_\theta^{+1}u_z^{-1}+\frac{i}{r}\bar{u}_\theta^{-1}u_z^{+1}\right)\Bigg]\,r\,\mathrm{d}r\\
& -i\int_\Omega\Bigg[u_z^{0*}\left(\frac{\mathrm{d}\bar{u}_z^0}{\mathrm{d}r}u_r^0+\frac{\mathrm{d}\bar{u}_z^{-1}}{\mathrm{d}r}u_r^{+1}+\frac{\mathrm{d}\bar{u}_z^{+1}}{\mathrm{d}r}u_r^{-1}\right)\\
& \qquad +u_z^{0*}\frac{i}{r}\left(\bar{u}_z^{+1}u_\theta^{-1}-\bar{u}_z^{-1}u_\theta^{+1}\right)\Bigg]\,r\,\mathrm{d}r\\
& +(k-k^*)\int_\Omega u_z^{0*}p^0\,r\,\mathrm{d}r
\end{aligned}
\tag{C.6}
$$

The $n=+1$ equation is:

$$
\begin{aligned}
-k\int_\Omega \bar{u}_z^0\left(|u_z^{+1}|^2\right)\,r\,\mathrm{d}r \qquad & = -i\int_\Omega\Bigg[-i\omega\left(|u_z^{+1}|^2\right)\\
-k\int_\Omega u_z^{+1*}\left(\bar{u}_z^{+1}u_z^{0}+\bar{u}_z^{-1}u_z^{+2}\right)\,r\,\mathrm{d}r \qquad & \qquad +u_z^{+1*}\left(\bar{u}_r^{+1}\frac{\mathrm{d}u_z^{0}}{\mathrm{d}r}+\bar{u}_r^{-1}\frac{\mathrm{d}u_z^{+2}}{\mathrm{d}r}\right)\\
& \qquad +u_z^{+1*}\left(\frac{2i}{r}\bar{u}_\theta^{-1}u_z^{+2}\right)\Bigg]\,r\,\mathrm{d}r\\
& -i\int_\Omega\Bigg[u_z^{+1*}\left(\frac{\mathrm{d}\bar{u}_z^0}{\mathrm{d}r}u_r^{+1}+\frac{\mathrm{d}\bar{u}_z^{+1}}{\mathrm{d}r}u_r^{0}+\frac{\mathrm{d}\bar{u}_z^{-1}}{\mathrm{d}r}u_r^{+2}\right)\\
& \qquad +u_z^{+1*}\frac{i}{r}\left(\bar{u}_z^{+1}u_\theta^{0}-\bar{u}_z^{-1}u_\theta^{+2}\right)\Bigg]\,r\,\mathrm{d}r\\
& +(k-k^*)\int u_z^{+1*}p^{+1}\,r\,\mathrm{d}r
\end{aligned}
\tag{C.7}
$$

The $n=+2$ equation is:

$$
\begin{aligned}
-k\int_\Omega \bar{u}_z^0\left(|u_z^{+2}|^2\right)\,r\,\mathrm{d}r \qquad & = -i\int_\Omega\Bigg[-i\omega\left(|u_z^{+2}|^2\right)\\
-k\int_\Omega u_z^{+2*}\left(\bar{u}_z^{+1}u_z^{+1}+\bar{u}_z^{-1}u_z^{+3}\right)\,r\,\mathrm{d}r \qquad & \quad +u_z^{+2*}\left(\bar{u}_r^{+1}\frac{\mathrm{d}u_z^{+1}}{\mathrm{d}r}+\bar{u}_r^{-1}\frac{\mathrm{d}u_z^{+3}}{\mathrm{d}r}\right)\\
& \quad +u_z^{+2*}\frac{i}{r}\left(\bar{u}_\theta^{+1}u_z^{+1}+3\bar{u}_\theta^{-1}u_z^{+3}\right)\Bigg]\,r\,\mathrm{d}r\\
& -i\int_\Omega\Bigg[u_z^{+2*}\left(\frac{\mathrm{d}\bar{u}_z^0}{\mathrm{d}r}u_r^{+2}+\frac{\mathrm{d}\bar{u}_z^{+1}}{\mathrm{d}r}u_r^{+1}+\frac{\mathrm{d}\bar{u}_z^{-1}}{\mathrm{d}r}u_r^{+3}\right)\\
& \quad +u_z^{+2*}\frac{i}{r}\left(\bar{u}_z^{+1}u_\theta^{+1}-\bar{u}_z^{-1}u_\theta^{+3}\right)\Bigg]\,r\,\mathrm{d}r\\
& +(k-k^*)\int u_z^{+2*}p^{+2}\,r\,\mathrm{d}r
\end{aligned}
\tag{C.8}
$$

The $n=+3$ equation is:

$$
\begin{aligned}
-k\int_\Omega \bar{u}_z^0\left(|u_z^{+3}|^2\right)\,r\,\mathrm{d}r \qquad & = -i\int_\Omega\Bigg[-i\omega\left(|u_z^{+3}|^2\right)\\
-k\int_\Omega u_z^{+3*}\left(\bar{u}_z^{+1}u_z^{+2}\right)\,r\,\mathrm{d}r \qquad & \quad +u_z^{+3*}\left(\bar{u}_r^{+1}\frac{\mathrm{d}u_z^{+2}}{\mathrm{d}r}\right)\\
& \quad +u_z^{+3*}\frac{i}{r}\left(2\bar{u}_\theta^{+1}u_z^{+2}\right)\Bigg]\,r\,\mathrm{d}r\\
& -i\int_\Omega\Bigg[u_z^{+3*}\left(\frac{\mathrm{d}\bar{u}_z^0}{\mathrm{d}r}u_r^{+3}+\frac{\mathrm{d}\bar{u}_z^{+1}}{\mathrm{d}r}u_r^{+2}\right)\\
& \quad +u_z^{+3*}\frac{i}{r}\left(\bar{u}_z^{+1}u_\theta^{+2}\right)\Bigg]\,r\,\mathrm{d}r\\
& +(k-k^*)\int u_z^{+3*}p^{+3}\,r\,\mathrm{d}r
\end{aligned}
\tag{C.9}
$$

The $n=-1$ equation is:

$$
\begin{aligned}
-k\int_\Omega \bar{u}_z^0\left(|u_z^{-1}|^2\right)\,r\,\mathrm{d}r \qquad & = -i\int_\Omega\Bigg[-i\omega\left(|u_z^{-1}|^2\right)\\
-k\int_\Omega u_z^{-1*}\left(\bar{u}_z^{-1}u_z^0+\bar{u}_z^{+1}u_z^{-2}\right)\,r\,\mathrm{d}r \qquad & \quad +u_z^{-1*}\left(\bar{u}_r^{-1}\frac{\mathrm{d}u_z^0}{\mathrm{d}r}+\bar{u}_r^{+1}\frac{\mathrm{d}u_z^{-2}}{\mathrm{d}r}\right)\\
& \quad +u_z^{-1*}\left(-\frac{2i}{r}\bar{u}_\theta^{+1}u_z^{-2}\right)\Bigg]\,r\,\mathrm{d}r\\
& -i\int_\Omega\Bigg[u_z^{-1*}\left(\frac{\mathrm{d}\bar{u}_z^0}{\mathrm{d}r}u_r^{-1}+\frac{\mathrm{d}\bar{u}_z^{-1}}{\mathrm{d}r}u_r^0+\frac{\mathrm{d}\bar{u}_z^{+1}}{\mathrm{d}r}u_r^{-2}\right)\\
& \quad +u_z^{-1*}\frac{i}{r}\left(\bar{u}_z^{+1}u_\theta^{-2}-\bar{u}_z^{-1}u_\theta^0\right)\Bigg]\,r\,\mathrm{d}r\\
& +(k-k^*)\int u_z^{-1*}p^{-1}\,r\,\mathrm{d}r
\end{aligned}
\tag{C.10}
$$

The $n=-2$ equation is:

$$
\begin{aligned}
-k\int_\Omega \bar{u}_z^0\left(|u_z^{-2}|^2\right)\,r\,\mathrm{d}r \qquad & = -i\int_\Omega\Bigg[-i\omega\left(|u_z^{-2}|^2\right)\\
-k\int_\Omega u_z^{-2*}\left(\bar{u}_z^{-1}u_z^{-1}+\bar{u}_z^{+1}u_z^{-3}\right)\,r\,\mathrm{d}r \qquad & \quad +u_z^{-2*}\left(\bar{u}_r^{-1}\frac{\mathrm{d}u_z^{-1}}{\mathrm{d}r}+\bar{u}_r^{+1}\frac{\mathrm{d}u_z^{-3}}{\mathrm{d}r}\right)\\
& \quad -u_z^{-2*}\frac{i}{r}\left(\bar{u}_\theta^{-1}u_z^{-1}+3\bar{u}_\theta^{+1}u_z^{-3}\right)\Bigg]\,r\,\mathrm{d}r\\
& -i\int_\Omega\Bigg[u_z^{-2*}\left(\frac{\mathrm{d}\bar{u}_z^0}{\mathrm{d}r}u_r^{-2}+\frac{\mathrm{d}\bar{u}_z^{-1}}{\mathrm{d}r}u_r^{-1}+\frac{\mathrm{d}\bar{u}_z^{+1}}{\mathrm{d}r}u_r^{-3}\right)\\
& \quad +u_z^{-2*}\frac{i}{r}\left(\bar{u}_z^{+1}u_\theta^{-3}-\bar{u}_z^{-1}u_\theta^{-1}\right)\Bigg]\,r\,\mathrm{d}r\\
& +(k-k^*)\int u_z^{+2*}p^{+2}\,r\,\mathrm{d}r
\end{aligned}
\tag{C.11}
$$

The $n=-3$ equation is:

$$
\begin{aligned}
-k\int_\Omega \bar{u}_z^0\left(|u_z^{-3}|^2\right)\,r\,\mathrm{d}r \qquad =& -i\int_\Omega\Bigg[-i\omega\left(|u_z^{-3}|^2\right)\\
-k\int_\Omega u_z^{-3*}\left(\bar{u}_z^{-1}u_z^{-2}\right)\,r\,\mathrm{d}r \qquad & +u_z^{-3*}\left(\bar{u}_r^{-1}\frac{\mathrm{d}u_z^{-2}}{\mathrm{d}r}\right)\\
& -u_z^{-3*}\frac{i}{r}\left(2\bar{u}_\theta^{-1}u_z^{-2}\right)\Bigg]\,r\,\mathrm{d}r\\
& -i\int_\Omega\Bigg[u_z^{-3*}\left(\frac{\mathrm{d}\bar{u}_z^0}{\mathrm{d}r}u_r^{-3}+\frac{\mathrm{d}\bar{u}_z^{-1}}{\mathrm{d}r}u_r^{-2}\right)\\
& -u_z^{-3*}\frac{i}{r}\left(\bar{u}_z^{-1}u_\theta^{-2}\right)\Bigg]\,r\,\mathrm{d}r\\
& +(k-k^*)\int u_z^{-3*}p^{-3}\,r\,\mathrm{d}r
\end{aligned}
\tag{C.12}
$$

Bibliography

Aadhishwaran, A.B. & Diwan, S.S. 2021 Predominance of pressure transport in spatial energy budget for a mixing layer approaching absolute instability. *Phys. Rev. Fluids* **6**, L091901.

Agarap, A.F. 2018 Deep learning using rectified linear units (relu). *arXiv preprint arXiv:1803.08375* .

Åkervik, E., Brandt, L., Henningson, D.S., Hœpffner, J., Marxen, O. & Schlatter, P. 2006 Steady solutions of the Navier-Stokes equations by selective frequency damping. *Physics of Fluids* **18** (6), 068102.

Alizard, F. & Robinet, J.C. 2007 Spatially convective global modes in a boundary layer. *Physics of Fluids* **19** (11), 114105.

Alves, L. 2006 Transerve Jet Shear-Layer Instabilities: Linear Stability Analysis and Numerical Simulations. Ph.D. thesis, University of California, Los Angeles.

Alves, L.S.d.B. & Kelly, R.E. 2008 A uniformly valid asymptotic solution for a transverse jet and its linear stability analysis. *Philosphical Transactions of the Royal Society A, Mathematical, Physical, and Engineering Sciences* **366**, 2729–2744.

Alves, L.S.d.B., Kelly, R.E. & Karagozian, A.R. 2007 Local stability analysis of an inviscid transverse jet. *Journal of Fluid Mechanics* **581**, 401–418.

Alves, L.S.d.B., Kelly, R.E. & Karagozian, A.R. 2008 Transverse-jet shear-layer instabilities. Part 2. Linear analysis for large jet-to-crossflow velocity ratio. *Journal of Fluid Mechanics* **602**, 383–401.

Anderson, E., Bai, Z., Bischof, C., Blackford, S., Demmel, J., Dongarra, J., Du Croz, J., Greenbaum, A., Hammarling, S., McKenney, A. & Sorensen, D. 1999 *LAPACK Users' Guide*, 3rd edn. Philadelphia, PA: Society for Industrial and Applied Mathematics.

Andersson, P., Berggren, M. & Henningson, D.S. 1999 Optimal disturbances and bypass transition in boundary layers. *Physics of Fluids* **11** (1), 134–150.

Andreopoulos, J. 1985 On the structure of jets in a crossflow. *Journal of Fluid Mechanics* **157**, 163–197.

Appel, T. 2020 Boundary layer instabilities due to surface irregularities: a harmonic Navier-Stokes approach. Ph.D. thesis, Imperial College London.

Appel, T., Mughal, M.S. & Ashworth, R. 2019 Global stability analysis of a boundary layer with surface indentations .

Arakawa, A. 1966 Computational design for long-term numerical integration of the equations of fluid motion: Two-dimensional incompressible flow. Part I. *Journal of Computational Physics* **1** (1), 119–143.

Arnoldi, W.E. 1951 The principle of minimized iterations in the solution of the matrix eigenvalue problem. *Quarterly of Applied Mathematics* **9** (1), 17–29.

Ashpis, D.E. & Reshotko, E. 1990 The vibrating ribbon problem revisited. *Journal of Fluid Mechanics* **213**, 531–547.

Bagheri, S., Schlatter, P., Schmid, P.J. & Henningson, D.S. 2009 Global stability of a jet in crossflow. *Journal of Fluid Mechanics* **624**, 33–44.

Baines, P.G., Majumdar, S.J. & Mitsudera, H. 1996 The mechanics of the Tollmien-Schlichting wave. *Journal of Fluid Mechanics* **312**, 107–124.

Balachandar, S. & Malik, M.R. 1995 Inviscid instability of streamwise corner flow. *Journal of Fluid Mechanics* **282**, 187–201.

Balay, S., Abhyankar, S., Adams, M.F., Benson, S., Brown, J., Brune, P., Buschelman, K., Constantinescu, E., Dalcin, L., Dener, A., Eijkhout, V., Faibussowitsch, J., Gropp, W.D.,

Hapla, V., Isaac, T., Jolivet, P., Karpeev, D., Kaushik, D., Knepley, M.G., Kong, F., Kruger, S., May, D.A., McInnes, L.C., Mills, R.T., Mitchell, L., Munson, T., Roman, J.E., Rupp, K., Sanan, P., Sarich, J., Smith, B.F., Zampini, S., Zhang, H., Zhang, H. & Zhang, J. 2023 PETSc/TAO users manual. *Tech. Rep.* ANL-21/39 - Revision 3.19. Argonne National Laboratory.

Barletta, A. & Alves, L.S.d.B. 2014 Transition to Absolute Instability for (not so) Dummies. *arXiv e-prints* p. arXiv:1403.5794.

Batchelor, G.K. 2000 *An Introduction to Fluid Dynamics*. Cambridge University Press.

Batchelor, G.K. & Gill, A.E. 1962 Analysis of the stability of axisymmetric jets. *Journal of Fluid Mechanics* **14** (4), 529–551.

Becker, H.A. & Massaro, T.A. 1968 Vortex evolution in a round jet. *Journal of Fluid Mechanics* **31** (3), 435–448.

Berenger, J.P. 1994 A perfectly matched layer for the absorption of electromagnetic waves. *Journal of Computational Physics* **114** (2), 185–200.

Berkooz, G., Holmes, P. & Lumley, J.L. 1993 The Proper Orthogonal Decomposition in the Analysis of Turbulent Flows. *Annual Review of Fluid Mechanics* **25** (1), 539–575.

Bers, A. 1973 Theory of absolute and convective instabilities. In *International Congress on Waves and Instabilities in Plasmas* (ed. G. Auer & F. Cap), pp. B1–B52.

Besnard, A. 2019 External Asymmetric Forcing of Convectively Unstable Transverse Jets. Ph.D. thesis, University of California, Los Angeles.

Besnard, A., Harris, E.W. & Karagozian, A.R. 2022 Asymmetric forcing of convectively unstable transverse jets. *Phys. Rev. Fluids* **7**, 063902.

Bhoraniya, R. & Vinod, N. 2017 Global stability analysis of axisymmetric boundary layer over a circular cone. *Phys. Rev. Fluids* **2**, 063901.

Bhoraniya, R. & Vinod, N. 2018 Global stability analysis of axisymmetric boundary layer over a circular cylinder. *Theoretical and Computational Fluid Dynamics* **32**, 425–449.

Bidan, G., Vézier, C. & Nikitopoulos, D.E. 2012 Study of Unforced and Modulated Film-Cooling Jets Using Proper Orthogonal Decomposition—Part I: Unforced Jets. *Journal of Turbomachinery* **135** (2), 021037.

Bishop, C.M. & Nasrabadi, N.M. 2006 *Pattern Recognition and Machine Learning*, 1st edn., *Information Science and Statistics*, vol. 4. Springer.

Blackford, S.L., Demmel, J., Dongarra, J., Duff, I., Hammarling, S., Henry, G., Heroux, M., Kaufman, L., Lumsdaine, A., Petitet, A., Pozo, R., Remington, K. & Whaley, R.C. 2002 An Updated Set of Basic Linear Algebra Subprograms (BLAS). *ACM Transactions on Mathematical Software* **28** (2), 135–151.

Bockhorn, H., Mewes, D., Peukert, W. & Warnecke, H.J., ed. 2010 *Micro and Macro Mixing: Analysis, Simulation and Numerical Calculation. Heat and Mass Transfer* . Berlin: Springer-Verlag Berlin Heidelberg.

Bodony, D.J. 2006 Analysis of sponge zones for computational fluid mechanics. *Journal of Computational Physics* **212** (2), 681–702.

Bons, J.P., Sondergaard, R. & Rivir, R.B. 2001 The Fluid Dynamics of LPT Blade Separation Control Using Pulsed Jets. *Journal of Turbomachinery* **124** (1), 77–85.

de Boor, C. 1978 *A Practical Guide to Splines*, 1st edn. Springer-Verlag New York.

Boronin, S.A., Healey, J.J. & Sazhin, S.S. 2013 Non-modal stability of round viscous jets. *Journal of Fluid Mechanics* **716**, 96–119.

Bowman, C.T. 1992 Control of combustion-generated nitrogen oxide emissions: Technology driven by regulation. *Symposium (International) on Combustion* **24** (1), 859 – 878, Twenty-Fourth Symposium on Combustion.

Boyd, J.P. 2001 *Chebyshev and Fourier Spectral Methods*, 2nd edn. Courier Corporation.

Bridges, T.J. & Morris, P.J. 1984 Differential eigenvalue problems in which the parameter appears nonlinearly. *Journal of Computational Physics* **55** (3), 437 – 460.

Briggs, R.J. 1964 *Electron-Stream Interaction with Plasmas*, 1st edn. MIT Press.

Broadhurst, M.S. & Sherwin, S.J. 2008 The parabolised stability equations for 3D-flows: implementation and numerical stability. *Applied Numerical Mathematics* **58** (7), 1017–1029, Spectral Methods in Computational Fluid Dynamics.

Broadhurst, M.S., Theofilis, V. & Sherwin, S.J. 2006 Spectral element stability analysis of vortical flows. In *IUTAM Symposium on Laminar-Turbulent Transition* (ed. Rama Govindarajan), pp. 153–158. Dordrecht: Springer Netherlands.

Broadwell, J.E. & Breidenthal, R.E. 1984 Structure and mixing of a transverse jet in incompressible flow. *Journal of Fluid Mechanics* **148**, 405–412.

Broyden, C. 1965 A Class of Methods for Solving Nonlinear Simultaneous Equations. *Mathematics of Computation* **19**, 577–593.

Broze, G. & Hussain, F. 1994 Nonlinear dynamics of forced transitional jets: periodic and chaotic attractors. *Journal of Fluid Mechanics* **263**, 93–132.

Brzenski, J. & Castillo, J.E. 2023 Solving Navier—Stokes with mimetic operators. *Computers & Fluids* **254**, 105817.

Butler, K.M. & Farrell, B.F. 1992 Three-dimensional optimal perturbations in viscous shear flow. *Physics of Fluids A: Fluid Dynamics* **4** (8), 1637–1650.

Casacuberta, J., Groot, K.J., Tol, H.J. & Hickel, S. 2018 Effectivity and efficiency of selective frequency damping for the computation of unstable steady-state solutions. *Journal of Computational Physics* **375**, 481–497.

Castillo, J.E. & Miranda, G.F. 2013 *Mimetic Discretization Methods*. CRC Press.

Chandrasekhar, S. 1961 *Hydrodynamic and Hydromagnetic Stability*. *International Series of Monographs on Physics* . Oxford University Press.

Chauvat, G. 2020 Receptivity, Stability and Sensitivity analysis of two- and three-dimensional flows. Ph.D. thesis, KTH Royal Institute of Technology.

Chauvat, G., Peplinski, A., Henningson, D.S. & Hanifi, A. 2020 Global linear analysis of a jet in cross-flow at low velocity ratios. *Journal of Fluid Mechanics* **889**, A12.

Chomaz, J.M. 2005 Global instabilities in spatially developing flows: Non-Normality and Nonlinearity. *Annual Review of Fluid Mechanics* **37** (1), 357–392.

Chomaz, J.M., Huerre, P. & Redekopp, L.G. 1988 Bifurcations to Local and Global Modes in Spatially Developing Flows. *Physical Review Letters* **60**, 25–28.

Coelho, S.L.V. & Hunt, J.C.R. 1989 The dynamics of the near field of strong jets in crossflows. *Journal of Fluid Mechanics* **200**, 95–120.

Coenen, W., Sevilla, A. & Sánchez, A.L. 2008 Absolute instability of light jets emerging from circular injector tubes. *Physics of Fluids* **20** (7), 074104.

Cohen, J. & Wygnanski, I. 1987 The evolution of instabilities in the axisymmetric jet. Part 2. The flow resulting from the interaction between two waves. *Journal of Fluid Mechanics* **176**, 221–235.

Colonius, T. 2004 Modeling Artificial Boundary Conditions for Compressible Flow. *Annual Review of Fluid Mechanics* **36** (1), 315–345.

Constantinescu, G. & Lele, S. 2002 A highly accurate technique for the treatment of flow equations at the polar axis in cylindrical coordinates using series expansions. *Journal of Computational Physics* **183** (1), 165–186.

Coppola, G., Capuano, F. & de Luca, L. 2019 Discrete Energy-Conservation Properties in the Numerical Simulation of the Navier–Stokes Equations. *Applied Mechanics Reviews* **71** (1), 010803.

Corke, T.C. & Kusek, S.M. 1993 Resonance in axisymmetric jets with controlled helical-mode input. *Journal of Fluid Mechanics* **249**, 307–336.

Cortelezzi, L. & Karagozian, A.R. 2001 On the formation of the counter-rotating vortex pair in transverse jets. *Journal of Fluid Mechanics* **446**, 347–373.

Cotrell, D.L., McFadden, G.B. & Alder, B.J. 2008 Instability in pipe flow. *Proceedings of the National Academy of Sciences* **105** (2), 428–430.

Crighton, D.G. & Gaster, M. 1976 Stability of slowly diverging jet flow. *Journal of Fluid Mechanics* **77** (2), 397–413.

Criminale, W.O., Jackson, T.L. & Joslin, R.D. 2003 *Theory and Computation of Hydrodynamic Stability*. Cambridge University Press.

Crow, S.C. & Champagne, F.H. 1971 Orderly structure in jet turbulence. *Journal of Fluid Mechanics* **48** (3), 547–591.

Curran, E.T. 2001 Scramjet Engines: The First Forty Years. *Journal of Propulsion and Power* **17** (6), 1138–1148.

Dalcin, L.D., Paz, R.R., Kler, P.A. & Cosimo, A. 2011 Parallel distributed computing using python. *Advances in Water Resources* **34** (9), 1124 – 1139, new Computational Methods and Software Tools.

Daly, C.A. 2013 Nonlinear and Non-Modal Stability of Structures Evolving in Shear Flows. Ph.D. thesis, University of Cambridge.

Danaila, I. & Boersma, B.J. 2000 Direct numerical simulation of bifurcating jets. *Physics of Fluids* **12** (5), 1255–1257.

Danckwerts, P. 1952 The definition and measurement of some characteristics of mixtures. *Applied Scientific Research* **3**, 279–296.

Davey, A. & Drazin, P.G. 1969 The stability of Poiseuille flow in a pipe. *Journal of Fluid Mechanics* **36** (2), 209–218.

Davey, A. & Nguyen, H.P.F. 1971 Finite-amplitude stability of pipe flow. *Journal of Fluid Mechanics* **45** (4), 701–720.

Davitian, J., Getsinger, D., Hendrickson, C. & Karagozian, A.R. 2010 Transition to global instability in transverse-jet shear layers. *Journal of Fluid Mechanics* **661**, 294–315.

Dimotakis, P.E. & Miller, P.L. 1990 Some consequences of the boundedness of scalar fluctuations. *Physics of Fluids A: Fluid Dynamics* **2** (11), 1919–1920.

Drazin, P.G. & Reid, W.H. 1981 *Hydrodynamic Stability*, 1st edn. *Cambridge Monographs on Mechanics* . Cambridge University Press.

Ellingsen, T. & Palm, E. 1975 Stability of linear flow. *The Physics of Fluids* **18** (4), 487–488.

Ericsson, T. 1986 A Generalised Eigenvalue Problem and The Lanczos Algorithm. In *Large Scale Eigenvalue Problems* (ed. Jane Cullum & Ralph A. Willoughby), *North-Holland Mathematics Studies*, vol. 127, pp. 95 – 119. North-Holland.

Farrell, B.F. 1988 Optimal excitation of perturbations in viscous shear flow. *The Physics of Fluids* **31** (8), 2093–2102.

Ferziger, J.H. & Perić, M. 1980 *Numerical heat transfer and fluid flow*, 1st edn. McGraw-Hill.

Ferziger, J.H. & Perić, M. 2002 *Computational Methods for Fluid Dynamics*, 3rd edn. Springer-Verlag Berlin.

Fletcher, C.A. 1991 *Computational Techniques for Fluid Dynamics Volume II Specific Techniques for Different Flow Categories*, 2nd edn. New York: Springer-Verlag.

Freitas, R.B. 2019 Estudo de Diferentes Ferramentas para Análise de Estabilidade Linear e Modal em Escoamentos Incompressíveis e Compressíveis. Ph.D. thesis, Universidade Federal Fluminense.

Freymuth, P. 1966 On transition in a separated laminar boundary layer. *Journal of Fluid Mechanics* **25** (4), 683–704.

Fric, T.F. & Roshko, A. 1994 Vortical structure in the wake of a transverse jet. *Journal of Fluid Mechanics* **279**, 1–47.

Gareev, L., Zayko, J., Chicherina, A., Trifonov, V., Reshmin, A. & Vedeneev, V. 2022 Experimental validation of inviscid linear stability theory applied to an axisymmetric jet. *Journal of Fluid Mechanics* **934**, A3.

Garg, V.K. & Rouleau, W.T. 1972 Linear spatial stability of pipe Poiseuille flow. *Journal of Fluid Mechanics* **54** (1), 113–127.

Garnaud, X., Lesshafft, L., Schmid, P.J. & Huerre, P. 2013 The preferred mode of incompressible jets: linear frequency response analysis. *Journal of Fluid Mechanics* **716**, 189–202.

Gaster, M. 1962 A note on the relation between temporally-increasing and spatially-increasing disturbances in hydrodynamic stability. *Journal of Fluid Mechanics* **14** (2), 222–224.

Getsinger, D., Gevorkyan, L., Smith, O. & Karagozian, A. 2014 Structural and stability characteristics of jets in crossflow. *Journal of Fluid Mechanics* **760**, 342–367.

Getsinger, D., Hendrickson, C. & Karagozian, A. 2012 Shear layer instabilities in low-density transverse jets. *Experiments in Fluids* **53**, 783–801.

Gevorkyan, L., Shoji, T., Getsinger, D.R., Smith, O.I. & Karagozian, A.R. 2016 Transverse jet mixing characteristics. *Journal of Fluid Mechanics* **790**, 237–274.

Gevorkyan, L., Shoji, T., Peng, W.Y. & Karagozian, A.R. 2018 Influence of the velocity field on scalar transport in gaseous transverse jets. *Journal of Fluid Mechanics* **834**, 173–219.

Gharib, M., Rambod, E. & Shariff, K. 1998 A universal time scale for vortex ring formation. *Journal of Fluid Mechanics* **360**, 121–140.

Ghosh, D. & Baeder, J. 2010 A High Order Conservative Upwind Algorithm for the Incompressible Navier Stokes Equations. In *40th Fluid Dynamics Conference and Exhibit*.

Giannetti, F. & Luchini, P. 2007 Structural sensitivity of the first instability of the cylinder wake. *Journal of Fluid Mechanics* **581**, 167–197.

Gibbs, J. 1898 Fourier's series. *Nature* **59**, 200.

Gill, A.E. 1965 On the behaviour of small disturbances to Poiseuille flow in a circular pipe. *Journal of Fluid Mechanics* **21** (1), 145–172.

Gipon, M. 2018 Shear flow instabilities in pipes and channels. Ph.D. thesis, Imperial College.

Gmelin, C. & Rist, U. 2001 Active control of laminar-turbulent transition using instantaneous vorticity signals at the wall. *Physics of Fluids* **13** (2), 513–519.

Godrèche, C. & Manneville, P., ed. 1998 *Hydrodynamics and Nonlinear Instabilities*. *Collection Alea-Saclay: Monographs and Texts in Statistical Physics* . Cambridge University Press.

Goldberg, D. 1991 What every computer scientist should know about floating-point arithmetic. *ACM Comput. Surv.* **23** (1), 5–48.

Goodfellow, I., Bengio, Y. & Courville, A. 2016 *Deep Learning*. *Adaptive Computation and Machine Learning* . MIT press.

Groot, K., Pinna, F. & van Oudheusden, B. 2015 On Closing the Streamwise BiGlobal Stability Problem: The Effect of Boundary Conditions. *Procedia IUTAM* **14**, 459–468, iUTAM$_A BCM Symposium on Laminar Turbulent Transition$.

Groot, K.J. 2018 BiGlobal Stability of Shear Flows: Spanwise & Streamwise Analyses. Ph.D. thesis, Delft University of Technology.

Gubanov, O. & Cortelezzi, L. 2010 Towards the design of an optimal mixer. *Journal of Fluid Mechanics* **651**, 27–53.

Gudmundsson, K. & Colonius, T. 2019 Parabolized stability equation models for turbulent jets and their radiated sound. In *15th AIAA/CEAS Aeroacoustics Conference (30th AIAA Aeroacoustics Conference)*.

Gurka, R., Liberzon, A. & Hetsroni, G. 2006 POD of vorticity fields: A method for spatial characterization of coherent structures. *International Journal of Heat and Fluid Flow* **27**, 416–423.

Gustavsson, L.H. 1989 Direct Resonance of Nonaxisymmetric Disturbances in Pipe Flow. *Studies in Applied Mathematics* **80** (2), 95–108.

Gutmark, E. & Ho, C. 1983 Preferred modes and the spreading rates of jets. *The Physics of Fluids* **26** (10), 2932–2938.

Gutmark, E., Ibrahim, I. & Murugappan, S. 2011 Dynamics of single and twin circular jets in cross flow. *Experiments in Fluids* **50**, 653–663.

Hagen, G.H.L. 1839 Ueber die Bewegung des Wassers in engen cylindrischen Röhren. *Annalen der Physik* **122** (3), 423–442.

Hall, P. & Horseman, N.J. 1991 The linear inviscid secondary instability of longitudinal vortex structures in boundary layers. *Journal of Fluid Mechanics* **232**, 357–375.

Hama, F., Williams, D. & Fasel, H. 1980 Flow field and energy balance according to the spatial linear stability theory of the blasius boundary layer. In *Laminar-turbulent transition; Proceedings of the Symposium, Stuttgart, West Germany, September 16-22, 1979.* (ed. Richard Eppler & Hermann Fasel), pp. 73–85. Berlin, Heidelberg: Berlin, Springer-Verlag.

Hama, F.R. & de la Veaux, S. 1980 Energy balance equations in the spatial stability analyses of boundary layers with and without parallel-flow approximation. Princeton University.

Han, G., Tumin, A. & Wygnanski, I. 2000 Laminar–turbulent transition in Poiseuille pipe flow subjected to periodic perturbation emanating from the wall. Part 2. Late stage of transition. *Journal of Fluid Mechanics* **419**, 1–27.

Harlow, F.H. & Welch, J.E. 1965 Numerical Calculation of Time-Dependent Viscous Incompressible Flow of Fluid with Free Surface. *The Physics of Fluids* **8** (12), 2182–2189.

Harris, E. 2020 Structure, Mixing, and Dynamics of Controlled Single and Coaxial Jets in Crossflow. Ph.D. thesis, University of California, Los Angeles.

Harris, E.W., Besnard, A. & Karagozian, A. 2021 Effect of tabs on transverse jet instabilities, structure, vorticity dynamics and mixing. *Journal of Fluid Mechanics* **918**, A8.

Harris, E.W., Schein, S.G., Ren, D.D.W. & Karagozian, A.R. 2023 Synchronization and dynamics of the axisymmetrically excited jet in crossflow. *Phys. Rev. Fluids* **8**, 033902.

Hastie, T., Tibshirani, R., Friedman, J.H. & Friedman, J.H. 2009 *The Elements of Statistical Learning: Data Mining, Inference, and Prediction*, , vol. 2. Springer.

Heeg, R.S. & Geurts, B.J. 1997 Spatial Instabilities of the Incompressible Attachment-Line Flow Using Sparse Matrix Jacobi–Davidson Techniques. *Applied Scientific Research* (59), 315—329.

Herbert, T. 1997 Parabolized Stability Equations. *Annual Review of Fluid Mechanics* **29** (1), 245–283.

Hernandez, V., Roman, J.E. & Vidal, V. 2005 Slepc: A scalable and flexible toolkit for the solution of eigenvalue problems. *ACM Trans. Math. Softw.* **31** (3), 351–362.

Ho, C.M. & Huerre, P. 1984 Perturbed Free Shear Layers. *Annual Review of Fluid Mechanics* **16** (1), 365–422.

Hosseinverdi, S. & Fasel, H.F. 2023 High-order-accurate incompressible flow solver for high-fidelity numerical simulations and linear stability analysis. *AIAA Journal* **61** (4), 1772–1789.

Huang, L.M. & Chen, T.S. 1974 Stability of developing pipe flow subjected to non-axisymmetric disturbances. *Journal of Fluid Mechanics* **63** (1), 183–193.

Huerre, P. & Monkewitz, P. 1985 Absolute and convective instabilities in free shear layers. *Journal of Fluid Mechanics* **159**, 151–168.

Huerre, P. & Monkewitz, P. 1990 Local and Global Instabilities in Spatially Developing Flows. *Annual Review of Fluid Mechanics* **22** (1), 473–537.

Hussain, A.K.M.F. & Zaman, K.B.M.Q. 1978 The free shear layer tone phenomenon and probe interference. *Journal of Fluid Mechanics* **87** (2), 349–383.

Hussain, A.K.M.F. & Zaman, K.B.M.Q. 1981 The 'preferred mode' of the axisymmetric jet. *Journal of Fluid Mechanics* **110**, 39–71.

Itoh, N. 1977*a* Nonlinear stability of parallel flows with subcritical Reynolds numbers. Part 1. An asymptotic theory valid for small amplitude disturbances. *Journal of Fluid Mechanics* **82** (3), 455–467.

Itoh, N. 1977*b* Nonlinear stability of parallel flows with subcritical Reynolds numbers. Part 2. Stability of pipe Poiseuille flow to finite axisymmetric disturbances. *Journal of Fluid Mechanics* **82** (3), 469–479.

Ivanov, O., Ashurov, D., Gareev, L. & Vedeneev, V. 2023 Non-modal perturbation growth in a laminar jet: an experimental study. *Journal of Fluid Mechanics* **963**, A8.

Iyer, P.S. & Mahesh, K. 2016 A numerical study of shear layer characteristics of low-speed transverse jets. *Journal of Fluid Mechanics* **790**, 275–307.

Jendoubi, S. & Strykowski, P.J. 1994 Absolute and convective instability of axisymmetric jets with external flow. *Physics of Fluids* **6** (9), 3000–3009.

Jiménez-González, J.I., Brancher, P. & Martínez-Bazán, C. 2015 Modal and non-modal evolution of perturbations for parallel round jets. *Physics of Fluids* **27** (4), 044105.

Johari, H., Pacheco-Tougas, M. & Hermanson, J.C. 1999 Penetration and Mixing of Fully Modulated Turbulent Jets in Crossflow. *AIAA Journal* **37** (7), 842–850.

Juniper, M.P., Hanifi, A. & Theofilis, V. 2014 Modal Stability Theory. *Applied Mechanics Review* **66**, 024804.

Kambe, T. 1969 The Stability of an Axisymmetric Jet with Parabolic Profile. *Journal of the Physical Society of Japan* **26** (2), 566–575.

Kamotani, Y. & Greber, I. 1972 Experiments on a Turbulent Jet in a Cross Flow. *AIAA Journal* **10** (11), 1425–1429.

Karagozian, A.R. 2010 Transverse jets and their control. *Progress in Energy and Combustion Science* **36** (5), 531 – 553.

Kaskel, A. 1961 Experimental Study of the Stability of Pipe Flow. II. Development of Disturbance Generator. *Tech. Rep.* NASA Technical Report 32-138. Jet Propulsion Laboratory, California Inst. of Tech. Pasadena.

Keffer, J.F. & Baines, W.D. 1963 The round turbulent jet in a cross-wind. *Journal of Fluid Mechanics* **15** (4), 481–496.

Kelso, R.M., Lim, T.T. & Perry, A.E. 1996 An experimental study of round jets in cross-flow. *Journal of Fluid Mechanics* **306**, 111–144.

Kelso, R.M. & Smits, A.J. 1995 Horseshoe vortex systems resulting from the interaction between a laminar boundary layer and a transverse jet. *Physics of Fluids* **7** (1), 153–158.

Kerswell, R.R. & Davey, A. 1996 On the linear instability of elliptic pipe flow. *Journal of Fluid Mechanics* **316**, 307–324.

Khorrami, M.R., Malik, M.R. & Ash, R.L. 1989 Application of spectral collocation techniques to the stability of swirling flows. *Journal of Computational Physics* **81** (1), 206 – 229.

Kingma, D.P. & Ba, J. 2014 Adam: A method for stochastic optimization. *arXiv preprint arXiv:1412.6980* .

Kiwata, T., Usuzawa, T., Komatsu, N., Kimura, S. & Oshkai, P. 2011 Flow Structure of a Coaxial Circular Jet with Axisymmetric and Helical Instability Modes. *Journal of Fluid Science and Technology* **6**, 437–452.

Kollman, W. 1990 The pdf approach to turbulent flow. *Theoretical and Computational Fluid Dynamics* **1**, 249–285.

Kuzo, D.M. 1995 An experimental study of the turbulent transverse jet. Ph.D. thesis, California Institute of Technology.

Lanczos, C. 1950 An iteration method for the solution of the eigenvalue problem of linear differential and integral operators. *Journal of Research of the National Bureau of Standards* **45** (4), 255 – 282.

Landahl, M.T. 1980 A note on an algebraic instability of inviscid parallel shear flows. *Journal of Fluid Mechanics* **98** (2), 243–251.

Landau, L. & Lifshitz, E. 1987 *Fluid Mechanics*, 2nd edn., *Course of Theoretical Physics*, vol. 6. London: Pergammon.

Lessen, M., Sadler, S.G. & Liu, T. 1968 Stability of Pipe Poiseuille Flow. *The Physics of Fluids* **11** (7), 1404–1409.

Lessen, M. & Singh, P.J. 1973 The stability of axisymmetric free shear layers. *Journal of Fluid Mechanics* **60** (3), 433–457.

LeVeque, R.J. 2007 *Finite difference methods for ordinary and partial differential equations: steady-state and time-dependent problems*. SIAM.

Li, F. & Malik, M.R. 1996 On the nature of PSE approximation. *Theoretical and Computational Fluid Dynamics* **8**, pages 253–273.

Li, L.K. & Juniper, M.P. 2013 Lock-in and quasiperiodicity in hydrodynamically self-excited flames: Experiments and modelling. *Proceedings of the Combustion Institute* **34** (1), 947 – 954.

Li, L.K.B. 2011 Forcing of globally unstable jets and flames. Ph.D. thesis, University of Cambridge.

Lin, C. 1955 *The Theory of Hydrodynamic Stability*, 1st edn. Cambridge University Press.

Lock, R. 1951 The velocity distribution in the laminar boundary layer between parallel streams. *The Quarterly Journal of Mechanics and Applied Mathematics* **4** (1), 42 – 63.

Luchini, P. 2000 Reynolds-number-independent instability of the boundary layer over a flat surface: optimal perturbations. *Journal of Fluid Mechanics* **404**, 289–309.

Lumley, J. 1967 The Structure of Inhomogeneous Turbulent Flows. In *Proceedings of the International Colloquium on the Fine Scale Structure of the Atmosphere and Its Influence on Radio Wave Propagation* (ed. A.M. Yaglam & V.I. Tatarsky), pp. 166–177. Nauka, Moscow: Doklady Akademii Nauk SSSR.

Macaraeg, M.G., Streett, C.L. & Hussaini, M.Y. 1988 A spectral collocation solution to the compressible stability eigenvalue problem. *Tech. Rep.* NASA-TP-2858. Langley Research Center, Langley Station, Hampton, Virginia.

Mahesh, K. 2013 The Interaction of Jets with Crossflow. *Annual Review of Fluid Mechanics* **45** (1), 379–407.

Mallier, R. 1998 Interactions between a pair of helical waves on an axisymmetric jet. *Fluid Dynamics Research* **23** (5), 267.

Margason, R.J. 1968 The path of a jet directed at large angle to a subsonic freestream. *Tech. Rep.* NASA TN-4919. Langley Research Center, Langley Station, Hampton, Virginia.

Martin, J.E. & Meiburg, E. 1991 Numerical investigation of three-dimensionally evolving jets subject to axisymmetric and azimuthal perturbations. *Journal of Fluid Mechanics* **230**, 271–318.

Mathew, G., Mezić, I. & Petzold, L. 2005 A multiscale measure for mixing. *Physica D: Nonlinear Phenomena* **211** (1), 23 – 46.

Mathew, G.M., Mezic, I. & Petzold, L. 2003 A multiscale measure for mixing and its applications. In *42nd IEEE International Conference on Decision and Control (IEEE Cat. No.03CH37475)*, , vol. 3, pp. 2314–2321 Vol.3.

Mattingly, G.E. & Chang, C.C. 1974 Unstable waves on an axisymmetric jet column. *Journal of Fluid Mechanics* **65** (3), 541–560.

Megerian, S., Davitian, J., Alves, L.S.d.B. & Karagozian, A.R. 2007 Transverse-jet shear-layer instabilities. Part 1. Experimental studies. *Journal of Fluid Mechanics* **593**, 93–129.

Merle, X., Alizard, F. & Robinet, J.C. 2010 Finite difference methods for viscous incompressible global stability analysis. *Computers & Fluids* **39** (6), 911–925.

Merle, X. & Robinet, J.C. 2010 Staggered finite difference scheme for global stability analysis of incompressible flows .

Metcalfe, R.W. & Orszag, S.A. 1973 Numerical calculations of the linear stability of pipe flows. *Tech. Rep.*. Flow Research Inc.

Michalke, A. 1964 On the inviscid instability of the hyperbolictangent velocity profile. *Journal of Fluid Mechanics* **19** (4), 543–556.

Michalke, A. 1965 On spatially growing disturbances in an inviscid shear layer. *Journal of Fluid Mechanics* **23** (3), 521–544.

Michalke, A. 1970 A note on the spatial jet-instability of the compressible cylindrical vortex sheet. *Tech. Rep.* DLR Research Report No. FB-70-51. DLR Institute for Turbulence, Berlin.

Michalke, A. 1971 Instabilität eines kompressiblen runden Freistrahis unter Beruecksichtigung des Einflusses der Strahigrenzschichtdicke (instability of a compressible circular jet considering the influence of the thickness of the jet boundary layer). *Tech. Rep.*. Deutsche Forschungs- und Versuchsanstalt für Luft- und Raumfahrt (DFVLR).

Michalke, A. 1984 Survey on jet instability theory. *Progress in Aerospace Sciences* **21**, 159 – 199.

Michalke, A. & Hermann, G. 1982 On the inviscid instability of a circular jet with external flow. *Journal of Fluid Mechanics* **114**, 343–359.

Mohan Rai, M. & Moin, P. 1991 Direct simulations of turbulent flow using finite-difference schemes. *Journal of Computational Physics* **96** (1), 15–53.

Mohseni, K. & Colonius, T. 2000 Numerical treatment of polar coordinate singularities. *Journal of Computational Physics* **157** (2), 787–795.

Moin, P. 2010 *Fundamentals of Engineering Numerical Analysis*, 2nd edn. Cambridge University Press.

Moler, C.B. & Stewart, G.W. 1973 An Algorithm for Generalized Matrix Eigenvalue Problems. *SIAM Journal of Numerical Analysis* **10** (2), 241–256.

Mollendorf, J.C. & Gebhart, B. 1973 An experimental and numerical study of the viscous stability of a round laminar vertical jet with and without thermal buoyancy for symmetric and asymmetric disturbances. *Journal of Fluid Mechanics* **61** (2), 367–399.

Monkewitz, P., Bechert, D., Barsikow, B. & Lehmann, B. 1990 Self-excited oscillations and mixing in a heated round jet. *Journal of Fluid Mechanics* **213**, 611–639.

Monkewitz, P.A. & Sohn, K.D. 1988 Absolute instability in hot jets. *AIAA Journal* **26** (8), 911–916.

Morinishi, Y., Lund, T., Vasilyev, O. & Moin, P. 1998 Fully conservative higher order finite difference schemes for incompressible flow. *Journal of Computational Physics* **143** (1), 90–124.

Morris, P.J. 1976 The spatial viscous instability of axisymmetric jets. *Journal of Fluid Mechanics* **77** (3), 511–529.

Morse, N. & Mahesh, K. 2023 Effect of tabs on the shear layer dynamics of a jet in cross-flow. *Journal of Fluid Mechanics* **958**, A6.

Muldoon, F. & Acharya, S. 2010 Direct Numerical Simulation of pulsed jets-in-crossflow. *Computers & Fluids* **39** (10), 1745 – 1773.

Muppidi, S. & Mahesh, K. 2005 Study of trajectories of jets in crossflow using direct numerical simulations. *Journal of Fluid Mechanics* **530**, 81–100.

M'Closkey, R.T., King, J.M., Cortelezzi, L. & Karagozian, A.R. 2002 The actively controlled jet in crossflow. *Journal of Fluid Mechanics* **452**, 325–335.

Nair, V., Wilde, B., Emerson, B. & Lieuwen, T. 2019 Shear Layer Dynamics in a Reacting Jet in Crossflow. *Proceedings of the Combustion Institute* **37** (4), 5173 – 5180.

Narayanan, S., Barooah, P. & Cohen, J.M. 2003 Dynamics and Control of an Isolated Jet in Crossflow. *AIAA Journal* **41** (12), 2316–2330.

New, T., Lim, T. & Luo, S. 2006 Effects of jet velocity profiles on a round jet in cross-flow. *Journal of the Hydraulics Division* **40**, 859 – 875.

Nicoud, F. 2000 Conservative high-order finite-difference schemes for low-mach number flows. *Journal of Computational Physics* **158** (1), 71–97.

Olendraru, C., Sellier, A., Rossi, M. & Huerre, P. 1999 Inviscid instability of the Batchelor vortex: Absolute-convective transition and spatial branches. *Physics of Fluids* **11** (7), 1805–1820.

Otto, S. & Denier, J.P. 1999 Numerical solution of a generalized elliptic partial differential eigenvalue problem. *Journal of Computational Physics* **156** (2), 352–359.

Panton, R.L. 2013 *Incompressible Flow*, 4th edn. John Wiley & Sons, Ltd.

Paredes, P., Theofilis, V., Rodriguez, D. & Tendero, J. 2011 The PSE-3D instability analysis methodology for flows depending strongly on two and weakly on the third spatial dimension. In *6th AIAA Theoretical Fluid Mechanics Conference*.

Patel, J.M., Groot, K.J., Saiyasak, C., Coder, J.G., Stefanski, D.L. & Reed, H.L. 2022 Energy-budget analysis of the crossflow instability on a hypersonic yawed cone. In *AIAA AVIATION 2022 Forum*. AIAA.

Patera, A.T. & Orszag, S.A. 1982 Instability of Pipe Flow. In *Nonlinear Problems: Present and Future* (ed. Alan Bishop, David Campbell & Basil Nicolaenko), *North-Holland Mathematics Studies*, vol. 61, pp. 367 – 377. North-Holland.

Peplinski, A., Schlatter, P. & Henningson, D. 2015 Global stability and optimal perturbation for a jet in cross-flow. *European Journal of Mechanics - B/Fluids* **49**, 438 – 447, trends in Hydrodynamic Instability in honour of Patrick Huerre's 65th birthday.

Perić, M., Kessler, R. & Scheuerer, G. 1988 Comparison of finite-volume numerical methods with staggered and colocated grids. *Computers & Fluids* **16** (4), 389–403.

Petersen, R.A. & Samet, M.M. 1988 On the preferred mode of jet instability. *Journal of Fluid Mechanics* **194**, 153–173.

Peterson, S.D. & Plesniak, M.W. 2004 Evolution of jets emanating from short holes into cross-flow. *Journal of Fluid Mechanics* **503**, 57–91.

Peyret, R. & Taylor, T.D. 1983 *Computational Methods for Fluid Flow*, 2nd edn. New York: Springer-Verlag.

Plaschko, P. 1979 Helical instabilities of slowly divergent jets. *Journal of Fluid Mechanics* **92** (2), 209–215.

Poiseuille, J.L.M. 1840 Recherches expérimentales sur le mouvement des dans les tubes de tres petits diametrès; I. Influence de la pression sur la quantité de liquide qui traverse les tubes de très petits diametrès. *Comptes rendus de l'Académie des Sciences* **11**, 961–967.

Pratte, B.D. & Baines, W.D. 1967 Profiles of the round turbulent jet in a cross flow. *Journal of the Hydraulics Division* **93** (6), 53 – 64.

Press, W.H., Teukolsky, S.A., Vetterling, W.T. & Flannery, B.P. 2007 *Numerical Recipes: The Art of Scientific Computing*, 3rd edn. Cambridge University Press.

Provansal, M., Mathis, C. & Boyer, L. 1987 Bénard-von Kármán instability: transient and forced regimes. *Journal of Fluid Mechanics* **182**, 1–22.

R. B. Lehoucq, D.C.S. & Yang, C. 1998 *ARPack User's Guide: Solution of Large-Scale Eigenvalue Problems with Implicitly Restarted Arnolid Methods*, 1st edn. SIAM.

Raman, G., Rice, E.J. & Reshotko, E. 1991 Naturally occurring and forced azimuthal modes in a turbulent jet. *Tech. Rep.* NASA-TM-103692. NASA Lewis Research Centre, NASA Lewis Research Center Cleveland, OH., United States.

Ran, W., Zare, A., Nichols, J.W. & Jovanovic, M.R. 2017 The effect of sponge layers on global stability analysis of blasius boundary layer flow .

Reddy, S.C. & Henningson, D.S. 1993 Energy growth in viscous channel flows. *Journal of Fluid Mechanics* **252**, 209–238.

Reddy, S.C., Schmid, P.J. & Henningson, D.S. 1993 Pseudospectra of the Orr-Sommerfeld operator. *SIAM Journal on Applied Mathematics* **53** (1), 15–47.

Regan, M.A. & Mahesh, K. 2017 Global linear stability analysis of jets in cross-flow. *Journal of Fluid Mechanics* **828**, 812–836.

Regan, M.A. & Mahesh, K. 2019*a* Adjoint sensitivity and optimal perturbations of the low-speed jet in cross-flow. *Journal of Fluid Mechanics* **877**, 330–372.

Regan, M.A. & Mahesh, K. 2019*b* Stability and Sensitivity Analysis of a Low-speed Jet in Cross-flow. In *AIAA Scitech 2019 Forum*. AIAA Journal.

Rempfer, D. 2006 On Boundary Conditions for Incompressible Navier-Stokes Problems. *Applied Mechanics Reviews* **59** (3), 107–125.

Reshotko, E. & Tumin, A. 2001 Spatial theory of optimal disturbances in a circular pipe flow. *Physics of Fluids* **13** (4), 991–996.

Reynolds, O.F.R.S. 1883 An experimental investigation of the circumstances which determine whether the motion of water shall be direct or sinuous, and of the law of resistance in parallel channels. *Philosophical Transactions of the Royal Society of London* **174**, 935–982.

Rhie, C.M. & Chow, W.L. 1983 Numerical study of the turbulent flow past an airfoil with trailing edge separation. *AIAA Journal* **21** (11), 1525–1532.

Riherd, Paul Markey, I. 2013 The control of boundary layers and channel flows using plasma actuators. PhD thesis, copyright - Database copyright ProQuest LLC; ProQuest does not claim copyright in the individual underlying works; Last updated - 2023-03-04.

Saad, Y. 2011 *Numerical Methods for Large Eigenvalue Problems: Revised Edition*, 2nd edn. *Classics in Applied Mathematics* . Philadelphia, PA: Society for Industrial and Applied Mathematics.

Salwen, H., Cotton, F.W. & Grosch, C.E. 1980 Linear stability of Poiseuille flow in a circular pipe. *Journal of Fluid Mechanics* **98** (2), 273–284.

Sau, R. & Mahesh, K. 2007 Passive scalar mixing in vortex rings. *Journal of Fluid Mechanics* **582**, 449–461.

Sau, R. & Mahesh, K. 2010 Optimization of pulsed jets in crossflow. *Journal of Fluid Mechanics* **653**, 365–390.

Schlichting, H. 1933 Laminare Strahlausbreitung. *ZAMM - Journal of Applied Mathematics and Mechanics / Zeitschrift für Angewandte Mathematik und Mechanik* **13** (4), 260–263.

Schlichting, H. 1968 *Boundary-Layer Theory*, 6th edn. *Series in Mechanical Engineering* . New York: McGraw-Hill.

Schmid, P.J. & Henningson, D.S. 1994 Optimal energy density growth in Hagen–Poiseuille flow. *Journal of Fluid Mechanics* **277**, 197–225.

Schmid, P.J. & Henningson, D.S. 2001 *Stability and Transition in Shear Flows*, 1st edn., *Applied Mathematical Sciences*, vol. 142. New York: Springer-Verlag.

Shaabani-Ardali, L., Sipp, D. & Lesshafft, L. 2020 Optimal triggering of jet bifurcation: an example of optimal forcing applied to a time-periodic base flow. *Journal of Fluid Mechanics* **885**, A34.

Shan, J.W. & Dimotakis, P.E. 2006 Reynolds-number effects and anisotropy in transverse-jet mixing. *Journal of Fluid Mechanics* **566**, 47–96.

Shapiro, S.R., King, J.M., M'Closkey, R.T. & Karagozian, A.R. 2006 Optimization of Controlled Jets in Crossflow. *AIAA Journal* **44** (6), 1292–1298.

Shoji, T., Besnard, A., Harris, E.W., M'Closkey, R.T. & Karagozian, A.R. 2019 Effects of Axisymmetric Square-Wave Excitation on Transverse Jet Structure and Mixing. *AIAA Journal* **57** (5), 1862–1876.

Shoji, T., Harris, E.W., Besnard, A., Schein, S.G. & Karagozian, A.R. 2020*a* On the origins of transverse jet shear layer instability transition. *Journal of Fluid Mechanics* **890**, A7.

Shoji, T., Harris, E.W., Besnard, A., Schein, S.G. & Karagozian, A.R. 2020*b* Transverse jet lock-in and quasiperiodicity. *Phys. Rev. Fluids* **5**, 013901.

Sipp, D. & Lebedev, A. 2007 Global stability of base and mean flows: a general approach and its applications to cylinder and open cavity flows. *Journal of Fluid Mechanics* **593**, 333–358.

Sirovich, L. 1987 Turbulence and the dynamics of coherent structures Part I: Coherent Structures. *Quarterly of Applied Mathematics* **45** (3), 561–571.

Sleijpen, G.L.G. & der Vorst, H.A.V. 2000 A Jacobi-Davidson Iteration Method for Linear Eigenvalue Problems. *SIAM Review* **42** (2), 267–293.

Smith, S.H. & Mungal, M.G. 1998 Mixing, structure and scaling of the jet in crossflow. *Journal of Fluid Mechanics* **357**, 83–122.

de Souza, D.B., Freitas, R.B. & de B. Alves, L.S. 2021 Criterion for the linear convective to absolute instability transition of a jet in crossflow: The countercurrent viscous and round mixing-layer analogy. *Phys. Rev. Fluids* **6**, L041901.

Sreenivasan, K., Raghu, S. & Kyle, D. 1989 Absolute instability in variable density round jets. *Experiments in Fluids* **7**, 309–317.

Stewart, G.W. 2002 A Krylov–Schur Algorithm for Large Eigenproblems. *SIAM Journal on Matrix Analysis and Applications* **23** (3), 601–614.

Strykowski, P.J. & Niccum, D.L. 1991 The stability of countercurrent mixing layers in circular jets. *Journal of Fluid Mechanics* **227**, 309–343.

Suzuki, T. & Colonius, T. 2006 Instability waves in a subsonic round jet detected using a near-field phased microphone array. *Journal of Fluid Mechanics* **565**, 197–226.

Tam, C.K. & Webb, J.C. 1993 Dispersion-relation-preserving finite difference schemes for computational acoustics. *Journal of Computational Physics* **107** (2), 262–281.

Tam, C.K.W. & Morris, P.J. 1980 The radiation of sound by the instability waves of a compressible plane turbulent shear layer. *Journal of Fluid Mechanics* **98** (2), 349–381.

Theofilis, V. 2003 Advances in global linear instability analysis of nonparallel and three-dimensional flows. *Progress in Aerospace Sciences* **39** (4), 249–315.

Theofilis, V. 2011 Global linear instability. *Annual Review of Fluid Mechanics* **43** (1), 319–352.

Theofilis, V. 2017 The linearized pressure poisson equation for global instability analysis of incompressible flows. *Theoretical and Computational Fluid Dynamics* **31**, 333–358.

Theofilis, V. & Colonius, T. 2004 Three-dimensional instabilities of compressible flow over open cavities: Direct solution of hte biglobal eivenvalue problem .

Thomson, W. 1871 XLVI. Hydrokinetic solutions and observations. *The London, Edinburgh, and Dublin Philosophical Magazine and Journal of Science* **42** (281), 362–377.

Trefethen, L. & Embree, M. 2005 *Spectra and Pseudospectra: The Behavior of Nonnormal Matrices and Operators*, 1st edn. Princeton: Princeton University Press.

Trefethen, L.N., Trefethen, A.E., Reddy, S.C. & Driscoll, T.A. 1993 Hydrodynamic Stability Without Eigenvalues. *Science* **261** (5121), 578–584.

Tumin, A. 1996 Receptivity of pipe Poiseuille flow. *Journal of Fluid Mechanics* **315**, 119–137.

Tumin, A. & Reshotko, E. 2001 Spatial theory of optimal disturbances in boundary layers. *Physics of Fluids* **13** (7), 2097–2104.

Tyliszczak, A. & Boguslawski, A. 2007 LES of Variable Density Bifurcating Jets. In *Complex Effects in Large Eddy Simulations* (ed. Stavros C. Kassinos, Carlos A. Langer, Gianluca Iaccarino & Parviz Moin), pp. 273–288. Berlin, Heidelberg: Springer Berlin Heidelberg.

Van Dyke, M. 1964 *Perturbation Methods in Fluid Mechanics*, 1st edn., *Applied Mathematics and Mechanics: an International Series of Monographs*, vol. 8. New York: Academic Press.

Vernet, R., Thomas, L. & David, L. 2009 Analysis and reconstruction of a pulsed jet in crossflow by multi-plane snapshot POD. *Experiments in Fluids* **47**, 707–720.

Von Helmholtz, H. 1868 XLIII. On discontinuous movements of fluids. *The London, Edinburgh, and Dublin Philosophical Magazine and Journal of Science* **36** (244), 337–346.

Wang, C., Lesshafft, L., Cavalieri, A.V.G. & Jordan, P. 2021 The effect of streaks on the instability of jets. *Journal of Fluid Mechanics* **910**, A14.

Wang, K., Smith, O. & Karagozian, A. 1995 *In-flight imaging of transverse gas jets injected into subsonic and supersonic crossflows*, pp. 1–9. AIAA.

Wang, S. & Rusak, Z. 1996 On the stability of an axisymmetric rotating flow in a pipe. *Physics of Fluids* **8** (4), 1007–1016.

Watkins, D.S. 2000 Performance of the QZ Algorithm in the Presence of Infinite Eigenvalues. *SIAM Journal of Numerical Analysis* **22** (2), 364–375.

Xu, H.H.A. & Yang, X.I.A. 2021 Treatment of unphysical numerical oscillations via local grid refinement. *Physics of Fluids* **33** (7), 077104.

Zang, Y., Street, R.L. & Koseff, J.R. 1994 A Non-staggered Grid, Fractional Step Method for Time-Dependent Incompressible Navier-Stokes Equations in Curvilinear Coordinates. *Journal of Computational Physics* **114** (1), 18–33.

Zaturska, M.B. & Banks, W.H. 1995 Flow in a pipe driven by suction at an accelerating wall. *Acta Mechanica* **110**, 111–121.

Zayko, J., Teplovodskii, S., Chicherina, A., Vedeneev, V. & Reshmin, A. 2018 Formation of free round jets with long laminar regions at large Reynolds numbers. *Physics of Fluids* **30** (4), 043603.

Zhong, X. 1998 High-Order Finite-Difference Schemes for Numerical Simulation of Hypersonic Boundary-Layer Transition. *Journal of Computational Physics* **144** (2), 662–709.

Zikanov, O.Y. 1996 On the instability of pipe Poiseuille flow. *Physics of Fluids* **8** (11), 2923–2932.

Zwietering, T. 1959 The degree of mixing in continuous flow systems. *Chemical Engineering Science* **11** (1), 1 – 15.